

# Simulation and Optical Analysis of Objects Re-entering Earth's Atmosphere:

On the Detection and Tracking of Meteors and  
Re-entering Capsules Observed from GEO

---

by Rimsky Wolfs

M A S T E R   T H E S I S

15 APRIL 2019



# Master Thesis

## Simulation and Optical Analysis of Objects Re-entering Earth's Atmosphere:

On the Detection and Tracking of Meteors and Re-entering  
Capsules Observed from GEO.

by

Rimsky Wolfs

to obtain the degree of Master of Science  
at the Delft University of Technology,  
to be defended publicly on May 3, 2019 at 13:00.

April 15, 2019

Student number: 4017536  
Project duration: May 1, 2018 – April 15, 2019  
External supervisor: Dr. S. Stabroth, Airbus, supervisor  
Thesis committee: Dr. B. Root, TU Delft, supervisor  
Dr. E.J.O. Schrama, TU Delft, chair  
Dr. J.M. Kuiper, TU Delft, committee member

This thesis is **CONFIDENTIAL** and cannot be made public until April 15th, 2024.  
An electronic version of this thesis will then be available at <http://repository.tudelft.nl/>.

*Cover: Made by my sister T. Wolfs. The image of the Earth is a copyright free image from NASA.*



# AIRBUS

## Academic thesis at Airbus Defence and Space

### Confidentiality agreement and restriction notice

The academic thesis entitled "Simulation and optical analysis of objects re-entering Earth's atmosphere" contains sensitive internal information/data belonging to Airbus Defence and Space GmbH (henceforth "Airbus");

In accordance with the legal obligations of the university, the work will be placed under embargo in the library repository of the university for five years following its publication;

During the embargo period, this work will only be viewed by experts designated by Airbus as well as by authorized members of the examination board designated by TU Delft;

During the embargo period, the academic work, including in digital form, will only be reproduced or published, in whole or in part, with the express written consent of Airbus;

During the embargo period, third parties may only access this work with the express written consent of Airbus.

### Mentor and departmental manager (Airbus Defence and Space):

Sebastian Stabroth



Axel Wagner

Place / Date / Signature 19.03.2018



Student

Rimstey Wolfs  


Place / Date / Signature

19.03.2018

immerstaed

### Mentor (university)

Surname, first name, address

Bart Root, TU Delft, Kluyverweg 1, 2629 HS Delft



Place / Date / Stamp / Signature

Delft 20/03/2018



*I would rather be a superb meteor, every atom of me in magnificent glow, than a sleepy and permanent planet.*

–Jack London



# Summary

Meteors, or more commonly known as shooting stars, have been observed by humans since the ancient civilizations. Accidental detections of this phenomenon have occurred from geostationary orbit (GEO) by weather, reconnaissance and other Earth observation satellites. Not all of the data of the accidental detections of meteors is open to the public. Therefore, it is of interest for surveillance and meteor science to investigate a dedicated meteor observation satellite system. The main focus is on what optical instruments are needed in GEO to detect and track meteors. Since it is at the same time also interesting to look at other re-entering objects, re-entering capsules are investigated as well, next to meteors.

In order to determine what optical instruments are needed to detect and track meteors and re-entry capsules, these objects their re-entry characteristics should be known. In order to fill the gap between the available and needed re-entry data on both objects, a re-entry simulation code is written. This code takes into account the ballistic trajectory dynamics, aerothermodynamics, and, in case of meteors, fragmentation to determine an object's fingerprint during the whole re-entry. A fingerprint is a term used for an object's typical values during re-entry, such as, but not limited to, velocity, flight path angle, size, surface temperature, luminosity, emitted spectral irradiance and duration in which it is observable.

The simulated re-entry data is used to determine what optical instrument is needed to detect or track meteors and re-entry capsules. This is done for wavelengths between 100 nm and 3000 nm, for detector integration times between 10 ms and 1 second, at a bandwidth of 100 nm. The calculations take into account the reflected sunlight, Earth's thermal irradiance and atmospheric transparency. The limited signal-to-background ratio and signal-to-noise ratio are leading parameters to determine the found optical instrument's theoretical performance. The most important determined optical instrument parameters are aperture diameter and the focal length. For each different object the smallest physical possible system, with at least an aperture diameter smaller than 1 meter, is prioritized and proposed as a final optimal solution. The difference between the detecting and tracking solutions is that for detecting the object is visible in just one observation, and for tracking the object is visible in at least 3 consecutive observations.

From the meteor re-entry simulations done over a wide range of velocities and masses it can be concluded that meteors have a maximum luminosity between  $5 \times 10^2$  W and  $2 \times 10^{11}$  W. Furthermore, their peak luminosity altitude is in between 26 km and 70 km altitude, meteors of less than 1,000 kg have durations shorter than half a minute, and per day between 3,000 and 250,000 meteors heavier than 0.1 gram enter Earth's atmosphere. In the simulations the trajectory was simulated with a maximum of 10% velocity error, the peak absolute magnitudes could be matched with observational data with at most 0.4 absolute magnitude error and fragmentation was successfully validated. However, from an internal check in the code it was concluded that the luminosities calculated can have errors of significant amounts. This is probably due to the not used temperature gradient over the surface of the meteors, the sublimation reduction fraction used and the incorporated fragmentation.

The re-entry simulations of the 2 investigated Hayabusa and Stardust capsules could be done with much smaller errors as for meteors. The velocity error during re-entry was at most 0.3 km/s and the surface temperature errors calculated were never more than 4-8 % compared to other researches.

With the simulated re-entry data the optical instrument parameters were determined for 5 meteors and the Hayabusa and Stardust re-entry capsules. All determined minimal apertures and focal lengths for tracking were larger or equal than for detecting. Furthermore, daytime observations always require larger apertures than nighttime observations.

All 5 meteor and capsule detecting aperture diameters found were smaller than 1 m. For 5 second tracking only 3 of the 5 meteors could be tracked with a sub 1 m aperture. When reducing the tracking time for some meteors, for all meteors a sub 1 m aperture could be found for which at least 2 or 3 consecutive observations could be made. Taking into account the errors in the meteor found luminosity, the apertures might need to be increased by maximum 25-220%, and can in some cases be reduced by 68%. 4 out of 5 solutions would still have aperture diameters below 1 meter in size. The aperture diameters needed for detecting or 20 second tracking of the two capsule were in all cases 10 cm.

With the outcome of the research it has been shown that instruments with aperture diameters smaller than 1 meter can track re-entry capsules like Hayabusa and Stardust. Furthermore, meteors with an absolute

magnitude of minimal -2.9 can be tracked as well with sub 1 meter aperture diameters. In order to update meteor influx models with a GEO satellite system, or to track capsules like Stardust every second with a GEO satellite system, less than 1 cubic meter of space is required on a GEO satellite.

# Acknowledgments

Hereby I want to thank all the people that made the writing of this thesis achievable and durable. First I want to thank both my supervisors Bart Root and Sebastian Stabroth for guiding me and keeping me at the tip of my toes to achieve a good and useful results. I want to thank them both, representing the TU Delft and Airbus respectively, for allowing and creating this collaboration. Next to that also Daphne Stam gave some really useful feedback during my mid-term review, which has undoubtedly added to the quality of the overall work. Secretary Relly van Wingarden has been very helpful in the last few weeks of the project, regarding the logistics. Next to that my mom and dad have been helpful during my all phases of the research.

As for the non-direct thesis related people, I want to thank all my friends I made during my time in Konstanz, helping it become the best abroad experience so far. Also my friends back at home have been there for me all the time.



# Contents

<b>Summary</b>	<b>vii</b>
<b>Acknowledgments</b>	<b>ix</b>
<b>List of Abbreviations</b>	<b>xv</b>
<b>List of Symbols</b>	<b>xvii</b>
<b>1 Introduction</b>	<b>1</b>
1.1 The Meteor Phenomenon . . . . .	2
1.2 Re-entry Capsules . . . . .	4
1.3 Optical Geostationary and Geosynchronous Satellite Systems . . . . .	4
1.4 Research Questions . . . . .	5
1.5 Outline Report . . . . .	5
<b>2 Methodology</b>	<b>7</b>
2.1 Re-entry Simulation . . . . .	8
2.1.1 Re-entry Simulations by Propagating the Object States . . . . .	8
2.1.2 Trajectory Dynamics . . . . .	9
2.1.3 Fragmentation . . . . .	11
2.1.4 Aerothermal Aspects . . . . .	12
2.1.5 Luminosity, Filter Bands and Absolute Magnitude . . . . .	13
2.2 GEO Optical Instrument Parameter Determination . . . . .	15
2.2.1 Procedure for Calculating Optical Instrument Parameters . . . . .	15
2.2.2 Signal, Background and Noise Ratios . . . . .	17
2.2.3 Atmosphere, Reflectance and Earth's Thermal Irradiance . . . . .	19
2.2.4 Iterative Optical Instrument Parameter Calculations . . . . .	19
2.2.5 Detecting Versus Tracking Solutions . . . . .	20
<b>3 Verification and Validation</b>	<b>23</b>
3.1 Re-entry Simulations . . . . .	23
3.1.1 Capsule Trajectory Verification and Validation . . . . .	23
3.1.2 Stardust and Hayabusa Capsule Absolute Magnitude Validation . . . . .	23
3.1.3 Stardust and Hayabusa Capsules as Validation for Aerothermodynamics . . . . .	25
3.1.4 Meteor Trajectory Validation . . . . .	27
3.1.5 Assessment of Validation Data of Meteor Luminosities from Other Researches . . . . .	28
3.1.6 Validation of the Heat Flux Model with the Empirical Luminosities for Meteors . . . . .	30
3.1.7 Meteor Fragmentation Model . . . . .	31
3.1.8 Summary on the Validation of Re-entry Simulations . . . . .	33
3.2 GEO Optical Parameter Determination . . . . .	34
3.2.1 The DSP, DoD and DoE Satellite Meteor Observations as Validation . . . . .	34
3.2.2 Verification and Validation of the Reflected Sunlight and Atmosphere Model . . . . .	36
<b>4 Results</b>	<b>37</b>
4.1 Meteor Re-entry Simulations and Instrument Determination . . . . .	37
4.1.1 Meteor State Fingerprints . . . . .	37
4.1.2 Meteor Influx Rates . . . . .	39
4.1.3 Selected Sample Meteors . . . . .	42
4.1.4 Meteor Detection . . . . .	44
4.1.5 Meteor Tracking . . . . .	50
4.1.6 Preliminary Summary on Meteors . . . . .	53

4.2	Capsule Re-entry Simulations and Instrument Determination	54
4.2.1	Re-entry Capsules State Fingerprints	54
4.2.2	Re-entry Capsules Detection	54
4.2.3	Re-entry Capsules Tracking	56
4.2.4	Preliminary Summary on Re-entry Capsules	58
4.3	Analysis of Results Quality	59
4.3.1	Resolution of Bandwidth and Integration Time	59
4.3.2	Tracking Time Influence	62
4.3.3	Some Results from 3000 nm till 8000 nm Wavelengths	63
<b>5</b>	<b>Discussion</b>	<b>65</b>
5.1	The Re-entry Simulations of Meteors and Capsules	65
5.1.1	Meteor Fingerprints	65
5.1.2	Meteor Influx Rates	66
5.1.3	Meteor Validation Implications and Fragmentation Uncertainties	67
5.1.4	Capsule Fingerprints	68
5.1.5	Capsule Aerothermodynamics Uncertainties	68
5.2	GEO Optics Instrument Parameter Calculations	69
5.2.1	The Detection and Tracking of Each of the 7 Objects	69
5.2.2	Tracking Observations and Extractable Data Thereof	70
5.2.3	Integration Time, Ground Resolution and Bandwidth Interactions	71
5.2.4	Difference between Day and Night Observations	73
5.2.5	Telescope Limitations and Unaccounted for Detector Characteristics	74
5.3	Other Interesting Observable Phenomena	75
5.3.1	Space Debris	75
5.3.2	Space Planes	76
5.3.3	Nuclear Detonations	76
5.3.4	Rocket Launches and Ballistic Missiles	76
5.3.5	Lightning Strikes	77
5.3.6	Classification Based on Fingerprints	78
5.4	Possible Satellite Systems Based on This Research	78
<b>6</b>	<b>Conclusion and Recommendations</b>	<b>83</b>
6.1	Conclusion	83
6.2	Recommendations	86
6.2.1	Possible Updates to This Work	86
6.2.2	Follow-up Work	88
	<b>Appendices</b>	<b>89</b>
<b>A</b>	<b>Data on Different Detector Sensors</b>	<b>91</b>
<b>B</b>	<b>Code Layout</b>	<b>93</b>
<b>C</b>	<b>Assumptions List for Both Written Codes</b>	<b>95</b>
C.1	Assumptions on the Re-entry State Simulation	95
C.2	Assumptions on the GEO Instrument Parameter Determination	95
<b>D</b>	<b>Input Data for Re-entry Simulations</b>	<b>97</b>
D.1	Meteors	98
D.1.1	Small Generic Meteors	98
D.1.2	Chelyabinsk	98
D.2	RE-entry Capsules	100
D.2.1	Stardust	100
D.2.2	Hayabusa	100

---

<b>E</b>	<b>Circle Overlap Calculations in a Square</b>	<b>101</b>
<b>F</b>	<b>The Halliday Correction Factor</b>	<b>103</b>
<b>G</b>	<b>All Results for Instrument Parameter Calculations Per Object</b>	<b>105</b>
G.1	Met1Model . . . . .	106
G.2	Met2Rate . . . . .	108
G.3	Met3Common . . . . .	110
G.4	Met4VV . . . . .	113
G.5	Met5Pers . . . . .	115
G.6	Hayabusa . . . . .	118
G.7	Stardust . . . . .	120
	<b>Bibliography</b>	<b>123</b>



# List of Abbreviations

<b>ATV</b>	Automatic Transfer Vehicle
<b>BSI</b>	Back Side Illuminated
<b>CCD</b>	Charge-Coupled Device
<b>FCM</b>	Fragment-Cloud Model
<b>DoE</b>	Department of Energy
<b>DoD</b>	Department of Defense
<b>DSP</b>	Defense Support Program
<b>FWHM</b>	Full Width at Half Maximum
<b>GEO</b>	Geostationary Orbit
<b>GLM</b>	Geostationary Lightning Mapper
<b>GNU</b>	GNU's Not Unix! (Operating system)
<b>GOES</b>	Geostationary Operational Environment Satellite
<b>GPS</b>	Global Positioning System
<b>GSO</b>	Geosynchronous Orbit
<b>ISS</b>	International Space Station
<b>IWM</b>	Independent Wake Model
<b>MORP</b>	Meteor Observation and Recovery Project
<b>MSSWG</b>	(Japanese) Meteor Science Seminar Working Group
<b>MWIR</b>	Medium Wave Infrared / Mid-wave infrared
<b>NASA</b>	National Aeronautics and Space Administration
<b>NEP</b>	North Ecliptic Pole
<b>NREL</b>	National Renewable Energy Laboratory
<b>PSF</b>	Point Spread Function
<b>RAM</b>	Random Access Memory
<b>SBIRS</b>	Space-Based Infrared System
<b>SBR</b>	Signal-to-Background Ratio
<b>SCNR</b>	Signal-to-Clutter-and-Noise Ratio
<b>SNR</b>	Signal-to-Noise Ratio
<b>SWIR</b>	Short Wave Infrared
<b>TU</b>	Technische Universiteit / University of Technology
<b>UTC</b>	Coordinated Universal Time



# List of Symbols

Symbol	Unit	Description	Value
$\alpha$	–	Strength Scaling	
$\beta$	$m^{-1}$	Inverse scale height	
$\Delta\lambda$	$Hz$	operating bandwidth	
$\delta$	$deg$	Latitude	
$\eta$	$rad$	Sensor look angle	
$\gamma$	$rad$	Flight path angle	
$\gamma_E$	$rad$	Entry flight path angle	
$\lambda$	$m$	Wavelength	
$\mu$	–	Rotation constant	
$\pi$	–	Mathematical constant Pi	3.14159
$\rho$	$kg/m^3$	Density	
$\rho_0$	$kg/m^3$	Density atmosphere at sea level	1.225
$\rho_a$	$kg/m^3$	Density atmosphere	
$\rho_E$	$rad$	Angular radius of Earth	
$\rho_m$	$kg/m^3$	Density meteoroid	
$\sigma$	$W/(m^2K^4)$	Stefan-Boltzmann constant	$5.67051 \times 10^{-8}$
$\sigma$	$MPa$	Strength	
$\tau$	–	Transmission factor	
$\tau$	$deg$	Longitude	
$\tau(\lambda)$	–	Transmissivity of wavelength $\lambda$	
$\tau_0$	–	Luminosity coefficient	
$\theta$	$rad$	Angle between centers of point sources	
$\theta_r$	$rad$	Rayleigh limit	
$\varepsilon$	–	Emissivity	
$\varepsilon$	$rad$	Elevation angle	
$\xi$	$Kj/mol$	Heat of sublimation	
$b$	$Km$	Wien's constant	$2.89777 \times 10^{-3}$
$c$	$m/s$	Speed of light	$2.99792458 \times 10^8$
$c_d$	–	Aerodynamic drag coefficient	
$c_h$	–	Heat transfer coefficient	
$c_l$	–	Lift coefficient	
$d'$	$m$	Diameter of diffraction disk	
$d$	$m$	Pixel size	
$D$	$m$	Diameter of aperture	
$D$	$N$	Drag	
$d_{max}$	$m$	Maximum distance	
$E$	$J$	Energy	
$E$	$W/m^2$	Irradiance / Flux density	
$E_\lambda$	$W/m^3$	Spectral irradiance at wavelength $\lambda$	
$f$	$m$	Focal length	
$FOV$	$deg$	Field of view of sensor	
$g$	$m/s^2$	gravitational acceleration	
$G$	$m^3/kg/s^2$	Gravitational constant	$6.67408 \times 10^{-11}$
$g_0$	$m/s^2$	gravitational acceleration at Earth surface	9.81
$h$	$Js$	Planck's constant	$6.626075 \times 10^{-34}$
$h$	$m$	Height / Altitude	
$h_0$	$m$	Scale height	
$I$	$W$	Luminosity	
$I_m$	$W$	Luminosity meteoroid	
$I_p$	$W$	Luminosity particle	

Symbol	Unit	Description	Value
$IFOV$	$deg$	Instantaneous field of view of pixel	
$k$	$Ws/K$	Boltzmann's constant	$1.380658 \times 10^{-23}$
$L$	$N$	Lift	
$L$	$W/m^2/sr$	Radiance	
$L$	$W/sr$	Radiant intensity	
$L_\lambda$	$W/m^2/\mu m/sr$	Spectral radiance	
$L_{int}$	$W/m^2/sr$	Integrated upwelling radiance over bandwidth	
$L_{upi}$	$W/m^2/\mu m/sr$	Upwelling radiance	
$L_E$	$W/sr$	Radiant intensity of Earth's surface	
$L_o$	$W/sr$	Radiant intensity of object	
$m$	–	Magnitude	
$M$	$kg$	Mass	
$M_e$	$kg$	Mass at entry	
$M_m$	$kg$	Mass of meteoroid	
$M_p$	$kg$	Mass of particle	
$N$	$px$	Number of pixels	
$N_m$	–	Pixels in sensor	
$N_n$	–	Noise electrons	
$N_p$	–	Available photons	
$N_r$	–	Read-out noise electrons	
$N_t$	–	Total amount of noise electrons	
$P_D$	$W$	Detector input power	
$P_{in}$	$W$	Input power	
$Q$	–	Quality factor	
$\dot{q}$	$W/m^2$	Heat flux	
$\dot{q}_c$	$W/m^2$	Convective heat flux	
$\dot{q}_r$	$W/m^2$	Radiative heat flux	
$QE$	–	Quantum efficiency	
$R$	$m$	Radius of object	
$R_{max}$	$m$	Maximum range	
$R_E$	$m$	Equatorial radius of Earth	6,378,136
$R_N$	$m$	Nose radius	
$R_o$	$m$	Radius object	
$R_S$	$m$	Slant range	
$S$	$m^2$	Effective middle cross-section	
$S_m$	$m^2$	Effective middle cross-section meteoroid	
$S_p$	$m^2$	Effective middle cross-section particle	
$SNR$	–	Signal to noise ratio	
$T$	$K$	Temperature	
$t$	$s$	Time	
$T_d$	$s$	Detector time constant	
$T_i$	$s$	Integration period	
$V$	$m/s$	Velocity	
$V_e$	$m/s$	Entry velocity	
$W$	$N$	Weight	
$W_b$	$W/m^2$	Total radiance emittance / Irradiance / Flux density	
$X'$	$m$	Cross-track ground resolution	
$X$	$m$	Pixel cross-track ground resolution	
$X_{max}$	$m$	Maximum pixel cross-track resolution	
$Y$	$m$	Pixel along-track ground resolution	
$Y_{max}$	$m$	Maximum pixel along-track resolution	
$Z$	–	Total pixel count	
$Z_a$	–	Along track pixel count	
$Z_c$	–	Cross-track pixel count	

# Introduction

Imagine yourself on a warm summer night on a beach, while the waves softly touch the still warm sand. You are lying on your back and watch the clear and pitch dark sky with its millions of stars. All of a sudden you see a shooting star of merely a second long crossing in between the constellations of Ursa Minor and Cassiopeia. Little do you know that it comes from far away in the Solar system and brings a history of billions of years back to Earth.

Probably everyone has seen a shooting star, or scientifically called a meteor, in his or her life. Although this phenomenon has already been seen since the ancient Egyptian, Chinese and Japanese civilizations, not yet everything about these bright objects is well understood (Beech, 1987). For example, in the wake of the meteor the trail of particles light up and sometimes a faint colorful train can be seen for several minutes after the meteor has disappeared (McKinley, 1961). Especially this last phenomenon has had many different explanations on how it comes to life; from a purely atmospheric phenomenon to that of still burning vapors, and most recently being believed to be the result of excited air molecules reverting back to their original state emitting light in the process (Beech, 1987). In order to get a better understanding of the whole meteor phenomena, specialized meteor observations networks emerged, of which the first in 1936 and a small peak of new networks occurred in the last 20 years (Gritsevich, 2009).

A lot of research has been done on meteors (Ceplecha et al., 1998), however the group of dedicated researchers is still quite small compared to some other disciplines. The knowledge gained from meteors might tell us more on how the solar system formed, where their parent bodies are, and might even tell us something on the origin and history of life<sup>1</sup>. Not many dedicated space borne systems exist for observing meteors<sup>2</sup>, however, in some Earth observation, weather and reconnaissance satellites meteors have been observed by accident (Tagliaferri et al., 1994, 1995). Even meteors have been observed from the International Space Station<sup>3</sup>, a photo of such a meteor event is given in Figure 1.1. Not all of the observation data of meteors is open to the public, especially the (high resolution) reconnaissance based observations, and therefore ideas exist to look into dedicated meteor observation satellite systems (Ortega, 2016). Observations have also been made of artificial "meteors" including imitation meteors, space debris and re-entry of man made vehicles, like capsules, missiles and space planes (Ayers et al., 1970; Grinstead et al., 2011; Trumble et al., 2010; Kellogg and Passman, 1955; Horvath et al., 2007).

In the interest of increasing the understanding of non-accidental meteor and capsule re-entry observations, a feasibility study into the re-entry and optical observation possibilities from a Geo Synchronous Orbit (GSO) or Geo Stationary Orbit (GEO) is presented. For example, observations of meteors add to the further tuning of empirical models, and observations of capsules could be used as validation data for re-entry models (Szasz et al., 2005; Hawkins and Upton, 1958; Ueda et al., 2011). Later, a similar research could be performed to extend the observations to other objects like space debris, ballistic missiles and space planes. However, capsules are a good starting point, since theoretical models and observations already exist (Suzuki et al., 2014; Löhle et al., 2013). The added GEO aspect will allow for a coverage of any part of the Earth's atmosphere. The aim is to simulate the re-entry of those objects and assess what instrument is needed to observe these re-entries from GEO, based on their calculated emissions. Furthermore, on the other non-investigated

<sup>1</sup>"Why are meteorites important?" meteorites.asu.edu <https://meteorites.asu.edu/meteorites/importance-of-meteorites> (Accessed July 9, 2018).

<sup>2</sup>"ISS: Meteor." directory.eoportal.org <https://directory.eoportal.org/web/eoportal/satellite-missions/content/-/article/iss-meteor> (Accessed July 9, 2018).

<sup>3</sup>"Meteor Investigation Makes a Quick Recovery" www.nasa.gov [https://www.nasa.gov/mission\\_pages/station/research/news/meteor\\_investigation](https://www.nasa.gov/mission_pages/station/research/news/meteor_investigation) (Accessed March 8, 2019).

re-entry objects that could be observed; due to the complexity of space debris, as shown for example by [Klinkrad \(2005\)](#), it is left out of the core of this research. Missiles are left out since not enough information can be found on such objects publicly. Since space planes mostly heat up on the belly, or Earth facing side of the vehicle, these are also not investigated for now ([Horvath et al., 2007](#)).

Meteors and capsules will be discussed below briefly, to allow the reader to get familiar with the two different objects or to refresh the knowledge. Furthermore, some known GEO satellite systems will be presented that currently exist and could possibly observe meteors and capsules. After that the research questions will be presented, which form the basis for the rest of the research in this thesis.



Figure 1.1: Perseid meteor photographed from the International Space Station as seen past a solar panel (right) and a docked spacecraft (left).

## 1.1. The Meteor Phenomenon

The meteor phenomenon happens when a meteoroid re-enters in a planetary atmosphere. Such a re-entry will in most cases look similar to the one in [Figure 1.1](#). In that figure a presumed Perseid<sup>4</sup> meteoroid enters and burns up in Earth's atmosphere at about 61 km/s in less than 1 second ([Jenniskens, 2014](#); [Halliday et al., 1996](#)). In this section a basis for the understanding of meteors is presented, from naming conventions to some more scientific information like typical velocities, masses and temperatures.

First the difference between meteor, meteoroid and meteorite needs to be clarified. A meteor is the scientific name for the light emitting phenomenon that we also call a shooting or falling star, so it is not the object itself. When a meteor is very bright (absolute magnitude<sup>5</sup> > -8), the term fireball is sometimes used, and when it detonates the name bolide can be given. The physical object itself that burns up is called a meteoroid, it can originate from an asteroid, comet or other orbiting body that crosses path with Earth's orbit and leaves material behind. A sporadic meteor is a meteor not belonging to a timely event, whilst a meteor shower is usually a collection of meteors directly and predictably correlated to a parent body. A meteorite is the meteoroid after it has survived the re-entry and has landed on the Earth's surface. Thus meteorites are the leftovers of the meteor phenomenon ([Ceplecha et al., 1998](#)).

Different phases can be identified during the whole meteoroid's path to the Earth surface. First, the meteoroid orbits the Sun after being separated from its parent body. Usually this separation occurred long before its getting caught by the gravity of the to be re-entered body. The perturbation redirects the meteoroid towards the surface of the body. Then, the preheating phase starts, at a height of 300 km altitude (in case of Earth) the meteoroid encounters the first atmospheric atoms and molecules. During this preheating phase sputtering might occur, which leads to the first ionization of atmospheric particles that the meteoroid encounters ([Vojacek, 2011](#)). As soon as the meteoroid plunges into the thicker parts of the atmosphere, the meteoroid gets heated up more and starts to melt, evaporate and possibly fragmentate. This stage is called

<sup>4</sup>Perseid is a name for a meteor belonging to the Perseid meteor shower that occurs every year around July to August. Perseids are dust particles left over by the comet Swift-Tuttle. Their name comes from the fact that they appear from the constellation Perseus ([Ceplecha et al., 1998](#)).

<sup>5</sup>The absolute magnitude is a way to describe the brightness of an object, similar to the apparent magnitude. A magnitude of 0 is the brightness of the star Vega, taken as basis for the apparent magnitude. The Sun has an apparent magnitude of -26.74, so the lower the value the brighter the object. It is furthermore based on a logarithmic scale with magnitude +6 being 100 times more bright than an object with magnitude +1. However, for meteor scientists it is most common to define the absolute magnitude as the brightness compared to a 100 km altitude 0 magnitude meteor. The absolute magnitude should not to be confused with the absolute magnitude of stellar astronomy, which is defined as the brightness as seen from 10 parsecs. The reference luminosity in Watts for the meteor absolute magnitude has been determined by different researchers, ranging from 270 to 1800 Watts ([Weryk and Brown, 2013](#); [Halliday et al., 1996](#)).

the ablation stage and is the stage in which the meteor phenomenon becomes most apparent. It is also the stage that is most important for this research, since the meteoroid reaches the highest temperature during its re-entry and thus emits the most radiation. After this stage, if there is enough material left, the meteoroid enters a dark flight. The meteoroid has become too slow to ablate or emit visible light. The dark flight can take several minutes before the meteoroid lands on the surface and becomes a meteorite (Ceplecha et al., 1998).

Some special phenomenon can happen to meteors during their ablation phase. Meteor flares can happen; a sudden increase in brightness of at least one magnitude. The reason for this can be sudden fragmentation or a sudden change in physical circumstances, increasing the evaporation for example. The phenomenon of fragmentation can be, and was certainly for big meteors like Park Forest, Marshall Island and Chelyabinsk, of big influence on the brightness of the meteor (Brown et al., 2004; Tagliaferri et al., 1995; Popova et al., 2013a). Luckily, meteor fragmentation can be simulated with models (Register et al., 2017; Mathias et al., 2017), although small changes to the inputs, like aerodynamic strength, can have a big influence on the outcome of the simulation. Therefore, the inputs are usually determined based on found left over pieces from the respective meteoroid if possible (Popova et al., 2013a).

During a meteor event also meteor trails can occur. This is a phenomenon in which there is radiation in the wake behind the meteor, opposed to the head radiation directly surrounding the meteor. Usually the trail's origin is the deceleration of small ablated particles or gas from the meteoroid itself that emit radiation. The duration of the trail is usually several tenths of seconds and the trail's dimension can be several hundred meters to kilometers behind the meteor (McCrosky, 1958; Bronshten, 1983).

The last known phenomenon is the meteor (ion) train, which is a radiation emitted after the meteoroid's passing for several seconds or minutes. Most of the spectral lines originate from neutral or ionized oxygen and active nitrogen from the interaction of the meteor particles with the air, instead of the particles from the meteoroid itself (Beech, 1987; Bronshten, 1983; McCrosky, 1958). Some trains might have different colors ranging from red to green to yellow (Beech, 1987) and some trains may last for hours (Ceplecha et al., 1998).

Most meteors that are visible to the naked eye originate from meteoroids larger than 1 mm (Ceplecha et al., 1998). Meteoroids of bigger sizes, with diameters ranging from 1.9 m to 20 m and masses from 11,000 kg to 13,000,000 kg, do exist, such as the Park Forest (Brown et al., 2004), Marshall Island (Tagliaferri et al., 1995) and Chelyabinsk (Popova et al., 2013a) meteors as introduced before.

The entry velocity of meteors in Earth's atmosphere is restricted by two bounds. The lower limit is at 11.2 km/s due to a meteoroid only being influenced by Earth's gravity, this is the lowest velocity a meteor can have. The upper limit is at 72.8 km/s due to Earth's velocity of 30.3 km/s at its perihelion plus the meteoroids 42.5 km/s at its perihelion when it comes in contact with Earth (Ceplecha et al., 1998).

During re-entry the surface temperatures of the meteoroids may rise as high as 2200 K during the ablation phase, usually between 80–90 km, at which material starts to sublime and starts to surround the meteoroid body. The light emitted by the meteoroid consist usually of discrete emission spectral lines belonging to the materials the meteoroid usually consists of metals like iron. About 90% of the meteor's light comes from the single-excited atoms of meteoroid material that start to radiate. This can be several electron Volts (eV) and temperatures can be between 3,000 K and 5,000 K. The air and gasses behind the body can be even hotter than 10,000 K, depending on the entry velocity (Silber et al., 2017). The ablation phase slows down the meteoroid and after several tens of kilometers it may lose all its mass and stop emitting light. During this phase it slows down only a few percent with respect to its initial velocity (Ceplecha et al., 1998).

The time, location and season of the observer's location on Earth do play a role on when meteors can be seen. Most meteor events happen in the first half of the day between 00 : 00 UTC and 12 : 00 UTC (Szasz et al., 2005). That most meteor events happen during the first half of the day is explained by the fact that the 6 : 00 UTC time line is equal to the eclipse line, which points in positive along-track direction of Earth in its orbit. The Earth's eclipse line frontal area sweeps space, and thus comes in contact with more objects floating in space. The observer's latitude also plays an important role. When observing the North Ecliptic Pole (NEP) from Earth, a consistent lower meteor flux is observed during Autumnal Equinox, as well as a consistent lower flux overall compared to other viewing directions. This suggests that less meteoric events happen at the poles, compared to the overall number of events (Szasz et al., 2005). This shows that seasonal variations play a role in the latitudinal meteoric event flux.

So meteors re-entering Earth's atmosphere with a wide variety of entry velocity and masses exist, while exhibiting different phenomenon like trails, trains and fragmentation. Temperatures up to 10,000 K are not uncommon during the re-entry and their influx rate is highest near the equator in the Earth's positive along-track orbit direction, as on Earth between 00:01 and 11:59 UTC.

## 1.2. Re-entry Capsules

Unlike meteors, (ballistic) capsules are man made and re-enter usually at about equal or lower velocities than the slowest possible meteors at 11 km/s. Capsules may come from an interplanetary or lunar trajectory, like the Stardust and more recent Hayabusa sample-return missions entering at velocities of about 12 km/s (Loehle et al., 2017). In the past, in the Apollo program to the Moon, the capsules re-entered at velocities of 11.2 km/s. The Soyuz re-entry capsule used to get to the ISS and back enters usually at a much lower velocity of about 7.9 km/s (Hirschel and Weiland, 2009). Capsules have also been used on extraterrestrial bodies like Venus, Mars, Jupiter and Titan (Davies, 2006).

As with the meteors discussed before, heat is generated during capsule re-entry (Kellogg and Passman, 1955), this should make the re-entry passively observable and is assumed to be able to be simulated with ballistic object equations (Allen and Eggers, 1961; Mooij, 2016). Unlike meteors though, they do ideally not fragmentate and ablate just minimally.

The re-entry of some ballistic capsules has been filmed and photographed by amateurs, government instances and space agencies. For example, observations of the Hayabusa sample return capsule (and spacecraft) have been made during the controlled re-entry in the near-infrared, visible and ultra violet spectra from the ground and aircraft (Abe et al., 2011; Snively et al., 2014).

With the use of the visible and ultra violet observations, it was concluded that the gray-body temperature of the Hayabusa capsule reached about 2482 K at about 42.7 km. However, this was not the maximum temperature during the re-entry (Abe et al., 2011). The capsule had a maximum  $-4$  absolute magnitude at about 55 km compared to the burning accompanying Hayabusa spacecraft of maximum  $-12.6$  at 66.9 km. The work by Borovička et al. (2011) on the Hayabusa sample return capsule re-entry concludes that it was radiating dominantly in the visible spectrum by black-body radiation. Since there is almost no ablation, not so much radiation can be observed from released plasma compared to meteors.

Concluding, capsules are man made ballistic vehicles that re-enter usually at lower velocities than average meteors. Furthermore, they do not fragmentate and convert less lost kinetic energy into luminosity compared to meteors. Good observations have been made of some capsules like Hayabusa and Stardust.

## 1.3. Optical Geostationary and Geosynchronous Satellite Systems

A geostationary/geosynchronous satellite is a satellite that stays on the same longitude during its orbit. It orbits at such a velocity that it goes as fast as the Earth rotates underneath it. The altitude that corresponds to this orbit is roughly 35,800 km, about 6 times the radius of the Earth itself. Whether it is stationary or synchronous depends on the orbits inclination. If the orbit inclination is equal to the Earth's tilt and the right ascension of the ascending node is correctly chosen, the satellite will be above the same location on Earth during all its orbits. A synchronous orbit can have any inclination, but then the satellite will periodically change its latitude once per orbit.

Some geostationary and geosynchronous orbit satellite systems exist that observe the Earth in different spectra. For example, the American Space-Based Infrared System (SBIRS) (Everett, 1993) and Defense Support Program (DSP) (Lapin, 1975) observe Earth for ballistic missile launches and other phenomena in the infrared spectrum. Furthermore, weather satellites like the Geostationary Operational Environment Satellite (GOES)<sup>6</sup> and Meteosat (MSG)<sup>7</sup> observe the Earth's climate in both infrared and visible light spectrum. The Chelyabinsk meteor's trajectory could be determined with observations from the MSG satellites (Proud, 2013). Next to this also a Geostationary Lightning Mapper (GLM) with a resolution of 10 km and a 2 ms scan interval was proposed for GOES-NEXT satellite. The GLM is capable of observing meteors with a magnitude brighter than  $-13$  (Jenniskens et al., 2018). The SBIRS is also able to detect re-entering spacecraft and space debris<sup>8</sup>, making this system a good example for this research. The system is claimed to use two Short Schmidt Telescope sensors for its infrared observations, of which one short-wave infrared (SWIR) scanner with a 3 s revisit time (whole Earth) and 2 km footprint and a mid-wave infrared (MWIR) starrer with a 0.5 s revisit time and also a 2 km footprint in a 1000 km  $\times$  1000 km field-of-view (Everett, 1993).

These systems show that geostationary satellite systems exist and have been used to detect, sometimes accidentally, re-entries of meteors and ballistic missiles. None of them were specially designed for meteor or capsule observations, but it shows that a similar technology is feasible.

<sup>6</sup>"GOES-R Instruments." goes-r.gov. <https://www.goes-r.gov/spacesegment/instruments.html> (Accessed May 18, 2018).

<sup>7</sup>"Meteosat Design." Eumetsat.int. <https://www.eumetsat.int/website/home/Satellites/CurrentSatellites/Meteosat/MeteosatDesign/index.html> (Accessed May 18, 2018).

<sup>8</sup>"SBIRS Satellite Overview." spaceflight101.com. <http://spaceflight101.com/spacecraft/sbirs/> (Accessed May 18, 2018).

## 1.4. Research Questions

As explained before this research is focused on non-accidental observations of meteors and re-entry capsules, by looking into the possibilities of a GEO satellite systems needed instrument parameters. To determine what is needed for such a system, first the objects' characteristics should be known. A wide variety of data on meteors and re-entry capsules based on real observations can be found in literature (Halliday et al., 1996; Löhle et al., 2013). However, the data on meteors and capsules is in these cases limited to the available data. It is also of interest to be able to predict what the characteristics are of both the discussed re-entry objects with other entry or object conditions. Different entry velocities, angles and masses than the ones found in available data might want to be investigated, and therefore a re-entry simulator will be written. This re-entry simulator can then be used to determine and output typical characteristic values, like emissions, irradiance, wavelengths, velocities, orientation and more, for a re-entry of a specific object not found in readily available data.

The found characteristic parameters and their values over a whole re-entry trajectory of an object can be used to determine what a satellite instrument should look like in GEO. Using atmospheric, Earth reflection and Sun models together with optical calculations and different detector inputs, it is possible to get an estimation on what kind and what size of instrument is needed to observe the object for certain requirements (Wertz and Larson, 2010). These requirements can range from desired observation wavelength, tracking time, classification accuracy or otherwise desired. It is also of interest how the different requirements influence the to be designed optical instrument and detector settings. The size of the instruments aperture diameter is restricted to 1 m. This has to be done such that the calculated instrument parameters can be realized in a GEO satellite.

To get a structured approach to this problem the main research question can be formulated as follows:

*What are the typical optical instrument parameter values and detector settings needed to detect and track, meteors and capsules observed from GEO?*

This main research question can be subdivided into a set of sub research questions:

1. What are the characteristics of meteors regarding their observability during re-entry and how well can this be simulated?
2. What are the optical instrument parameter values and detector settings needed for a GEO satellite system to detect and track meteors?
3. What are the characteristics of re-entry capsules regarding their observability during re-entry and how well can this be simulated?
4. What are the optical instrument parameter values and detector settings needed for a GEO satellite system to detect and track capsules?
5. How does changing the detector settings or instrument parameters influence each other in general?

With the answers to these subquestions it should be possible to answer the main research question. Questions 1 and 2 deal with meteor re-entry simulation and their detecting and tracking, questions 3 and 4 extend this problem to re-entry capsules. Finally question 5 deals with the general influence of different detector settings on the needed instrument parameters values. In all the optical instrument findings the aperture diameter will be restricted to 1 m where possible.

## 1.5. Outline Report

The report is structured as follows: First the methodology on how the research will be conducted is given in Chapter 2. In this chapter the theory on the re-entry simulations and GEO optical instrument parameter calculations are discussed, as well as the written programs and the flow of information and parameters within those programs. After that the results of both these programs are verified and validated with the use of existing data in Chapter 3. The results of the research are given in Chapter 4, in which fingerprints, influx rates, detection and tracking solutions of meteors and re-entry capsules are given. In Chapter 5 the results are discussed. Also links between the research and other observable objects, telescope limitations and possible satellite systems will be addressed. After that the answers and recommendation with respect to the research and research questions are given in Chapter 6.



# 2

## Methodology

To find the instrument parameters values and detector settings that are needed to observe meteors and capsules, one needs to know how those objects can be detected. Since it is already given that the objects should be optically detected it is of importance to know how long and at what wavelengths meteors and capsules emit radiation that can be observed.

A re-entry simulation code is made to calculate the states of the re-entering objects over time. What a state exactly is will be explained in Section 2.1.1. From these states, the surface temperatures can be determined. The objects can be simulated for several entry conditions in order to determine the so called fingerprint of these objects. Fingerprints refer here to the ranges of typical values that those objects can have within their states, surface temperatures and observation wavelengths during re-entry.

It is an essential part to understand each of the objects as good as possible for the further optical analysis. This concludes then the first part of the research, when meteors and capsules have been simulated and their typical characteristics have been identified. With the obtained knowledge from the re-entry simulations it should be possible to answer questions 1 and 3,

From the calculated re-entry states of each of the to be investigated objects, optical instrument parameters for a GEO satellite system can be calculated for a given wavelength band and exposure time, such that the re-entering object can be detected. Optical instrument parameters calculated include for example: (effective) focal-length, aperture diameter, ground resolution, detector size, field-of-view, number of photon noise electrons and signal photon electrons (Wertz and Larson, 2010). The re-entry states of the objects are used for the GEO optical instrument parameter calculations. These states give the temperature and orientation of the object per time, and thus with that the irradiance of the object can be calculated per wavelength.

The needed signal-to-noise ratio (SNR) and signal-to-background-ratio (SBR) are of importance, because these determine if the object can be distinguished or filtered from the background in the observations by a computer algorithm. The background radiation is calculated with the reflected irradiance of the Sun by the Earth's surface and the thermal irradiance of the Earth itself. The background irradiance travels a long path through the atmosphere, so the absorption and transparency of the atmosphere is taken into account as well. If an object goes through multiple pixels per exposure, it means the signal in each pixel by the object is less than if it stays within the same pixel during that time. To address this, the effective SNR and effective SBR are calculated, based on the object's movement through the pixels.

In the calculations diffraction limited optical systems are assumed (Appeah, 2017; Giancoli, 2009). Diffraction limited means that the system's resolution performance is at the instrument's theoretical limit, as such that two point sources can just be distinguished.

Different detector inputs or settings, like for example, exposure time, integration time, readout time, detector noise, pixel pitch and quantum efficiency need to be taken into account as well. Example detectors can be found in Appendix A.

Furthermore, the instrument parameters are differently calculated for detecting and for tracking of the re-entering object. Detection is defined as such that an object is observed in only one exposure. This means the optical instrument parameters are calculated based on the maximum luminosity emitted by the object. Tracking is defined such that an object can be observed over a given time span in multiple exposures. This means a fraction of the maximum luminosity is used. The fraction is based on the defined tracking time, such that the object's luminosity during the tracking time is higher or equal to the to be used luminosity for the calculations.

With the detector inputs and settings, and the found optical instrument parameter values it is possible to answer questions 2, 4 and 5.

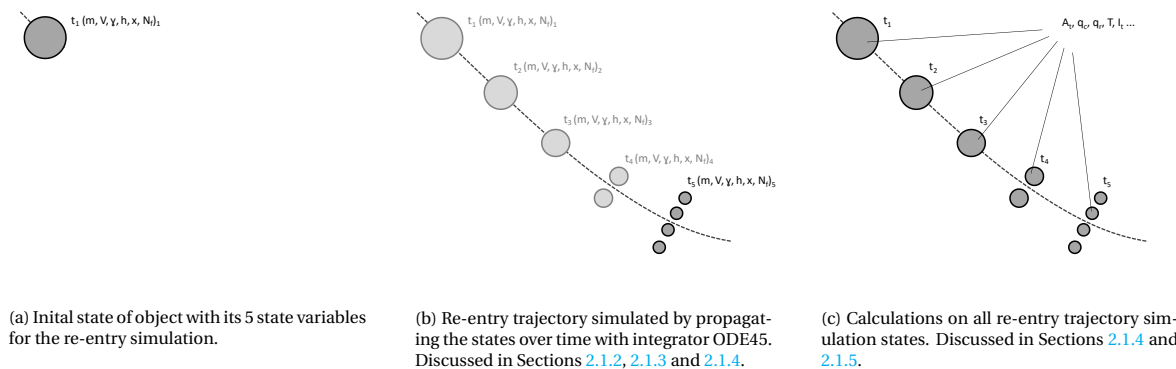


Figure 2.1: General steps within the re-entry simulation code. Initial state (a), state propagation (b) and post re-entry trajectory simulation calculations done on all calculated states along the trajectory (c). Not all variables are shown.

In order to answer question 5, the optical parameter calculations, as just discussed, can be ran for a set of different detector settings. For example, different exposure times and different observed wavelengths are used. The outcome will be a set of different optical instrument parameters. For the analysis changes will be made to: integration times, filter bandwidths, detector sensitive wavelengths and tracking time.

With the answers to the 5 subquestions the main research question can be answered, as giving a general answer on what typical optical instrument parameter values and detector settings are needed to detect and track meteors and capsules. Furthermore, the interactions between some changes in detector settings and the adjusted needed optical instrument parameter values are identified.

A code overview and a summary of the used assumptions can be found in Appendices B and C respectively. The theory of the code will be discussed in the two upcoming sections.

## 2.1. Re-entry Simulation

In this section the first part of the research is discussed with regard to the re-entry simulation code that calculates the so called fingerprints of the different objects during re-entry. The inputs for these simulations are given in Appendix D. A code overview can be found in Appendix B.

First the integration and propagation of the states is explained. Then the underlying trajectory dynamics that are integrated are derived and ablation is discussed. After that the fragmentation model used for meteors is explained. Then the aerothermal aspects during re-entry are addressed, which leads to the average temperature of the object. Finally the calculation of the spectral irradiance of the object and absolute magnitude are explained, and the filter bands used in this research are defined.

### 2.1.1. Re-entry Simulations by Propagating the Object States

It is of interest to know an object's fingerprint over its whole re-entry period. A fingerprint of an object can be derived from its velocity, size, altitude, orientation and some constant material properties. To address the fingerprint along the whole trajectory, it should be calculated at multiple points along the trajectory. At each of those points in time the object is in a certain object state. Such an object state is in this research defined with the following parameters: horizontal distance traveled  $x$ , current altitude  $h$ , current velocity  $V$ , current flight-path-angle  $\gamma$  and the current mass  $M$ .

A way to achieve these object states at every point in time, is to propagate the initial object state over time using an integrator. This starts at the moment the object encounters the first atmospheric particles, and it ends when the object does not have any significant mass, when it reaches a certain altitude or when it reaches the Earth's surface. The initial object state can be taken from other researches or chosen adequately by the user. See Figure 2.1a for an initial state illustration for the re-entry simulation. Other parameters needed for the research, such as surface area, radius or temperature, can be calculated or derived based on these state variables, with sometimes using certain assumptions. Propagating the initial state of the object over the whole re-entry, at every epoch, is done using a RungeKutta45 integrator available within GNU Octave<sup>1</sup>, see Figure 2.1b. In order to integrate the states, a dynamic model of the object is needed. These dynamics will be

<sup>1</sup>"24.1.1 Matlab-compatible solvers" octave.org. [https://octave.org/doc/v4.4.0/Matlab\\_002dcompatible-solvers.html](https://octave.org/doc/v4.4.0/Matlab_002dcompatible-solvers.html) (Accessed Dec 6, 2018).

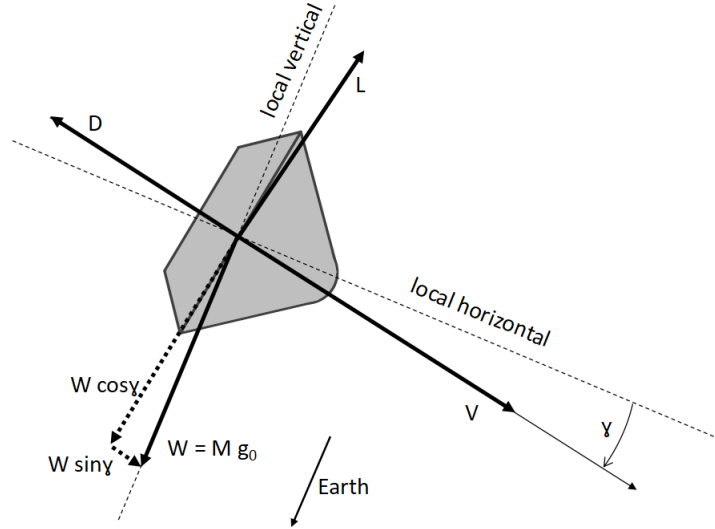


Figure 2.2: Two dimensional planar motion of a ballistic capsule, can be substituted for a meteor or other re-entering object.

explained in the upcoming section, Section 2.1.2.

Important for the ODE45 integrator are the set tolerances to at least  $10^{-12}\%$ , this is derived from the fact that a desired precision of at least 10 m (Cepelcha et al., 1998) and 0.01 gram (10% of smallest to be simulated meteor, which is 0.1 gram) is wanted. With starting altitudes of about  $10^5$  m and maximum starting masses of about  $10^7$  kg (Chelyabinsk (Popova et al., 2013a)), the limiting parameter is the starting mass of  $10^7$  kg and precision of grams ( $10^{-5}$  kg) desired, leading to the  $10^{-12}\%$  tolerances. The time step in ODE45 is not constant, and is based on the tolerances.

What is left after propagating the trajectory from the initial object state, is the state of the object at each calculated point in time, see Figure 2.1c. In the next section the trajectory dynamic model used to determine the object state with the 5 variables at each point in time is discussed.

### 2.1.2. Trajectory Dynamics

The first step is to simulate the trajectory of each of the different kind of objects. To do this, the 2 dimensional planar dynamics are used, since they are applicable to meteors (Gritsevich, 2007; Stulov, 1993) and ballistic vehicles (Mooij, 2016; Putnam and Braun, 2015; Allen and Eggers, 1961). The fact that planar dynamics are used means it is assumed that no sideways forces are present.

See Figure 2.2 for a sketch of the forces and motion of a re-entering capsule. From this Equations (2.1) to (2.4) can be derived.

$$\frac{dV}{dt} = -\frac{D}{M} + g_0 \sin \gamma \quad (2.1)$$

$$\frac{d\gamma}{dt} = \frac{g_0}{V} \cos \gamma - \frac{V}{R} \cos \gamma - \frac{L}{MV} \quad (2.2)$$

$$\frac{dh}{dt} = -V \sin \gamma \quad (2.3)$$

$$\frac{dx}{dt} = V \cos \gamma \quad (2.4)$$

The derivation is done by looking at the velocity vector  $V$ , which can be split up by using sines and cosines into a vertical and horizontal position change per time, Equations (2.3) and (2.4). The change in velocity in Equation (2.1) is derived by looking at the velocity vector and the forces that cause changes in it, namely the drag  $D$  and the weight  $W$  vectors. Of course velocity is not a force, but remembering that  $F = Ma$ , the change of velocity, equal to acceleration is equal to a force causing the acceleration divided by the mass, as  $\frac{F}{M} = a = \frac{dV}{dt}$ . The expression for the change in flightpath angle  $\frac{d\gamma}{dt}$  is found by looking at the force balance in the lift direction, as was just done in the velocity direction. This leads to the normal acceleration being equal to  $-(\frac{d\theta}{dt} + \frac{d\gamma}{dt})VM = L - g_0M \cos \gamma$  (Mooij, 2016). Here the first term is the negative centrifugal force of the object, where  $\frac{d\theta}{dt}$  is the angular velocity of the object around the Earth and  $\frac{d\gamma}{dt}$  is the change of flight path angle, which together lead to the total turn made around the Earth's center. Projecting the velocity due to the

rotation about Earth's center on the velocity vector gives  $R \frac{d\theta}{dt} = -V \cos \gamma$ . This last relation can be substituted in the expression of the normal acceleration and will lead to Equation (2.2).

The lift  $L$  and drag  $D$  are defined as commonly used in aerospace engineering, see Equations (2.5) and (2.6).

$$L = \frac{1}{2} c_L \rho_a V^2 S \quad (2.5) \quad D = \frac{1}{2} c_d \rho_a V^2 S \quad (2.6)$$

Furthermore,  $g_0$  is the gravitational acceleration at sea level (thus it is assumed that the gravity does not change with altitude, which is not the case in reality. At 150 km it is about 5% lower than at sea level (Mooij, 2016), which is assumed to be an acceptable error),  $M$  is the mass of the body,  $V$  is the velocity,  $t$  is the time,  $h$  is the height above the planetary surface,  $\gamma$  is the flight path angle between the flight path and the horizon,  $S$  is the effective middle cross-sectional area of the body,  $\rho_a$  is the atmospheric density,  $R$  is the planetary radius plus altitude and finally  $c_d$  and  $c_L$  are the drag and lift coefficient respectively.

To get the atmospheric density  $\rho_a$  an ideal gas is assumed, it allows for the construction of a so called exponential atmosphere. This then allows for the easy calculation of the atmospheric density and/or pressure at any altitude, which is needed in Equations (2.5) and (2.6). The exponential atmosphere is a simplified isothermal model for an atmosphere, as in Equation (2.7) (Mooij, 2016).

$$\rho = \rho_0 e^{-\beta h} = \rho_0 e^{-h/h_0} \quad (2.7)$$

In this the scale height is  $h_0 = 1/\beta = \frac{RT}{g_0}$  (so  $\beta = \frac{g_0}{RT}$ , having no actual physical meaning), where  $T$  is the constant total temperature (somewhere between 240 K and 250 K),  $R$  is the gas constant equal to 286.9 JK/kg and  $g_0$  is the gravitational constant of the Earth equal to 9.81 m/s<sup>2</sup>. Depending on the used values the scale height values for Earth are in the range of 7000 m to 8500 m (Mooij, 2016; Putnam and Braun, 2015). For the rest of the research a nominal value for the scale height of 7000 m is taken, unless otherwise stated. For a given altitude  $h$  the atmospheric density can be calculated.

In case of ablation, which happens during re-entry of meteors and in a small manner during re-entry of capsules, the mass of the objects will change. The mass loss can be represented with Equation (2.8) (Gritsevich, 2007). Here  $\xi$  is the heat of ablation of the material in j/kg and  $c_h$  is the heat transfer coefficient.

$$\frac{dM}{dt} = -\frac{1}{2\xi} c_h \rho_a V^3 S \quad (2.8)$$

The heat of ablation  $\xi = 8.3 \times 10^6$  J/kg for meteors (Johnston et al., 2018), unless otherwise specified, and  $100 \times 10^6 < \xi < 500 \times 10^6$  J/kg for Phenolic Impregnated Carbon Ablator (PICA) heat shields in capsules (Ricci et al., 2017). For PICA the heat of ablation is a function of the convective heat flux. The calculation of the convective heat flux will be explained in Section 2.1.4. The PICA heat shield is assumed to be representative for all capsules, since it was the only heat shield material where the heat of ablation could be found for. In this formulation it is needed to assume that all the heat from the ambient gases is spent on the evaporation of the material of the body (Lyytinen and Gritsevich, 2016).

It is quite common to assume a  $c_h$  of 0.1 for meteor threat assessment studies (Johnston et al., 2018), for the use in Equation 2.8. However, Johnston et al. (2018) gives two relations for both laminar, see Equation (2.9), and turbulent flows to estimate the value of  $c_h$  based on the velocity, radius and altitude of the meteor as given in Equation (2.9). This latter expression is used in this research. A laminar flow is assumed in this research, for stable re-entry conditions.

$$c_h = \frac{1.107 \times 10^{-3}}{\frac{V^{1.0}}{1000} R_N^{0.22}} e^{-8.5818 \times 10^{-4} \left(\frac{h}{1000}\right)^2} + 0.1753 \frac{h}{1000} \quad (2.9)$$

The variational heat transfer coefficient  $c_h$  is generally lower than the commonly used constant one (Johnston et al., 2018). This leads to less mass loss per time compared to using the constant value of 0.1. This must be taken into consideration when comparing our data with other researches.

As a side note, the drag coefficient  $c_d$  can be taken as 1.0 for chunky shape or spherical body (Halliday et al., 1981; Nemtchinov et al., 1997) or about 2.0 for a cylindrical body (Nemtchinov et al., 1997). The lift coefficient  $c_L$  is thereafter, for meteors, primarily a function of the rotation speed, which means that if the meteoroid is assumed to be spherical and rotating it could generate a small positive or negative lift coefficient or even sideways force components. This phenomena can also be described by the Magnus effect. Research has shown that this effect can increase throw distances for baseballs by up till 9% and can lead to  $c_L$  values

of 15 for supersonic velocity rotating cylinders (Sarafian, 2011; Hall, 1960). This Magnus effect for spinning cylinders and balls can be proven to be connected<sup>2</sup>. Bouquet et al. (2014) showed that two-third of the meteoroids rotate at such a speed that the heat distribution can be assumed homogeneous and no change of shape occurs. This however, does not give an indication of how fast the meteoroid is rotating exactly. The meteoroid rotation is not added in the simulations regarding the additional lift, but only regarding the heat distribution being homogeneous, thus no change of shape occurs.

To conclude, the  $c_d$  and  $c_L$  used for capsules is given by literature (Mitcheltree et al., 1999; Marraffa, 2008) and for meteors a  $c_d$  of 1.0 is assumed. For meteors no lift is assumed, although they are assumed to be rotating, which should cause a Magnus effect, but this is not taken into account.

With the above explained dynamics the trajectory of the object can be determined with the propagation of the states through time. Also the change in mass, and thus area and radius, of the object at all epochs is then known. Next, in Section 2.1.3, the possible fragmentation of the object into multiple smaller objects is discussed. For each of the smaller objects the same dynamics as just explained are used. In Section 2.1.4 the heat fluxes are addressed, which are needed to determine the heat of ablation  $\xi$  for capsule PICA heat shields.

### 2.1.3. Fragmentation

Fragmentation can happen to meteors and can be split up in two sorts, continuous fragmentation and sudden/discreet fragmentation. The first is usually assumed to be part of the ablation and is already implemented with the use of Equation (2.8) (Silber et al., 2018). The sudden/discreet sort of fragmentation deals with the breaking up of the meteoric bodies and will be discussed below.

The method implemented for fragmentation is developed for meteoroids (Register et al., 2017). It assesses the dynamic pressure, defined as in Equation (2.10), during the re-entry. Here  $V$  is again the velocity of the object and  $\rho_a$  is the atmospheric density at the altitude of the object. When the aerodynamic strength  $\sigma_m$  of the object is reached by the dynamic pressure  $p_d$  ( $\sigma_m = p_d$ ), it breaks up in a set amount of fragments with mass  $M_p$  and a dust cloud (Wheeler et al., 2017; Mathias et al., 2017). The strength of those new fragments or particles  $\sigma_p$  is increased by using a strength scaling  $\alpha$  and both object's mass  $M_m$  and new particle mass  $M_p$  ratio, see Equation (2.11). This procedure keeps continuing till the aerodynamic strength becomes too much or till the fragments are totally ablated.

$$p_d = \rho_a V^2 \quad (2.10) \quad \sigma_p = \sigma_m (M_m / M_p)^\alpha \quad (2.11)$$

The dust cloud can be omitted if the total mass is instead divided over the fragments. Although this method is less precise than the one with a dust cloud, it is easier to be implemented. This method is called the discrete independent wake model (IWM) and can simulate the peak luminosity, but is unable to simulate secondary peaks like the fragment-cloud model (FCM) (Mathias et al., 2017; Register et al., 2017).

Consequences of different dust cloud fractions means that for 10 m radius meteoroids the peak energy deposition, released energy at break-up, is within the same range for cloud fractions between 10% and 90% (Wheeler et al., 2017). Next to that, the peak altitude gets higher for less cloud fractions, from 28 km to 38 km for a 10 m meteoroid. Also, a bigger cloud fraction leads to a more smooth energy deposition curve. As explained before the dust clouds are not implemented. This is due to simulation difficulties (change of density and not similar sized objects). Not implementing any cloud will thus lead to about the same peak energy deposition, but the peak will be at higher altitudes and the curve will not be smooth. It will be proven later in Section 3.1.7 that this model gives a better solution than a non-fragmentation solution for fragmentating meteoroids (Register et al., 2017).

The 3 inputs for the fragmentation model determine greatly how the model behaves. It is impossible to know these parameters beforehand for a meteor fragmentation simulation. However, a fit of a luminosity or energy deposition curve on the ones from observations can be made with those 3 parameters (Register et al., 2017). Typical values are an initial strength of  $0.1 \text{ MPa} < \sigma_m < 100 \text{ MPa}$ , strength scaling  $0.05 < \alpha < 1$  and number of fragments  $N_F$  between 2 and 16 (Wheeler et al., 2017). As baseline for the research initial strength is set to 1.5 MPa, strength scaling to 0.1 and amount of fragments to 2.

The fragmentation just discussed influences the propagation of object states. The simulation is initiated with a set of inputs as discussed in Section 2.1.1 and propagates the states over time. However, for meteors a break-up can happen, called fragmentation, which will be addressed in Section 2.1.3. When the first "break-up" happens, which is only used for meteors, the meteoroid mass is divided to a specified amount of equal mass fragments, and their aerodynamic strength  $\sigma_p$  is updated based on the strength scaling  $\alpha$ . Then the

<sup>2</sup>"Ideal life of a spinning ball" grc.nasa.gov. <https://www.grc.nasa.gov/WWW/K-12/airplane/beach.html> (Accessed Juli 20, 2018).

propagator is started again from the last end point, with the new parameters of one of the new fragments, till the aerodynamic strength is reached again. This continues till an altitude after a full propagation is reached below 20 km. During this simulation the amount and times of the break-ups and the amount of fragments at each time are recorded. Thus the same dynamics hold as discussed in 2.1.2, but the propagation of states as discussed in 2.1.1 has an extra termination condition for a break-up, after which it continues with a smaller mass object.

#### 2.1.4. Aerothermal Aspects

For re-entry simulations it is possible to determine the radiative and convective heat flux to the body,  $q_{gw}$  using stagnation heat flux formulas. This is important to determine the temperature of the object, and to determine the heat of ablation  $\xi$  for heat shields, which is a function of the heat flux. Different methods exist to determine the radiative and convective heat flux into a re-entry vehicle. Authors Mooij (2016); Anderson (2006); NASA (2012); Hirschel (2015) all give slightly different equations to calculate both heat fluxes. The heat flux calculation method opted in this research is the one proposed by (Brandis and Johnston, 2014).

Within the integrator, and also afterwards, the convective heat flux  $\dot{q}_c$  and radiative heat flux  $\dot{q}_r$  in the stagnation point are calculated at each epoch, using an updated version of the Tauber-Sutton relations (Brandis and Johnston, 2014). The calculation of the heat fluxes is needed inside the integrator, because it determines the heat of ablation  $\xi$  for a PICA heat shield. However, the change of the heat fluxes per time can not be calculated and thus they cannot be propagated to the other states. Their values are again calculated after the propagation of the object states so they can be used to calculate with.

The updated version of the Tauber-Sutton relations are given in Equations (2.12) till (2.16) (Brandis and Johnston, 2014). For convective heat flux in  $\text{W}/\text{cm}^2$ , at a range of  $3 \text{ km/s} < V < 9.5 \text{ km/s}$ :

$$\dot{q}_c = 7.455 \times 10^{-9} \rho^{0.4705} V^{3.089} R_N^{-0.52} \quad (2.12)$$

And for  $9.5 \text{ km/s} < V < 17 \text{ km/s}$ :

$$\dot{q}_c = 1.270 \times 10^{-6} \rho_a^{0.4678} V^{2.524} R_N^{-0.52} \quad (2.13)$$

In these equations  $V$  is again the velocity in  $\text{m/s}$ ,  $\rho_a$  is the atmospheric density and  $R_N$  the nose radius, or in case of a meteoroid the meteoroid radius. For radiative heat flux in  $\text{W}/\text{cm}^2$ :

$$\dot{q}_r = 3.416 \times 10^4 R_N^a \rho_a^{1.261} \left( -53.26 + \frac{6555}{1 + (16000/V)^{8.25}} \right) \quad (2.14)$$

Here  $a$  is defined as:

$$a = \min(3.175 \times 10^6 V^{-1.80} \rho_a^{-0.1575}, a_{max}) \quad (2.15)$$

$$a_{max} = \begin{cases} 0.61 & \text{if } 0 < R_N < 0.5 \\ 1.23 & \text{if } 0.5 < R_N < 2 \\ 0.49 & \text{if } 2 < R_N < 10 \end{cases} \quad (2.16)$$

In Equation (2.15)  $\min$  is a minimal compare function, which takes the lowest of the two inputted values.

With the convective and radiative heat fluxes known the amount of energy transported to the object's stagnation point is known, based on aerothermal effects during the re-entry.

In general the object's surface, or also called wall, heat flux balance is the sum of the heat going into the material minus outward re-radiation, conduction, and material response. However, for vehicles, usually no conduction into the vehicle is wanted, thus assuming that the capsule designers designed their capsules correctly, this is set to zero. Also the material response can be neglected in case for example of no ablation. However, for non-reusable vehicles, like most re-entry capsules, and meteors there is usually (some) ablation. For the simulations in this research, the heat flux into the wall  $\dot{q}_w$  is set to zero. For meteoroids this is not necessarily true. However, due to the low heat of ablation compared to capsules it is assumed that the sublimation/ablation happens so fast that no significant heat is transferred into the meteoroid itself. This means that the heat flux balance is as given in Equation (2.17), see also Figure 2.3.

Here  $\dot{q}_s$  is the energy heat flux going into sublimation or ablation of the material, the rest of the incoming heat flux has to be radiated out in case an equilibrium exists (conduction is zero). From the CFD simulations of the Stardust capsule by Olynick et al. (1998) it was concluded that this sublimation/ablation heat flux  $\dot{q}_s$  is about 35% of the total heat flux. This energy goes directly into ablation and/or sublimation of the material

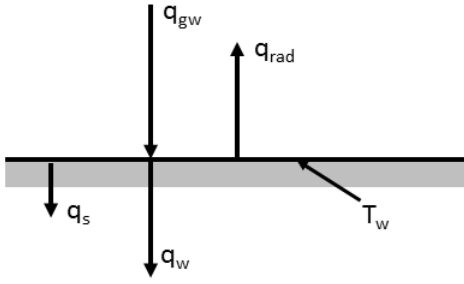


Figure 2.3: Figure showing the thermal state.  $T_w$ : temperature of the wall,  $\dot{q}_{gw}$ : heat flux from gas to the wall,  $\dot{q}_w$ : wall heat flux,  $\dot{q}_s$ : sublimation heat flux,  $\dot{q}_{rad}$ : surface radiation heat flux.

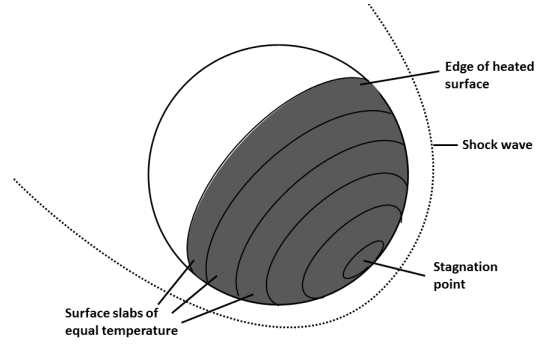


Figure 2.4: Figure of the temperature distribution of a spherical forebody, showing the shock-wave and boundary temperature conditions.

that goes away from the object. Therefore, the total heat flux into the object is the remaining 65% of the sum of the two heat fluxes at any time.

With the assumptions of a gray or black body ( $\epsilon < 1$  or  $\epsilon = 1$ , true for meteors (Yanagisawa, 2015) and capsules (Abe et al., 2011; Ohnishi et al., 2011)), an optically thin shock-boundary (as done by Weryk and Brown (2013)) and no heat absorption, the stagnation temperature  $T_{stag}$  can be calculated at the surface with the Stefan-Boltzmann Law (Wertz and Larson, 2010; Giancoli, 2009). The Stefan-Boltzmann Law is given in Equation (2.18).

$$\dot{q}_{r,out} = \dot{q}_{c,in} + \dot{q}_{r,in} - \dot{q}_s \quad (2.17) \quad \dot{q}_{out} = \sigma \epsilon T^4 \quad (2.18)$$

In the Stefan-Boltzmann Law  $\epsilon$  is the emissivity and  $T$  is the surface temperature of the object.

From Hayabusa surface temperature calculations it can be concluded from Suzuki et al. (2014) that the edge of the surface capsule is about 70% of the temperature at the stagnation point. With this knowledge the average total temperature  $T_{avg}$  of the object can be calculated, taking into account the increasing surface area per radius or slab away from the stagnation point if applicable, see Figure 2.4.

With the known average surface temperature the last, but very important, parameter during the re-entry is known of the object. With this the luminosity of the object can be determined, which will be explained in Section 2.1.5.

### 2.1.5. Luminosity, Filter Bands and Absolute Magnitude

Now that the average temperature of the object is known at every epoch, the luminosity can be determined. First the irradiance per wavelength, called spectral irradiance, can be calculated with Planck's law (Wertz and Larson, 2010; Giancoli, 2009), as function of the total average temperature. Here  $h$  is Planck's constant,  $c$  the speed of light,  $k$  the Boltzmann constant,  $T$  the surface temperature (taken here as  $T_{avg}$ ), and  $\lambda$  the evaluated wavelength, all in SI units. The output is the spectral irradiance  $E_\lambda$  in  $\text{Wm}^{-2}\text{nm}^{-1}$ .

$$E_\lambda = \frac{2\pi hc^2}{\lambda^5} \frac{1}{e^{ch/kT\lambda} - 1} \quad (2.19)$$

Multiplying the spectral irradiance with the emitting wet surface and integrating over the desired wavelengths, the emitted luminosity can be calculated over a desired wavelength band. This is then later in used Section 2.2 to determine how much energy reaches the pixels in the satellite instrument.

It is also of interest to look at the so called empirical luminosity. The empirical luminosity is calculated with Equations (2.20) and (2.21). These equations assume that a part, equal to the luminous coefficient  $\tau_0$ , of the change in kinetic energy  $E$  is converted into luminosity in Watts, and is used a lot in meteor science (Ceplecha et al., 1998; Gritsevich and Koschny, 2011).

$$I = -\tau_0 \frac{dE}{dt} \quad (2.20) \quad \frac{dE}{dt} = \frac{d(MV^2/2)}{dt} = \left( \frac{V^2}{2} \frac{dM}{dt} + MV \frac{dV}{dt} \right) \quad (2.21)$$

The kinetic energy can be obtained, as in Equation 2.21, from the differences in the calculated masses and velocities per epoch. The empirical luminosity is an estimation of how much luminosity a meteor radiates, but is not derived from any physical models with respect to aerothermodynamics. In Equation 2.20 the luminous coefficient is taken to be defined as by [Stokan and Campbell-Brown \(2015\)](#), based on [\(Weryk and Brown, 2013\)](#), given in Equation (2.22).

$$\tau_0 = 10^{\left( -0.09 \left( \frac{V}{1000} \right)^{0.5} - 3.00 \log_{10} \left( \frac{V}{1000} \right) - \left( \frac{9.56}{\log_{10} \left( \frac{V}{1000} \right)} \right) + 10.11 \right)} \quad (2.22)$$

The calculated luminosity based on this luminous coefficient is the bolometric empirical luminosity ([Stokan and Campbell-Brown, 2015](#)). This empirical luminosity can later be compared with the calculated luminosities based on heat fluxes, fragmentation and from other literature.

The integration of the spectral irradiance over a wavelength band can be done over any range of wavelengths. However, it is convenient to specify some common filter bands to address regions of the electromagnetic spectrum. In this research the filter bands are defined as follows: ultra violet (10-400 nm), visible light (400-700 nm), near infrared (700-1400 nm), shortwave infrared (1400-3000 nm), midwave infrared (3000-8000 nm) and longwave infrared (8000-10,000 nm), see also Table 2.1.

With the known luminosity of an object  $I_{obj}$ , it being the empirical bolometric luminosity or the one calculated with the heat flux method, the absolute magnitude  $M$  can be calculated. This is important to check the found luminosities from the simulations with actual observations of meteors, which are usually given in absolute magnitudes ([Halliday et al., 1996](#); [Stokan and Campbell-Brown, 2015](#)). As stated in the introduction, the absolute magnitude used in this research is not the absolute magnitude used in stellar astronomy, where the base luminosity taken is one at 10 parsec distance. For meteor scientists the zero absolute magnitude is defined for a meteor of zero magnitude at 100 km distance. This definition for absolute magnitude is used in this research, and can be calculated using Equation (2.23). In this equation,  $I_{ref}$  is the reference luminosity of a zero absolute magnitude meteor at 100 km distance.

Table 2.1: Table with different filter bands and their spectral ranges.

Filter Name	Abbrev.	Wavelengths [nm]
Ultra-Violet	UV	10-400
Visible light	VIS	400-700
Near Infrared	NIR	700-1400
Short-Wave Infrared	SWIR	1400-3000
Mid-Wave Infrared	MWIR	3000-8000
Long-Wave Infrared	LWIR	8000-10000

$$M = -2.5 \log \left( \frac{I_{obj}}{I_{ref}} \right) \quad (2.23)$$

Many values for the  $I_{ref}$  can be chosen and have been used to calculate the absolute magnitude in many meteor researches. For most researches it is not clearly stated if the reference luminosity is of the whole meteor in all directions or only the luminosity towards the observer. Therefore, the method used by the other research should be used when comparing the absolute magnitudes.

In Table 2.2 some possible reference luminosities are presented used by different scientists. Note that the magnitude scale is logarithmic, thus a deviation as small as  $\Delta M = 0.4$  can lead to a difference in actual outputted luminosity  $I$  as big as 50% ([Gritsevich and Koschny, 2011](#)).

Table 2.2: Table with reference luminosities for meteors used for calculating the absolute magnitudes.

$I_{ref}$ [W]	Spectral Band	Source
820	Observed Bolometric	<a href="#">(Stokan and Campbell-Brown, 2015; Weryk and Brown, 2013)</a>
1800	Total Bolometric	<a href="#">(Halliday et al., 1996)</a>
270	Observed Visible	<a href="#">(Weryk and Brown, 2013)</a>
500	Total Visible	<a href="#">(Jenniskens, 2014)</a>

With this last section the method on how the re-entry simulations are simulated has been explained. The outputs are the trajectory and states of the objects per time step. The results that will be found can be used

to answer research questions 1 and 3. Furthermore, the results are a basis for the GEO optical instrument parameter calculations.

## 2.2. GEO Optical Instrument Parameter Determination

To determine the optical instrument parameters of a GEO satellite system that can detect or track an object, a code was written. The code overview can be found in Appendix B. The optical instrument parameters are the aperture diameter, focal length, SNR and SBR. These parameters dictate what the size of a system needs to be and if the object can be subtracted from the background and noise. The calculations can be done for any desired bandwidth and wavelength. The ones used in this research will be discussed in Section 4.1.4.

As input to the optical instrument parameters the calculated average temperatures of the surface, size of emitting area, orientation and velocity per time are taken from the re-entry simulations.

First the general procedure for calculating the optical instrument parameters is presented. These calculations result in the aperture diameter and focal length, based on an assumed ground resolution, quality factor and pixel size. After that the method is explained that calculates with the found aperture diameter and the object states the resulting SNR and SBR. Then shortly the atmosphere, sunlight, thermal irradiance of the Earth and Earth's reflectance are discussed. This is of importance for understanding the iterative calculations of the aperture diameter and focal length as discussed before, such that the required SNR and SBR are reached. Finally, the difference between detecting and tracking calculations are explained, as well as some of the effects due to the moving of the object through multiple pixels per exposure time.

### 2.2.1. Procedure for Calculating Optical Instrument Parameters

Space based optical systems are complex and deal with different aperture sizes and focal lengths compared to most systems on Earth. The preliminary parameter design of such a system is summarized in [Wertz and Larson \(2010, Table 9-15\)](#). This method is implemented to great extend in this part of the research.

First of all, a GEO satellite system is to be designed. Typical characteristics of a GEO satellite system are that it has no effective ground speed and has a period around the Earth of exactly one day. In order to have a period of exactly one Earth day the satellite needs to orbit at an (here assumed circular) orbit of 35,800 km. Then the angular radius of the Earth  $\rho_E$ , defined as the angle seen from the GEO satellite between nadir and the seen edge of the Earth, can be calculated with Equation (2.24).

$$\rho_E = \sin^{-1} \left( \frac{R_E + h_{obj}}{R_E + h} \right) \quad (2.24)$$

Here Earth's equatorial radius  $R_E$  equals 6378.136 km and the orbital altitude  $h$  is as explained before for a GEO satellite equal to 35,800 km. When observing something high up in the atmosphere, for example at 200 km altitude for a meteor ([Vinković, 2007](#)), this value  $h_{obj}$  needs to be added to the numerator of Equation (2.24). This will result in a bigger value for  $\rho_E$ , which increases the required total field-of-view. The maximum distance to the observed object can be found with Equation (2.25).

$$d_{max} = \sqrt{(R_E + h)^2 - (R_E + h_{obj})^2} \quad (2.25)$$

Here, the 200 km for a meteor height could be added to the Earth radius  $R_E$  as well, since meteors can become visible at such altitudes ([Vinković, 2007](#)). To determine the maximum slant range  $R_S$  (maximum range to be observed spot on Earth or object), it is assumed that the sensor is to observe the whole atmosphere till 200 km altitude. Therefore, the slant range is exactly the same as the max distance to the observed object  $d_{max}$ .

The swath width is defined as the area under the satellite of interest where the sensor will scan or take pictures, perpendicular to the orbit track. The swath width is effectively the same as 2 times  $\rho_E$  computed before. If the whole Earth needs to be observed it equals two times the angle  $\rho_E$  defined as from nadir till the seen edge of the Earth. This can be changed in case a smaller field-of-view sensor might be used in some spotlight mode.

The along-track resolution at maximum distance can be defined as  $Y_{max}$  in meters, this is defined as a requirement (for example 2 by 2 km). With this the instantaneous field-of-view can be determined, which is the width of one pixel in degrees. The maximum cross-track pixel resolution  $X_{max}$  can be determined at the maximum distance and at maximum incidence angle ( $IA$ ), which is in GEO/GSO full Earth coverage equal to  $\rho_E$ . Both equations are given below:

$$IFOV = \frac{Y_{max}}{R_S} \frac{180deg}{\pi} \quad (2.26)$$

$$X_{max} = \frac{Y_{max}}{\cos(IA)} \quad (2.27)$$

The along- and cross-track,  $Y$  and  $X$ , resolution at nadir can be determined with (2.28). The pixel count in the cross-track direction can be determined with (2.29). This is not per se the amount of pixels on the detector, but rather the total cross-track swath width or area of interest expressed in pixels.

The sensor look angle  $\eta$  can be taken equal to  $\rho_E$  in case the sensor is side looking and needs to observe from nadir (zero degrees) till  $\rho_E$ . If the instrument is not side looking, and points to nadir  $\eta$  and needs to observe the whole Earth in its swath width, it is equal to  $2\rho_E$ .

$$X \wedge Y = IFOV \left( \frac{h\pi}{180deg} \right) \quad (2.28)$$

$$Z_c = \frac{2\eta}{IFOV} \quad (2.29)$$

The total number of pixels recorded per second is equal to  $Z_c \cdot Z_a = Z$ . For a GSO/GEO satellite the total amount of pixels needed to be recorded per second (or any other time frame) is equal to, in case of a square observed area,  $Z_c^2 = Z$ .

There are a few options regarding how to proceed. Either way a scanning sensor is used that takes images over a matrix of instances with a pixel count equal to  $N_m$ , or the whole area is observed at once, which means  $N_m = Z$ . Depending on the application of the sensor either one of the two could be used. Both options allow for different exposure times and care needs to be taken with the pixel integration period  $T_i$ , which needs to be bigger than the detector time constant  $T_d$ . For now a sensor is assumed that stares at a whole area at once.

The actual sensor optics can be determined using the pixel size  $d$ , or called pixel pitch, and ground resolution  $X$ . To continue the design process a pixel size  $d$ , as small as  $1.2 \mu\text{m}$  for visible light BSI sensors and  $10 \mu\text{m}$  for infrared sensors (Filachev et al., 2003), a quality factor  $Q$ , usually 1.0, standing for  $Q$  times the Rayleigh criterion number of 1.22 (Wertz and Larson, 2010), and desired operating wavelength  $\lambda$  (for example  $1.8 \mu\text{m}$ ) are defined. When the quality factor  $Q=1.0$ , it represents a diffraction limited system. With the 3 parameters and the before found pixel count  $N_m$ , altitude  $h$ , cross-track resolution  $X$  and the instantaneous field-of-view  $IFOV$ , the needed focal-length  $f$ , aperture diameter  $D$  and field-of-view of the optical sensor  $FOV$  can be determined with Equations (2.30), (2.31) and (2.32).

$$f = \frac{h \cdot d}{X} \quad (2.30) \quad D = \frac{2.44\lambda f Q}{d} \quad (2.31)$$

$$FOV = IFOV \cdot N_m \quad (2.32)$$

With these equations the basic optic instrument parameters, aperture diameter  $D$ , focal length  $f$  and field-of-view  $FOV$  are known.

The quality factor  $Q$  is an important parameter, since it has a direct influence on the aperture diameter  $D$ . The quality factor  $Q$  can be defined as in Equation (2.33).

$$Q = d/d' = X/X' \quad (2.33)$$

Here  $d$  is the pixel size and  $d'$  is the diameter of the first dark ring in the Airy disk, and  $X$  is the ground resolution and  $X'$  the Rayleigh criterion limited ground resolution (Wertz and Larson, 2010). If  $X$  is smaller than  $X'$ ,  $Q$  is smaller than 1 and the system is unable to distinguish two light point sources and the system is not diffraction limited anymore. An Airy disk is the best focused spot of light that a lens or mirror with a circular aperture can make, limited by the diffraction of light. It consists of a concentric circle pattern with periodic less photon energy per circle outwards, as depicted in Figure 2.5. The quality factor  $Q$  states how much of the airy disk energy falls in 1 pixel. If  $Q = 0.82$ , the Dawes criterion is reached, which means that the edge of the full width at half maximum (FWHM) of the point spread function (PSF) touches the edge of the pixel, about 50% of the encircled light will fall onto the pixel. If  $Q = 1.0$  this means the Rayleigh criterion is reached and the minimum of the first dark circle of the PSF will touch the edge of the pixel, about 83.8% of the encircled energy will fall onto the pixel, and is a very much used value. For higher  $Q$ s of 1.83, 2.65 and 3.48 the amount of encircled energy detected in the pixel will be 91.0%, 93.8% and 95.3% respectively, see also Figure 2.5<sup>3</sup>. For the simulation a value of 1.0 is used for  $Q$ , meaning that 83.8% of the encircled energy will fall onto each pixel.

For actual data on the detector parameters, like pixel size, see Appendix A.

<sup>3</sup>"Astronomical Optics, Part 3: The Astronomical Image" handprint.com. <https://www.handprint.com/ASTRO/ae3.html#resolution> (Accessed January 15, 2019).

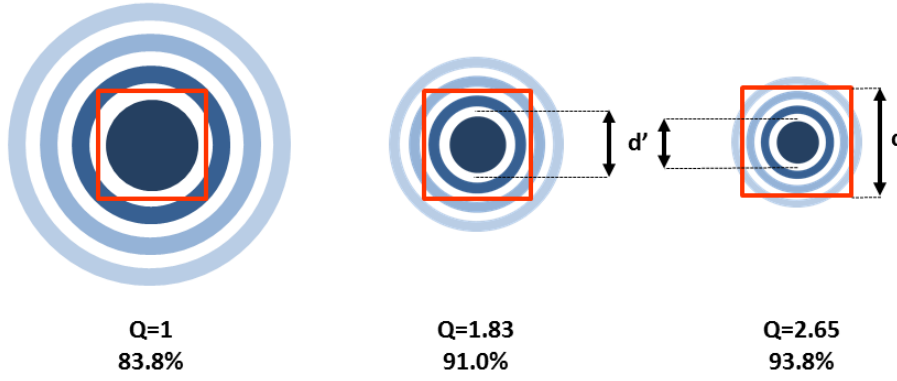


Figure 2.5: Schematic representation (not to scale) of the percentage of the energy of an Airy disk of a point source (blue) falling onto the pixel area (red), for different values of  $Q$  (thus different diffraction criteria).

### 2.2.2. Signal, Background and Noise Ratios

The sensor radiometry gives insight on whether the signal strength is high enough. If certain objects want to be observed in front of Earth's surface these objects need to have a higher signal power than the background or other noise and clutter sources. Therefore, both signal powers of the Earth's surface and the objects are computed per pixel. See Table 2.3 for an overview of the radiometric units used.

The spectral irradiance  $E_\lambda$  can be calculated by using Planck's Law in Equation (2.19) for each wavelength (on nanometer scale)  $\lambda$  in the used bandwidth and the average black body temperature  $T_{avg}$  in Kelvin, resulting from the re-entry simulations. This is done for the background, being the sum of the reflected sunlight and the thermal irradiance of the Earth, and for the re-entering object that is to be observed.

If the found  $E_\lambda$  for the background and object are divided by  $4\pi$  steradians the spectral radiance  $L_\lambda$  is obtained in  $W/m^2/\mu m/sr$ . If this is multiplied by  $\tau(\lambda)$ , the transmissivity of the atmosphere at wavelength  $\lambda$ , the upwelling radiance  $L_{up_i}$  is found. For sunlight the spectral radiance is multiplied twice by the transmissivity to accounting for the two travels through the atmosphere. The integrated upwelling radiance  $L_{int}$  in  $Wm^{-2}sr^{-1}$  is found by integrating over the operating bandwidth as  $L_{int}(\lambda) = \sum_i L_{up_i}(\lambda_i - \lambda_{i+1})$ . The operating bandwidth  $\Delta\lambda$  can be defined as desired, taken baseline as 100 nm.

The integrated upwelling radiances  $L_{int,E}$  and  $L_{int,obj}$  for both the background and object respectively are known. These are the energies that leave the atmosphere in a selected bandwidth for both the background and the object. In order to get just Watts reaching the detector the integrated upwelling radiances need to be multiplied by a surface that emits the radiance and by an amount of steradians.

The objects and background signal powers will be computed slightly different. This is done because the object has a different shape than the background, the surface of the Earth. The radiated power from a ground pixel at nadir is done for Earth via Equation (2.34).

$$L_{E,E} = L_{int,E} \cdot X \cdot Y \quad (2.34)$$

Here  $X$  and  $Y$  are the cross-track and the along-track pixel ground resolution respectively. When nadir pixels are assessed for square pixels, this means that  $X = Y$ . The ground resolution determines how much ground is visible in one pixel, and thus how much radiant intensity in  $Wsr^{-1}$  comes from that piece of Earth.

For the radiant intensity coming from the object high in the atmosphere the integrated upwelling irradiance is multiplied with the heated surface emitting the integrated upwelling radiance. This surface is equal to  $\pi R_o^2$ , where  $R_o$  is the radius of the object, see Equation (2.35).

$$L_{E,o} = L_{int,obj} \cdot \pi R_o^2 \quad (2.35) \quad L_{E,o,eff} = \frac{1}{2} L_{E,o} \cos \gamma \quad (2.36)$$

However, only the perpendicular heated surface of that object will emit the radiant intensity to the sensor,

see Figure 2.6. Therefore the just found radiant intensity is corrected by the orientation of the object with Equation (2.36). It is assumed that for a flight-path-angle of  $0^\circ$  only half of the radiance is observed. When it is  $90^\circ$  no radiance is observed.

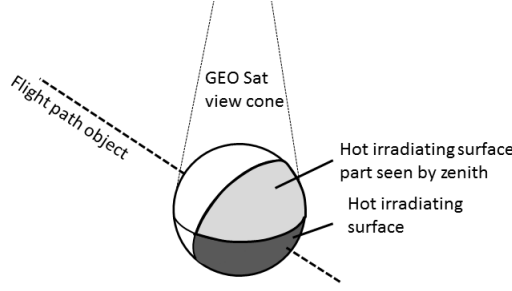


Figure 2.6: Figure showing the assumed orientation of the re-entering objects and how it influences the observed irradiance by a satellite.

The just found radiant intensities of the background and the object can be propagated towards the GEO instrument. The input power on each sensor pixel at distance  $d_o$  from the to be observed object or area is defined by (2.37).  $d_o$  is taken to be equal to the maximum distance to the object  $d_{max}$ .  $L_E$  is the radiant intensity of either the object  $L_{E,o,eff}$  or the background  $L_{E,E}$ , and  $D$  is the before found aperture diameter.

$$P_{in} = \frac{L_E \pi}{d_o^2} \left( \frac{D}{2} \right)^2 \quad (2.37)$$

With this calculation the power in Watts going into a pixel, depending on the used radiant intensity source, can be calculated.

Since optical systems are not perfect, and lenses and mirrors are used, the input power  $P_{in}$  is not the actual power reaching the pixels. Therefore, this value needs to be multiplied by the transmission factor giving the input power at the detector  $P_D = P_{in} \cdot \tau_0$ . The transmission factor for the instrument  $\tau_0$  needs to be defined; a value of 0.95 is reasonable for mirrors, which are assumed to be used for the system (Wertz and Larson, 2010). When lenses are used this value could be lower.

Next to the just described reduction in energy by the transmission factor, the encircled energy of the PSF as result of the chosen  $Q$  is applied here as well. As explained in Section 2.2.1, the fraction of the object energy reaching the detector must be multiplied by 83.8%, for a diffraction limited system where  $Q = 1$ . Also the place of the PSF with respect to the pixel area has an effect on how much energy is actually received in that pixel. A few different options exist to approach this. A worst case of 25% can be assumed, when the PSF is located on the corner of a pixel. However, assuming that the PSF is always on the corner of a pixel does not give a realistic view of the problem, and is seen as too conservative. Therefore, a program was written that calculates the average amount of a circular signal that is visible in the pixel, assuming that the circle is random uniformly placed on that pixel, see Appendix E. The outcome of this analysis is that on average 61.5% of a circle with the same diameter as the pixel size is inside the pixel area, and the rest is distributed among any neighboring pixels. This means then that for  $Q = 1$ , the encircled energy in the analyzed circle is 83.8% of the total object power. So, under the assumption that only the inside encircled energy is present in the PSF the total object power reaching the pixel on average is  $83.8\% \times 61.5\% = 51.5\%$  of the object power reaching the optical system. In reality the amount is a little bit higher, since some of the lower energy circles around the center of the PSF will also be in the pixel, so the used value is still a conservative one. This is better than an overestimation. Both the just described phenomena are used to calculate the energy reaching the pixel as  $P_P = P_D \times 0.838 \times 0.615 = P_D \times 0.515$ .

The available energy, in Joules, after integration time in the pixel can be determined with (2.38).

$$E = P_P \cdot T_i \quad (2.38)$$

Here  $T_i$  is the integration time in seconds and  $P_P$  is the amount of energy reaching the pixel. Therefore, a higher integration time allows for more photons to be absorbed by the pixel.

The amount of available photons  $N_p$  in that energy is calculated with (2.39).

$$N_p = E \lambda / h c \quad (2.39)$$

Here  $\lambda$  is the wavelength in the middle of the bandwidth,  $h$  is Planck's constant and  $c$  is the speed of light. When the (detective) quantum efficiency  $QE$  is known, the amount of electrons available  $N_e$  in the detector can be calculated with (2.40).

$$N_e = N_p \cdot QE \quad (2.40)$$

Usually the quantum efficiency is not uniform over the whole bandwidth. To reduce complexity it is taken as uniform (see again Appendix A for usable data for the detector parameters, like the quantum efficiency  $QE$ ).

When the number of read-out noise electrons  $N_r$  is defined (typically  $N_r = 25$  (Wertz and Larson, 2010), see again Appendix A for real detector read out noises) and the number of noise electrons from the signal is calculated with (2.41), the total amount of noise electrons  $N_t$  can be determined with (2.42).

$$N_n = \sqrt{N_e} \quad (2.41) \quad N_t = \sqrt{N_n^2 + N_r^2} \quad (2.42)$$

With the use of Equations (2.43) and (2.44), the SNR and SBR can be calculated. Again a distinction is made between object electrons with subscript *obj* and background electrons with subscript *b*.

$$SNR = \frac{N_{e,obj}}{N_{t,obj} + N_{t,back}} \quad (2.43) \quad SBR = \frac{N_{e,obj}}{N_{e,back}} \quad (2.44)$$

It should be noted that this defined SNR differs from the one defined by Wertz and Larson (2010).

### 2.2.3. Atmosphere, Reflectance and Earth's Thermal Irradiance

Taking into account the atmospheric transmittance and absorbance it is assumed that 20% of the atmosphere, density wise, is between the object and the observer. This is true when putting the object based on an exponential atmosphere at a minimal altitude of 12 km. This means that some wavelength irradiance is absorbed by the atmosphere and does not or less reach the observer. The transmittance of the atmosphere behaves homogeneously and proportional to the altitude (Murcray et al., 1965). This means that the amount of blocked signal is proportional to the amount of atmosphere blocking it. The model used in this research is an adapted version of data found on this matter by NREL<sup>4</sup>. In order to obtain the spectral irradiance after reflection and absorption, the whole spectrum is multiplied by this atmospheric transmittance model per nanometer. This also applies, in full effect to the Earth and Sun clutter/background sources discussed next.

The Earth has an effective black-body temperature of 288 K, this means that it emits in the Midwave-Infrared (MWIR) and Longwave-Infrared (LWIR) spectrum. When observing the object during night time the Earth's spectral irradiance will be present in the background.

The Sun's effective temperature is about 5800-6000 K and has its peak in the visible and NIR spectra during day time. Assuming an average albedo of 30% this adds to the clutter in the observations (clutter is unwanted signal). Reflectance over the oceans can reach up till 100% for the sub- and near sub-satellite point, making observations of re-entries over oceans in the sub-satellite point almost impossible. In the code one case is considered, full land surface with an albedo of 30%.

The Moon reflected sunlight (Albedo about 0.12) reflected from Earth's surface is not taken into account.

### 2.2.4. Iterative Optical Instrument Parameter Calculations

With the procedure described before, the total amount of electrons excited in the detector can be calculated for a given bandwidth: for the object, the Earth, the reflected sunlight and the detector itself. With this the SBR and the redefined SNR are determined, revisit Equations (2.43) and (2.44).

In order to find a system where the required SBR and SNR are reached, the code reduces the pixel resolution, till the object generates  $X$  amount electrons compared to the background. With some sophisticated algorithms this SBR can be as low as 0.04 to 0.23 (Tartakovsky and Brown, 2008; Salmond and Birch, 2001; Zhang et al., 2007). The code reduces the pixel size till the amount of electrons generated by the object is a desired amount of times (with 0.1 taken as baseline for the rest of the research) the background signal (Earth and Sun). This works because the object is smaller than the pixel resolution, thus the object signal is not

<sup>4</sup>"Reference Air Mass 1.5 Spectra" nrel.gov. <https://www.nrel.gov/grid/solar-resource/spectra-am1.5.html> (Accessed November 21, 2018).

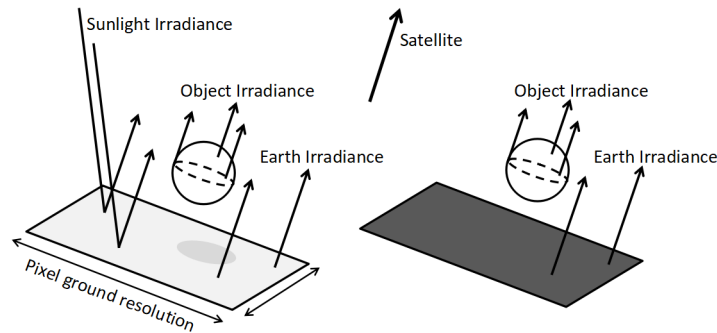


Figure 2.7: Comparison of an object within a pixel, with and without the sunlight reflection as background component. Essentially the difference between day (left) and night (right) observations.

affected. The pixel ground resolution starts as baseline at 2 by 2 km and decreases every iteration by a set amount of meters. See also Figure 2.7.

Next to the SBR check, a check is done whether the SNR is bigger than 3. The SNR is here defined as the signal over the noise electrons due to the signal, background, and detector noise. See Equation (2.44). Note that only in the background noise  $N_{t,back}$  the detector's read out noise  $N_{r,det}$  is accounted for. In case the SNR is below 3, the program also reduces the pixel ground resolution, which in turn increases the aperture diameter and increases the SNR. The latter case happens when the object is very faint and bright enough compared to the background, but too faint compared to the detector generated noise electrons.

With the discussed iterative nature of the case, the needed overall instrument parameters have been determined: aperture diameter  $D$ , focal length  $f$ , signal-to-noises ratio SNR, signal-to-background ratio SBR, ground resolution  $X$  and detector size. What is left to discuss is the detecting versus tracking solutions, and the effective SNR and effective SBR due to the object's velocity. These topics will be discussed in Section 2.2.5.

### 2.2.5. Detecting Versus Tracking Solutions

The research not only deals with detecting, but also with tracking of objects, so the code has an initialization option. If the mode is set to "detecting", the code will use the highest temperature found during the re-entry for the calculation of the spectral irradiance  $E_\lambda$ . However, if the code is set to "tracking", the code will use a lower temperature for the calculation of the spectral irradiance  $E_\lambda$  to make sure it can observe the object for a longer period of time.

A tracking time (baseline being 5 seconds for meteors and 20 seconds for capsules) can be specified. A value is used to multiply with the maximum temperature during re-entry to find the new temperature for which the code is ran, starting at 0.9. The code calculates how much time the object is above this temperature, and thus the time it can track the object. If the possible tracking time is not enough, the temperature reduction fraction is lowered till the right amount of tracking time is found. The code can use the integration  $T_i$  and readout  $T_r$  times to calculate how much observations are made during the tracking of the object, see Figures 2.8a and 2.8b.

Note that for detecting calculations one luminosity value is used, equal to the maximum luminosity calculated during re-entry. If the integration times used are larger than the simulation time step, this leads to an overestimation of the total luminosity reaching the detector (horizontal red line in Figure 2.8a). For tracking a lower amount of luminosity is used, equal to the specified  $T_{track}$ , see Figure 2.8b. The tracking has thus no overestimation of the luminosity reaching the detector, but rather an underestimation for most of the luminosity curve.

It is important to understand that the calculations done are based on propagation time steps during the re-entry simulation of for example 10 ms. This means that the precision of the simulations have that temporal resolution. In other words, when calculations are done for smaller exposure times, based on those re-entry simulations, it means that the observation occurs somewhere in those 10 ms. This means that the calculated luminosity could be a little higher or a little lower in those 10 ms, influencing the actual outcome of the calculated optical instrument parameters. When the exposure time is taken longer than those 10 ms, for example 100 ms, it means that the program now uses the maximum luminosity value in the trajectory for 10 consecutive times, and calculates the optical instrument parameters based on that. This means that the

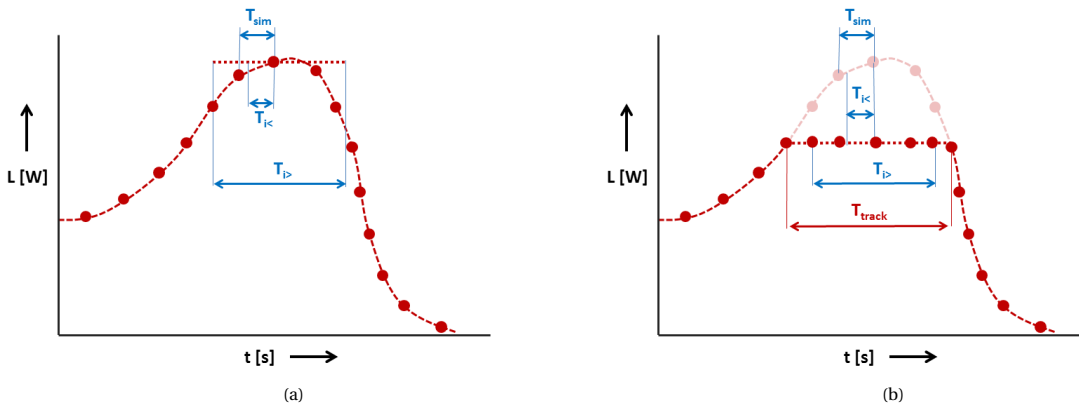


Figure 2.8: Used luminosity point for detecting (a) and tracking (b) calculations.  $T_{sim}$  is the used simulation time step,  $T_i >$  is an integration or exposure time bigger than the simulation time step and  $T_i <$  is an integration or exposure time smaller than the simulation time step.  $T_{track}$  is the desired tracking time.

result is too optimistic, since less energy reaches the detector in the other 90 ms than the intended 10 ms. This effect is of course even more prominent in the 1000 ms exposure time cases.

With the tracking setup some other optical problems arise, compared to just detecting. For example, if an observed object is only a fraction of the exposure time in the pixel, during the rest of the exposure time only the background is being observed. This reduces the effective SBR and SNR in that observation. In case the exposure time is shorter than the time that the object is in the pixel, the SBR and SNR stay the same for all those observations, see Figure 2.9. This latter event creates a problem regarding the spatial resolution of the pixel array w.r.t. the object. If the object is not in the middle of the pixel not all the diffraction limited energy is going to this one pixel. It is split over multiple pixels, reducing the SBR and SNR, see Figure 2.10<sup>5</sup>. As explained before in Section 2.2.2 a program was written to address how much of the energy goes on average in the pixel, see Appendix E.

The problem described above is addressed using the fraction  $\frac{X}{V \times T_i}$ , which dictates how much of the integration time the object is actually in a pixel. Here  $V$  is the velocity of the object at time of observing,  $T_i$  is the integration time and  $X$  is the ground resolution of the pixel. It divides the pixel ground resolution  $X$  by the distance traveled in one integration cycle  $V \times T_i$ . This leads to an amount of seconds it took to cross the pixel. If these amount of seconds are divided by the integration time  $T_i$ , a fraction of the integration that the object was in the pixel is found. This can be directly applied to the SBR, since it affects only the numerator (signal of the object, background is still in the pixel the whole time) of that fraction and the SBR is calculated using the integration time  $T_i$ . For the SNR both the object part in the numerator and partially in the denominator need

<sup>5</sup>cloudynights.com. [https://www.cloudynights.com/uploads/monthly\\_01\\_2017/post-219375-0-95631600-1485404418.jpg](https://www.cloudynights.com/uploads/monthly_01_2017/post-219375-0-95631600-1485404418.jpg) (Accessed Dec 6, 2018).

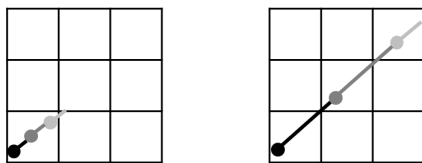


Figure 2.9: Comparison of two pixel arrays with a each 3 observations for assumed same exposure time each. First scenario has almost 3 observations in 1 pixel, second scenario has first observation spread out from first to second point, reducing the SBR and SNR in that first pixel, since there is observation time of just only the background as well.

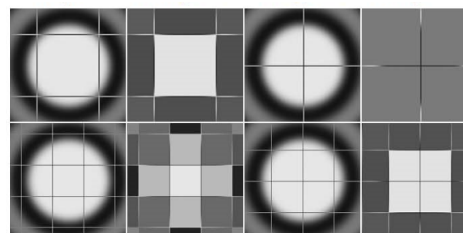


Figure 2.10: Comparison of object's PSF in different pixel configurations. 1st and 3rd column are alignments of pixel w.r.t. the same observed airy disc. Columns 2 and 4 are the resulting intensities in the pixels. Increased rows add extra pixels to the array. Especially the first row is important, it shows that for certain conditions the object's PSF will be observed and depending on its place compared to the pixels it will be much more faint. This is important in determining the effective SBR. See text for source.

to be adjusted. Again the background is still always in the pixel during the integration time. The formulas for the just described corrections are shown in Equations 2.45 and 2.46. The detector readout noise is for these calculations removed from the object's signal total noise so it is not counted double.

$$SBR_{eff} = SBR \times \frac{X}{V \times T_i} \quad (2.45)$$

$$SNR_{eff} = \frac{N_{e,obj} \frac{X}{V \times T_i}}{\sqrt{\frac{X}{V \times T_i} N_{e,obj} + \sqrt{N_{e,back} + N_r^2}}} \quad (2.46)$$

These effective SNR and SBR values are further on used in the calculations for the GEO optical instrument parameters when the "tracking" mode is chosen.

With this last section the whole procedure of calculating the optical instrument parameters has been addressed for both detecting and tracking requirements. Aperture diameter, focal length, SBR and SNR can be calculated such that the objects can be either detected or tracked, for given detector settings. With the results following from these calculations the remaining research questions 2, 4, and 5 should be able to be answered.

# Verification and Validation

Verification and validation was performed on the results produced by the re-entry trajectories and state simulations, and on the found optical instrument parameters, using data from real observations and satellite systems. The verification and validation is split up respectively in the re-entry simulation part in Section 3.1 and the GEO optical instrument parameter calculation part in Section 3.2.

## 3.1. Re-entry Simulations

In this section the verification and validation with respect to the re-entry state simulations are discussed. Within the below subsections as much as possible the model outputs are validated.

The calculated trajectory is compared with real observations from the Hayabusa and Stardust capsules to validate that the code produces accurate results in Sections 3.1.1 and 3.1.2. The used Aerothermodynamics used in the re-entry simulations are validated by using data from other researches in Section 3.1.3. It will show that the used sublimation factors and surface temperature gradients result in errors of less than 10% in heat fluxes and surface temperatures, compared to heat fluxes and surface temperatures found in other researches.

The calculated trajectory is compared with real observations for meteors in Sections 3.1.4 and 3.1.5. Reasoning why another validation method could be used is discussed, due to some incompatibilities with the re-entry simulator used in this research. Still this topic is discussed to show that this method was successful in validating the produced luminosity profiles for meteors. In Section 3.1.6 the calculated luminosities via the heat flux model are validated with the calculated empirical luminosities. The empirical luminosity is calculated via a much used method by meteor scientists and thus gives results as if from another research. This allows for the identification of the difference between our method and the empirical one.

In Section 3.1.7 the fragmentation model is validated with the use of data from the Park Forest and Chelyabinsk meteors (Popova et al., 2013a; Brown et al., 2004).

### 3.1.1. Capsule Trajectory Verification and Validation

The simulated capsule trajectories are as expected, being similar to other research data (Mooij, 2016). In Table 3.1 the data calculated from the Hayabusa simulation and the trajectory data derived from 7 stations video observations of the re-entry of Hayabusa are shown (Ueda et al., 2011). The error in the velocity per same altitude is shown in the last column. It can be observed in the last column that the error is always lower than the uncertainty in the validation data from Ueda et al. (2011). From this it can be concluded that the calculated trajectory based on the presented model for the capsule re-entry is equal to the one made from actual video observations.

### 3.1.2. Stardust and Hayabusa Capsule Absolute Magnitude Validation

A check whether the simulated states absolute magnitudes are correct, based on the validated trajectory calculations, is performed. In Table 3.2 the calculated maximum absolute magnitudes and the corresponding altitude for both capsules are given calculated with Equation (2.23) using the different reference luminosities given in Table 2.2. Keep in mind that in the calculations sometimes the visible (400-700nm) and sometimes the bolometric luminosities are used. For both capsules the absolute magnitude values and their corresponding altitudes found in literature are given as well. These absolute magnitudes from literature are either from simulations or from real observations.

Table 3.1: Trajectory data of the Hayabusa capsule re-entry from both this research (left two columns) and from video observations given in another research (Ueda et al., 2011). The errors ranging from +0.1 km/s till +0.3 km/s, are always equal or less than the uncertainty from the validation data equal to  $\pm 0.3$  km/s.

This research		(Ueda et al., 2011)		Error [km/s]
Altitude [km]	Velocity [km/s]	Altitude [km]	Velocity [ $\pm 0.3$ km/s]	
52.0	9.9	52.0	9.9	0
51.0	9.7	51.0	9.6	+0.1
50.0	9.4	50.0	9.4	0
49.0	9.1	49.0	9.1	0
48.0	8.8	48.0	8.8	0
47.0	8.5	47.0	8.4	+0.1
46.0	8.1	46.0	8.0	+0.1
45.0	7.7	45.0	7.6	+0.1
44.0	7.2	44.0	7.2	0
43.0	6.7	43.0	6.7	0
42.0	6.2	42.0	6.1	+0.1
41.0	5.6	41.0	5.6	0
40.0	5.1	40.0	5.0	+0.1
39.0	4.5	39.0	4.4	+0.1
38.0	3.9	38.0	3.7	+0.2
37.0	3.3	37.0	3.1	+0.2
36.0	2.8	36.0	2.5	+0.3
35.7	2.6	35.0	2.4	+0.2

First, looking at the Stardust data given by Jenniskens et al. (2005) in Table 3.2 it can be observed that our calculated maximum absolute magnitude of -5.2 and the corresponding altitude of 59 km is within the range,  $-5 < M < -7$  and  $55 < h_{max,M} < 60$ , of the ones given by Jenniskens et al. (2005).

The value calculated by ReVelle and Edwards (2007) for the altitude of maximum absolute magnitude is the same as the one presented by (Jenniskens et al., 2005). However, the absolute magnitude given by ReVelle and Edwards (2007) is 4 magnitudes brighter. It is unclear what the cause for this is. However, consulting other work of the last named researchers, it seems that their absolute magnitude is differently calculated and also referred to as stellar magnitude (Ceplecha et al., 1998; Ceplecha and ReVelle, 2005). The possibly used equation is given in Equation (3.1) (Ceplecha and ReVelle, 2005). Here  $I$  is the luminosity in W, multiplied by  $10^7$  to go from W to ergs/s, and  $M$  is the absolute magnitude.

$$M = -2/5 \times (\log_{10}(I \times 10^7) - 10.185) \quad (3.1)$$

However, using equation (3.1) leads to a absolute magnitude of Stardust of -1.2, which is obviously wrong, since the value of Jenniskens et al. (2005) just confirmed that our found absolute magnitude value was accurate within the range of -5 till -7. On closer inspection Equation (3.1) seems to exhibit an error. Looking at other absolute magnitude calculations (Stokan and Campbell-Brown, 2015; Ceplecha et al., 1998), the here used 2/5 fraction should be written as 5/2 or 2.5, most possibly this is a typo in the paper of Ceplecha and ReVelle (2005). This is indeed confirmed by Gritsevich and Koschny (2011) after private communications with Ceplecha and ReVelle (2005). Correcting this leads to Equation (3.2).

$$M = -2.5 \times (\log_{10}(I \times 10^7) - 10.185) \quad (3.2)$$

Using this corrected Equation (3.2) leads to a absolute magnitude of -7.4, which is lower than the given -9 by ReVelle and Edwards (2007), but this is reasonable since our found value of -5.2 is also lower than the value of -5.5 given by Jenniskens et al. (2005).

The found Hayabusa absolute magnitude data summarized in Table 3.2 also exhibits some contingencies. First of all, the altitude of maximum luminosity calculated by Ueda et al. (2011) and Ohnishi et al. (2011) are off by respectively -16% and +10% respectively. So, it should be noted that even the data used to validate our found absolute magnitude values are between themselves not consistent.

Looking at the absolute magnitude calculated by Ueda et al. (2011) of -5, it can be observed that it is close to the calculated absolute magnitude of -4.9 using a 270 W reference luminosity. If the same approach is used as Ueda et al. (2011) to calculate the absolute magnitude via Equation (3.3), at our peak luminosity the absolute magnitude is -4.1, which is lower than the value of Ueda et al. (2011).

$$M \pm 0.6 = 4.0170 \log_{10} I + 13.581 \quad (3.3)$$

If Equation (3.3) is used on our calculated trajectory states at 43 km, an absolute magnitude of -1.6 is found, which is about 3 to 4 magnitudes lower than the value given by Ueda et al. (2011) at this altitude.

Ohnishi et al. (2011) gives an altitude of 56 km at a maximum absolute magnitude of -5.0. Here our calculated absolute magnitude of -5.2 with a reference luminosity of 270 W is a bit higher than the -5.0, but in the same range. If the same approach is done at the altitude given by Ueda et al. (2011) the found maximum luminosity is equal to -3.4, which is about 1 to 2 magnitudes lower.

Lastly a non-maximum absolute magnitude of -4 is observed at 62.7 km by Abe et al. (2011). Our found value for the absolute magnitude at that altitude is -3.8, which is within the same range.

Table 3.2: Values for absolute magnitude and the corresponding altitudes from our simulations and literature, given for the Stardust and Hayabusa capsules.

Stardust			
Source	$h_M$ [km]	$M$ [-]	Method
This research	59	-5.8	$I_{vis}/(270W)$
This research	59	-5.2	$I_{vis}/(500W)$
This research	59	-8.1	$I_{bol}/(820W)$
This research	59	-7.2	$I_{bol}/(1800W)$
(Jenniskens et al., 2005)	55-60	$-5.5 \pm 1.5$	$I_{vis}/(500W)$
(ReVelle and Edwards, 2007)	55-60	-9	Possibly eq. (3.1) or eq. (3.2)
This research	59	-7.4	See eq. (3.2)
Hayabusa			
Source	$h_{M,m}$ [km]	$M$ [-]	Method
This research	51	-4.9	$I_{vis}/(270W)$
This research	51	-4.3	$I_{vis}/(500W)$
This research	51	-5.9	$I_{bol}/(820W)$
This research	51	-6.8	$I_{bol}/(1800W)$
(Ueda et al., 2011)	43	$-5 \pm 1$	See eq. (3.3)
This research	51	$-4.1 \pm 0.6$ (at 51 km)	See eq. (3.3)
This research	43	$-1.6 \pm 0.6$ (at 43 km)	See eq. (3.3)
(Ohnishi et al., 2011)	56	$-5.0 \pm 0.3$	Saturn as reference luminosity
This research	56	-3.4	$I_{vis}/(270W)$
(Abe et al., 2011)	62.7 (not max)	-4	Unknown reference luminosity
This research	62.7 (not max)	-3.8	$I_{vis}/(270W)$

Concluding, for Stardust our calculated peak absolute magnitude is well within range and at the correct altitude as with values found by Jenniskens et al. (2005). Unfortunately, the stellar absolute magnitude of -9 presented by ReVelle and Edwards (2007) can only be approached but not met. The reason for this is also that it is uncertain how their stellar magnitude is exactly calculated. However, our altitude of maximum absolute magnitude is equal to the one given by ReVelle and Edwards (2007). From this can be concluded that the altitude of the maximum peak absolute magnitude is correctly found with our simulations.

From the Hayabusa absolute magnitude validation it can be concluded that our peak absolute magnitudes of -4.9 is close to absolute magnitude peaks found in literature of  $-5 \pm 1$  and  $-5.0 \pm 0.3$  (Ueda et al., 2011; Ohnishi et al., 2011). However, our found altitude of the peak absolute magnitude is off, but in between the ones given in literature. From this can be concluded that our simulation produces the right peak absolute magnitude values. The altitude differences between the values found in literature can not be explained, since they are both determined from real video observations.

Although the validation in this section seems to be successful, the wavelength bandwidth over which the spectral irradiance is integrated determines greatly the outcome of the calculated luminosity and absolute magnitude. Next to that, an error or change in absolute magnitude can lead to a big change in the corresponding luminosity. For example, a small magnitude difference of 0.4 leads to a luminosity difference of 50%. Also the used reference luminosities to calculate the absolute magnitude can change the resulting absolute magnitude. Therefore, an absolute magnitude comparison is not a very reliable way to do validation. In Section 3.1.3 a comparison of the calculated heat fluxes and object temperatures is done with those from literature, such to eliminate the ambiguity of the chosen filter bandwidths and reference luminosities.

### 3.1.3. Stardust and Hayabusa Capsules as Validation for Aerothermodynamics

The re-entry simulated surface temperatures and heat fluxes can be validated with data from other researches. This is especially possible for capsules, and lacking for meteors, since the vehicles are well known and can be timely observed with prior knowledge and simulated accordingly. Therefore, the aerothermodynamics will be validated with the use of capsules.

Table 3.3: Results of validation of capsule re-entry data simulation. Temperatures  $T$  in Kelvin, altitude  $h$  in km and stagnation heat fluxes  $q$  in  $\text{W}/\text{cm}^2$ .  $s$  stands for stagnation,  $m$  for maximum,  $c$  for convective,  $r$  for radiative,  $h_0$  for scale height and  $t$  for total. All simulations use 35% ablation heat flux loss (before ablation) (Olynick et al., 1998) and 0.7 temperature gradient (Suzuki et al., 2014). Note that the maximum total heat flux does not coincide with the sum of both maxima from each separate heat flux, due to both maxima being at a different altitude.

Stardust								
Source	$T_{s,m}$	$T_{s,abl,m}$	$T_{avg,m}$	$h_{T,m}$	$q_{s,c}$	$q_{s,r}$	$q_{s,t}$	Comment Source
This research (Sim1)	3649	3276	2621	59	919	90	1005	$h_0 = 7000$ m
This research (Sim2)	3616	3247	2598	72	891	83	969	$h_0 = 8500$ m
(Trumble et al., 2010)	-	3375	2775	61	940	-	-	Figures CFD
(Trumble et al., 2010)	-	3240	2810	65	-	-	-	Figures telescope
(Dec and Braun, 2006)	3789	3394	-	-	1020	100	1126	Text, figures
(Olynick et al., 1998)	3735	3380	-	-	-	119	1200	Text, figures
(Davies, 2006)	-	-	-	-	-	130	1200	Text
(Jenniskens et al., 2005)	-	3373	2630	-	-	-	-	Text, figures
RMS all papers	3762	3353	2739	63	980	117	1176	This table
Error Sim1 and RMS	-3.0%	-2.3%	-4.3%	-6.3%	-6.2%	-23.1%	-14.5%	
Hayabusa								
Source	$T_{s,m}$	$T_{s,abl,m}$	$T_{avg,m}$	$h_{T,m}$	$q_{s,c}$	$q_{s,r}$	$q_{s,t}$	Comment Source
This research (Sim1)	3895	3497	2798	52	1241	109	1305	$h_0 = 7000$ m
This research (Sim2)	3818	3428	2743	62	1153	89	1205	$h_0 = 8500$ m
(Suzuki et al., 2014)	-	3300	-	-	1250	200	1450	Text DC-8
(Snively et al., 2014)	-	-	-	57	-	-	-	Text CFD
(Davies, 2006)	-	-	-	-	-	300	1500	Text
(Löhle et al., 2013)	-	3308	-	-	-	-	-	Text CID
(Löhle et al., 2013)	-	3200	-	-	-	-	-	Text S2000
(Grinstead et al., 2011)	-	3200	-	-	-	-	1100	Figure, TRAJ code
(Winter et al., 2012)	-	3206	-	-	920	180	1090	Figure, TRAJ code
RMS all papers	-	3243	-	57	1097	233	1299	This table
Error Sim1 and RMS	-	+7.8%	-	-8.7%	+13.1%	-53.2%	+0.5%	

Temperature and stagnation heat flux data has been gathered from the simulation tool and available papers, and is summarized in Table 3.3. From this table it can be observed that there is more data available from the Stardust mission than from the Hayabusa mission. This is probably so, since Stardust was a NASA mission and the first extraterrestrial sample return capsule (SRC) ever made. In Table 3.3 all the data for each capsule is shown regarding the maximum stagnation temperature  $T_{s,m}$ , maximum stagnation temperature taking into account ablation  $T_{s,abl,m}$ , the maximum average temperature  $T_{avg,m}$ , altitude at maximum average temperature  $h_{T,m}$ , maximum convective heat flux  $q_{s,c}$ , maximum radiative heat flux  $q_{s,r}$  and maximum total heat flux without ablation  $q_{s,t}$ . In the last rows for each capsule the root mean square (RMS) is given of all the found data from the papers and the difference between the simulated data and the RMS of the data from the papers is given in percentages. Whether the data from the papers is observed or simulated, and is taken from the text or from a figure, is given in the last column.

For the Stardust mission it can be observed that the simulated results for the baseline of 7000 m scale height  $h_0$  are consistently underestimated. Using a higher scale height (thus a denser atmosphere) increases this difference, since the values obtained are lower for all parameters, except the altitude of max temperature, which increases. The differences in obtained temperatures are within a 5% bound, which is noteworthy since all the obtained heat fluxes are way more underestimated up till about 23%. The coupling between the total heat flux and the temperature is the Stefan-Boltzmann law as in Equation 2.18. This seems to be in the right order of magnitude, as the error propagated from the total heat flux to the temperature is to the power  $1/4$ ,  $\sqrt[4]{14.5} = 1.95$ , which is just a little bit lower than the found error of 2.3%. From the Stardust comparison the simulation can be said to be validated for the used inputs and gives temperature values in the expected ranges, being below 5% error.

Looking at the data simulated and found on Hayabusa there is a bigger discrepancy and more unexpected behavior in those errors. In general, our simulation and the literature data gathered in Table 3.3 for Hayabusa show big differences for the temperatures and heat fluxes. What can be observed is that for the total stagnation heat flux  $q_{s,t}$  the DC-8 aircraft observations give a higher estimation than the simulations with the TRAJ code (Grinstead et al., 2011; Winter et al., 2012; Suzuki et al., 2014). The value given by Davies (2006) is even

higher, but that data is from an estimation in 2003. It is more likely that the observations are more accurate than the older simulations. Based on the error values found in Table 3.3, the total heat flux is well simulated, at less than 1% off. If the weight would be only on the observations, the simulations done for this research underestimate the heat flux by about 10%. However, this latter observation is more in line with what was just found for the Stardust case, where also the total stagnation heat flux was underestimated by 14.5%. So, if that is the case the Brandis and Johnston (2014) model for heat fluxes, which is used in our simulations and although verified based on CFD calculations, is still underestimating the radiative heat flux by about 20–60% and the convective heat flux by about 1–6%<sup>1</sup>. The conclusion is that the Brandis and Johnston (2014) model underestimates the total stagnation heat flux by about 10–15%. A higher scale height  $h_0$  for the exponential atmosphere would increase the error even more, see the second row of the Hayabusa simulations in Table 3.3.

Looking further at Table 3.3, the only other reasonable value to compare for Hayabusa is the stagnation temperature including ablation  $T_{s,abl,m}$ , since much data has been found on this parameter. All given values by the papers are reasonably close, but are still about 8% lower than the simulated values. This means that the heat flux taken away by ablation and sublimation in our simulation might be too low. This could be possible; first of all, an assumption was done that Hayabusa uses PICA, which is not the case, since it uses a Carbon-Phenolic Rayon based ablator (Snively et al., 2014). Detailed information on the Carbon-Phenolic Rayon based ablator could not be found, so PICA was used instead. The Carbon-Phenolic Rayon Ablator has a higher density and lower ablative capacity (Riccio et al., 2017), which means that during re-entry it ablates more mass faster. Hayabusa had a TPS mass fraction of about 43% and Stardust about 22%, which means, taking into account their total masses, that Hayabusa's TPS was weighting 7 kg and Stardust's TPS 10 kg. This implies that in reality more material needed to be ablated for Hayabusa's TPS and thus also more energy, percentage wise, goes into ablation compared to with Stardust's TPS. This could explain the higher stagnation temperature calculated for Hayabusa by using Stardust's PICA TPS, compared to the value from literature.

All in all, the conclusion is that Stardust's temperatures are well simulated within 5% compared to data found in papers, which is the most important concerning the further steps in this research. As for Hayabusa, the results are more off, but still within a 10% bound. The sublimation factor for Hayabusa could be increased to about 46%, such to get much closer to the expected stagnation temperature.

Furthermore the scale height could be adjusted a little to account for the altitude being underestimated in both cases. However, this increases the temperature errors for Stardust, but makes the solution for Hayabusa a little bit better by a few percent.

### 3.1.4. Meteor Trajectory Validation

Just like the capsule re-entry trajectories the calculated meteor trajectories could be validated. The meteor trajectory calculations are verified by the fact that capsules and meteors are both exhibiting a ballistic flight, and that the ballistic flight simulations have been verified in Section 3.1.1.

To validate the outcome of the re-entry simulations for meteors, data from Halliday et al. (1996) can be used. For 259 fireballs the observed altitude versus velocity is determined. A meteor with the ID MORP (Meteorite Observation and Recovery Project) 223, having a mass of 232 kg, is taken from Halliday et al. (1996) to use as validation data. For the simulation the fragmentation parameters are found, by manually tuning, to be 0.62 strength scaling, 2 fragments per breakup and 0.32 MPa initial strength, such to get an adequate fit on the velocity versus altitude data from Halliday et al. (1996).

The results of the computed meteor trajectory and the data from Halliday et al. (1996) are shown in Table 3.4. As can be seen the error between the outcome of the simulation and the data from Halliday et al. (1996) have a maximum error of about 0.8 km/s at maximum, which is less than 10% of the velocity at any point in the evaluated interval.

The same has been done for another meteor with a much lower mass of only 0.350 kg, MORP 287. The simulated trajectory results and the observation data from Halliday et al. (1996) are given in Table 3.5. For the simulation the fragmentation parameters are found, by manually tuning, to be 0.6 strength scaling, 2 fragments per breakup and 0.3 MPa initial strength. The maximum error between the velocities at the same altitudes does not exceed 0.9 km/s, which is at no point more than 6% of the velocity.

From these two different meteors assessed it can be concluded that the trajectories of meteors can be

<sup>1</sup>This heat flux model is only proven to be correct between 3 and 17 km/s and for nose radii between 0.2 m and 10 m, and for atmospheric densities at altitudes between 40 km and 85 km. Therefore, these underestimations can not be linked to wrong use of the model (Brandis and Johnston, 2014).

adequately simulated. The fragmentation parameters play an important role, and by no means the 3 used fragmentation parameters for these 2 simulations are the overall best fit. But, it has shown that the simulator is capable of calculating a trajectory with less than 10% velocity error at the same altitude.

Table 3.4: Trajectory data of meteor MORP 223 for both this research ( $h_0=7000$  m) and from observations taken from [Halliday et al. \(1996\)](#). Fragmentation parameters for MORP 223 are 0.62 strength scaling, 2 fragments per breakup and 0.32 MPa initial strength.

Time [s]	Altitude [km]	This research		(Halliday et al., 1996)			Error [km/s]	Error $M_{bol} - M_H$
		Velocity [km/s]	$M_{bol}$ $I_{bol}/(1800W)$	Altitude [km]	Velocity [km/s]	$M_H$ [-]		
0.00	78.5	27.1	-8.1	78.50	27.1	-9.4	0	+1.3
1.09	68.6	27.1	-9.0	68.60	27.1	-11.6	0	+2.6
2.20	58.6	27.0	-10.1	58.60	27.0	-14.0	0	+3.9
3.31	49.0	26.8	-12.0	49.00	27.0	-14.7	-0.2	+2.7
3.76	45.2	26.5	-12.8	45.20	26.8	-14.6	-0.3	+1.8
4.30	40.9	25.5	-13.7	40.90	26.1	-14.3	-0.6	+0.6
4.85	37.0	23.6	-14.5	37.00	24.1	-13.5	-0.5	-1.0
5.16	35.0	22.1	-14.7	35.00	22.1	-12.8	0	-1.9
5.84	31.3	17.4	-15.0	31.30	17.4	-11.3	0	-3.7
6.12	30.0	15.3	-14.6	30.00	15.4	-10.7	-0.1	-3.9
6.40	28.9	13.5	-13.9	28.90	13.5	-10.2	0	-3.7
6.70	27.8	11.6	-12.8	27.80	11.5	-9.6	+0.1	-3.2
6.92	27.1	10.3	-11.9	27.10	9.5	-9.0	+0.8	-2.1

Table 3.5: Trajectory data of meteor MORP 287 for both this research (left two columns,  $h_0 = 7000$  m) and from observations taken from [Halliday et al. \(1996\)](#). Fragmentation parameters are 0.6 strength scaling, 2 fragments per breakup and 0.3 MPa initial strength.

Time [s]	Altitude [km]	This research		(Halliday et al., 1996)			Error [km/s]	Error $M_{bol} - M_H$
		Velocity [km/s]	$M_{bol}$ $I_{bol}/(1800W)$	Altitude [km]	Velocity [km/s]	$M_H$ [-]		
0.0	69.6	23.4	-4.9	69.6	23.4	-6.2	0	+1.3
0.4	61.7	23.3	-5.5	61.7	23.2	-6.7	+0.1	+1.2
0.7	55.7	23.1	-6.1	55.7	22.8	-7.6	+0.3	+1.5
1.1	49.8	22.7	-7.0	49.8	22.2	-7.6	+0.5	+0.6
1.4	44.0	21.2	-7.8	44.0	21.0	-7.6	+0.2	-0.2
1.7	38.6	17.2	-8.0	38.6	18.1	-7.2	-0.9	-0.8
2.1	34.6	12.2	-6.5	34.6	12.0	-6.5	+0.2	+0

### 3.1.5. Assessment of Validation Data of Meteor Luminosities from Other Researches

In order to validate the produced absolute magnitudes for meteor re-entries, a look is taken again at the data simulated from meteor MORP 287 in Table 3.5. The temperature gradient is set to 0, since there is no reason to believe that there is a temperature gradient over such a small surface, and the sublimation fraction to 0.33. This latter value is taken from a research in which it was estimated that 33% of the kinetic energy of a 15 km/s meteor goes into reflection of atmospheric particles, and thus not into heating up meteoric material and the meteor body ([Bronshnten, 1983](#)).  $M_{bol}$  is calculated using the bolometric luminosity (all wavelengths) and the 1800 W reference luminosity as done by [Halliday et al. \(1996\)](#). As can be observed the error between the absolute magnitude data from [Halliday et al. \(1996\)](#) as  $M_H$  and calculated  $M_{bol}$  is maximum about  $\pm 1.5$  absolute magnitudes, but reaches the peak absolute magnitude with an error of  $\pm 0.2$ . From this can be concluded, that the peak absolute magnitude can be estimated with an error of about 0.2 absolute magnitudes compared to real observations. However, the overall absolute magnitude curve per altitude of the object can be off by as much as almost 1.5 absolute magnitudes.

The validation done for meteor MORP 287 gives good results, however, the usable velocity and mass ranges for the heat flux model used in this simulation were violated ([Brandis and Johnston, 2014](#)). The mass was way lower (350 grams instead of minimal 150 kg) than allowed and the velocities were too high (maximum 17 km/s allowed).

Therefore, meteors needed to be found of more than 150 kg, such that at a mean density of 3500 kg/m<sup>3</sup> the radius would be more than 0.2 m. Next to that their entry velocities should be below 17 km/s. This is necessary to comply with the used heat flux model by [Brandis and Johnston \(2014\)](#) in our simulations, and thus needed for adequate validation.

[Halliday et al. \(1996\)](#) gives only two meteoroids (MORP 223 and MORP 925) with a mass larger than 150 kg, but both with a velocity of about 27 km/s. The data for MORP 223 was already given in Table 3.4. From this

Table 3.6: Trajectory data of meteor MORP 925 for both this research (for two different entry angles,  $h_0 = 7000$  m) and from observations taken from [Halliday et al. \(1996\)](#). Fragmentation parameters are 0.98 strength scaling, 2 fragments per breakup and 0.15 MPa initial strength for the  $\gamma = 7.5^\circ$  case and 0.53 strength scaling, 2 fragments per breakup and 0.22 MPa initial strength for the  $\gamma = 8.1^\circ$  case. Given are time  $t$  in seconds, altitude  $h$  in km, velocity  $V$  in km/s and absolute magnitudes  $M_{bol}$  and  $M_H$ .

Meteor MORP 925																
This research $\gamma = 7.5^\circ$					This research $\gamma = 8.1^\circ$					(Halliday et al., 1996)				$\Delta \gamma = 8.1^\circ$ and $H$		
t	h	V	$M_{bol}$	$M_H$	t	h	V	$M_{bol}$	$M_H$	t	h	V	$M_H$	$\Delta V$	$\Delta M_{bol}$	$\Delta M_H$
0.00	91.2	26.4	-8.0	NaN	0.00	91.2	26.4	-8.0	NaN	0	91.2	26.4	-6.0	+0	-2.0	
2.06	84.3	26.4	-8.5	-7.9	1.90	84.3	26.4	-8.5	-7.9	2	84.3	26.4	-8.6	+0	+0.1	+0.7
4.32	77.2	26.4	-9.1	-9.4	3.96	77.2	26.4	-9.1	-9.4	4	77.2	26.3	-10.9	+0.1	+1.7	+1.5
6.65	70.4	26.4	-9.8	-10.6	6.05	70.4	26.4	-9.8	-10.5	6	70.4	26.2	-12.7	+0.2	+2.9	+2.2
9.11	63.8	26.4	-10.5	-11.6	8.22	63.8	26.4	-10.5	-11.6	8	63.8	26.0	-14.0	+0.4	+3.5	+2.4
11.69	57.5	26.3	-11.3	-12.6	10.46	57.5	26.3	-11.3	-12.6	10	57.5	25.8	-14.6	+0.5	+3.3	+2.0
14.13	52.2	26.0	-12.3	-13.6	12.49	52.2	26.1	-12.6	-13.8	12	52.2	25.5	-14.8	+0.6	+2.2	+1.0
16.52	47.6	25.4	-13.3	-14.3	14.43	47.6	25.5	-13.5	-14.6	14	47.6	24.9	-14.9	+0.6	+1.4	+0.3
19.17	43.3	24.0	-14.1	-14.7	16.47	43.3	23.9	-14.6	-15.2	16	43.3	23.7	-14.4	+0.2	-0.2	-0.8
21.19	40.6	22.2	-14.4	-14.6	17.96	40.6	21.8	-14.9	-15.1	17.5	40.6	22.1	-13.9	-0.3	-1.0	-1.2
24.29	37.4	18.7	-14.6	-14.2	20.12	37.4	18.1	-14.9	-14.6	19.5	37.4	18.7	-12.9	-0.6	-2.0	-1.7
31.94	33.0	10.7	-11.6	-12.7	24.73	33.0	10.6	-11.9	-13.1	21.5	33.0	10.7	-10.4	-0.1	-1.5	-2.7
36.16	31.7	7.9	-9.6	-11.8	26.91	31.7	8.2	-10.4	-12.4	25.5	31.7	7.7	-9.3	+0.5	-1.1	-3.1
40.50	30.7	6.0	-8.7	-11.0	29.07	30.7	6.4	-9.7	-11.7	27.5	30.7	5.8	-8.4	+0.6	-1.3	-3.3
44.09	30.0	4.9	-8.1	-10.4	30.92	30.0	5.3	-9.1	-11.2	29.5	30.0	4.5	-7.8	+0.8	-1.3	-3.4
45.18	29.8	4.6	-7.9	-10.3	31.50	29.8	5.0	-8.9	-11.0	30.1	29.8	4.2	-7.6	+0.8	-1.3	-3.4

can be concluded that the magnitude at any altitude compared to [Halliday et al. \(1996\)](#) can be off as much as  $\pm 3.9$  absolute magnitudes. However, the peak absolute magnitude, although found at a different altitude, is off by only 0.3 absolute magnitudes. With the tweaking of the scale height  $h_0$  or sublimation factor the peak absolute magnitude value can be found equal as that of [Halliday et al. \(1996\)](#), but this is not shown for now.

The data for MORP 925 is given in Table 3.6. First the 1242 kg meteor was simulated at the given entry angle by [Halliday et al. \(1996\)](#) of  $7.5^\circ$ . The results are given in Table 3.6 on the most left section. As can be observed the duration of the re-entry simulated this way takes 15 seconds longer to reach the final altitude as given by [Halliday et al. \(1996\)](#), given in the 3rd section of the Table. Since no lift has been simulated and thus the lift can not be the problem of the meteor not plunging fast enough in the atmosphere, the most probably cause is the used entry angle. Since the given altitude versus velocity data by [Halliday et al. \(1996\)](#) is based on reduction of the observation data it has been assumed to be a linear line ([McCrosky and Posen, 1968](#)). The entry angle will be calculated more shallow by assuming a linear line for long trajectories, since the trajectory is in reality of a convex nature in most early parts of a re-entry trajectory ([Mooij, 2016](#); [Gritsevich, 2007](#)). The simulation of meteor MORP 925 was ran again, but now changing the entry angle to a bit more steep value such that the duration of the re-entry was the same as observed by [Halliday et al. \(1996\)](#). The result of the second run is given in the 2nd section of Table 3.6.

The differences between the simulation at an entry angle of  $\gamma = 8.1^\circ$  and the data given by [Halliday et al. \(1996\)](#) on meteor MORP 925 are given in the most right section of Table 3.6. From this can be concluded that the differences in velocity are never more than  $\pm 0.8$  km/s, which is only at the very slow parts of the trajectory ( $< 5$  km/s) more than 10% error.

Regarding the absolute magnitudes,  $M_{bol}$  is calculated by using Equation (2.23), using a 1800 W reference luminosity, and  $M_H$  is calculated as by using Equations (2.20) and (2.21) with a value of 0.04 for the luminous coefficient  $\tau$ . The value of  $M_H$  is not further used in this research, but gives insight in how our results compare using the same method to the results of [Halliday et al. \(1996\)](#). Comparing both differences in absolute magnitudes at any point in the trajectory it can be observed that the differences are smaller with the  $M_H$  (max  $\pm 2.9$ ) than the  $M_{bol}$  (max  $\pm 3.5$ ) method for fast parts of the trajectory ( $> 10$  km/s). Also the peak absolute magnitude of the simulation along the trajectory happens closer to the altitude given by [Halliday et al. \(1996\)](#) with the  $M_H$  method. However, the  $M_H$  method overestimates the value of the maximum absolute magnitude by  $-0.2$ , whilst the  $M_{bol}$  method gives the exact same value of  $-14.9$ .

Most of the other estimated meteoroid masses by [Halliday et al. \(1996\)](#) are at least a factor 1000 lower. It was also concluded that [Halliday et al. \(1996\)](#) does not use the gravitational acceleration, but it is applied in this research. This means that the objects simulated in this research do get a gravitational acceleration during their re-entry in the atmosphere, and keep an overall bigger velocity because of that. Next to that, [Halliday et al. \(1996\)](#) assumes brick shapes for the determination of the mass, which leads to about 2 times higher masses than if he used the same method, see also appendix F. This means that the masses found by [Halliday](#)

Table 3.7: Different peak luminosities given in Watt for entry angle  $\gamma_E$  of  $45^\circ$ , and different entry velocities and entry masses. Assuming a density of  $3500 \text{ kg/m}^3$ , the heat flux luminosities of the meteors above 150 kg and below 20 km/s are within the bounds of the used heat flux model (shown in bold font) (Brandis and Johnston, 2014). Simulation model is adjusted by using the ablation reduction factor of 33% (Bronshnten, 1983). All shown for baseline fragmentation case with strength scaling of 0.1, 2 fragments per break-up and initial strength of 1.5 MPa. Empirical Luminosity calculated with the luminosity coefficient as calculated by the method of Stokan and Campbell-Brown (2015).

$V_E$ [km/s]	Mass [kg]			Difference w.r.t.		
	1	150	5000	heat flux bolometric luminosity		
	Heat Flux Bolometric Luminosity [W]					
70	1.80E+08	2.01E+10	6.19E+11			
50	6.82E+07	9.66E+09	3.08E+11			
30	2.34E+07	4.22E+09	1.52E+11			
20	7.76E+06	2.06E+09	7.98E+10			
11	2.30E+05	3.73E+07	1.49E+09			
	Empirical Luminosity [W]					
70	1.10E+09	1.87E+11	5.81E+12	512.17%	827.10%	837.43%
50	4.72E+08	7.05E+10	2.31E+12	591.72%	629.79%	648.35%
30	4.54E+07	7.94E+09	2.58E+11	94.29%	88.21%	70.14%
20	2.78E+06	8.40E+08	2.87E+10	-64.17%	<b>-59.18%</b>	<b>-64.01%</b>
11	2.52E+04	6.51E+06	2.61E+08	-89.03%	<b>-82.55%</b>	<b>-82.49%</b>

et al. (1996), since they are differently propagated backwards, are only to some extent usable as validation data. This all above shows that our simulation outcomes are comparable to the data from Halliday et al. (1996), but that the data from Halliday et al. (1996) is not very reliable detailed validation data due to its big differences with our simulation method.

In order to get another validation done on meteor re-entry simulations for their absolute magnitude, the next section will show a different way to do this, using the luminosity instead of absolute magnitude itself, eliminating the ambiguity of the chosen reference luminosity used in this section.

### 3.1.6. Validation of the Heat Flux Model with the Empirical Luminosities for Meteors

It has been shown in Section 3.1.3 that the heat flux model can be used for capsules rather well. But since no surface temperatures have been measured directly of meteors, only indirectly with a lot of specific assumptions (Popova, 2005; Yanagisawa, 2015), a different approach is needed here.

The idea is to use the luminosity coefficient models by Stokan and Campbell-Brown (2015); Weryk and Brown (2013), as explained in Section 2.1.2 which is based on the Canadian Meteor Orbit Radar (CMOR) data. This model can be used to validate whether the heat flux model from Brandis and Johnston (2014) used in this research, with a sublimation heat flux reduction of 0.33 for meteors (Bronshnten, 1983) and zero temperature gradient over the meteor wet surface, can be used adequately for meteors. This allows for a good comparison between the luminosity derived from the heat flux method incorporated in this research and the luminosities as would be calculated by others of the meteor scientists community.

Next to this, in Section 3.1.5 only meteors with a velocity below 30 km/s have been investigated. With the use of the empirical luminosity model also meteors with velocities above 30 km/s can be addressed, regarding their luminosity calculated with the heat flux model.

Table 3.7 shows the results for fragmentation simulations with the luminosities using the heat flux model and the luminous coefficient of Stokan and Campbell-Brown (2015). Also on the right side of the table the differences between the shown empirical luminosities and the calculated luminosity via the heat flux model are shown in percentages. It can be observed that the empirical luminosity model predicts a 590-840 % higher luminosities than the luminosities calculated with our used heat flux model for velocities of 50-70 km/s. This is expected, since the heat flux model should only be used till 20 km/s Brandis and Johnston (2014). Furthermore, within the applicable ranges of 10-20 km/s and 150+ kg of the heat flux model, the empirical model from Stokan and Campbell-Brown (2015) underpredicts the luminosity output compared to our results. From more simulations, of which the results are not shown, the maximum overestimation is just about 35% when using the constant luminous coefficient 4% of Halliday et al. (1996).

Our luminosities at or below 20 km/s are overestimated by 900 % (which is equivalent to the empirical luminosity being 90% lower than our heat flux luminosity), which means a -2.4 differences in absolute magnitude using Equation (2.23). In Section 3.1.5 most peak absolute magnitude values were overestimated using our heat flux model by at most -0.4 absolute magnitudes. Thus the overestimations of the peak absolute magnitude values in Section 3.1.5 at velocities of at most 20 km/s and the overestimations in this section

at those velocities are not in agreement. Moreover, the heat flux model in those velocities and masses used in this section are within its allowable ranges. This means that for meteor simulations the used reduction of ablation fraction at velocities below 20 km/s should be a little bit higher than 0.33 or that a temperature gradient should be applied, such that the average temperature of the meteor is lower and thus less luminosity is emitted.

For velocities at or above 30 km/s the underprediction of the luminosity by our heat flux model is at maximum 900%. This leads to a difference in absolute magnitude of about +2.4. The most probably reason for this is the heat flux model, since in that case it is used outside of its applicable range and the reduction of ablation of 33% can not make up for this error when removed.

Regarding the use of the heat flux model, the errors in the luminosity seem to be unaffected by the too low mass used of 1 kg compared to the 150 kg mass, of which the first isn't and the latter one is in the applicable range for the heat flux model. Based on that, the heat flux model seems to be applicable for meteors of smaller sizes than the official applicable lower limit radius of 0.2 m.

What was also found is that for lower fragmentation parameters, of for example a strength scaling of 0.1, 2 fragments per break-up and initial strength of 0.1 MPa, the underestimations at higher velocities dropped till a maximum of 33%. The overestimations at lower velocities stayed at 900%. It could be that since the trail of the meteor is not taken into account with the heat flux model, but the empirical luminosity coefficient is derived from meteor observations with trails (Stokan and Campbell-Brown, 2015), that with the lower fragmentation strength, and thus more fragmentation, a trail situation is approached. Nothing is changed regarding the baseline fragmentation parameters, but this is an interesting hypothesis.

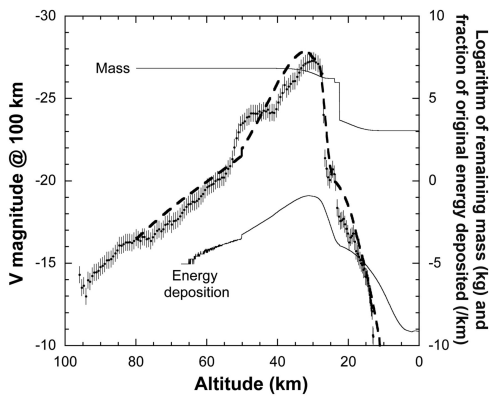
From the above validation can thus be concluded that for meteors with a velocity at or below 20 km/s the luminosity is overestimated by at maximum 900% and underestimated at velocities above that by at maximum 900% (+2.4 absolute magnitude). These errors are the differences between our used luminosity calculation method based on heat flux and the luminosities as if they were obtained by other meteor scientist using the luminous coefficient (Stokan and Campbell-Brown, 2015). When using the luminous coefficient of Halliday et al. (1996) the maximum overestimation is just about 35%. The cause for the errors below 20 km/s is most probably the not used temperature gradient over the surface over the meteor. The cause for the errors above 20 km/s is most probably the not applicable ranges of the heat flux model. This means that when calculating GEO instrument parameters based on this the aperture diameters for meteors with velocities below 20 km/s will be underestimated and the aperture diameters above 20 km/s will be overestimated. More fragmentation led to less underestimation of the luminosity with the heat flux model. The hypothesis for this is that the more fragmentation events approach a meteor trail situation, that phenomenon is seen in most meteors on which the empirical luminosity coefficient is based. No changes are made to the used settings in the re-entry simulations, but the error induced on the aperture diameters will be discussed in Chapter 5.

### 3.1.7. Meteor Fragmentation Model

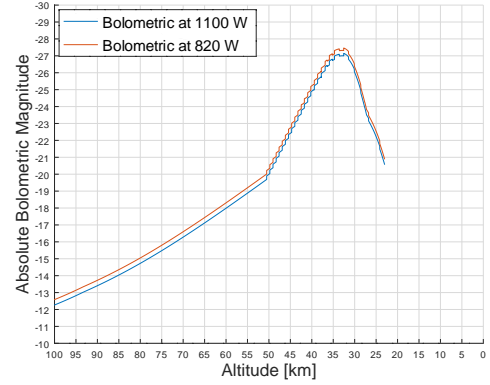
Using a non-cloud independent wake fragmentation model (Register et al., 2017), similar to the one from (Mathias et al., 2017; Wheeler et al., 2017), but without the dust cloud modeling, big meteors can be modeled better for their luminosity profile compared to non-fragmentating simulations. To show the differences, results from fragmentating model and actual observations for the Chelyabinsk and Park Forest meteors are shown in Figures 3.1a till 3.2b.

As can be observed from Figures 3.1b and 3.2b, the fragmentating model predicts a similar curve as the observed ones, as given in Figures 3.1a and 3.2a. Clear fragmentation steps can be seen, due to the model's approximations. This proves that the fragmentation model is sufficient for predicting the max magnitude of fragmentating meteors. One other thing is that the calculated absolute magnitude curve is very susceptible to the input parameters. The fragmentation parameters found for Chelyabinsk are a strength scaling of 0.15, 2 fragments per break-up and an initial strength of 0.3 MPa (Register et al., 2017; Popova et al., 2013b), for Park Forest these are 0.035, 4 and 2.4 MPa respectively (Brown et al., 2004). Note that for both cases the researchers used a 6000 K black body for a zero absolute magnitude meteor irradiating 1100 W as from Ceplecha et al. (1998), which takes into account conversion between observed V-band to bolometric luminosity, and one with 1800 W reference luminosity (Halliday et al., 1996).

From Figure 3.1a, taken from Popova et al. (2013b), it can be observed that Chelyabinsk had a peak absolute magnitude observed at  $-27.3 \pm 0.5$ , and a simulated peak at -27.8. From our research the peak is estimated to be -27.1 and -27.5 absolute magnitudes for 1100 W and 820 W reference luminosities respectively, see Figures 3.1b. Since the 1100 W was used by Popova et al. (2013b) as reference luminosity, this should be the value compared with the simulation. Comparing the 1100 W simulation magnitudes shows that our

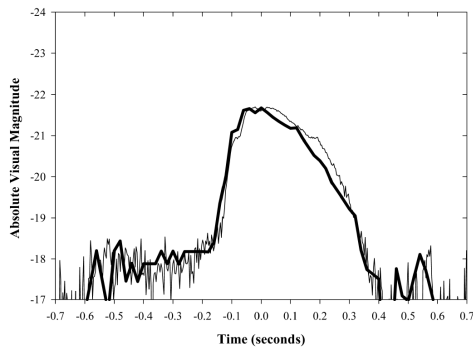


(a) Absolute visual magnitude for the Chelyabinsk meteor (Popova et al., 2013a). Bold line is estimation, thin line is observed.

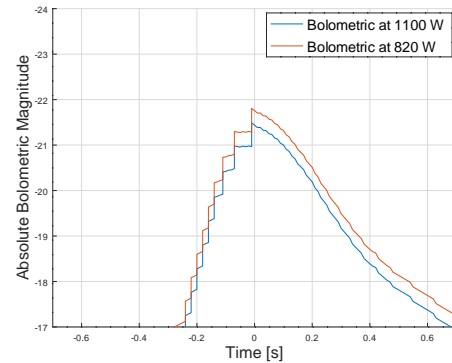


(b) Simulated absolute bolometric magnitude curves per altitude for Chelyabinsk meteor. Blue line uses 1100 W reference luminosity (Popova et al., 2013b; Ceplecha et al., 1998) and red line uses 1800 W reference luminosity (Halliday et al., 1996).

Figure 3.1: Absolute magnitude curves from other researches and our simulations for the Chelyabinsk Meteor.



(a) Absolute visual magnitude for the Park Forest meteor (Brown et al., 2004). Bold line is estimation, thin line is observed.



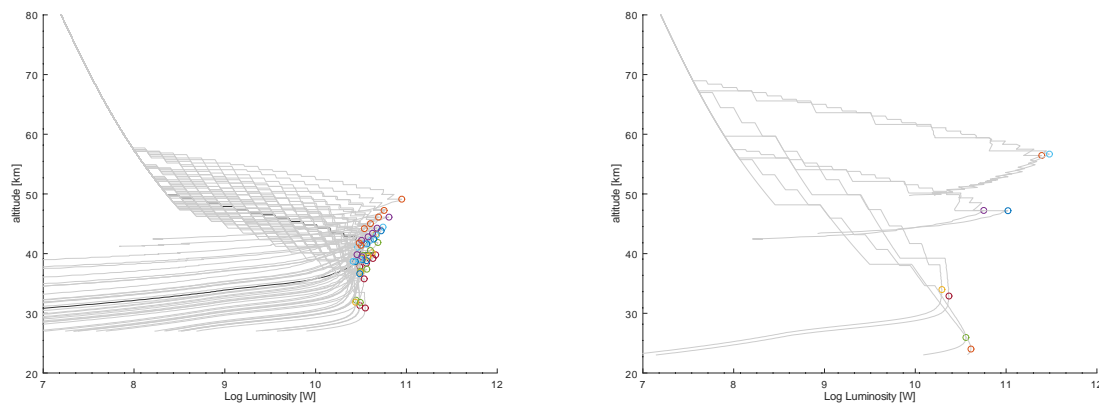
(b) Simulated absolute bolometric magnitude curves per altitude for Chelyabinsk meteor. Blue line uses 1100 W reference luminosity (Ceplecha et al., 1998) and red line uses 1800 W reference luminosity (Halliday et al., 1996).

Figure 3.2: Absolute magnitude curves from other researches and our simulations for the Park Forest Meteor.

simulation has the peak at the right altitude of about 33 km as the simulated altitude by Popova et al. (2013b). However, our peak absolute magnitude is -27.1, where the simulated peak absolute magnitude of Popova et al. (2013b) is equal to -27.8, which is a 0.7 magnitude difference. This 0.7 difference in absolute magnitude means an underestimation of about 90% of the luminosity in our simulation compared to the simulation of Popova et al. (2013b). This value is still within the bounds of the error of the observed magnitude and can be deemed valid. Our simulation finds the peak altitude the same as the simulation from Popova et al. (2013b), but the peak absolute magnitude value in very close agreement with the sobered peak absolute magnitude by Popova et al. (2013b).

The Park Forest meteor was observed to have a absolute magnitude peak of about -21.7, see Figure 3.2a. In Figure 3.2b our simulated results are given, with a peak absolute magnitude for 1100 W reference luminosity at -21.5. This is off by 0.2, which translates to a luminosity error of 20%. Our simulated curve is a bit convex, whilst the data from Brown et al. (2004) is more concave. This means, that if integrated over the same time span of 0.4 seconds around the peak the total energy of our simulation would be lower than that of Brown et al. (2004). Furthermore, our simulations cross the -18 absolute magnitude at about -0.2 and 0.45 seconds, where Brown et al. (2004) crosses these magnitudes at -0.6 to -0.2 and 0.35 seconds. This means that our peak is a bit shifter later in time than was observed. From this validation it can be concluded that the peak absolute magnitude can be simulated with less than 0.2 absolute magnitude (or 20% luminosity error) precision for the Park Forest meteor.

From papers it can not be concluded whether gross/sudden/discreet fragmentation occurs at a certain minimal mass for meteoroids. However, Ceplecha and ReVelle (2005) shows that their different fragmentation



(a) Fragmentation parameters: strength scaling: 0.08-1, amount of fragments per break-up: 2, and initial strength: 0.5MPa-2MPa. (b) Fragmentation parameters: strength scaling: 0.1 and 0.5, amount of fragments per break-up: 2 and 16, and initial strength: 0.1 MPa and 0.5 MPa.

Figure 3.3: Logarithmic luminosity versus altitude for a 40 km/s meteor at 45° entry angle of 1000 kg. Grey lines are non-baseline, black line is baseline fragmentation parameters [0.1,2,1.5MPa]. Colored circles indicate maximums for one set of fragmentation parameters.

model is applicable to Leonids as well, which are shown to be as light as several grams. Jones and Kaiser (1966) determined that meteors smaller than 0.1 cm do not fragmentate. With the assumption of a density of 3500 kg/m<sup>3</sup> a 0.1 cm radius sphere is 0.02 grams. The discrete independent wake fragmentation model will thus be applied in the rest of this research to any meteors with a radius bigger than 0.1 cm and to any meteors with a mass greater than 0.02 grams.

Another set of simulations was ran to check whether the baseline parameters chosen for the fragmentation parameters is adequate. As can be observed in Figure 3.3a the baseline is a good approximation of a general meteor. The baseline curve is in the middle of all the simulation runs over the whole expected strength scaling range between 0.05 and 1 (Register et al., 2017) and in close range of known initial strengths of meteors, like Chelyabinsk at 0.2 MPa (Popova et al., 2013b) and Park Forest (Brown et al., 2004) at about 2.4 MPa, of 0.5 MPa till 2 MPa.

The amount of fragments do not play a big role, see Figure 3.3b. Here, for the lower burst pressure at the highest altitude of 0.1 MPa and the lowest strength scaling of 0.1, the 2 or 16 fragments simulations end up in about the same place at about 50-60 km with a log<sub>10</sub> luminosity of about 11.5.

From these small simulation sets can be concluded that the baseline parameters of strength scaling equal to 0.1, fragments per break-up of 2, and initial strength of 1.5 MPa is a good approximation and average for meteor fragmentation.

### 3.1.8. Summary on the Validation of Re-entry Simulations

The validation results from Section 3.1.1 till 3.1.7 can be summarized as follows:

- The Hayabusa capsules trajectory could be very well simulated with at most 0.3 km/s difference compared to the data observed by Ueda et al. (2011), which is equal or below the error margin of  $\pm 0.3$  km/s as given by the same researcher. At no point was there a deviation of the velocity versus altitude curve of more than 12%.
- The maximum absolute magnitudes of both the Hayabusa and Stardust capsules could be within 0.4 absolute magnitudes (50% Luminosity error), but this hugely depends on the researches compared to. For Hayabusa the results were more agreeing with other researches than for Stardust. However, for Stardust all the researches found were not agreeing with each other as well.
- The aerothermodynamics were validated using data from 6-8 researches per capsule. The temperature errors were never more than 8% off for Stardust, and for Hayabusa never more than 4.3%. This shows that the aerothermodynamics can be well simulated.
- The trajectories simulated for meteors MORP 223 and MORP 287 show good agreement with the velocity versus altitude data derived by Halliday et al. (1996). At no point our results deviated more than 10% from those of Halliday et al. (1996), using manual fitted fragmentation parameters for each meteor. By no means could those fragmentation parameters for those meteors be validated.

- The simulated peak absolute magnitude and the corresponding altitude could not be simulated to fit with the data from [Halliday et al. \(1996\)](#), when also the trajectory was to be kept the same as in accordance with the one from [Halliday et al. \(1996\)](#). However, the simulated peak absolute magnitude value could be found with an error of  $\pm 0.3$ , just not at the right altitude. The altitude error is in the range of  $\pm 10 - 19$  km at maximum. It is unclear why the peak absolute magnitude value can be met, but not at the same altitude. However, it was identified that [Halliday et al. \(1996\)](#) has computed the trajectories with assumptions like a linear trajectory (resulting in lower entry angles), no gravitational acceleration (resulting in slower meteors, thus also burning brighter later) and different meteor shapes (brick instead of sphere, leading to more drag per mass). These different assumptions make the data not directly comparable. But then again, the validation showed that the peak absolute magnitude can be found, only not at the right altitude.
- An internal check was done simulating the luminosity via our used heat flux model and comparing it to the luminosity that would have been obtained using an empirical luminosity formula ([Stokan and Campbell-Brown, 2015](#)). From this validation was found that for a simulated meteor at  $45^\circ$  entry angle, the luminosity was overestimated by about 900% when it entered at  $< 20$  km/s and was underestimated by 590% – 900% when entering at velocities  $> 20$  km/s. When using the constant luminous coefficient of [Halliday et al. \(1996\)](#) the underestimation is just 35%. The not used temperature gradient is seen as the cause for the overestimations of the luminosity at velocities below 20 km/s. The heat flux model its applicable range is seen as the cause for the underestimations of the luminosity above 20 km/s. No changes are made to the re-entry simulation, but the error will be addressed in Section 5.
- The non-cloud independent wake fragmentation model used in this research is able to simulate the re-entry absolute magnitude curves of Chelyabinsk and the Park Forest meteor precisely. The chosen baseline parameters ( $\alpha = 0.1$ ,  $N_F = 2$ ,  $\sigma_m = 1.5$  MPa) result in a good average bolometric luminosity when addressing a wide range of realistic input parameters ( $0.08 < \alpha < 1.0$ ,  $N_F = 2$ ,  $0.5 < \sigma_m < 2$  MPa). The number of fragments do not play a very significant role in the outcome of the altitude and peak bolometric luminosity.

## 3.2. GEO Optical Parameter Determination

Next to the re-entry simulations also the optical parameter determination calculations need to be validated. This will be done using the knowledge on GEO satellite systems, like DSP, that have detected certain meteor events. After that the atmospheric model will be discussed briefly on how it is validated.

### 3.2.1. The DSP, DoD and DoE Satellite Meteor Observations as Validation

The Defense Support Program (DSP) Satellites from the United States have detected multiple meteors re-entering Earth's atmosphere in the visible and infrared (IR) wavelengths ([Brown et al., 2013](#); [Tagliaferri et al., 1995](#); [Tagliaferri, 2010](#)). To see if the determination of the instrument parameters is done correctly, the program was used to simulate an instrument that could detect the two meteors provided in the papers (Park Forest meteor and Marshall Island Fireball).

[Brown et al. \(2013\)](#) reports that from the observation data from the visible light sensors on satellites of the U.S. Department of Energy (DoE) lead to a total peak radiant intensity of  $4.2 \times 10^{10}$  W/sr in the visible spectrum. However, it is unclear how this is obtained, and if it is the value at the satellite observed or at the meteor itself. Therefore, the Park Forest simulation data from our simulation was used, since this was already well simulated and validated (with a 20% underestimation compared to observations) in Section 3.1.7. Checking the outputted W/sr for half a sphere from our simulation (without atmosphere or taking into account the wet area facing the satellite, and between 400 and 1200 nm as the DoE optical satellites) is equal to  $1.71 \times 10^{10}$  W/sr, thus 0.4 of that of the value given by [Brown et al. \(2004\)](#). If taken into account that [Brown et al. \(2004\)](#) probably found the peak radiant intensity for the whole meteor and in our simulation half a meteor surface is taken, we can find the total outputted radiant intensity of our meteor by multiplying our found value by 2, leading to  $3.42 \times 10^{10}$  W/sr. This last value is 80% of the value of [Brown et al. \(2004\)](#), which is then in good agreement with our simulation underestimating the luminosity by 20% as proved in Section 3.1.7.

For the Marshall Island meteor the visible peak radiant intensity measured by the DoE satellite was about  $2.75 \times 10^{12}$  W/sr ([Tagliaferri et al., 1995](#)) [Fig. 5]. The peak visible (400-1200) absolute magnitude of -25 ([Tagliaferri et al., 1995](#)) could be simulated with an error of  $\pm 0.2$  magnitudes (1100 W reference luminosity for the used pass band of 400-1200 nm), using a strength scaling equal to 0.05, 4 fragments per break-up, an initial

strength of 5 MPa, a mass of  $16 \times 10^5$ , entry velocity of 24 km/s and an entry angle of  $45^\circ$ . This resulted in a simulated peak radiant intensity of  $1.4 \times 10^{12}$  W/sr for half a sphere. Multiplying this by 2 for a whole sphere leads to about the same value as given by Tagliaferri et al. (1995) of  $2.75 \times 10^{12}$ .

Therefore, both simulated meteor's radiant intensities can be used within the GEO optical parameter calculations. The used inputs are given in Table 3.8. The meteor's radiant intensity peaks have been validated to overlap the observed total radiant intensities derived from the DPS observations.

Table 3.8: Inputs for the validation of the optics code using the DSP satellite observations. Shown are the initial 2 meteors used simulation parameters (Brown et al., 2013; Tagliaferri et al., 1995). Radiant intensity given over a range of 400nm to 1200nm.

Meteor	Mass [kg]	Radius [m]	Velocity [km/s]	Radiant Intensity [ $Wsr^{-1}$ ]
Park Forest Meteor	$11 \times 10^3$	0.91	19.5	$4.2 \times 10^{10}$
Marshall Island Fireball	$16 \times 10^5$	4.78	24	$2.7 \times 10^{12}$

The optical instrument parameters calculated for those two meteors should give a minimum instrument requirement of a smaller aperture than that of DSP, which is equal to 24 inch or about 0.6 m. Next to that the f-number is equal to 1.5, which means it has a focal effective length of 0.9 m. Furthermore, the detector pixels are 0.001 to 0.003 inch, which is about 25 to 75 microns (Lapin, 1975). The given pixel size was reasonable for the time of the development of the DSP satellites (Wertz and Larson, 2010), at about 1989. The DSP satellites work in an IR band restricted to the pass-band interval of 2.69 to 2.95 microns (Lapin, 1975) (taken a mean as 2.82 microns), which falls within the before proposed short-wave infrared band (1.40 to 3.00 microns). Using Equations (2.31) and (2.33) pixel sizes of 25 and 75 microns suggest that the ground resolution  $X'$  of the DSP system at max range  $R_S = 42.7 \times 10^6$  m (this no side looking, but actually tilting the whole telescope in that direction, like a DSP could) is about 1182 m and 3555 m respectively, with both a quality factor  $Q$  of about 2.42 and 7.27 respectively, meaning that the diffraction pixel ground resolution is 489 m. For the simulations a quantum efficiency of 0.5 and integration/exposure time of 50  $\mu s$  were taken. Using the found ground resolution  $X'$  for the maximum resolution the GEO optical code was ran on the Park Forest and Marshall Island meteors.

The simulated aperture diameters to observe each meteor in the short-wave infrared band using the DSP inputs described before are shown in Table 3.9[Rows PF1 and MI1]. Both meteors calculated aperture diameters are the same for a pixel size of 25  $\mu m$ , since the upper limit for the ground resolution was set to 1183 m and was already reached by the Park Forest meteor. A bigger more bright meteor, like the Marshall Island meteor, will result in the same outcome. The calculated aperture diameter and focal length are for both meteors also the same for the pixel size of 75  $\mu$ , due to being limited by the calculated ground resolution of 3555 m and not by the SNR or SBR of the objects. Since the Marshall Island meteor is brighter than the Park Forest meteor, the SNR and SBR are also higher for the same optical system.

Table 3.9: Results of validation of GEO optics software using the DSP satellite observations of Park Forest Meteor (Brown et al., 2013) and Marshall Island Meteor (Tagliaferri et al., 1995). DSP aperture diameter  $D = 0.6$  m, focal-length  $f = 0.9$  m and band-pass from 2.69 to 2.95 microns (middle 2.82  $\mu m$ ). Ground resolution restricted to maximum 1.183 km and 3.56 km, depending on the pixel size of either 25 or 75 microns respectively. This all such that the system adheres to the found parameters (Lapin, 1975), where quality factor  $Q$  is 2.42 or 7.27 respectively. Bold values in the simulated rows are inputs for that simulation.

		Aperture Dia. $D$ [m]	Focal-length $f$ [m]	Pixel size $d$ [ $\mu m$ ]	Quality factor $Q$	Ground res. $X_{max,dist}$ [km]	SBR	SNR
	DSP found	0.6	0.9	25 $\times$ 75				
	DSP calculated				2.42 - 7.27	1.183 - 3.555		
Simulations to check if optical parameters are found correctly for Park Forest Meteor								
PF1	DSP simulated 25 $\mu m$	0.607	0.912	<b>25</b>	<b>2.42</b>	<b>1.18</b>	9141	482
	DSP simulated 75 $\mu m$	0.601	0.902	<b>75</b>	<b>7.27</b>	<b>3.56</b>	993	423
Smallest optical system needed to detects Park Forest Meteor with DSP								
PF2	DSP simulated 25 $\mu m$	0.015	0.023	<b>25</b>	<b>2.42</b>	46.7	5.7	3.0
	DSP simulated 75 $\mu m$	0.016	0.024	<b>75</b>	<b>7.27</b>	135.1	0.686	3.0
Simulations to check if optical parameters are found correctly for Marshall Island Meteor								
MI1	DSP simulated 25 $\mu m$	0.607	0.912	<b>25</b>	<b>2.42</b>	<b>1.18</b>	859506	4885
	DSP simulated 75 $\mu m$	0.601	0.902	<b>75</b>	<b>7.27</b>	<b>3.56</b>	93361	4832
Smallest optical system needed to detects Marshall Island Meteor with DSP								
MI2	DSP simulated 25 $\mu m$	0.002	0.002	<b>25</b>	<b>2.42</b>	453.1	5.7	3.0
	DSP simulated 75 $\mu m$	0.002	0.002	<b>75</b>	<b>7.27</b>	1309.6	0.686	3.0

Also the GEO optical parameter calculations were ran without a ground resolution limit, allowing the code

to calculate the smallest possible optical parameters which adhere to the requirements of minimal 0.1 SBR and minimal 3 SNR. The results of this are shown in Table 3.9[Rows PF2 and MI2]. As can be seen from the Park Forest meteor optical parameter results, the calculated minimal aperture diameter needed is 1.5 to 1.6 centimeters, with a focal length of 2.3 to 2.4 centimeters. The ground resolution would be in the order of tens of km. These small apertures are limited by their SNR in both cases and do not allow for a detector with more than 40x40 pixels behind the aperture due to physical limitations.

For the Marshall Island meteor the minimal needed aperture and focal length are for all cases calculated to be 2 mm, which is undoubtedly unfeasibly small. This small aperture would theoretically be possible due to the amount of luminosity the Marshall Island meteor produces.

From the validation done in this section, it can be concluded that the software calculates the minimal correct optical instrument parameters. The found SBR and SNR in Table 3.9[Rows PF1 and MI1] can not be validated. This means that the calculations might be too optimistic. However, if values for SBR below 0.1 and for SNR below 3 were found in Table 3.9[Rows PF1 and MI1], the code would have been incorrect. This can be stated since those are the most state of the art values needed to make GEO optical observations (Tartakovsky and Brown, 2008). The code would then have calculated smaller apertures than needed and thus the meteors would not be observable.

### 3.2.2. Verification and Validation of the Reflected Sunlight and Atmosphere Model

To validate and verify the used reflected sunlight from Earth's surface, a dataset from the National Renewable Energy Laboratory (NREL) was obtained for zero air mass extraterrestrial solar irradiance spectra of the Thullier and Kurucz models<sup>2</sup>. This dataset gives the solar irradiance in  $W/m^2/nm$  for a non-existent atmosphere. This dataset is used to tune the calculated solar irradiance via a black body model. The NREL data itself is not used, since it uses a different wavelength spacing compared to the needed one (per nanometer, starting at 10 nm). The first chosen 5772 K black body temperature of the Sun results in an underestimation of the peak irradiance. Substituting this temperature by the NREL suggested 6000 K, the irradiance peak is the same as the NREL data. However, it overestimates the irradiance at wavelengths. The fact that the background irradiance will be overestimated is assumed to be conservative, since it will reduce the SBR, and thus 6000 K is used as baseline.

After the baseline for the Sun's irradiance was established the atmospheric transparency model had to be verified. This was done by making a transmittance vector for each wavelength, and then multiplying this with the irradiance at each wavelength. For tuning and validation the NREL Direct and Circumsolar Air Mass 1.5 spectra model was used<sup>3</sup>, using a non-latitude-correcting surface. The NREL data corresponds to applying the transmittance model one time. In case of the GEO satellite the transmittance model needs to be applied twice, since the radiance goes through the atmosphere twice (down to Earth and back to the satellite).

<sup>2</sup>"Solar Spectra" nrel.gov. <https://www.nrel.gov/grid/solar-resource/spectra.html> (Accessed November 20, 2018).

<sup>3</sup>"Reference Air Mass 1.5 Spectra" nrel.gov. <https://www.nrel.gov/grid/solar-resource/spectra-am1.5.html> (Accessed November 21, 2018).

# 4

## Results

In this chapter the results of the research are shown. The first results presented are the meteor fingerprints; this is data on maximum luminosities, absolute magnitudes, altitude of maximum luminosity and duration above 0 absolute magnitude. The influx rates are calculated, based on two typical occurrence calculation methods. After that, 5 sample meteors are introduced based upon specific requirements. The the optical instrument parameters results will be shown for each of the 5 meteors, both for detecting and tracking purposes.

The same is done for the Hayabusa and Stardust capsules; first the fingerprints are given, after that the optical instrument parameter results are presented which were calculated for both Hayabusa and Stardust for detecting and tracking purposes.

In the end an analysis of the results is done, by looking at the influence of changing the simulation parameters, like integration time and bandwidth. Also a correlation matrix is given for the different output parameters.

### 4.1. Meteor Re-entry Simulations and Instrument Determination

In this section the results regarding systems for meteor detecting and tracking are given, but first the re-entry simulation results need to be presented. First the meteor fingerprints as calculated for different velocities and masses, with our baseline fragmentation parameters and sublimation fraction are presented. Then the meteor influx rates are shown as determined by other researches and calculated in this research. After that 5 typical meteors are identified that will be sued for the optical instrument parameter calculations, based on typical requirements. For the five identified meteors the detection and tracking optical instrument parameter results will be presented. Lastly a preliminary summary on the meteor fingerprints, influx rates and optical instrument parameters will be given.

#### 4.1.1. Meteor State Fingerprints

From the re-entry state simulations, including fragmentation, fingerprints could be made for a wide range of meteors. For these meteors with a flight-path-angle of  $45^\circ$  (most common entry angle as by [Mathias et al. \(2017\)](#)) was chosen together with a mass range in between 0.1 grams and 1,000 kg in increments of factors of 10. For the velocities the whole range from 11 km/s to 70 km/s was taken in increments of 10 km/s. Only the 0.33 ablation shielding factor ([Bronshten, 1983](#)) was used as this was validated in Sections 3.1.4 and 3.1.5. Other settings for tolerances and termination conditions were changed w.r.t. the baseline values given before in Section 2.1.1. Those adjusted settings can be found in Appendix D. The results for the maximum bolometric luminosity (W), bolometric absolute magnitude, altitude of maximum luminosity (km) and duration of absolute magnitude brighter than 0 absolute magnitude (s) of each meteor's track are shown in Tables 4.1 till 4.4. The maximum luminosity can be used to determine the peak wavelength via the black body radiation, which determines the band in which the most energy is emitted. The wavelengths of peak emitted irradiances are in between 50 and 500 nm and are therefore in the Ultra-Violet and Visible light bands.

As expected, see Table 4.1, the maximum luminosity of per mass class is higher for higher velocities. Also as expected, for each velocity class a higher mass leads to a higher maximum luminosity. This is logical, since higher mass and velocity meteors have higher kinetic energy to release. Heat flux is also a function of size (indirectly mass) and velocity, and determines the amount of heat generated and the amount of energy released.

Table 4.1: Maximum bolometric luminosity of simulated fragmentating meteors with a certain mass and velocity at an entry angle of  $45^\circ$ . As expected, the fastest meteors dominate in each mass class. The dashed line shows above what velocities the heat flux model produces underestimated luminosities, and under which velocities is overestimates the luminosities.

Maximum bolometric luminosity [W]								
$V_\infty$ [km/s]	$M_\infty$ [kg]							
	0.0001	0.001	0.01	0.1	1	10	100	1000
70	<b>2.65E+04</b>	<b>1.18E+05</b>	<b>1.35E+06</b>	<b>1.75E+07</b>	<b>1.73E+08</b>	<b>1.57E+09</b>	<b>1.41E+10</b>	<b>1.39E+11</b>
60	2.02E+04	9.06E+04	8.44E+05	1.14E+07	1.18E+08	1.14E+09	9.35E+09	9.67E+10
50	1.46E+04	6.58E+04	4.42E+05	6.47E+06	6.84E+07	6.97E+08	6.76E+09	6.73E+10
40	9.68E+03	4.39E+04	2.06E+05	3.32E+06	3.89E+07	4.25E+08	4.36E+09	4.30E+10
30	5.52E+03	2.56E+04	1.31E+05	1.38E+06	2.34E+07	2.73E+08	2.46E+09	2.80E+10
20	2.30E+03	1.09E+04	5.72E+04	3.86E+05	7.85E+06	1.18E+08	1.45E+09	1.43E+10
11	5.66E+02	2.53E+03	1.09E+04	4.79E+04	2.29E+05	1.29E+06	2.40E+07	3.19E+08

The data shown in Table 4.2 is merely the data converted from Table 4.1 to absolute magnitude with a 1800 W reference meteor. Therefore, the same conclusions hold as just discussed: the most bright meteors are always the heaviest and fastest meteors.

Table 4.2: Absolute bolometric magnitude of simulated fragmentating meteors with a certain mass and velocity at an entry angle of  $45^\circ$ . The dashed line shows above what velocities the heat flux model produces underestimated luminosities, and under which velocities is overestimates the luminosities.

Absolute bolometric magnitude								
$V_\infty$ [km/s]	$M_\infty$ [kg]							
	0.0001	0.001	0.01	0.1	1	10	100	1000
70	-2.9	-4.5	-7.2	-10.0	-12.5	-14.9	-17.2	-19.7
60	-2.6	-4.3	-6.7	-9.5	-12.0	-14.5	-16.8	-19.3
50	-2.3	-3.9	-6.0	-8.9	-11.4	-14.0	-16.4	-18.9
40	-1.8	-3.5	-5.1	-8.2	-10.8	-13.4	-16.0	-18.4
30	-1.2	-2.9	-4.7	-7.2	-10.3	-13.0	-15.3	-18.0
20	-0.3	-2.0	-3.8	-5.8	-9.1	-12.0	-14.8	-17.2
11	1.3	-0.4	-2.0	-3.6	-5.3	-7.1	-10.3	-13.1

The altitude of maximum (bolometric) luminosity is given in Table 4.3. From the data in this table can be seen that in each mass class the faster meteor has its peak at a higher altitude than the slower ones. For each velocity class the meteors have their maximum luminosity at a lower altitude for a higher mass. This both makes sense again; the bigger and heavier the meteor, the faster it still goes at a lower altitude compared to smaller and lighter ones. For the same mass meteors, a higher velocity means just that the maximum release of kinetic energy is reached earlier. The higher velocity at a certain atmospheric density plays a role in the heat flux to the meteor, and the same combined values are reached at a higher altitude for faster meteors, as can be observed from Equations (2.12) to (2.16) given in Section 2.1.4 for heat flux calculations (Brandis and Johnston, 2014). This altitude of maximum luminosity shows that the assumption of a meteor being brightest at 12 km regarding atmospheric absorption (20% atmosphere between satellite and meteor), made in Section 2.2.3 is a conservative assumption and could actually be higher to at least 27.2 km (lowest value in Table 4.3), leading to less absorption of the meteor's (or another object's) radiated energy.

The only data that shows some less obvious behavior is the data for the duration brighter than 0 absolute magnitude, see Table 4.4. As expected for the same velocity a heavier meteoroid has a longer time to burn up and has a longer duration of absolute magnitude brighter than 0. This checks out for the maximum per row. However, each row does not necessarily follow an upward trend. Especially the meteors above 100 kg at velocities below 50 km/s show non-linear behavior. The most probable cause here is the termination conditions of the simulation. The simulation might terminate too fast, after the peak brightness, due to a minimal mass or altitude reached, and so determines a shorter duration brighter than 0 absolute magnitude. However, in scope of this research, the most bright meteors will not be the limiting ones for the to be determined optical instrument parameters, but this proves that not everything can be well simulated yet.

Next, at the same mass, a faster (or slower) meteoroid does not necessarily produce a longer duration brighter than 0 absolute magnitude. The underlying reason is assumed to be that very fast meteors burn earlier, but also ablate faster and thus die-out faster, than a slower meteoroid, which might just have enough speed to reach a status where is it brighter than 0 absolute magnitude. Therefore, a duration shorter at a velocity faster than the maximum duration per mass class, possibly indicates a too fast ablating meteoroid. Meteors with a duration shorter at a slower velocity than the maximum duration per mass class possibly

Table 4.3: Altitude of maximum bolometric luminosity of simulated fragmentating meteors with a certain mass and velocity at an entry angle of  $45^\circ$ . As expected, faster meteors have a higher altitude for their maximum luminosity radiation, for the same mass class. Also can be observed that for the same velocity this altitude decreases with higher mass, also as expected, since these meteors can penetrate deeper into the atmosphere before slowing down. The dashed line shows above what velocities the heat flux model produces underestimated luminosities, and under which velocities is overestimates the luminosities.

Altitude of maximum bolometric luminosity [km]								
$V_\infty$ [km/s]	$M_\infty$ [kg]							
	0.0001	0.001	0.01	0.1	1	10	100	1000
70	70.9	65.5	55.0	53.8	52.2	51.7	50.2	48.7
60	68.7	63.3	53.1	52.0	50.6	49.3	48.4	47.1
50	66.8	61.2	50.2	49.8	48.5	47.1	45.3	43.6
40	64.5	59.1	53.0	46.7	45.6	44.1	42.4	40.2
30	62.0	55.8	50.1	42.7	40.8	39.4	39.5	37.6
20	59.6	54.0	50.0	42.4	35.9	35.5	34.0	33.5
11	59.0	53.6	48.2	42.9	37.5	34.4	28.3	27.2

indicate that the meteor is so slow that the meteor starts to radiate relatively late and decelerates then so quickly after, that it radiates in total a shorter duration than a faster meteoroid. All mass classes seem to follow this kind of trend. However, at 1000 kg the duration brighter than 0 absolute magnitude has a very fluctuating trend. Especially the 40 and 50 km/s meteors are the outliers of the trend for that mass class. The termination conditions for the simulation as described earlier in this paragraph cause this to happen. This seems probable since all the other simulation data shown in this section is consistent. The heat flux model could cause problems too due to being out of the verified usable range, but it was indirectly validated in Section 3.1.5 with the absolute magnitudes from [Halliday et al. \(1996\)](#).

Table 4.4: Duration under an absolute magnitude of 0 of simulated fragmentating meteors with a certain mass and velocity at an entry angle of  $45^\circ$ . Bold numbers are the longest duration per mass class, italic is longest duration per velocity class. The dashed line shows above what velocities the heat flux model produces underestimated luminosities, and under which velocities is overestimates the luminosities.

Duration under 0 absolute magnitude [s]								
$V_\infty$ [km/s]	$M_\infty$ [kg]							
	0.0001	0.001	0.01	0.1	1	10	100	1000
70	1.2	1.41	1.54	1.59	1.66	1.73	1.81	<i>1.9</i>
60	1.34	1.74	1.8	1.87	1.94	2.03	2.14	<i>2.25</i>
50	1.5	2.13	2.22	2.31	2.43	2.58	<i>3.41</i>	3.16
40	1.7	2.49	2.82	3.37	4.03	5.44	8.29	<i>13.73</i>
30	<b>1.83</b>	2.93	3.7	5.41	6.59	5.92	13.17	<i>21.03</i>
20	1.18	<b>3.42</b>	4.44	7.49	7.04	6.92	9.16	<i>25.57</i>
11	0	2.22	<b>5.12</b>	<b>10.45</b>	<b>11.63</b>	<b>11.95</b>	<b>13.21</b>	<b>30.87</b>

As for the fingerprints of common meteors given in this section, it can be concluded that between 0.1 gram and 1000 kg meteors a faster meteor of the same mass always has a larger maximum luminosity and also a higher altitude. For the same velocity meteors, a higher mass leads to a lower maximum luminosity altitude and again to a larger maximum luminosity. The duration of meteors brighter than 0 absolute magnitude has no lower or upper limit. From our fragmentation simulations meteors up till 1 kg will never have a duration longer than 12 seconds brighter than 0 absolute magnitude.

#### 4.1.2. Meteor Influx Rates

In order to be able to make a good decision on what kind of satellite system should be selected for meteor observations, it is important to know at what frequency certain type of meteors occur. [Halliday et al. \(1996\)](#) has done research to determine what the relation is between frequency of occurrence  $N$  of meteors above mass  $M_m$  in kg per year per million  $\text{km}^2$ . In his paper different formulas like Equations (4.1) and (4.2), which has also been used by [Bouquet et al. \(2014\)](#), are given to determine the frequency of events for a given mass, for different kind of meteors. The found value has to be multiplied by 510 to find the frequency of occurrence

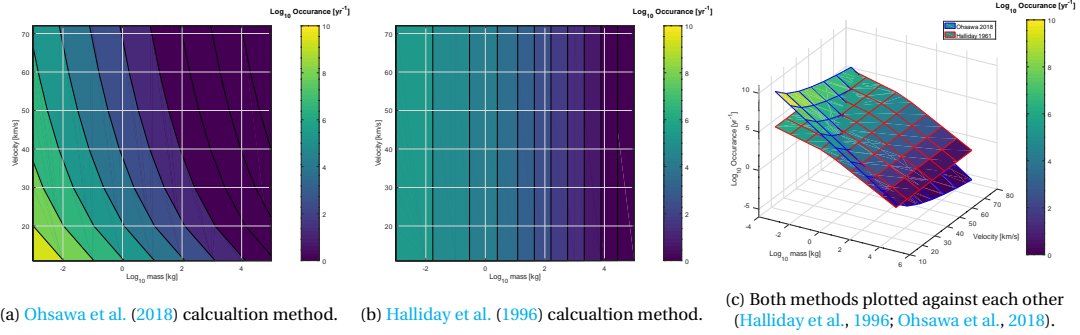


Figure 4.1: Cumulative meteor fluxes as by other researches over the whole Earth sky per year for given mass and velocity at an entry angle of  $45^\circ$ .

over the whole Earth atmospheric sphere.

$$\log N = -0.48 \log M_m + 3.3 \quad \text{with} \quad M_m < 2.4 \text{kg} \quad (4.1)$$

$$\log N = -1.06 \log M_m + 5.26 \quad \text{with} \quad M_m > 2.4 \text{kg} \quad (4.2)$$

Ohsawa et al. (2018) did a more recent research coupled to this topic, and uses the two Equations (4.3) and (4.4), of which the first one is based on the work of Jenniskens (2006).

$$\log_{10} M_m = 6.31 - 0.4 m_v - 3.91 \log_{10} V_\infty - 0.41 \log_{10} \sin(\gamma) \quad (4.3)$$

$$N = AN_0 r^{m_v} \quad (4.4)$$

Here  $A$  is the observed airspace (taken as whole Earth,  $510 \times 10^6 \text{ km}^2$ ),  $r = 3.4$ ,  $m_v$  the absolute (V-band) magnitude of the meteor,  $N_0 = 10^{-5.1}$  and  $N$  the number of occurrences per hour (and thus needs to be multiplied by  $24 \times 365$  to be comparable to Hallidays method above) of meteors that are brighter than the specified  $m_v$  magnitude (so it is a cumulative function). First the V-band magnitude is found with Equation (4.3), after which this magnitude is checked for its occurrence  $N$  with Equation (4.4).

A set of calculations for both methods was ran to determine the occurrence frequency of different type of meteors, with these two calculation models presented. The inputs ranged from masses of 0.1 gram till  $10^3 \text{ kg}$ , velocities from 11 till 72 km/s and an entry angle of  $45^\circ$ .

### Ohsawa and Halliday Influx Rates

The results of the before described influx rates are shown in Figure 4.1, where Figure 4.1a shows the results of the method of Ohsawa et al. (2018) and Figure 4.1b the results of the method of Halliday et al. (1996). Both methods plotted against each other is shown in Figure 4.1c.

It can be seen from Figure 4.1c that the method of Halliday et al. (1996) gives a higher number of occurrences at higher velocities than the method from Ohsawa et al. (2018), and is next to that not a function of the entry velocity. At lower velocities and lower masses, the method from Ohsawa et al. (2018) shows a much higher amount of occurrences  $N$ .

Figure 4.2 shows the data from Ohsawa et al. (2018), but now with equal occurrence lines per whole  $\log$  number, so similar to in Figure 4.1a. Figure 4.3 shows the accompanying magnitudes as calculated with Equation (4.3), that is needed to calculate the occurrences via Equation (4.4). The equal occurrences lines in Figure 4.2 also coincide with equal visual absolute magnitude lines. The intersection between the two planes in Figure 4.1c coincides almost with the  $\log_{10} = 6$  occurrences line in Figure 4.2, which in turn is almost equal to the absolute magnitude line of about  $-2$  or  $-3$  in Figure 4.3. So the lines in Figure 4.2 show that for a system that is able to detect a certain kind of meteor with a certain velocity and mass, it is also able to detect any number of meteors which have a lower occurrence in that figure. Remember that it is a cumulative curve.

Now an estimation can be made on how much meteors can be seen in a part of the sky with a certain optical system, it being on ground or in space. A side note is that there is no use in transforming Figure 4.1c into one with percentage of meteors observed, since the total amount is not known and increases fast for fainter meteors.

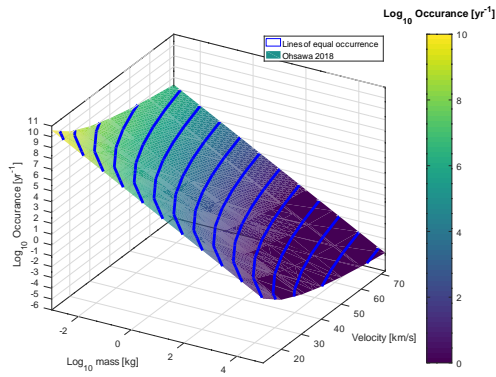


Figure 4.2: Meteor Fluxes over the whole Earth as by Ohsawa et al. (2018), presented with equal occurrence contour lines and thus equal magnitude lines.

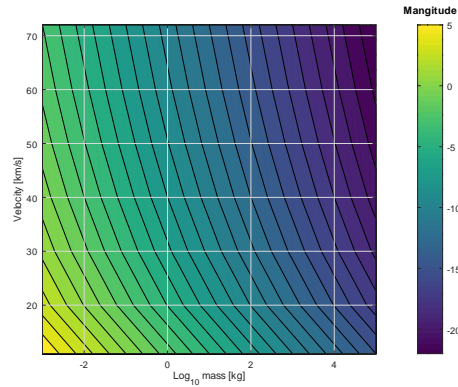
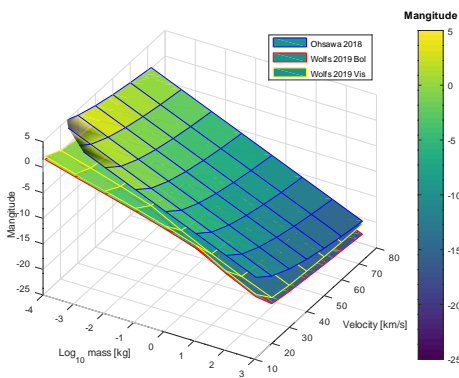
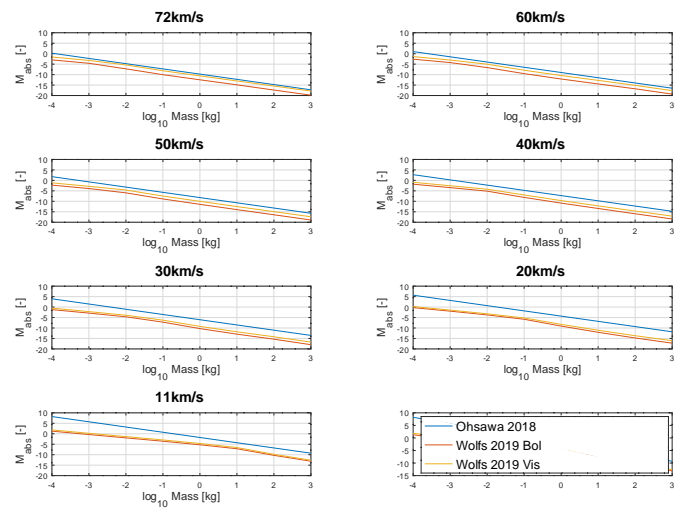


Figure 4.3: Meteor Magnitude as by Ohsawa et al. (2018) for given mass and velocity at an radiant angle of 45°.



(a) Surface plot of all 3 absolute magnitude calculations.



(b) Cutout of the absolute magnitudes versus log<sub>10</sub> mass per velocity.

Figure 4.4: Simulated meteor absolute magnitudes for zero magnitude meteors of 1100 W visible and 1800 W bolometric, and visual absolute magnitudes as calculated via the method of Ohsawa et al. (2018).

With the assessment of the meteor occurrences as calculated with two different methods, the next Section will deal with the occurrences as calculated using our own simulated meteor luminosities, absolute magnitudes and the corresponding occurrences as calculated with Equation (4.4).

### This Research Influx Rates

In this subsection the calculated influx rates calculated with Equation (4.4) from Ohsawa et al. (2018) are presented, with as inputs simulated re-entries of meteors. From the simulations the peak bolometric luminosities were taken and converted to absolute magnitudes via Equation (2.23), where 1800 W was taken for as the bolometric reference luminosity. This is done for fragmentating re-entry simulations over a range of 0.1 gram till 1000 kg and from 11 to 72 km/s, all at an entry angle of 45°. The results are shown in Figures 4.4. The used fragmentation parameters were 2 fragments per break-up, a initial break strength of 1.5 MPa and a strength scaling of 0.1.

In general it can be observed in Figure 4.4a that our produced data is always brighter than anticipated by Ohsawa et al. (2018). A confident reason for this can not be given at this point. From the subplots in Figure 4.4b it can be seen that at, for example, 30 km/s our results still give a 5 magnitude brighter absolute magnitude at masses below 1 kg. However, at higher velocities the overall difference between our absolute magnitudes and the absolute magnitudes of Ohsawa et al. (2018) gets smaller to about 2-3 magnitudes. For now it is assumed that the fragmentation is the cause for the difference in absolute magnitude.

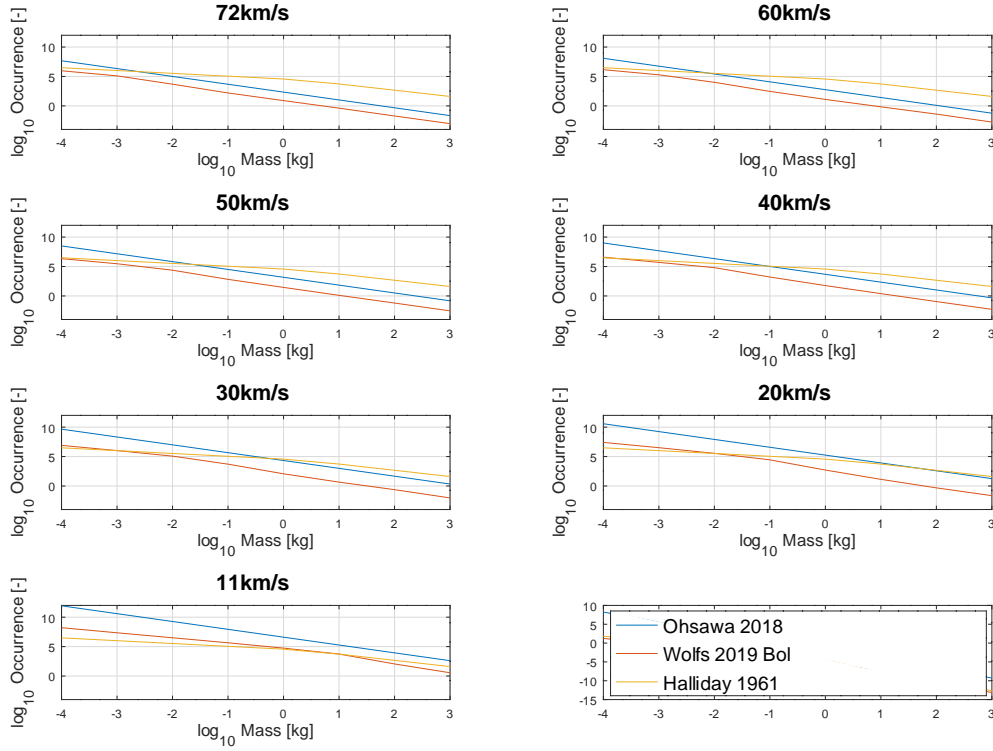


Figure 4.5: Cumulative occurrences of meteors calculated by this research, and the methods of [Ohsawa et al. \(2018\)](#) and [Halliday et al. \(1996\)](#). Results are given for different occurrences per mass at different velocities. Occurrences are the sum of occurrences of the meteors equal to the shown mass or higher.

In Figure 4.5 the magnitudes from Figure 4.4 were converted to meteor influx rate with Equation (4.4). Of course the results from this research follow the same trend as by [Ohsawa et al. \(2018\)](#), since that method (Equation (4.4)) was used to convert from magnitudes to occurrences. In general the results from this study underpredicts the amount of meteors of certain mass and velocity by a fraction of 100-1000 ( $\log_{10} 2 - \log_{10} 3$ ), compared to [Ohsawa et al. \(2018\)](#). Since only the absolute magnitudes are the inputs for the occurrence calculations, the same assumption holds as before, that the implementation of fragmentation causes us to find brighter meteors for the same mass and velocity meteor.

Our simulations predict brighter meteors for the same mass and velocities than [Ohsawa et al. \(2018\)](#), and thus less occurrences for the same mass and velocity meteors.

### 4.1.3. Selected Sample Meteors

Due to the vast parameter space of meteors and similarity between them, not all the possible combinations of masses, velocities, entry angles and fragmentation parameters will be simulated to find parameters for an optical system later on. In the scope of the project it is advantageous to select a few meteors that are typical for this problem and look at the results of those selected meteor observation outcomes. For each meteor separately the detection and tracking solutions will be discussed. It might be so that a different wavelength is optimal for each of the detection and tracking solutions, since they both influence the observed time  $T_{track}$  and to be separated spatial distance of  $N_{read}$  pixels. Below all the proposed meteors to be simulated are discussed.

- One meteor (**Met1Model**) is selected to update a given meteor model that currently exist. For example, models like the ones from [Ohsawa et al. \(2018\)](#) and [Halliday et al. \(1996\)](#) as discussed in Section 4.1.2 could be updated with the use of more meteor observations. From Figure 4.6 can be seen that the biggest differences between influx rate models from [Ohsawa et al. \(2018\)](#) and [Halliday et al. \(1996\)](#) exist in the extreme low and high absolute magnitudes; the areas where either meteors are not easily observed, but many exist, or the area where meteors are easily observed, but not many occur. A geosta-

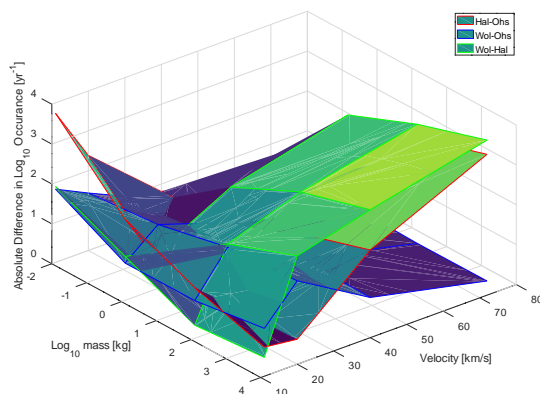


Figure 4.6: Differences between different meteor flux models (Ohsawa et al., 2018; Halliday et al., 1996).

tionary space system would not be ideal to observe very faint meteors due to the long distance towards the object. Another model, briefly discussed in Chapter 1, that can be updated is the latitude dependency as discussed by Szasz et al. (2005), a geostationary system would be ideal to assess the latitudinal influx per time of the day, since ground based observations over such a big area are limited. From Szasz et al. (2005) can be determined that at highest 350 meteors were observed per hour at maximum, this means in turn that 3 million are observed per year, which equals on  $\log_{10}$  basis a value of 6.5. Looking at Figure 4.1a (Ohsawa et al., 2018) this means that they observed meteors of about -4 absolute magnitude at its faintest. This means meteors between a velocity of 70 km/s at a mass of about 0.003 kg and velocities of 10 km/s at masses of 3 kg were observed. It is not trivial to give 1 meteor that adheres to these requirements. But since this research's model works better for low velocity heavy meteors, the heaviest meteor is taken in this case of 3 kg at 10 km/s as a baseline. So with this meteor not the model for influx from Ohsawa et al. (2018) and Halliday et al. (1996) will be tried to be updated, but the model for diurnal, latitudinal and longitudinal influx as presented by Szasz et al. (2005).

- The second meteor (**Met2Rate**) is selected for which 1 observation per 2 minutes occurs. This rate equals to half a million meteors per year and has thus a  $\log_{10}$  value of 5.7. The value of one meteor per 2 minutes is arbitrarily taken as example for the design process. From the research shown in Figure 4.1a, this should be equal to a meteor of about 30 kg and a velocity of about 10 km/s. However, since already a meteor at 10 km/s was taken, the model differences between Ohsawa et al. (2018) and this research are biggest at velocities of about 20 km/s and the heat-flux model is applicable to about 20 km/s, a meteor at 20 km/s is taken. This means it must have a mass  $\log_{10}$  value of about 0.3, which is equal to about 2 kg. With this meteor an example is given on how to design for a certain amount of meteor detection with a geostationary satellite system.
- The third meteor (**Met3Common**) is selected based on the statistic most common meteor, according to the data also present in the fragmentation model paper by Mathias et al. (2017). This means a meteor with a velocity of 14 km/s, a density of about 2200 kg/m<sup>3</sup> and entry angle of 45°. The diameter of meteors in this paper are derived from very big catastrophic meteors, therefore this will not be used. Instead the magnitude versus mass and velocity model given in Ohsawa et al. (2018) is used to determine the mass for this meteor at an absolute magnitude of 0. This should be for a 14 km/s zero magnitude meteor equal to about  $\log_{10}(M) = -1.5$ , see Figure 4.3, which is thus 0.03 kg.
- The fourth meteor (**Met4V&V**) is taken as one that fits the heat-flux model as by Stokan and Campbell-Brown (2015), to get a solution that works well within the bounds of the simulation conditions. A meteor with a velocity of 15 km/s (9 km/s < V < 17 km/s) and a mass of 200 kg (> 0.2 m radius at 3500 kg/m<sup>3</sup>) is selected.
- The fifth meteor (**Met5Pers**) is selected as one that is from a bright meteor shower. These kind of meteors are observed for different kind of research than sporadic meteors. Therefore, the option for a system for observations of bright meteor showers is looked into. The entry velocity is well known to be 59 km/s, with masses in between 0.001 and 0.2 kg Halliday et al. (1996) and the density is about 2200

kg/m<sup>3</sup> (Babadzhanov and Kokhirova, 2009). These values are taken, with the mass equal to 0.02, since this was the closest to the values found in Halliday et al. (1996). From Halliday et al. (1996), Perseids have an absolute magnitude of about  $-8$ , which is a bit higher (by  $-1.3$ ) than what to expect from this research and Ohsawa et al. (2018).

The identified meteors for the simulations are given in Table 4.5. Resulting in a diverse range of absolute magnitudes, and very big meteors like Park Forest and Chelyabinsk are not addressed in particular, since from the validation in Section 3.1.7 it was already clear that such meteors require very small aperture diameters of a few centimeters, and are thus not the limiting case for this research.

A point of attention is the difference between our absolute magnitudes and the ones found by the method of Ohsawa et al. (2016) using Equation (4.3). It seems that our simulations overestimate the absolute magnitude by 2.0 for the non-fragmentating meteors. In case of fragmentation the absolute magnitude is overestimated by 4.0, which is more expected, because of the implemented fragmentation. Only the Perseid is less overestimated. However, our simulations have been validated to reach the correct absolute magnitude peak and trajectory so the problem of having brighter absolute magnitudes than Ohsawa et al. (2018) is not addressed further.

Table 4.5: Table of meteors that will be used (all under 45 degree entry angle) in this results section to find possible geostationary satellite systems. Visual Absolute magnitude as by Ohsawa et al. (2018) method (assuming 90° radiant) and by fragmentation simulation at  $I_{vis}/1100$  W (Cepelcha et al., 1998; Popova et al., 2013b) denoted  $M_{vis}$  using baseline fragmentation parameters and meteor sublimation reduction fraction of 0.33 (Bronshen, 1983). Amount of fragmentation events are shown as well.

Meteor Name	$V_{\infty}$ [km/s]	$M_{\infty}$ [kg]	Radius [m]	$M_O$	$M_{vis}$	Fragments?	Reason
Met1Model	10	3	0.059	-2.7	-4.9	no	Update model
Met2Rate	20	2	0.051	-5.2	-9.1	yes (4x)	1 meteor per 2 minutes
Met3Common	14	0.03	0.015	0.9	-2.9	no	2200 kg/m <sup>3</sup> , Statistics
Met4V&V	15	200	0.239	-9	-13.1	yes (8x)	Fits heat Flux model
Met5Pers	59	0.02	0.013	-4.8	-5.5	yes (3x)	2200 kg/m <sup>3</sup> , meteor shower

#### 4.1.4. Meteor Detection

As pointed out in Chapter 1, one research question dealt with the detection of meteors. How this is different from tracking solutions was discussed in Section 2.2.5. As will be discussed later in Section 5.3.5, lightning strikes also pop-up in observations as single dots. For actual useful instrument parameters, where meteors can be distinguished from lightning strikes, one should consult Sections 4.1.5 and 5.3. In those solution meteors can be tracked for longer and thus leave a trail in the observations, which can be distinguished from stationary point sources like lightning strikes. Therefore, the results given here for detection of meteors, which will be observed as single dots, since the system will be calculated for the maximum luminosity of the meteors, are just the minimal required optical parameters.

First, the optical GEO code will be ran over a desired spectrum range (from 100 nm till 3000 nm in this case) at 100 nm intervals. The 100 nm interval is chosen as an arbitrary number, the impact of this chosen bandwidth is discussed in Section 4.3.1. Most detectors have a broad range of integration times that can be selected, see Appendix A, ranging from several micro seconds till hundreds or thousands of milliseconds. It is assumed that the integration times are not limited to what is shown in the Appendix, higher integration times are also explored. In the optic parameter determination integration times were selected from 10 ms, 100 ms, etc. till 1 second, thus in fractions of 10. Used inputs for each detector and its applied spectral range are given in Table 4.6, taken from Appendix A. The beginning ground resolution was set to 2 by 2 km. In this all, integration times in between the proposed ones are not evaluated. As explained in Section 2.2.4, the program searches for the biggest ground resolution that adheres to an  $SNR_{eff} > 3$  and a  $SBR_{eff} > 0.1$ .

In the next 5 sections, for each of the meteors given in Table 4.5, optical instrument parameter results for purely detection are presented. The results are based upon running the GEO optics instrument determination code over the just discussed spectral range, using all the data obtained from the trajectory state simulations for the respective meteor.

All separate raw data figures, as being less easy to interpret by the reader, containing the optical instrument parameters calculated per integration time, can also be found in Appendix G.

Table 4.6: Table of used detector parameters, as a compilation of data from existing detectors.

Detector	Spectral range [nm]	Pixel pitch [ $\mu\text{m}$ ]	Readout Noise [ $e^-$ ]	QE [%]
UV	100-400	5	10	40
VIS	400-700	7	45	55
NIR	700-1400	12.5	75	65
SWIR	1400-3000	30	150	70

### Meteor Met1Model

Meteor Met1Model was fragmentating simulated and the GEO optics code was ran to determine the resulting aperture diameter, focal length, effective SNR, effective SBR and nadir ground resolution, for just detection.

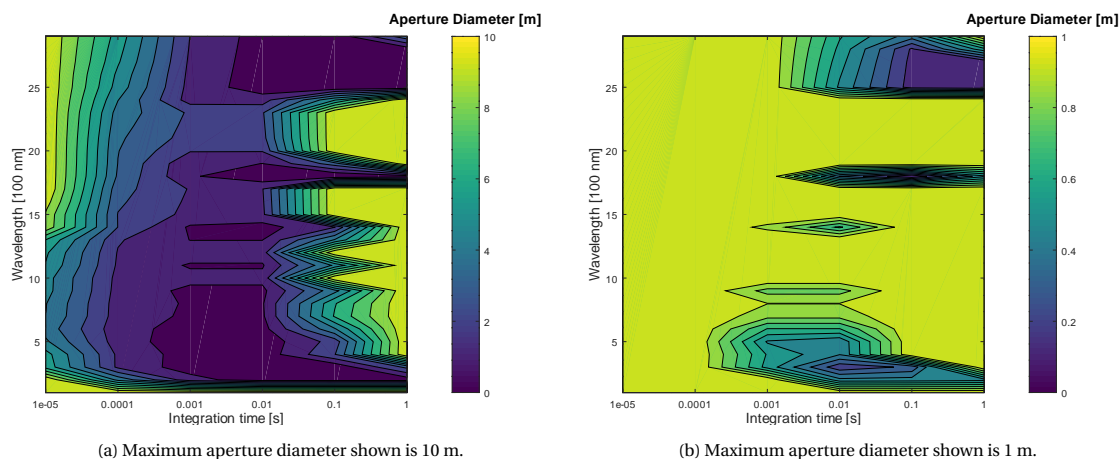


Figure 4.7: Aperture diameter  $D$  in meters, plotted against the integration time  $T_i$ , from  $10^{-5}$  to 1 second, and 100 nm bandwidths centered at wavelengths from 100nm to 3000nm for meteor Met1Model.

The results for the found aperture diameters are given in Figure 4.7. First from Figure 4.7a it can be observed that for the lowest and highest integration times of  $10^{-5}$ s and 1s, the calculated aperture diameters are the biggest, and at most of the wavelengths exceed 10m. From this figure, it could be concluded that, observing the concave nature of the aperture diameter values in the plot, that the smallest apertures to detect this meteor would be somewhere at integration times of 0.001 to 0.01. This observation is however not correct, as can be further observed from Figure 4.7b, where the aperture diameter is shown for smaller intervals between 0 m and 1 m. From Figure 4.7b it can be seen that the lowest apertures are at an integration time of 1 second in the wavelength bands between 2500-2700 nm. Other minimums in the aperture diameter can be observed at the 0.1 s integration time at the 1800nm wavelength and at the 0.01s integration time in the 300 nm wavelength. Most of the apertures calculated (about 75%) are bigger than 1 m.

All the identified minimums adhere to a big enough effective SNR and effective SBR as can be observed from Figure 4.8. At the 1s and 2500-2700 nm, 0.1 s and 1800 nm and 0.01 s and 300 nm points the SNR and SBR plots do not show any white areas, which means the  $\text{SNR} \geq 3$  and  $\text{SBR} \geq 0.1$ . The only white areas in Figures 4.8a and 4.8b are at 100-200 nm at all integration times and indicate not sufficient SBR and SNR, and thus the object can not be detected.

The aperture diameter and focal length are behaving proportional, as can be observed by comparing Figures 4.7b and 4.9. In both cases the trenches of minimal aperture diameters and focal length can be seen at the 2500-2700 nm and 1800 nm wavelengths. The point at 0.01s integration time at 300 nm is also in both cases a local minimum.

Another trend that is apparent is the inversely proportionality of the focal length and nadir ground resolution both shown in Figures 4.9 and 4.10 respectively. The places where the focal length are the smallest (the blue areas in Figure 4.9) are proportional to the biggest nadir ground resolutions (the green areas in Figure 4.10). The biggest ground resolutions lead also to the shortest focal length, and so also to the smallest aperture diameters.

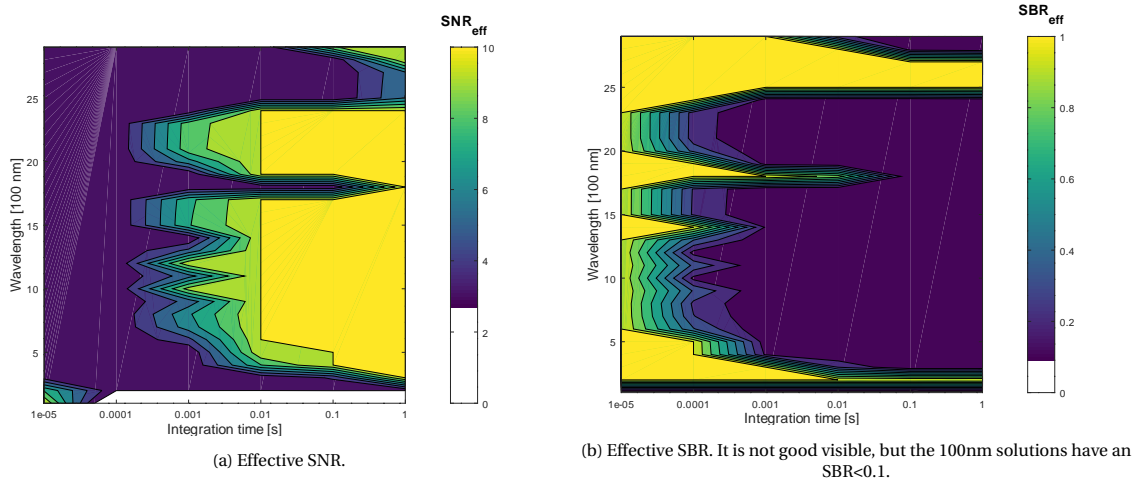


Figure 4.8: The effective SNR and effective SBR plotted against the integration time  $T_i$ , from  $10^{-5}$  to 1 second, and 100 nm bandwidths centered at wavelengths from 100nm to 3000nm for meteor Met1Model. White area indicates that the desired  $SNR \geq 3$  and  $SBR \geq 0.1$  were not met.

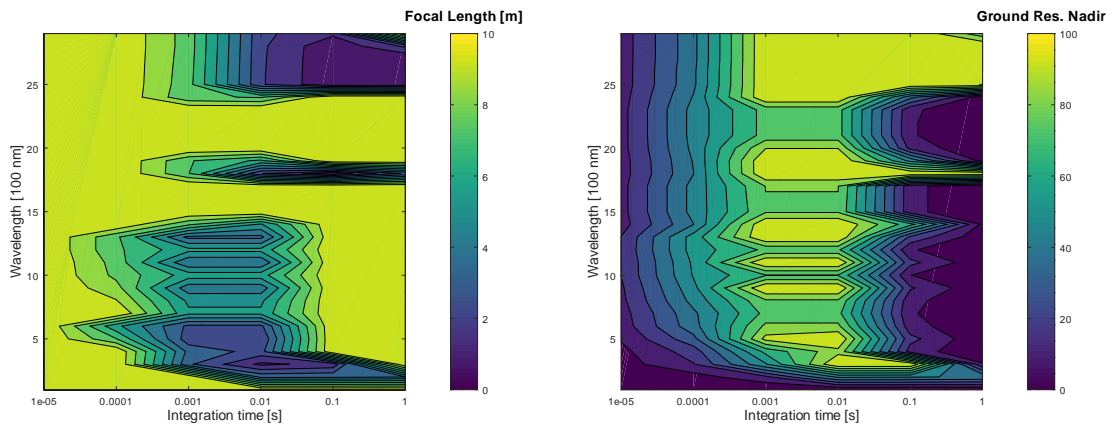


Figure 4.9: Focal length  $f$  in meters, plotted against the integration time  $T_i$ , from  $10^{-5}$  to 1 second, and 100 nm bandwidths centered at wavelengths from 100nm to 3000nm for meteor Met1Model.

Figure 4.10: Nadir ground resolution till 100m in meters, plotted against the integration time  $T_i$ , from  $10^{-5}$  to 1 second, and 100 nm bandwidths centered at wavelengths from 100nm to 3000nm for meteor Met1Model.

### Meteor Met2Rate

Meteor Met2Rate was just simulated in the same way as Met1Model. Also the input parameters for the optical instrument parameters were the same. From Table 4.5 it can be observed that this meteor is brighter than Met1Model, so it is expected that the apertures and focal lengths for Met2Rate are of a smaller size than those of Met1Model. This can be observed in Figure 4.11 if compared to Figure 4.7b, since the colors in the plot are way more shifted towards the blue, which means lower aperture diameters.

Also comparing Figure 4.11 with Figure 4.7b at 0.00001 s and 0.0001 s integration times, the meteor Met2Rate can already be observed with a sub 1 m aperture diameter, whilst this is not possible for Met1Model. It is clear that the choice for a instrument is very broad over a wide variety of integration times for the observation of meteor Met2Rate. With even sub 1 m aperture across all the integration times in the UV spectrum. Even sub 1 m aperture diameters exist in the visible spectrum and NIR spectrum, although not over the whole selected integration times. All these options are viable since the SNR and SRB are always sufficient.

At 1ms the limited ground resolution of 2 by 2 km leads to the same 13 cm aperture and 64 cm focal length like as with Met1Model in the 2500-2700nm wavelengths. Now also a viable instrument exists in the Ultra-Violet spectrum at 200 nm, with an aperture diameter of about 2 cm and a focal length of 11 cm, this is by far smaller than the SWIR optical parameters. From this can be concluded that for the same ground resolution a smaller wavelength leads to smaller instruments possible.

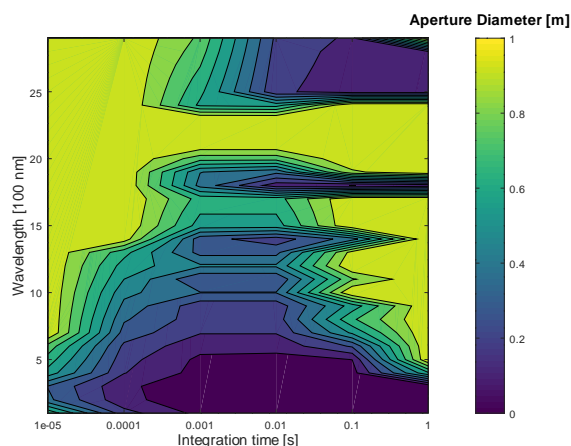


Figure 4.11: Aperture diameter  $D$  in meters, plotted against the integration time  $T_i$ , from  $10^{-5}$  to 1 second, and 100 nm bandwidths centered at wavelengths from 100nm to 3000nm for meteor Met2Rate.

**Meteor Met3Common**

From Table 4.5 it can be seen that Met3Common is a very faint meteor compared to the others. Therefore, systems with bigger apertures and focal lengths are to be expected than found for the two previous meteors. The aperture diameters derived from the fragmentation simulation of this meteor are shown in Figure 4.12.

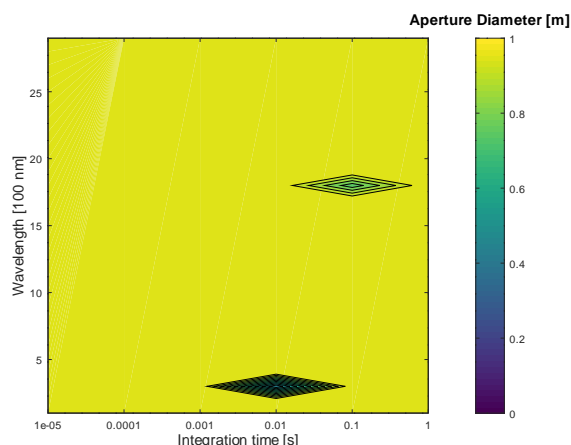


Figure 4.12: Aperture diameter  $D$  in meters, plotted against the integration time  $T_i$ , from  $10^{-5}$  to 1 second, and 100 nm bandwidths centered at wavelengths from 100nm to 3000nm for meteor Met3Common.

It can be observed from Figure 4.12 that the integration times of 0.01, 0.1, 1 and 1000 ms do not lead to any sub 1 meter aperture diameters. The smallest aperture diameter option is the one at the 300 nm at 0.01 s integration time point. This aperture diameter is 43 cm and has an effective focal length of 2.54 m. For this meteor the longer wavelength SWIR option, with an aperture of 76 cm and a focal length of 5.0 4m, at 1800 nm with a 0.1 s integration time does not come close regarding this smaller UV aperture diameter.

The 300 nm at 0.01 s integration time solution is bound by the SNR, whilst the 1800 nm at 0.1 s integration time solution is bound by the SBR, as can be observed from Figure 4.13.

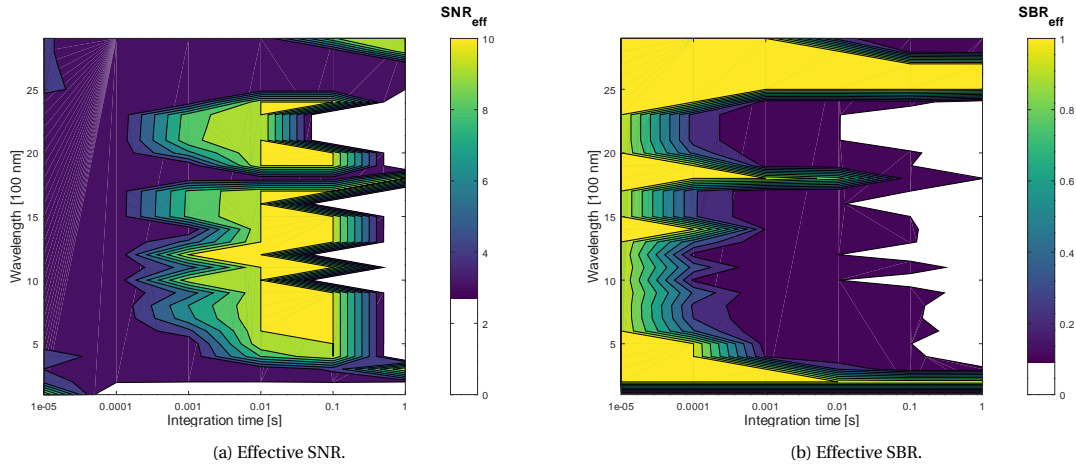


Figure 4.13: The effective SNR and effective SBR plotted against the integration time  $T_i$ , from  $10^{-5}$  to 1 second, and 100 nm bandwidths centered at wavelengths from 100nm to 3000nm for meteor Met3Common. White area indicates that the desired  $\text{SNR} \geq 3$  and  $\text{SBR} \geq 0.1$  were not met.

### Meteor Met4V&V

The meteor Met4V&V is intended to show a case in which is in accordance with the range for which the heat flux model initially was intended (Brandis and Johnston, 2014). The aperture diameter and SBR results for the fragmentating re-entry simulation and the optical GEO instrument parameters conducted for Met4VV are shown in Figure 4.14.

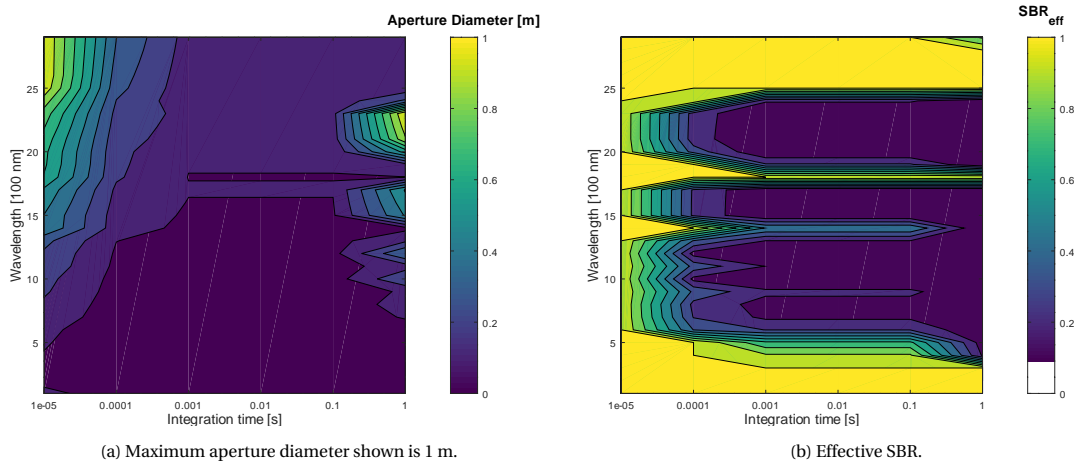


Figure 4.14: Aperture diameter  $D$  in meters and SBR, plotted against the integration time  $T_i$ , from  $10^{-5}$  to 1 second, and 100 nm bandwidths centered at wavelengths from 100nm to 3000nm for meteor Met4VV.

As expected from Table 4.5 this is the most bright meteor, so it will require the least aperture diameter and focal length to be observed. As can be seen from Figure 4.14b, over the whole shown integration time range a suitable system can be identified with sub 1 m aperture diameter. At 0.01ms integration time in the 2600nm+ wavelengths the aperture diameters get bigger than 1m, as well as at an integration time of 1s at 2300nm. In Figure 4.14a the UV and SWIR wavelength bands can be observed to have an SBR always bigger than 1. The atmospheric transparency per wavelength can be observed slightly in this figure. With higher integration times the SBR drops at the same wavelength, meaning more background radiation must have been captured in the observation. The opaque atmospheric bands show consistent yellow in Figure 4.14a across all integration times.

The overall smallest instrument calculated, with 2 cm aperture and 11 cm focal length, can be achieved in the UV spectrum with integration times in between 1 ms and 1000 ms.

### Meteor Met5Pers

From Table 4.5 the Perseid meteor has by far the highest entry velocity and is therefore expected to have the highest surface temperature. A high surface temperature is expected since the heat flux towards the meteor is proportional with the velocity of the object.

For the Perseid meteor Met5Pers the aperture diameter, SNR, and SBR results calculated based on its re-entry simulation are shown in Figure 4.15.

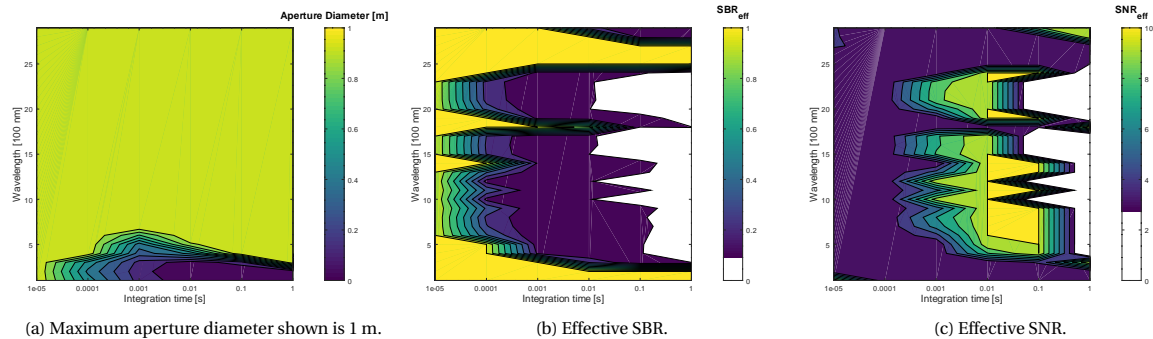


Figure 4.15: Aperture diameter  $D$  in meters, SBR and SNR, plotted against the integration time  $T_i$ , from  $10^{-5}$  to 1 second, and 100 nm bandwidths centered at wavelengths from 100nm to 3000nm for meteor Met5Pers.

As can be observed from Figure 4.15a is that the yellow green color dominates the plot, this means that most of the calculated apertures are bigger than 1 m. At the places where sub 1m apertures are possible, the SBR is in most cases not the limiting factor as can be seen from the yellow areas in Figure 4.15b. However, the SNR seems to be the limiting variable, with the places of possible aperture diameters being in the deep blue areas in Figure 4.15c. The low SNR makes sense, since the meteor is very small and thus radiates a low amount of electrons, which need to overcome the detector noise. The SBR is high, since the atmosphere is very opaque in these bands.

Interesting is that in the aperture diameter results, although the magnitude of Met5Pers is in between that of meteors Met1Model and Met2Rate, this meteor can not be optimally observed in the SWIR spectrum, but rather much better in the UV spectrum. This is due to the different sizes of the meteors and Met5Pers's much higher velocity than the other 2 meteors. Met5Pers will get much hotter due to its higher velocity, but emits overall less due to its smaller size. This means the peak in the UV is much higher than of the earlier two meteors, but since it is small it does not emit as much in the SWIR spectrum compared to the other two meteors.

An optimal system would have an integration time between 10 ms, Figure 4.15c, in the 300 nm band, a 12 cm aperture and a focal length of 0.72 m. The smallest visible instrument aperture is possible at an integration time of 1 ms, Figure 4.15a, with an aperture of 49 cm and focal length of 3.14 m. See Appendix G for the plots with more detailed information and values on the calculated aperture diameters and focal lengths. No sub 1 m aperture solutions exist at these integration times in NIR or SWIR bands.

### 4.1.5. Meteor Tracking

The results from Section 4.1.4 are of importance to this research, however, in most cases a purely detection system is not sufficient to distinguish different objects. As discussed in Sections 2.2.5 and 2.1.1 an error was introduced by differences in exposure time and simulation time resolutions. In this section those contingencies are addressed by using not the maximum temperature to calculate the object's luminosity, but a lower fraction thereof.

All meteors, except the Perseid, were tracked 5 seconds. The Met5Pers meteor and, as will be discussed later, the Met3Common meteor were tracked for 0.7 and 2 seconds respectively instead. 5 seconds tracking means that assuming a 500 ms readout time, leaves about 3.5 seconds of integration time, which allows the 1000 ms integration time to be used at maximum, if at least 3 observations are wanted. For 0.7 and 2 second tracking times the maximum allowed integration times to make 2 and 3 observations respectively, is 100 ms. This needs to be taken into account for the meteors Met3Common and Met5Pers.

In the next 5 sections, for each of the meteors given in Table 4.5, optical instrument parameter results for tracking are presented. The results are based upon running the GEO optics instrument determination code over the same spectral range and with the same re-entry simulation and detector inputs as discussed in the detection Section 4.1.4. However, the input data is tweaked as explained in Section 2.2.5, so for the length of the desired tracking time the object temperature is lower than its maximum value. All separate raw data figures containing the optical instrument parameters calculated per integration time can be found in Appendix G.

#### Meteor Met1Model

Aperture diameter results that allow for tracking of meteor Met1Model for 5 seconds are given in Figure 4.16. When comparing the tracking aperture diameter results with the detecting results in Figure 4.7b, it can be observed that more light green is present, meaning the apertures needed are bigger. In case of sub 1 m aperture diameters the feasible results in Figure 4.7b at, and below 1500 nm, and at shorter integration times than 0.001 s, have completely disappeared.

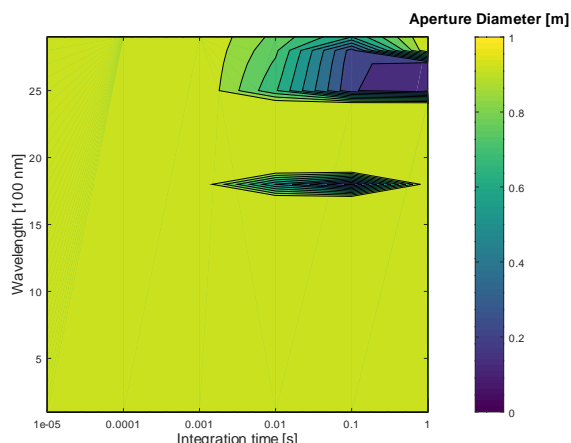


Figure 4.16: Aperture diameter  $D$  in meters and SBR, plotted against the integration time  $T_i$ , from  $10^{-5}$  to 1 second, and 100 nm bandwidths centered at wavelengths from 100nm to 3000nm for 5 second tracking meteor Met1Model.

Now the most optimal solution exists at 2500 nm SWIR with an aperture diameter of 13 cm and 0.64 m focal length, using a integration time of 1000 ms. A reasonable other solution is in the 1800 nm band with 100 ms integration time, leading to an aperture of 18 cm with a focal length of 1.19 m.

Comparing the detection SNR and SBR in Figure 4.8 to the new found tracking SNR and SBR in Figure 4.17, it can be observed that for both parameters more white space is present. Interesting is that the SNR in Figure 4.17a starts to become insufficient at the high integration times, although for detection calculations the SNR was more than 10 at the 1s integration time. The SNR became insufficient at the 1s integration time faster than at the low SNR integration times present in Figure 4.8a, such as the 10ms one.

Also the focal length has been increased and the ground resolutions reduced compared to the detection results, but no figures are shown here for that.

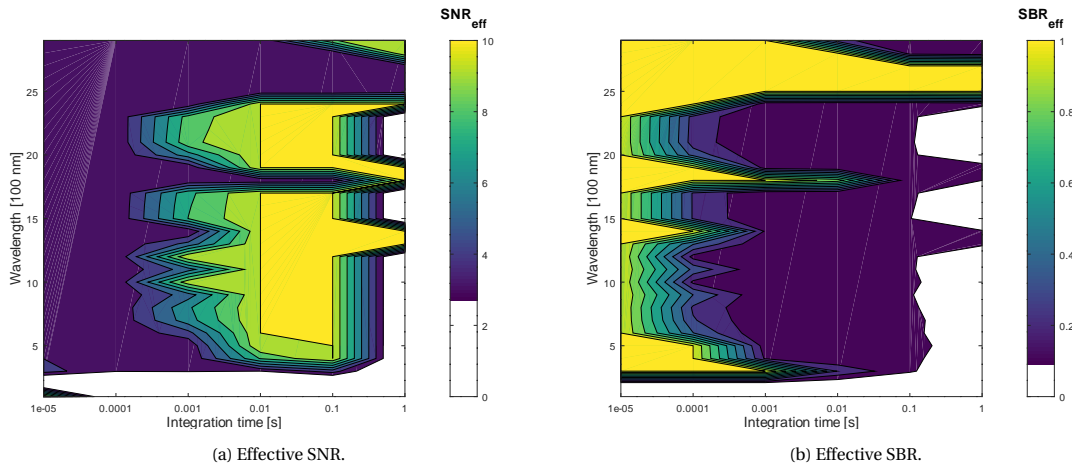


Figure 4.17: The effective SNR and effective SBR plotted against the integration time  $T_i$ , from  $10^{-5}$  to 1 second, and 100 nm bandwidths centered at wavelengths from 100nm to 3000nm for 5 second tracking of meteor Met1Model. White area indicates that the desired  $SNR \geq 3$  and  $SBR \geq 0.1$  were not met.

**Meteor Met2Rate**

Results for 5 second tracking of meteor Met2Rate are given in Figure 4.18. When comparing the detection aperture diameters for Met1Model in Figure 4.7b with the ones for Met2Rate in Figure 4.11 and the ones for Met2Rate tracking in Figure 4.18, something interesting has happened. Before Met2Rate had more sub 1 m aperture diameter options, now it has about the same amount of options left. A similar most optimal solution exists at 2500 nm SWIR with an aperture diameter of 13 cm and 0.64 m focal length as found for Met1Model, using a integration time of 1000 ms. The ultra violet option is not suitable anymore.

In Figure 4.18 can be observed that again no sub 1 m aperture diameters are possible below 1500 nm, except one at 0.01 s exposure time at 1400 nm.

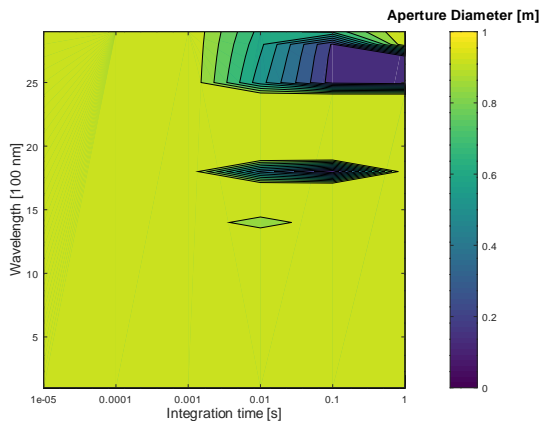


Figure 4.18: Aperture diameter  $D$  in meters and SBR, plotted against the integration time  $T_i$ , from  $10^{-5}$  to 1 second, and 100 nm bandwidths centered at wavelengths from 100nm to 3000nm for 5 second tracking meteor Met2Rate.

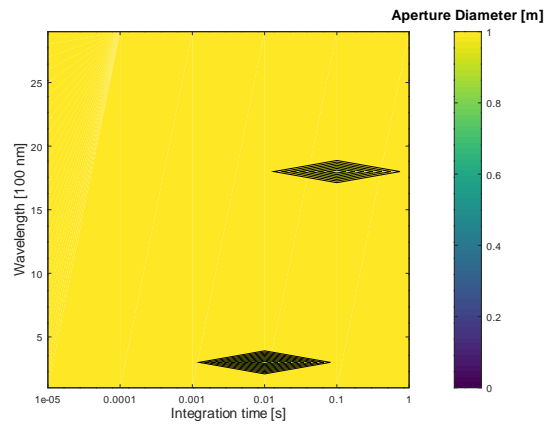


Figure 4.19: Aperture diameter  $D$  in meters and SBR, plotted against the integration time  $T_i$ , from  $10^{-5}$  to 1 second, and 100 nm bandwidths centered at wavelengths from 100nm to 3000nm for 2 second tracking meteor Met3Common.

### Meteor Met3Common

The 5 second tracking solutions did not produce any sub 1 m aperture diameters for the Met3Common meteor. The lowest possible aperture was 1.72 m. Therefore, the tracking was done for 2 seconds instead.

Aperture diameter results for the tracking, with a length of 2 seconds, of the most faint of the 5 meteors Met3Common, are given in Figure 4.19. As can be seen from Figure 4.19, only about 2 aperture diameters are smaller than 1m, namely at 0.01 s at 300 nm and at 0.1 s at 1800 nm. The corresponding aperture diameters are 87 cm and 90 cm respectively. It can be observed that these are aperture diameters found at the same wavelengths and integration times as for just detecting the Met3Common meteor, as in Figure 4.12.

### Meteor Met4V&V

Aperture diameter results for 5 second tracking of meteor Met4V&V are shown in Figure 4.20a. From these figures can be seen that for each of the integration time above 0.00001s a sub 1 meter aperture instrument can be used to track this meteor for 5 seconds. This is a bit worse than what was found for just detecting in Figure 4.14a, where just a few SWIR apertures were slightly above 1m at 0.01ms integration time. The smallest possible optical instrument with an aperture diameter of 10 cm and focal length of 64 cm, would work in the 1800 nm wavelength with an integration time of 10, 100 or 1000 ms.

From Figure 4.20b can be observed when compared with Figure 4.14b, that the tracking of 5 seconds, just as in other cases with other meteor, mainly decreases the SBR in the 100-200nm wavelengths and 1s integration times. For detection all SBRs were  $\geq 0.1$ , however, now the whole 100-200nm band has insufficient SBR and one 400nm wavelength at 1s integration time has insufficient SBR.

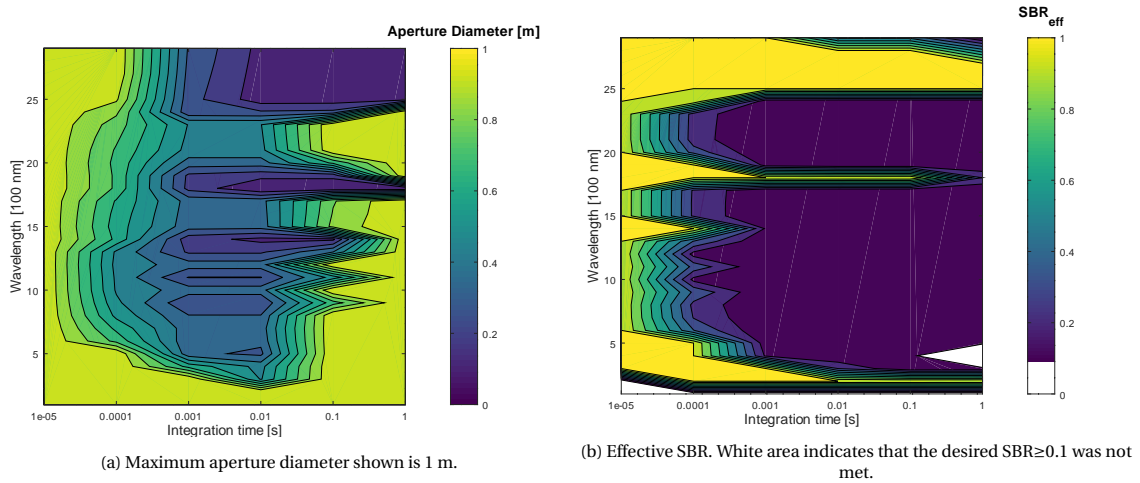


Figure 4.20: Aperture diameter  $D$  and effective SBR, plotted against the integration time  $T_i$ , from  $10^{-5}$  to 1 second, and 100 nm bandwidths centered at wavelengths from 100nm to 3000nm for 5 second tracking meteor Met4V&V.

### Meteor Met5Pers

Running the tracking optical GEO instrumentation parameter code with a desired tracking time of 2 seconds did deliver 2 usable instrument combinations below 1 m aperture diameter. These aperture diameter options are at 200-300 nm at 100 ms integration time and are equal to 24 cm and 76 cm respectively, see Appendix G.

On further inspection the low duration of the meteor is the cause of this. Even though this meteor is -2.6 magnitudes brighter than Met3Common, it burns up so fast that the 2 second tracking requirement requires very big apertures ( $>10$  m) to see the very faint parts in the trajectory. See Table 4.4, a meteor like Met5Pers would have a duration brighter than 0 magnitude of about 1.8 seconds, limited by total ablation, while Met3Common would have a duration of about 4.44 seconds.

Therefore, the code was ran on 0.7 second tracking time instead, these aperture diameter and SBR results are shown in Figure 4.21. Again, unlike the slower moving meteors, this meteor is best tracked in the ultra-violet spectrum. This allows then to have multiple sub 1m aperture diameters at integration times higher than 1ms in the 200-400nm wavelengths. The lowest aperture diameter for tracking of meteor Met5Pers is found at 300 nm with an integration time of 10 ms, the aperture here is 22 cm would allow for 2 observations of such a Perseid in 0.7 seconds.

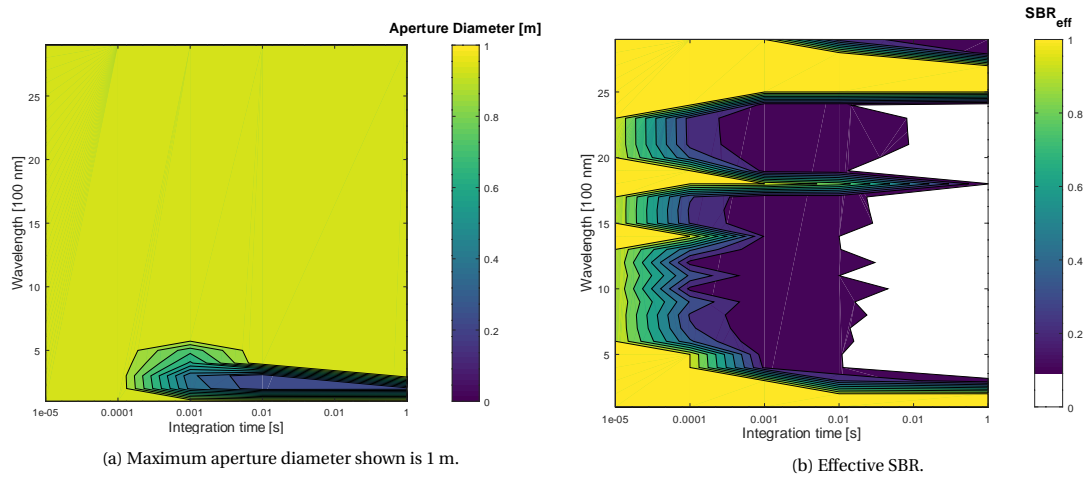


Figure 4.21: Aperture diameter  $D$  in meters and SBR, plotted against the integration time  $T_i$ , from  $10^{-5}$  to 1 second, and 100 nm bandwidths centered at wavelengths from 100nm to 3000nm for 0.7 second tracking meteor Met5Pers.

### 4.1.6. Preliminary Summary on Meteors

Based on the data presented on detecting and tracking of meteors it can be said that detecting solutions always have smaller aperture diameters and focal lengths.

Next to that the SBR and SNR start to become insufficient first at the 200-300nm wavelengths and high integration times such as 0.1s and 1s.

The most allowable sub 1m aperture diameters are for the 5 second tracking of Met4VV, which was to be expected due to its factor 100 bigger mass, which means also a bigger size, than the other meteors.

Although some meteors like Met5Pers and Met3Common are very small, the entry velocity can make them good observable, if their lifetime allows it.

The smallest detection and tracking aperture diameter solutions and their optical instrument parameters for the 5 sample meteors are summarized in Table 4.7.

Table 4.7: Table of the sample meteors and their global found minimal aperture diameters for detection and tracking and the corresponding focal length, wavelength and integration time.

Meteor Name	Inputs		$M_{vis}$	Outputs				
	$V_\infty$ [km/s]	$M_\infty$ [kg]		$D$ [m]	$f$ [m]	$\lambda$ [nm]	$T_i$ [ms]	
Met1Model	10	3	-4.9	Det	0.12	0.81	1800	100
				Track	0.13	0.64	2500	1000
Met2Rate	20	2	-9.1	Det	0.02	0.11	200	10-100-1000
				Track	0.13	0.64	2500	1000
Met3Common	14	0.03	-2.9	Det	0.43	2.54	300	10
				Track 5s	1.72	9.55	1800	100
				Track 2s	0.87	5.08	300	10
Met4V&V	15	200	-13.1	Det	0.02	0.11	300	1-10-100-1000
				Track	0.1	0.64	1800	10-100-1000
Met5Pers	59	0.02	-5.5	Det	0.12	0.72	300	10
				Track 2s	>10	-	-	-
				Track 0.7s	0.24	1.96	200-300	10-100

## 4.2. Capsule Re-entry Simulations and Instrument Determination

The same kind of simulations and instrument parameter calculations as for meteors are done for the Hayabusa and Stardust capsules.

First the fingerprints of the capsules are given. These give insight in what typical temperatures and luminosities are for such sample return capsules. After that the detection and tracking optical instrument parameters for both capsules are determined. And lastly, a preliminary summary is given, but now on only the two capsules.

### 4.2.1. Re-entry Capsules State Fingerprints

As part of the research so called fingerprints were to investigated for each of the objects. In this chapter the two different re-entry capsules Hayabusa and Stardust are investigated.

The results of the re-entry simulations are given in Table 4.8. Interesting is to observe that Stardust has a 3 times higher luminosity than Hayabusa, although the temperature of Hayabusa is about 200 degrees Kelvin higher than that of Stardust. This is due to the bigger size of Stardust, so it can radiate more of the heat away. Next to that the peak wavelength of those two capsules falls just in the Near-Infrared spectrum at about 740-800 nm. This is very close to the Geostationary Lightning Mapper observation wavelength as discussed later in Section 5.3.5.

The altitude of maximum illumination happens at a higher altitude for Stardust. This is also due to its bigger size. As can be shown, bigger re-entry vehicles have their peak heating earlier than smaller re-entry vehicles (Mooij, 2016).

Since Hayabusa is lighter and smaller it still goes at a higher velocity at a lower altitude, where, with its smaller nose radius, the convective heat flux into the vehicle must be higher than that of Stardust. This lead to a higher stagnation temperature for Hayabusa.

Table 4.8: Maximum luminosity, time and altitude of max luminosity, maximum average temperature and the peak wavelength of the Hayabusa and Stardust capsules.

	$I_{max}$ [W]	$t_{maxI}$ [s]	$h_{maxI}$ [km]	$T_{avg,max}$ [K]	$T_{stag,max}$ [K]	peak wavelength [nm]
Hayabusa	451,157	72.5	50.18	2814.2	3496.7	744.1
Stardust	1,402,875	46.1	58.83	2638.8	3275.8	794.3

### 4.2.2. Re-entry Capsules Detection

The detection of re-entry capsules is investigated. This is done below for the Hayabusa and Stardust return capsule. All settings regarding the optical instrument parameters calculations are exactly the same as for the meteors investigated before.

Again, ss will be discussed later in Section 5.3.5, lightning strikes also pop-up in observations as single dots. For actual useful instrument parameters, where meteors can be distinguished from lightning strikes, one should consult Sections 4.2.3 and 5.3.

#### Hayabusa Capsule

The aperture diameter, SNR and SBR results for detecting the Hayabusa capsule are shown in Figures 4.22 and 4.23.

In Figure 4.22 it can be observed that a lot of sub 1 m aperture diameters are not usable. The options are even smaller than for the detection of for example Met1Model, Met2Rate and Met4VV. Keep in mind the lower entry velocity than 4 of the 5 investigated meteors, and the proven temperature gradient over the surface of the capsule, reducing the average temperature of the capsule.

If Figure 4.23a is compared to for example the SBR calculations for the detection of Met5Pers in Figure 4.15b, the SBR of Hayabusa shows complete different insufficient ranges. Met5Pers has insufficient SBR at integration times of 1s, while Hayabusa has insufficient SBR and SNR just at the bands of 100-400nm. Met5Pers lacks the SBR at those points since it is rather small and can not overcome the noise. However, Hayabusa has a problem related to its temperature, since it has sufficient SBR and SNR over the whole range except at the UV spectra, which is the case due to its way lower temperature compared to for example Met5Pers.

The smallest instrument needed occurs at the 100 ms integration time. Here a 10 cm aperture would be enough together with a focal length of 64 cm to detect the Hayabusa capsule at a wavelength of 1800 nm. Due to the big size of Hayabusa compared to the investigated meteors before, it is good observable over a wide range of wavelengths if apertures are restricted to maximum of 1 m.

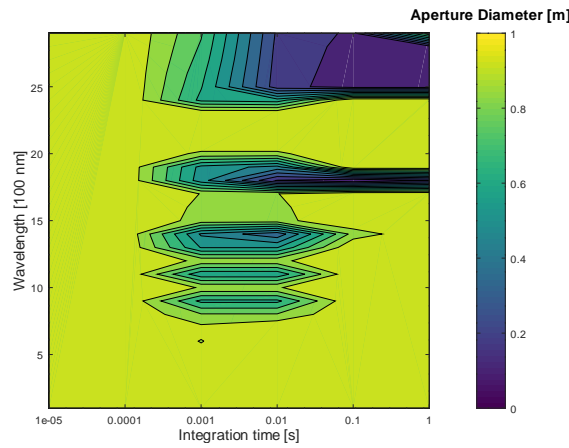


Figure 4.22: Aperture diameter  $D$  in meters, plotted against the integration time  $T_i$ , from  $10^{-5}$  to 1 second, and 100 nm bandwidths centered at wavelengths from 100nm to 3000nm for Hayabusa.

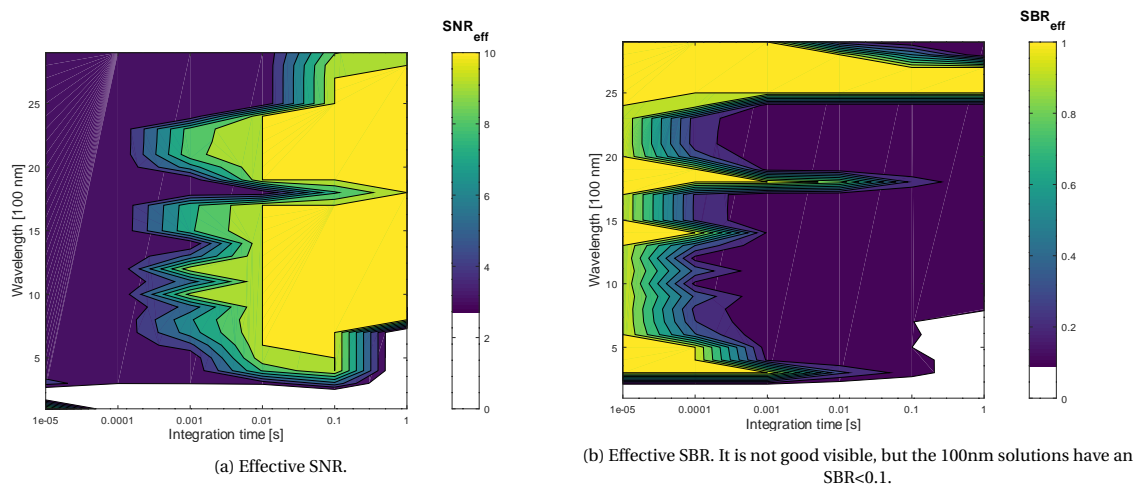


Figure 4.23: The effective SNR and effective SBR plotted against the integration time  $T_i$ , from  $10^{-5}$  to 1 second, and 100 nm bandwidths centered at wavelengths from 100nm to 3000nm for Hayabusa. White area indicates that the desired  $SNR \geq 3$  and  $SBR \geq 0.1$  were not met.

**Stardust Return Capsule**

Although Stardust gets less hot than Hayabusa, see again Table 4.8, it is bigger and radiates way more energy that can be observed. Over the whole integration time spectrum relatively small apertures are possible, which are always lower than the apertures needed for the Hayabusa capsule as can be seen when comparing Figures 4.24 and 4.22.

Interesting is that for integration times of 100ms and 1000ms no difference occurs in most optimal apertures in the 1800 nm and 2500 – 2700 nm bands. The lowest NIR aperture is 21 cm and the lowest visible light aperture is about 59 cm. The overall smallest aperture diameter is found when taking an integration time of 1s in the 1800nm wavelength, leading to a ground resolution limited 10cm aperture and 64cm focal length. This is the same optimal aperture diameter that was found for the detection of Hayabusa.

It was found that the SBR and SNR insufficient regions are similar to that of Hayabusa in the 200-400nm wavelengths.

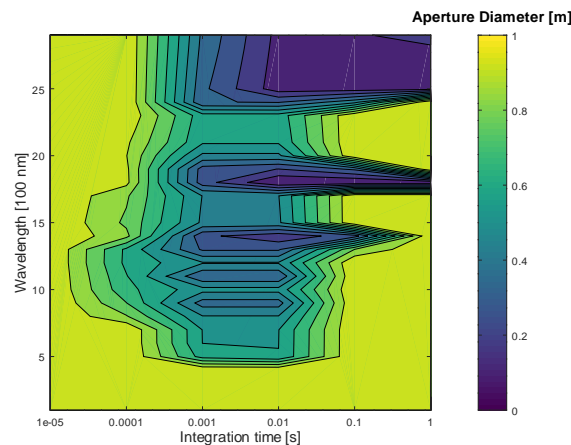


Figure 4.24: Aperture diameter  $D$  in meters, plotted against the integration time  $T_i$ , from  $10^{-5}$  to 1 second, and 100 nm bandwidths centered at wavelengths from 100nm to 3000nm for Stardust.

### 4.2.3. Re-entry Capsules Tracking

Detecting of re-entry vehicles is one thing, however, of great interest, probably more than for meteors, is the tracking of such objects. This is the case since they are human made objects and thus parameters are well known of these objects, unlike those for meteors. If a re-entering object can be tracked precisely it's trajectory can give more info on how well for example the object has been simulated in computer models and if the done calculations beforehand were correct. Of course this is only possible if the tracking is done with sufficient accuracy and precision. Ballistic vehicles might be used for deployment of damaging or explosive payloads. In that case, tracking of such an object could give information on how to eliminate such an object.

As a starting point to assess whether an optical system can be made that can track such objects, Hayabusa and Stardust are used in the tracking optical instrument parameters calculations.

Solution for the tracking of Hayabusa and Stardust for 20 seconds are presented. The 20 second tracking is derived from the fact that it is a length of observation that is not ambiguous with that of meteors, but shorter than the maximum length of about 30 seconds for a ballistic re-entry. All the calculation settings are the same as for detecting capsules and meteors, except the desired tracking time of 20 seconds.

#### Hayabusa Capsule

For the tracking results of the Hayabusa capsule of 20 seconds long see Figures 4.25 and 4.26.

From Figure 4.25 can be observed that there is a lot of green present the figure, this means that a lot of apertures found are bigger than 1 m. Also can be observed that tracking of the Hayabusa capsule is best done as expected in the SWIR spectra, no sub 1m aperture diameters are possible anymore at wavelengths below 1300 nm. In Figure 4.25 it can be seen that optimal wavelengths are in the 1400 nm, 1800 nm and 2500-2900 nm wavelengths at 0.001 to 1 seconds integration times.

For 100 ms at the 1800 nm wavelength and at 1000 ms at the 2500 nm wavelength the optimum aperture diameters can be found. The results are focal lengths of 64 cm and apertures of 10 cm and 13 cm respectively. The 13 cm aperture does not change for a shorter integration time of 100 ms.

When comparing the detection and tracking SNR and SBR for Hayabusa between Figures 4.26 and 4.23, it is quickly apparent that there is a lot more white areas in the plots. Interesting is also, unlike all meteors except Met4VV, that the SNR and SBR do not get totally insufficient at most 1s exposure times. For example in Figure 4.17a the SNR at 1s exposure times at suitable aperture diameters starts to diminish, which is not the case for Hayabusa. The bigger size of the capsule must have something to do with this fact, it emits more photons and thus has a higher SNR.

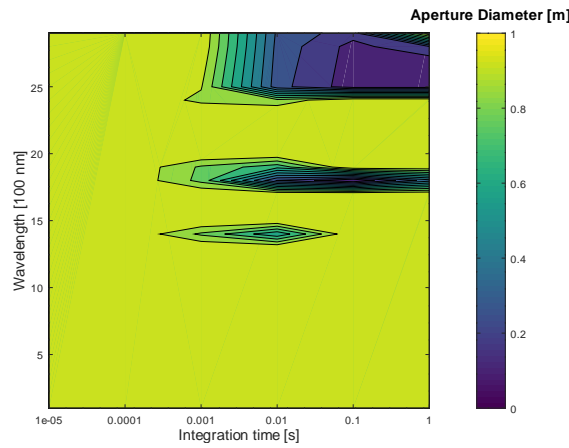


Figure 4.25: Aperture diameter  $D$  in meters and SBR, plotted against the integration time  $T_i$ , from  $10^{-5}$  to 1 second, and 100 nm bandwidths centered at wavelengths from 100nm to 3000nm for 20 second tracking of Hayabusa.

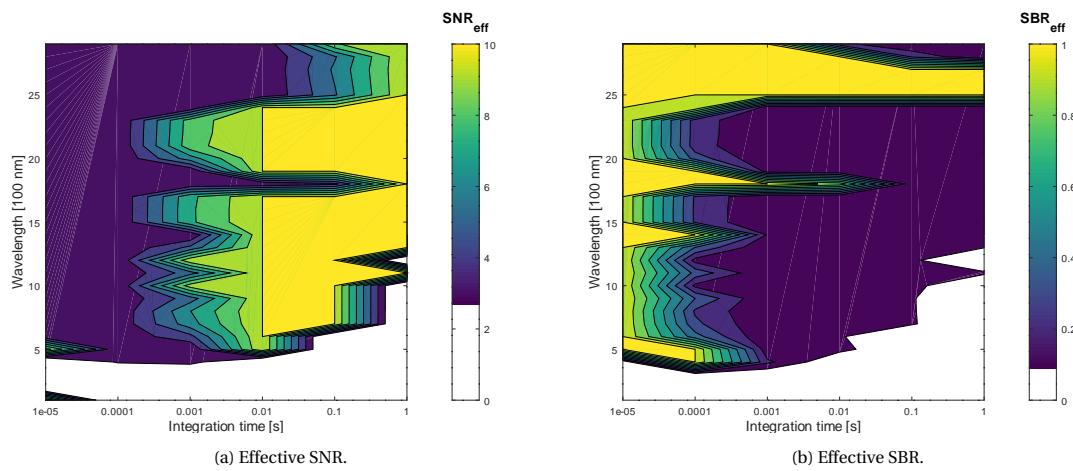


Figure 4.26: The effective SNR and effective SBR plotted against the integration time  $T_i$ , from  $10^{-5}$  to 1 second, and 100 nm bandwidths centered at wavelengths from 100nm to 3000nm for 20 second tracking of Hayabusa. White area indicates that the desired  $SNR \geq 3$  and  $SBR \geq 0.1$  were not met.

### Stardust Return Capsule

Results for the Stardust capsule tracking of 20 seconds long is shown in Figures 4.27 till 4.28.

First of all, comparing the tracking versus the detection aperture diameters for Stardust in Figures 4.24 and 4.27, it is clear that no sub 1m aperture diameters exist at wavelengths lower than 700 nm. Again as with the detection results for Stardust here the 100 ms and 1000 ms results show no difference for most optimal aperture diameters, being again 10 cm and 13 cm respectively in the 1800 and 2500nm wavelengths. The smallest visible light (700nm) aperture is now 95cm at an integration time of 1 ms, and the smallest NIR aperture is 27 cm at 10 ms.

When looking at the SNR and SBR in Figure 4.28, the same can be said as was observed at the Hayabusa SNR and SBR in Figure 4.26, the ultra violet wavelengths are not providing enough SNR and SBR anymore. What is also interesting is that Stardust has more sufficient SBR and SNR values than Hayabusa in the low wavelength regions. This has to be the case since Stardust is bigger. Stardust has a less high surface temperature than Hayabusa and thus should actually radiate less in that region, but this result suggests otherwise. This again has to do with the bigger size of Stardust compared to Hayabusa.

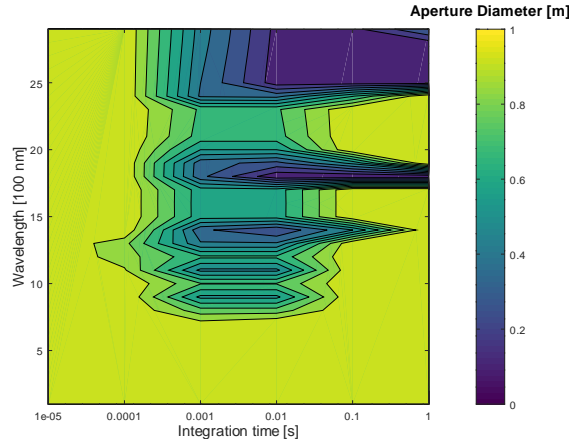


Figure 4.27: Aperture diameter  $D$  in meters and SBR, plotted against the integration time  $T_i$ , from  $10^{-5}$  to 1 second, and 100 nm bandwidths centered at wavelengths from 100nm to 3000nm for 20 second tracking Stardust.

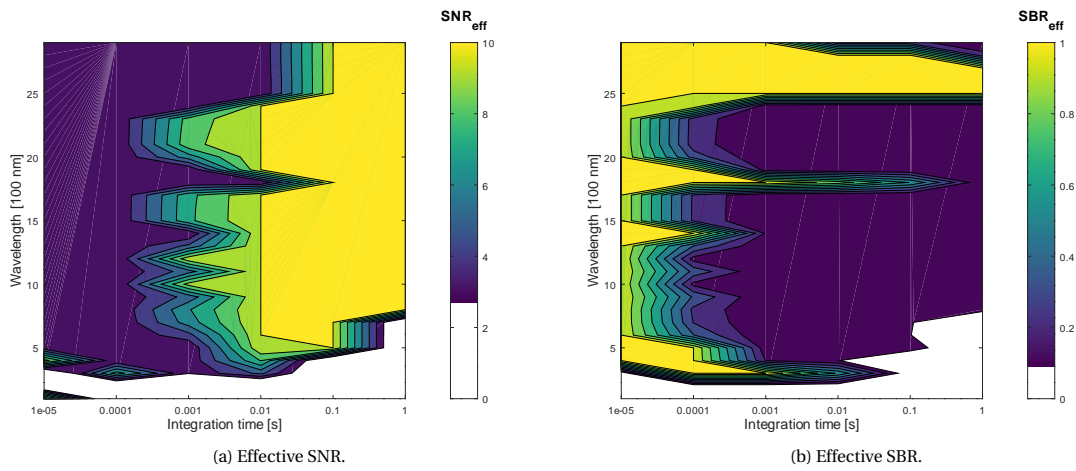


Figure 4.28: The effective SNR and effective SBR plotted against the integration time  $T_i$ , from  $10^{-5}$  to 1 second, and 100 nm bandwidths centered at wavelengths from 100nm to 3000nm for 5 second tracking of Stardust. White area indicates that the desired  $\text{SNR} \geq 3$  and  $\text{SBR} \geq 0.1$  were not met.

#### 4.2.4. Preliminary Summary on Re-entry Capsules

Based on the data presented on detecting and tracking of the re-entry capsules Hayabusa and Stardust it can be said that detecting solutions always have smaller aperture diameters and focal lengths. Optimal aperture diameters and their focal lengths are the same for both capsules in their detection and tracking calculations. In all cases the 10cm aperture diameter at 1800nm is the best solution when using either 100ms or 1s exposure time.

Unlike meteors, capsules start to have their insufficient SNR and SBR regions always emerging in the ultra violet spectrum. Meteors tend to have the insufficient SBR and SNR regions emerging from longer exposure times.

The smallest detection and 20 second tracking aperture diameter solutions and their optical instrument parameters for the 2 sample return capsules are summarized in Table 4.9.

Table 4.9: Table of the capsules and their global found minimal aperture diameters for detection and 20 s tracking and the corresponding focal length, wavelength and integration time.

Meteor Name	Inputs		Outputs				
	$V_\infty$ [km/s]	$M_\infty$ [kg]	$D$ [m]	$f$ [m]	$\lambda$ [nm]	$T_i$ [ms]	
Hayabusa	11.3	17.3	Det	0.10	0.64	1800	100
			Track	0.10	0.64	1800	100
Stardust	12.6	46.8	Det	0.10	0.64	1800	100-1000
			Track	0.10	0.64	1800	100-1000

### 4.3. Analysis of Results Quality

In order to get a better understanding of the results and the implications of changes in the future, an analysis of the used simulation parameters is discussed.

First, for Met1Model, the resolution of the bandwidth and integration time is checked, by varying the bandwidth from 10-50nm at a constant integration time. Also for Met1Model, a chosen bandwidth of 10nm is taken and the integration time is changed as done in the simulations before. Then, different tracking times are investigated with simulating Hayabusa for tracking times from 30 to 60 seconds. Finally a few simulations are done for tracking Hayabusa 20 seconds but over a wider wavelength spectrum from 100nm till 8000nm, to check whether the maximum 3000nm wavelength used in the simulations is justified.

#### 4.3.1. Resolution of Bandwidth and Integration Time

In this section the influence of different bandwidths than 100 nm combined with the difference in integration times is addressed. This is done with the re-entry fragmentation simulation of meteor Met1Model.

##### Different Bandwidths for Integration Time of 1 ms

To address the influence of a different bandwidth the optical instrument calculations of Met1Model were also ran on bandwidths of 10 and 50 nm. The results are shown in Figures 4.29 and 4.30. A trend that can be seen across those figures is that, the bigger the bandwidth the smaller the apertures and focal lengths are that can be used. This is understandable, since more photons can be collected per time with a bigger bandwidth. This means that in low bandwidth cases the SNR is usually the limiting variable.

Disadvantages of bigger bandwidths are that the full well capacity can be reached earlier, since more photons are collected. This would lead to over saturated pixels in the observations, which might not be necessarily bad, if those pixels are just the ones with the object in it. Next to that as already discussed very briefly in Section 4.1.4, some observation spectra where the atmosphere is opaque and objects should be observed ideally, might be smaller than the bandwidth and leak background radiation to the detector. In such a case a smaller bandwidth could be selected.

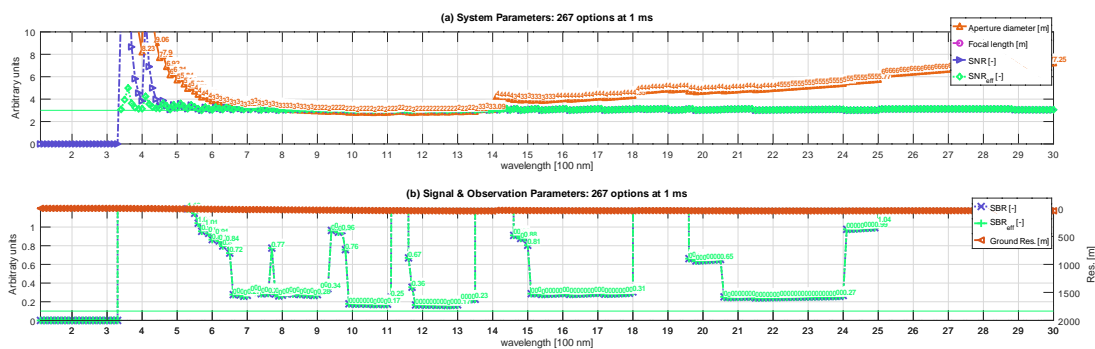


Figure 4.29: Detection optical parameters for Met1Model at 1 ms, between 100 and 3000 nm, at bandwidths of 10 nm.

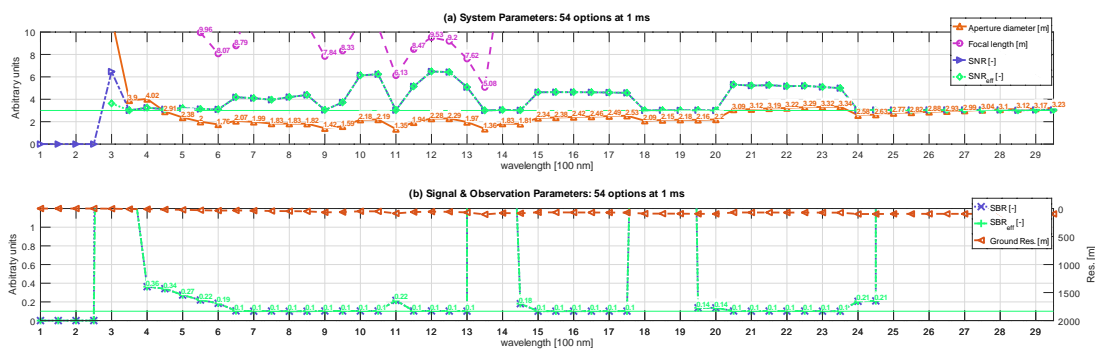


Figure 4.30: Detection optical parameters for Met1Model at 1 ms, between 100 and 3000 nm, at bandwidths of 50 nm.

For Met1Model with a bandwidth of 100 nm and integration time of 1 ms, recall Figure 4.7b, the smallest aperture of 1.3 m was possible at a wavelength of 1400 nm. When looking at Figure 4.30 it can be observed that this value of 1.3 m for 50 nm bandwidth is not reached at a wavelength of 1400 nm. A value of 1.83 is here the case. This is a big difference, but understandable because about 50% less photons are collected and the SNR still needs to be 3. Therefore, the 50 nm band probably needs a bigger aperture. Looking at the 900 nm and 1100 nm bands, the solutions of the 50 nm bandwidth give smaller apertures. The fact that an aperture is given of 1.42 m is interesting at 900 nm, since it is lower than at a bandwidth of 100 nm. At this 900 nm, the 100 nm solution has a SBR of 0.1 and a SNR of 5.5. The 50 nm solution has a SBR of 0.1, but a lower SNR of about 3-3.75. The fact that the SBR is the same and the SNR's are above 3 means that the SBR was the decisive parameter. Due to the smaller bandwidth less photons are captured, and the SNR's numerator and denominator drop, so it is hard to link this further to the same SBR, which due to the lower bandwidth also is made up of less overall photons.

The aperture of 1.42 instead of 1.5 m means that the ground resolution must be bigger. Since the object's amount of photons released is not influenced by the ground resolution, it is assumed to be smaller than 1 pixel, but the SBR is still 0.1 the same amount of photons fraction-wise should be reaching the detector. Since the ground resolution is bigger (smaller aperture means bigger ground resolution) this would mean more photons, but this isn't the case significantly, so this means the atmosphere in this smaller bandwidth of 50 nm is in total more opaque than for the 100 nm solution.

This shows that a smaller bandwidth can be used than the 100 nm used in the Results Section 4, but of course is also greatly dependent on how well known the atmospheric opaqueness is, which is in this research deterministic and an approximation of the found models. Therefore, smaller bandwidth calculations are not necessarily realistic. The smallest step in opaqueness per wavelength data is about per 50 nm, therefore this wavelength resolution does not allow really for assessments of smaller bandwidths than that.

Looking at Figure 4.29 the trend of the atmospheric opaqueness can be observed in the SBR, the higher the SBR the more opaque the atmosphere. The fact that this has no influence on the aperture diameters is because the SNR is limiting here, the small bandwidth means less photons are captured. This could be increased by increasing the integration time, which then would lead to a lower SBR.

One last phenomena that can be observed is that the 50 nm always has lower apertures as long as the SNR was not the limiting factor (so, where the SNR is bigger than 3). For example, the 1600 nm solution is in both cases not SNR limited but SBR limited. Looking at the corresponding apertures, the 100 nm bandwidth one gives an aperture of 2.45 m, whilst the 50 nm bandwidth gives an aperture of 2.42 m. Note that a sort of average should be taken of the 2 consecutive wavelengths investigated for the 50 nm bandwidth compared to the 100 nm bandwidths.

As a final conclusion, a smaller bandwidth can be better if it can precisely overlap with a opaque atmospheric band. A smaller spectral resolution allows for that. However, a smaller bandwidth also means a smaller SNR for the same integration time. Therefore, either the integration time, or the aperture can be increased when the SNR is insufficient. In turn, both those solutions decrease the SBR. A good balance between the integration time, bandwidth and aperture diameter is needed to get the most optimal solution in the end.

### 10 nm Bandwidth at Different Integration Times

To see the influence on the optical instrument parameters for a smaller bandwidth, the simulation is ran at the same 10 nm bandwidth, but at different integration times as used before. These results can be used to check whether the smaller bandwidths can be used effectively, when the SNR is not the limiting factor, which was the case in Figure 4.29. The results are shown in Figures 4.31 till 4.33, results for 0.01 ms, 0.1 ms and 1 ms are not shown, since the results only have apertures above 3 m, have 0 feasible solutions or are already shown in figures before (Figure 4.29).

Most interesting is here the smallest aperture possible in Figures 4.32 and 4.33, which is 0.42 m at about 1350 nm to 1400 nm. A value for the aperture for the Met1Model meteor calculated at these integration times with a 100 nm bandwidth does not even come close, and is over 10 m. As can be seen there the SBR is the limiting factor of about 0.14, the SNR is some value higher than 10. The SBR for the 10 nm bandwidth is somewhere above 1 and the SNR is here the limiting factor with a value of 3. From this can also be seen that the location of the bandwidth matters.

What is also interesting is that the smallest aperture at 1000 ms in Figure 4.8b is just 13 cm, but at wavelengths of 2500 – 2800 nm. For the 10 nm bandwidth, the aperture possible is about 92 cm, this is way bigger, but here the SNR is the limiting factor again. For the 100 nm bandwidth solution the maximum resolution is the limiting factor and even some extra margin is left on the SNR. This shows clearly that a bigger bandwidth

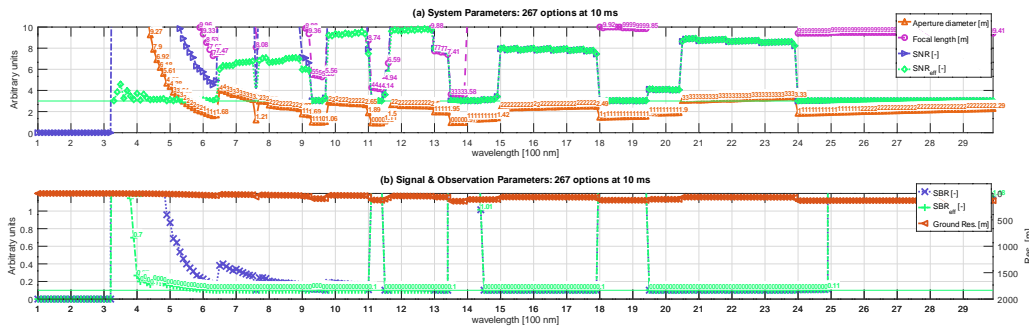


Figure 4.31: Detection optical parameters for Met1Model at 10 ms, between 100 and 3000 nm, at bandwidths of 10 nm.

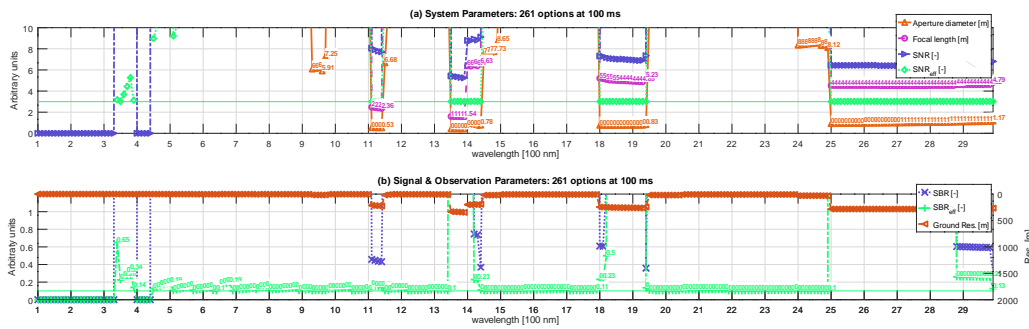


Figure 4.32: Detection optical parameters for Met1Model at 100 ms, between 100 and 3000 nm, at bandwidths of 10 nm.

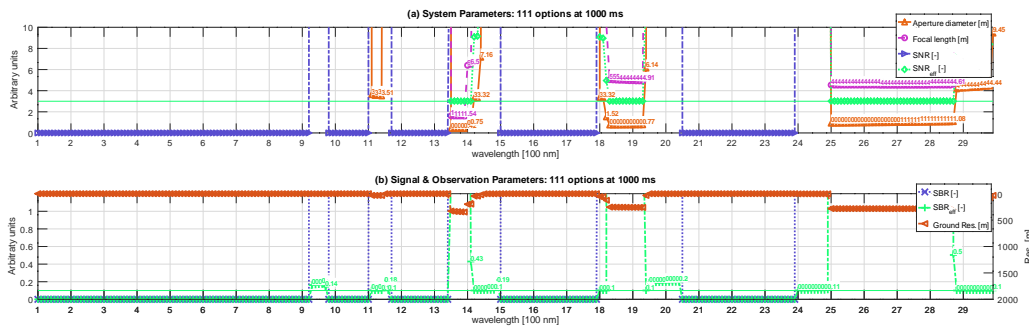


Figure 4.33: Detection optical parameters for Met1Model at 1000 ms, between 100 and 3000 nm, at bandwidths of 10 nm.

has higher SNR's and that a smaller bandwidth, however, too big bandwidths for the opaque bands of the atmosphere decrease the SBR on their own.

From this all can be concluded that the integration times play an important role in making up for the smaller bandwidth. For the same bandwidth a higher integration time can lead to smaller apertures if the SNR limit is reached at lower integration times. When the integration time is taken higher, the SNR will slowly decrease again (depending on dark current and background noise electrons), but the SBR will decrease faster, since more background electrons will be collected (and the background noise is less than the background signal, so the SNR will decrease slower, unless the dark current is more prominent). Because of this, the system is always SNR limited on shorter integration times till the integration time multiplied by the velocity is equal to the pixel ground resolution. Then, when the maximum SNR is achieved, it will slowly become lower again for higher integration times at the same ground resolution, while the SBR slowly decreases till it reaches 0.1. When that happens the ground resolution needs to be decreased, so an increased aperture. The SNR will increase because of this, but SBR keeps being the limited factor.

### 4.3.2. Tracking Time Influence

Another interesting aspect is the change of the tracking time required. For this the Hayabusa capsule was simulated for constant bandwidths of 100 nm and an integration time of 1000 ms, using 30, 40, and 50 seconds tracking time. The results are shown in Figures 4.34 till 4.36.

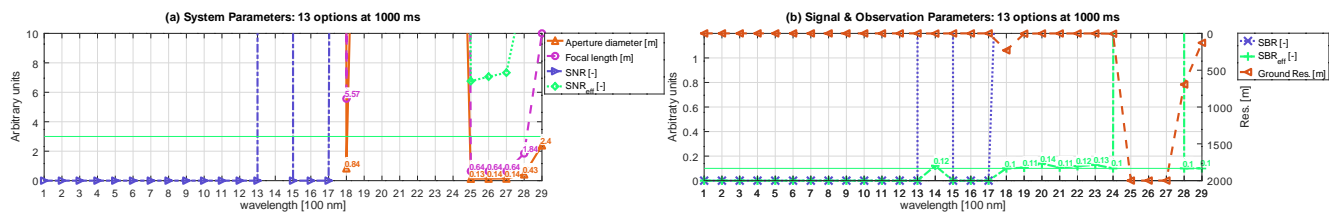


Figure 4.34: Tracking optical parameters for Hayabusa for 30 seconds at 1000 ms integration time, between 100 and 3000 nm, at bandwidths of 100 nm.

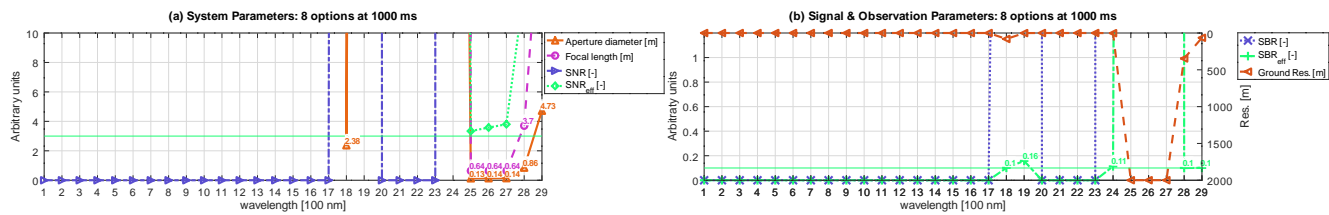


Figure 4.35: Tracking optical parameters for Hayabusa for 40 seconds at 1000 ms integration time, between 100 and 3000 nm, at bandwidths of 100 nm.

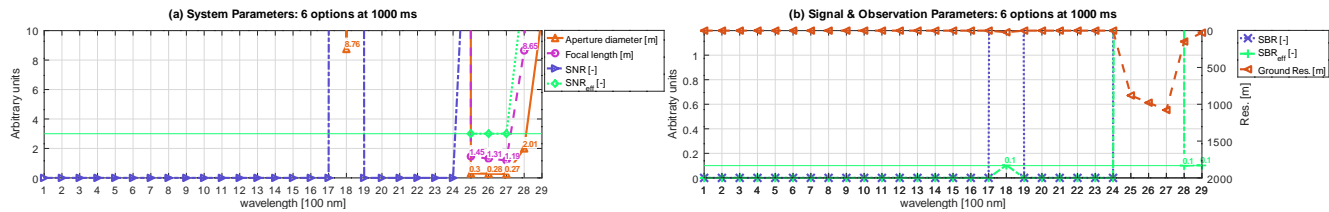


Figure 4.36: Tracking optical parameters for Hayabusa for 50 seconds at 1000 ms integration time, between 100 and 3000 nm, at bandwidths of 100 nm.

In these figures can be observed that longer required tracking times lead to bigger apertures, as expected, since the program uses a lower temperature than the maximum temperature during re-entry. Since the program calculates a longer tracking time with a lower temperature, this means also the black body radiation is less and more shifted towards the longer wavelengths. However, any warmer temperature has at least these used conditions or higher, so, the result is not necessarily an optimum, but it will be sufficient for observing the object for sure.

Figures 4.34 till 4.36 show that the SNR decreases for the same ground resolution/aperture for longer tracking times at the 2500 – 2800 nm wavelengths. The SNR is here the limiting variable. For the 1800 nm wavelength the SBR is the limiting variable. The transmittance of the atmosphere plays here an important role. The atmosphere is in the used model  $10^7$  less transparent in the 2500 – 2800 nm than in the 1800 nm band. Because of this the 1800 nm wavelength has more problems with the SBR and therefore it is limiting here than the 2500 nm wavelength, where the background almost has no influence thus the SNR becomes the limiting variable.

### 4.3.3. Some Results from 3000 nm till 8000 nm Wavelengths

In this research most detailed simulations, optic calculations and analyses have been performed on 100 nm till 3000 nm wavelengths. As a small extension the code is run for Hayabusa on the 3000 nm till 8000 nm wavelengths, 1 ms and 10 ms integration times, the results can be found in Figures 4.37 and 4.38. It can be observed in all those figures that no smaller apertures are possible in the 3000+ nm bands, than in the smaller wavelengths.

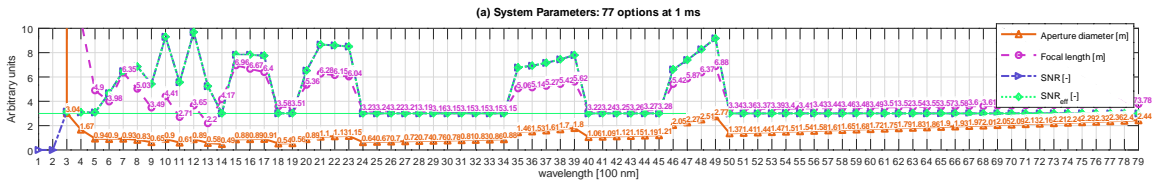


Figure 4.37: Tracking optical parameters for Hayabusa for 20 seconds at 1 ms integration time, between 3000 and 8000 nm, at bandwidths of 100 nm.

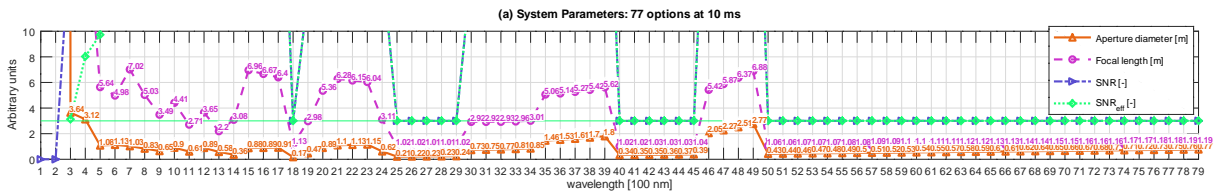


Figure 4.38: Tracking optical parameters for Hayabusa for 20 seconds at 10 ms integration time, between 3000 and 8000 nm, at bandwidths of 100 nm.



# 5

## Discussion

In this Chapter all the results, verification and validation will be discussed. First the re-entry simulation, fingerprints and influx rates (only for meteors) will be discussed for meteors and capsules. After that the GEO optics instrument parameter calculations are discussed, with the analysis of the tracking observations, instrument and detector interactions, day and night observations and telescope limitations and unaccounted for detector characteristics.

After that other interesting objects than analyzed in this research will be addressed together with the classification problem in the possible observations. And finally some possible satellite systems will be presented.

### 5.1. The Re-entry Simulations of Meteors and Capsules

Fingerprints and influx rates were obtained for a range of meteors with different masses and velocities. Also the fingerprints of the Hayabusa and Stardust capsules were obtained from our simulations.

In the upcoming subsections these fingerprint and influx rate results will be discussed. The outcome from our simulations is presented, the trends in the fingerprints are discussed where applicable and compared to reference data from other researches. Also the contingencies found in the validation process, and the fragmentation model and aerothermodynamics uncertainties within the done simulations will be discussed.

#### 5.1.1. Meteor Fingerprints

From the characteristics, or fingerprints, obtained of meteors between 0.1 g and 1,000 kg, and at velocities between 11 and 72 km/s, it can be concluded that these meteors have maximum bolometric luminosities ranging from  $5 \times 10^2$  W till  $2 \times 10^{11}$  W. The simulated meteors have an absolute magnitude between 2 and -20. In these simulations a sublimation reduction of ablation was used of 33% (Bronshten, 1983), meaning that 33% of the heat flux at the stagnation point of the meteor does not go into heating up the meteor. From the simulations was also concluded that the peak wavelength of the black body radiation of the meteor was in between the 50 and 500 nm wavelengths, and thus in the ultra violet and visible wavelengths.

Some trends can be observed in the simulated data. Such as that faster and heavier meteors always are brighter than slower or lighter ones with the same mass or velocity. Furthermore, faster meteors burn brighter at higher altitudes, and heavier meteors burn brighter later than their lighter counterparts, deeper in the atmosphere. Durations of meteors brighter than 0 absolute magnitude have also been calculated. Slower meteors always burn longer above 0 absolute magnitude than faster meteors of the same mass. There is an exception in cases where the meteors are so slow for their mass class, that they are burning shorter above 0 absolute magnitude than a faster meteor. An example of this is that a 0.1 g meteor burns longest above 0 absolute magnitude at 30 km/s equal to 1.82 s, and at 20 km/s it burns just 1.18 s above 0 absolute magnitude. However, the burn duration above 0 absolute magnitude fluctuates more per velocity at masses above 100 kg Reason for this could be the used termination conditions. This happens when the termination condition altitude is reached before the meteor stops burning above 0 absolute magnitude for example. The found burn durations above 0 absolute magnitude ranged from 1 second till at least 30 seconds, not taking into account very heavy meteors like Park Forest and Chelyabinsk (Brown et al., 2004; Popova et al., 2013a).

Our calculated visual absolute magnitudes  $M_{vis}$  of the 5 sample meteors presented in Table 4.5 showed different values as compared to what Equation (4.3), as used and given by Ohsawa et al. (2018); Jenniskens (2006), produces for these masses and velocities. All our meteors that do not fragmentate have a -2 to -3 higher absolute magnitude and fragmentating meteors -4 higher peak absolute magnitude. The Perseid meteor is only off by -0.7. The cause for these deviations is probably that Equation 4.3 was derived for masses

below 1 kg and at velocities above 25 km/s (Jenniskens, 2006). This also explains that the Perseid has the lowest deviation between the two computed visual absolute magnitudes, since it is the only one in the range of the allowable mass and velocity ranges. Next to the fact that 4 out of the 5 sample meteors are outside of the applicable ranges for Equation (4.3), fragmentation is incorporated in our simulations, which has been proved to be the source of most luminosity energy observed in meteors (McCrosky, 1958). The fact that 4 of our 5 sample meteors are outside the allowable ranges of Equation (4.3), and that we incorporated fragmentation, is the cause for the difference in the found visual absolute magnitudes.

Lastly, the fragmentation shown in the 5 sample meteors and all fingerprints is in agreement with Jones and Kaiser (1966), who state that fragmentation doesn't happen for meteoroids with a radius smaller than 0.1 cm. Assuming a density of  $3500 \text{ kg/m}^3$  this is equivalent to a mass of about 0.02 grams. This limit is lower than our smallest mass equal to 0.1 grams.

### 5.1.2. Meteor Influx Rates

Influx rates were determined from absolute magnitudes based on the method provided by Ohsawa et al. (2018), as shown in Equation (4.4). The method of Ohsawa et al. (2018); Jenniskens (2006) refers to Equation (4.4). The absolute magnitudes from our research, given in Table 4.2, were used as inputs for Equation (4.4).

The first set of comparison data was obtained with Equation (4.3), using as inputs the same masses and velocities that were used to construct Table 4.2. These absolute magnitudes could then be used in Equation (4.4), to obtain a comparison dataset of occurrences. A second occurrences dataset was obtained by using Equations (4.1) and (4.2), taken from Halliday et al. (1996). As inputs the masses and velocities used in Table 4.2 were again used. Further on in the text, the method of Halliday et al. (1996) refers to Equation (4.1) and (4.2). This whole procedure results in 3 influx rates for a range of meteors with different masses and velocities, as in Figure 4.5.

The occurrence line plots in Figure 4.5 show that Halliday et al. (1996) overpredicts the amount of occurrences compared to our results at any velocity and at masses above 100 kg. At low velocities of 11 km/s and 20 km/s the method of Halliday et al. (1996) underpredicts the amount of occurrences compared to our results. The method of Halliday et al. (1996) is not a function of the entry velocity. One should remember that the method of Halliday et al. (1996) is a cumulative function, and it calculated the number of occurrences greater or equal to the mass given. An explanation for the lower influxes at lower velocities could be that Halliday et al. (1996) did not observe very faint meteors below -0.8 absolute magnitudes with the used observation system (MORP) (Halliday et al., 1987), thus his model fit is not taking those well into account.

Looking at Figure 4.1c one might wonder why the used method of Ohsawa et al. (2018); Jenniskens (2006) underpredicts the amount of brighter meteors compared to Halliday et al. (1996). Halliday et al. (1996) do not distinguish between different velocities, thus it could be assumed that the found high mass meteors are the sum of all the different velocity occurrences by Ohsawa et al. (2018) at that mass. The intersection between the two planes in Figure 4.1c might be exactly the distinction between the sensitivity of the system from Jacchia et al. (1967) compared to MORP. That line would then be the sum of all the occurrences  $N$  at a lower velocity, for the same mass.

The model used by Ohsawa et al. (2018); Jenniskens (2006) does not necessarily take fragmentation into account. Therefore this model might give a too high mass for a meteor with a certain absolute magnitude. Usually the fragmentation of a meteor results in a higher absolute magnitude than if there would be no fragmentation. This hypothesis could be true, since occurrence data calculated with the method by Ohsawa et al. (2018) follows the same trend as the occurrence data from this research, but than shifted to a higher mass for the same absolute magnitude. Next to that, the method used by Ohsawa et al. (2018) to estimate the absolute magnitude is based on the velocity and mass via Equation (4.3). But, Equation (4.3) is derived for meteors of less than 1 kg and at velocities higher than 25 km/s Jenniskens (2006). Therefore, not taking into account fragmentation and wrongly use of Equation (4.3), the occurrence data by the model of Ohsawa et al. (2018) shown in Figure 4.5, is everywhere higher than our occurrence data.

The conclusions of these influx rate analyses are that the fragmentation, trajectories and absolute magnitude peaks have been validated before, but our influx rate data deviates from the influx rate data calculated with the model of Ohsawa et al. (2018); Jenniskens (2006). The fact that the absolute magnitude calculations of Ohsawa et al. (2018) are only valid for meteors lighter than 1 kg and faster than 25 km/s, and probably does not take into account fragmentation, leads to the conclusion that our model is on the correct side with its deviation from the values of Ohsawa et al. (2018). If our models would produce fainter meteors it would be illogical, since fragmentation was implemented in our simulations, and fragmentation always leads to brighter meteors than non-fragmentating meteors.

### 5.1.3. Meteor Validation Implications and Fragmentation Uncertainties

A comparison was done between a group of typical Perseids, with ID's MORP 575, MORP 576, MORP 581 and MORP 584 taken from [Halliday et al. \(1996\)](#), and a meteor with 0.01 kg mass at 60 km/s from our simulations, given in Section 4.1.1. The average mass and velocity of the Perseids taken from [Halliday et al. \(1996\)](#) were 0.013 kg and 60.1 km/s respectively. The differences in density between 2200 kg/m<sup>3</sup> for Perseids and our used density of 3500 kg/m<sup>3</sup> was not taken into account. The Perseids from [Halliday et al. \(1996\)](#) had their peak absolute magnitude between -7.8 and -8.5 at altitudes in between 82 km and 89 km, with a duration between 0.3 seconds and 0.8 seconds ([Halliday et al., 1996](#)). Compared to our 0.01 kg, 60 km/s meteor in Tables 4.2, 4.3 and 4.4, our peak absolute magnitude of about -6.7 is at least -1.1 absolute magnitudes lower, our altitude of peak absolute magnitude at 53 km about 30 km lower and our duration of 1.8 seconds more than twice the average duration given by [Halliday et al. \(1996\)](#).

From the validation in Section 3.1.5 it was already clear that our model predicts the peak absolute magnitudes lower than [Halliday et al. \(1996\)](#) observes, so the lower peak absolute magnitude altitude for our Perseid simulated is no surprise. The fact that our peak absolute magnitude does not match in magnitude is probably due to the baseline fragmentation parameters used. Running the code with baseline fragmentation parameter initial strength changed to 0.1 PMa instead of 1.5 MPa, the peak absolute magnitude is -9.7 at an altitude of 69 km with a duration of 1.5 seconds. From this simulation run it is clear that the peak absolute magnitude and its altitude change significantly depending on the fragmentation parameters, and if chosen such, the peak absolute magnitude value can be precisely found.

The duration over 0 absolute magnitude is overestimated in our code compared to the durations of [Halliday et al. \(1996\)](#). However, from [Halliday et al. \(1987\)](#) it seems the limiting absolute magnitude of the Meteor Observation and Recovery Project (MORP) is in between -0.8 and -1.1, therefore it is possible that the observed duration by [Halliday et al. \(1996\)](#) is indeed shorter than found in our research, which assumed a limiting magnitude of 0.

The higher altitude for the peak absolute magnitude observed by [Halliday et al. \(1996\)](#) compared to our simulations might be due to the used scale height for the exponential atmosphere of  $h_0 = 7,000$  m. Changing  $h_0$  to 8,500 m, as for example used by [Putnam and Braun \(2015\)](#) for re-entry simulations, in combination with the initial strength of 0.1 MPa, brings the altitude of the peak absolute magnitude to 83 km. The peak absolute magnitude is now -9.7 and the duration 1.2 seconds. This shows that the peak absolute magnitude altitude can be found by changing the scale height, at a cost of correctness in the value of the peak absolute magnitude.

For the reference luminosities of a 0 absolute magnitude meteor in the visible spectrum [Jenniskens \(2014\)](#) list a reference value for the total emitted luminosity, whilst [Weryk and Brown \(2013\)](#) gives the value for the observed luminosity. The difference of the total and the observed could explain the difference of about a factor of 2 in Table 2.2. The same is the case for the bolometric luminosities of [Halliday et al. \(1996\)](#) and [Stokan and Campbell-Brown \(2015\)](#). The total bolometric reference luminosity of 1800 W ([Ceplecha et al., 1998](#)) and total visible reference luminosity of 1100 W ([Ceplecha et al., 1998](#); [Popova et al., 2013b](#)) are used in this research, and a lot by other researchers. However, our calculated heat flux and empirical luminosities are only emitted by one side of the sphere or capsule. Therefore, it could be that we underestimate the absolute magnitude by at maximum 0.8 magnitude while using the total reference luminosities, since our luminosities are not emitted to all directions. However, a total emitted luminosity does not mean it is twice the amount of half a sphere as is calculated in this research, so the error is probably a bit lower than 0.8 absolute magnitudes.

For other meteors than the just discussed Perseids the simulations were harder to validate. Comparing the re-entry simulations directly with observation data as in Tables 3.5 and 3.6, gave very different outcomes. Either the trajectory was matched with a maximum of 10% velocity difference, but leading to the correct peak absolute magnitude at a wrong altitude, or the absolute magnitude peak could be matched perfectly at the right altitude, but the velocity per altitude would be off. This has been shown in Section 3.1.4, and is seen as validation of the trajectory dynamics, and peak absolute magnitude determination.

The fact that the determined altitude of the peak absolute magnitude was usually lower than in the validation data has been assumed to be due to the trajectory assumptions within the validation data ([Halliday et al., 1996](#)). A lot of assumptions in other researches are made on, for example, the trajectory, shapes, material densities, luminous efficiencies and usually fragmentation is not assumed ([Halliday et al., 1996](#); [Stokan and Campbell-Brown, 2015](#)). Some of these assumptions were not used in this research and those of importance, like the linear trajectory have been accounted for.

In Section 3.1.6 it was concluded that below 20 km/s our simulations overestimate the luminosities compared to empirical luminosities of meteors by maximum 900%, and underestimate the luminosities above 20

km/s, till at maximum 900% at 70 km/s. The cause for the overestimation below 20 km/s is probably due to not implementing a temperature gradient over the wet surface area of the meteor. A temperature gradient could reduce the overestimation of -0.4 absolute magnitudes. However, a temperature gradient was not applied to the meteors. The validation done in Section 3.1.5 would benefit from this as well, since all meteors had their luminosity overestimated and all their velocities at peak absolute magnitude were below 20 km/s. The underestimation of the luminosity above 20 km/s is most probably due to fact that the used heat flux model can not be applied at those velocities (Brandis and Johnston, 2014). Increasing the amount of fragmentation leads to lower errors above 20 km/s. It was hypothesized that increasing the amount of fragmentation approaches a meteor trail situation, which is a common meteor phenomenon in observed meteors, on which the used empirical luminosity coefficient is based (McCrosky, 1958; Stokan and Campbell-Brown, 2015). A work around can be to use the empirical luminosity calculated instead of the luminosity via the heat flux model. It should be noted that when using the empirical luminosity of constant 4% above 10 km/s the overestimation of the luminosity is lower at just about 35% (Halliday et al., 1996).

Fragmentation was included in the simulation based on an independent wake model. A combination model using a dust-cloud and unequal mass fragments has proven to give better results, but has not been implemented in the simulation due to complexity. Fragmentation modeling requires 3 distinct inputs that can not be known accurately beforehand (burst strength, strength scaling and number of fragments per breakup). So, usually the back-fitting of these parameters with the observations is done (Popova et al., 2013a). Therefore, simulating fragmentation with the chosen baseline fragmentation parameters does not necessarily give a accurate and precise solution. However, from a small grid search simulation done with different fragmentation parameters, it was concluded that our chosen baseline values lead to an average peak absolute magnitude at an average altitude amidst all of the outcomes. Using this fragmentation model is definitely more realistic than non-fragmentation solutions, since it is suggested that even the smallest meteors exhibit fragmentation (Cepplecha and ReVelle, 2005), and fragmented particles are the source of large luminosities (McCrosky, 1958).

The meteor simulation validation differences with Halliday et al. (1996) and the average, but not necessarily representative, fragmentation parameters used, should be taken into account when drawing conclusions from our simulated data. A different scale height or atmospheric model, or different materials, shapes and inhomogeneous densities might change the trajectories, absolute magnitude curves and fragmentation behavior of a meteor with a given mass and velocity.

Therefore, our presented fingerprints are one of the many possible solutions for meteors with given masses and velocities. Also the chosen entry angle of  $45^\circ$  is not in any way the only possible entry angle, although the most common one according to Mathias et al. (2017).

#### 5.1.4. Capsule Fingerprints

The capsule fingerprints were obtained by simulating the capsule re-entries using the input data from Appendix D. What sets the capsule simulations apart from those of meteors is first of all the used temperature gradient of about 30% over the surface of the object (Suzuki et al., 2014), secondly the value of 35% instead of 33% for the sublimation heat flux reduction (Olynick et al., 1998; Bronshten, 1983), and thirdly the different heat of ablation of the material from about  $\xi = 8.3 \times 10^6$  J/kg for meteors to  $100 \times 10^6$  J/kg  $< \xi < 500 \times 10^6$  J/kg for capsules based on the PICA heat shield (Riccio et al., 2017).

The Stardust capsule radiates about 3 times more energy than Hayabusa, as can be observed from the results presented in Table 4.8. The capsules radiate mostly in the near infrared spectrum at about 740 nm to 800 nm. The peak luminosities during the capsule re-entries was found at altitudes between 50 – 60 km, reaching an average surface temperatures of about 2600 – 2850 K. The average surface temperature for Stardust was very close in agreement with data from other papers (Trumble et al., 2010; Jenniskens et al., 2005).

From the validation done in Section 3.1.1 based on observations by Ueda et al. (2011) it could be concluded that the maximum velocity error over an altitude from 52 km till 35 km does not exceed 260 m/s or about 10%. However, over most of this trajectory the error is less than 100 m/s and mostly maximum 1% error. This proves that the dynamics can be well simulated with the program and is more precise than that for meteors. Re-entry simulations of capsules have been done numerous times before with adequate results (Mooij, 2016; Putnam and Braun, 2015).

#### 5.1.5. Capsule Aerothermodynamics Uncertainties

The aerothermal aspects during the re-entry, greatly determines the observability of the capsules. In Section 3.1.3 it was concluded that the differences in heat fluxes compared to other researches go up till 50%. However, these errors are reduced after multiple calculations from the heat fluxes to the average temperature, in

which a temperature gradient is used between the stagnation point and the trailing edge of the wet surface from [Suzuki et al. \(2014\)](#). The stagnation and average temperatures result in a value having an error that is below 10% compared to other researches ([Trumble et al., 2010](#); [Dec and Braun, 2006](#); [Olynick et al., 1998](#); [Jenniskens et al., 2005](#); [Suzuki et al., 2014](#); [Löhle et al., 2013](#); [Grinstead et al., 2011](#); [Winter et al., 2012](#)).

## 5.2. GEO Optics Instrument Parameter Calculations

With the validity proven of the re-entry simulation code, the next step was to use the simulation results of meteors and capsules, and use those to find optical instrument parameters to detect and track them. For the meteor optical instrument parameter calculations the 5 earlier identified meteors were used with velocities between 10 km/s and 59 km/s and masses between 0.02kg and 200kg, see Table 4.5. For the re-entry capsule observations the re-entry simulations of the Hayabusa and Stardust capsules were used, for their inputs see Appendix D.

All the results are discussed below. Then a discussion follows on the amount of tracking observations that can be made, the integration time, ground resolution and bandwidth interactions, the differences in day and night observations, and the telescope limitations and unaccounted for detector characteristics.

### 5.2.1. The Detection and Tracking of Each of the 7 Objects

The detection and tracking optical instrument parameters for the 5 sample meteors were summarized in Table 4.7. From the GEO optics instrument parameter calculations for meteors can be concluded that sub 1 meter aperture optical instruments can be used to observe all investigated re-entry capsules and all of the 5 investigated meteors, in both detecting and tracking modes. All of these solutions had an aperture diameter under 25 cm, except for 1 meteor. Met3Common, with an absolute magnitude of around 0.9 to -2.9, depending on [Ohsawa et al. \(2018\)](#) method or the developed re-entry simulation code, could be observed in detecting mode with a sub 1 meter aperture diameter of 0.87 m with a reduced tracking time of only 2 s.

The Met5Pers meteor was due to its short duration only tracked for 0.7 seconds. This resulted in an aperture diameter of about 24 cm in the ultra violet spectrum. Each of the sub 1 m aperture diameter requirements go hand in hand with effective focal lengths of less than 10 m. This is assumed to be feasible in case state of the art telescope designs are used, like Cassegrain or a three-mirror Anastigmat, which can reduce a physical focal length to 1/3rd to 1/13th of the effective focal length needed. For example, in case of a 10 m effective focal length, it can be reduced to about 3 m to <1 m using a state of the art telescope design. This has been done in existing GEO optical satellite systems ([Lapin, 1975](#)).

It can be observed from the data in Table 4.7 that for all tracking solutions the aperture diameters and observation wavelengths calculated are the same or higher for the same meteor, compared to their detection solutions. Faster meteors are usually better observable in the lower wavelengths, such as the ultra violet spectrum. The slowest meteor Met1Model is in both detection and tracking solutions best observable in the shortwave infrared, due to its lower velocity it heats up less on the surface and radiates more in the longer wavelengths.

The detection and 20 second tracking optical instrument parameters for the 2 sample return capsules were summarized in Table 4.9. From Table 4.9 can be observed that in both detection and tracking cases for both capsules a system with an aperture diameter of 10 cm and a focal length of 64 cm in the 1800 nm wavelength would be the smallest possible optical instrument.

Within those solutions the Hayabusa capsule can then only be observed using a 100 ms integration time, whilst for Stardust also a 1000 ms integration time can be used. Due to the bigger size of Stardust it allows for a smaller aperture to keep up the SBR compared to Hayabusa, which at 1000 ms needs a 29 cm bigger aperture to keep up the SBR above 0.1.

It was concluded in Section 3.1.6 that our heat flux model underpredicts the amount of luminosity generated by meteors compared to an empirical luminosity model by up till 900% ([Weryk and Brown, 2013](#); [Stokan and Campbell-Brown, 2015](#)). This underprediction means that our calculated apertures for meteors above 20 km/s are too big, since we use a lower amount of luminosity to calculate our apertures. Our calculated aperture diameters below 20 km/s are therefore too small, since our heat flux model overestimated the amount of luminosity by about 900% compared to the empirical luminosity. Taking into account Equation (2.37), a decrease of radiant intensity of factor 0.9 would result in also a decrease of the input power by 0.9. To keep the same input power the aperture diameter needs to be increased by factor 3.16. For an underestimated luminosity of maximum factor 9 the aperture diameter could be reduced by factor 0.32. These numbers are significant. However, if a constant luminous coefficient of 4% was used, like [Halliday et al. \(1996\)](#) does for

meteors above 10 km/s, our overpredictions would be at maximum 35%. In that case our aperture diameters would need to be increased by only 25%.

As a conclusion on the meteor luminosity, in further researches the temperature gradient and sublimation fraction for meteors should be reevaluated. For now the aperture diameters calculated for meteors at 11 km/s and 20 km/s should be larger by factor 1.25 to 3.16, and by factor 1.25 to 1.6 respectively. For meteors above 20 km/s the aperture is sufficient, but could be lower by up till 68%. Also depending on which luminosity coefficient model is used, the increase in aperture diameter at meteors below 20 km/s is at maximum 25%. In both cases all our determined tracking aperture diameters for the meteors except Met3Common would still be below 1 m aperture if increased by a worst case scenario factor of 3.16.

The influence of atmospheric windows, or rather the opposite atmospheric closed bands, plays a very important role. In all calculations for the GEO optical instrument parameters, the closed atmospheric windows are the most favorable. For an object the amount of radiation that is blocked is subject to the altitude, since that determines how much atmosphere is in between the object and the observer (Murcray et al., 1965). In our simulations it is set to 20 km altitude, and for most objects thus an overestimation of the amount of atmosphere in between the object and the observer, leading to bigger apertures than actually needed.

The combination of overestimating the amount of atmosphere in between the observer and the object, and the possible underestimation of the transparency of the atmosphere must be kept in mind with the shown results. For example, a difference of 15% in atmospheric transparency at wavelengths 1000 nm to 1200 nm, lead to an increase of 3% in aperture diameter for the SNR limited detection solution for Hayabusa at 0.1 ms.

### 5.2.2. Tracking Observations and Extractable Data Thereof

From the found tracking solutions it is interesting to look at how much observations/exposures can be made per tracking run of each of the 7 discussed objects. The optical instrument parameters found for the tracking of the 5 meteors and 2 capsules in Tables 4.7 and 4.9 are gathered and presented in the first 6 columns of Table 5.1. In the other 6 columns the specific tracking parameters are shown, which are explained next.

The pixel ground resolution  $X$  is taken from the optical instrument parameter calculations done before. The velocity of an object at time of observation  $V_{obj}$  is taken from the re-entry simulations. The velocity of the object in amount of pixels  $V_{pix}$  is obtained by dividing the velocity  $V_{obj}$  by the pixel ground resolution  $X$ . With the known integration/exposure time  $T_i$  and read out time  $T_{read}$ , taken equal to 500 ms (Appeah, 2017), the amount of pixels crossed by the object per observation/exposure  $N_{obs}$  and observation readout  $N_{read}$  are determined. Thus  $N_{obs}$  is the amount of pixels that will be lit up by the object and  $N_{read}$  is the amount of empty pixels between two consecutive observations of the object. The amount of observations/exposures that can be made in the tracking time "Obs" is calculated by assessment of the amount of integration times with read out times in between them can be fitted in the set tracking time. Finally the amount of pixels crossed during the whole tracking  $N_{track}$  is obtained by multiplying the pixel velocity by the tracking time. So  $N_{track}$  says something about how big the pixel array has to be in order to observe the object during the whole tracking time.

Table 5.1: Table of all objects and their tracking observation numbers. Readout time is 500 ms (Appeah, 2017). Given are tracking time  $T_{track}$ , aperture diameter  $D$ , focal length  $f$  observation wavelength  $\lambda$ , pixel ground resolution  $X$ , velocity of object at time of observation  $V_{obj}$ , velocity of object in amount of pixels  $V_{pix}$ , number of pixels crossed per observation/exposure  $N_{obs}$ , number of pixel crossed during read out of the data in 500 ms  $N_{read}$ , the number of observations/exposures made during the set tracking time "Obs" and the number of pixels crossed during the whole tracking of the object.

Object Name	$T_{track}$ [s]	$D$ [m]	$f$ [m]	$\lambda$ [nm]	$T_i$ [ms]	$X$ [m]	$V_{obj}$ [m/s]	$V_{pix}$ [px/s]	$N_{obs}$ [px]	$N_{read}$ [px]	Obs [-]	$N_{track}$ [px]
Met1Model	5	0.13	0.64	2500	1000	2000	6470	3.24	3.24	1.62	3	16.2
Met2Rate	5	0.13	0.64	2500	1000	2000	11755	5.88	5.88	2.94	3	29.4
Met3Common	5	1.72	9.55	1800	100	112	8967	80.06	8.01	40.03	9	400.3
	2	0.87	5.08	300	10	42	8967	213.5	2.14	106.75	4	427
Met4V&V	5	0.1	0.64	1800	10	2000	9733	4.87	0.05	2.44	10	24.35
		0.1	0.64	1800	100	2000	9733	4.87	0.49	2.44	9	24.35
		0.1	0.64	1800	1000	2000	9733	4.87	4.87	2.44	3	24.35
Met5Pers	0.7	0.22	1.3	300	10	164	36594	223.13	2.23	111.57	2	156.19
Hayabusa	20	0.1	0.64	1800	100	2000	9736	4.87	0.49	2.44	34	97.4
Stardust	20	0.1	0.64	1800	100	2000	10833	5.42	0.54	2.71	34	108.4
		0.1	0.64	1800	1000	2000	10833	5.42	5.42	2.71	13	108.4

Important is to understand that the tracking observation numbers presented in Table 5.1 are an approximation. For example at the moment of observing Stardust, the capsule goes at about 10.8 km/s, 10 seconds

before that it went about 12 km/s and 10 seconds after about 8 km/s. This means that the just found number of pixels, in a streak of a 1000 ms exposure, is equal to 5.42 pixels and will be a bit longer at the beginning of the tracking, and a bit shorter at the end of tracking. The difference in velocity is about 20%, therefore at the beginning the streak will be more in the range of 6.5 pixels and at the end of tracking more in the range of 4.4 pixels.

The amount of pixels crossed per observation/exposure of Hayabusa is for its global minimal aperture diameter, unlike the other objects, smaller than one pixel, as can be observed in Table 5.1. This makes Hayabusa harder to distinguish from other phenomena, which will be discussed later, such as lightning strikes, which typically are visible in 1 pixel. Hayabusa has the advantage of being tracked for 34 observations, and thus the line through these 34 observations can be used to exclude it as lightning strikes.

With Table 5.1 it is also possible to do an estimation on how accurate the velocity and location of objects can be determined. Lets analyze for example Met4VV. The pixel ground resolution is 2000 m, and our 1000 ms observation leaves a streak  $N_{Obs}$  of 4.87 pixels. This is in between 4 and 5 pixels. This means that we know that the object went in between  $4 \times 2000 = 8000$  and  $5 \times 2000 = 10000$  m/s. The estimation is thus at maximum 2000 m/s off. Lets now look at the 100 ms integration time. The number of pixels crossed during the 100 ms exposure is 0.49, which is in between 0 and 1. Therefore, taking into account the exposure time of 100 ms, the object must have gone in between  $0 \times 2000 = 0/0.1s = 0$  and  $1 \times 2000 = 2000/0.1 = 20000$  m/s. The estimation is thus a factor 10 more off. The pixel ground resolution and integration time are thus determining the accuracy of our velocity estimate. The maximum error can be calculated by dividing the pixel ground resolution by the integration time in seconds, leading to a m/s value. This means that the Met3Common 100 ms observation would give the lowest velocity error of maximum 1120 m/s.

In the just described velocity estimation method the amount of brightness of each pixel has not been taken into account. The brightness of the beginning and end pixel of each observation might be a fraction of the brightness at the middle of the streak. Looking at the fraction of brightness in the beginning and end pixel might tell something about how long the object was in those pixels, assuming an almost constant brightness over 1 exposure. This depends on the dynamic range of the pixels, which has not been assessed in this research (Wertz and Larson, 2010).

The discussed velocity determination also does not take into account the multiple observations made of one object. Multiple observations can all together also be used for a velocity estimation by fitting a curve through the middle points of all streak observations, leading to an estimation.

All in all, it can be concluded from Table 5.1 that all objects, except Hayabusa, can be observed in multiple pixels per exposure time. Next tot that, their velocity can be estimated per streak with an error equal to the pixel ground resolution divided by the integration time. This velocity determination is not better than done in other Earth based observations, which is usually in the range of a few 100 meters (Halliday et al., 1996; Jacchia et al., 1967).

### 5.2.3. Integration Time, Ground Resolution and Bandwidth Interactions

The integration times and ground resolutions used in this research have impact on each other, due to their coupling through the SNR and SBR. From the results and methodology the interactions can be identified. This is important to understand why bigger apertures are found in transparent atmosphere bands.

#### Integration Time

The integration time on its own has a big influence and has an effect, in the current state of the code, on the SNR only. If the object crosses less space than the ground resolution in one exposure, the SBR becomes less, see Figure 5.1.

The fact that the SBR does not change for exposures in which the object stays within the pixel, is due to the fact that with changing integration time  $T_i$  changes the amount of power  $E$  reaching the detector from the object or background by the same amount, see Equation (2.38). The procedure to get the amount of signal electrons from the background and object follow the exact same path via Equations (2.39) to (2.42). With the amount of usable electrons the SBR can be calculated in Equation (2.44). Thus the SBR's numerator and denominator are influenced by the integration time in the same way.

When the object crosses multiple pixels in one exposure, background photons are collected through the whole exposure time. Meanwhile, only object photons are captured in one pixel when the object is in the pixel. Thus for bigger exposure times than where  $V_o \times T_i$  matches the pixel resolution, the SBR drops.

The SNR increases with increased integration time, since the amount of photons of the object increase proportional to the increase in integration time  $T_i$ , see Equation (2.38). Meanwhile, the noises in the denom-

inator increase only by the square of the increased amount of photons of the object and photons together, see Equation (2.43). This denominator value increase is smaller than the numerator increase, and thus the SNR increases.

In case the object crosses multiple pixels in one exposure, background photons are collected through the whole exposure time. However, only the square of that amount is of influence on the decrease of the SNR. Meanwhile, only object photons are captured in one pixel when the object is in the pixel. Therefore, the SNR decreases slower again than the SBR when the object crosses more than 1 pixel per exposure time.

### Ground Resolution

The ground resolution changes and aperture diameter increases also have an interesting coupling regarding the background power reaching the detector. Decreasing the ground resolution  $X$  for example by factor 2, increases the aperture diameter  $D$  by factor 2 as well, as can be observed from combining Equations (2.30) and (2.31). Assuming then for easiness  $X = Y$ , the amount of radiant intensity calculated via Equation (2.34) reaching the detector from the background is reduced by 1/4. Putting the 2 times increased aperture diameter and the 1/4th of the radiant intensity in Equation (2.37) then leads to no change in the amount of background power reaching the detector.

The amount of power reaching the detector from the object for changing pixel ground resolution is different. Decreasing the ground resolution  $X$  again by factor 2, has again the same impact on the aperture diameter  $D$ , which increases by factor 2. However, the amount of radiant intensity of the object does not change, since it is no function of the ground resolution for small exposure times, see Equation (2.35). The object stays still within the same pixel even though the pixel ground resolution has been changed. This together means that with the lower pixel ground resolution only the aperture diameter in Equation (2.37) has increased by factor 2, and thus 4 times more power is obtained from the object. With the same amount of background power, the SBR has increased, as well as the SNR. See Figure 5.2.

When the exposure times are of such values that the object is indeed not the whole exposure time in one pixel, due to the decrease in pixel ground resolution, the radiant intensity of the object does decrease. This is then equivalent to the fraction of how much of the original trajectory the object is now in the pixel. Thus in case of a reduction of the ground resolution  $X$  by factor 2, the object's trajectory in 1 pixel for the same integration time is also reduced by factor 2. This leads to half as much radiant intensity in that pixel, and thus in Equation (2.37) leads then to 2 times more power instead of 4 times more power as before. This shows that the SNR always increases with smaller ground resolutions. Again, with the same amount of background power, the SBR has increased, as well as the SNR.

### Detector Bandwidth Influences

Next to the discussed ground resolution and the integration time, the bandwidth of the detector has an influence on the SNR mostly. See Figures 5.3 and 5.4.

A smaller bandwidth means of course that less overall photons are collected, and the SNR is overall lower ( $\frac{x}{\sqrt{x}}$  gets smaller when  $x$  decreases), see Equation (2.43). Therefore, as has been discussed in Section 4.3.1, the SNR's are mostly lower for smaller bandwidths.

However, there is an exception. This exception has to do with atmospheric windows and closed bands. An atmospheric window is defined as very transparent wavelengths in the atmosphere, and closed or opaque bands are defined as the wavelengths where the atmosphere is not very transparent, typically below 10% transparency.

If the chosen observation bandwidth is large enough that it overlaps over a closed and open band, the solution is, if assumed the same size for the bands, the average of the two. In this case if the bandwidth is

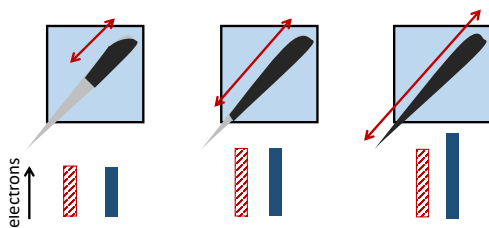


Figure 5.1: Effect of increased integration time. Red striped electrons are from object, blue from background pixel.

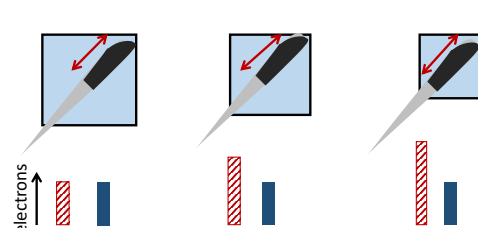


Figure 5.2: Effect of reduced pixel size. Red striped electrons are from object, blue from background pixel.

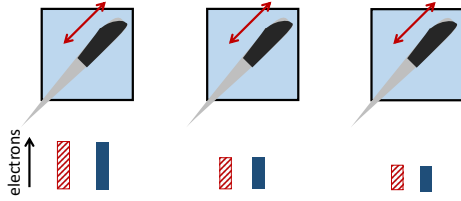


Figure 5.3: Effect of reduced bandwidth in an equal transparent atmosphere. Red striped electrons are from object, blue from background pixel.

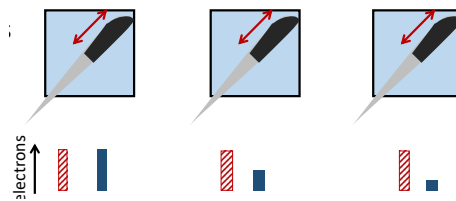


Figure 5.4: Effect of more opaque atmospheric windows at the same wavelengths. Red striped electrons are from object, blue from background pixel.

reduced and now only overlaps over the closed band, the SNR could be increased, depending on how strong the object was compared to the background and how much readout noise there was. The opposite is also true, the SNR could greatly decrease if after bandwidth reduction it only overlaps the open band, meaning now more background photons are captured compared to the average, and thus the SNR has decreased. This means that the bandwidth is very important and also the location of this bandwidth. The best would be if it overlaps at the wavelengths where the atmosphere is the most opaque.

Again this stresses out how important a good atmospheric transmission model is. So an as broad as possible bandwidth is desired with an overlap over just a closed band, such that from the object as much as possible photons are collected, but not from the background. This increases both the SNR and SBR. A high SBR is also possible with a very small bandwidth over a closed atmospheric band, the big as possible bandwidth is just desired for high SNR. See Figures 5.3 and 5.4. These both reduce the aperture needed, which is favorable for the satellite design.

#### 5.2.4. Difference between Day and Night Observations

An important aspect that needs to be addressed is the difference in day and night observations. Night observations in this case classify as an observation of Earth made where the Sun does not shine on the surface behind the to be observed object. With day time observations, the opposite is true, the Sun shines on the Earth surface behind the to be observed object.

It is important to stress out that the results that have been presented before are restricted to daylight observations. In daylight observations the aperture is not just restricted by the amount of energy reaching the instrument from the object and the thermal radiance of the Earth, but also by the amount of reflected sunlight coming from the background. The amount of photons of the background can not be more than a fraction for which the object can still be distinguished from the observed background in an observation. In night time observations this reflected sunlight is not present, and therefore the same or smaller apertures can be expected. Smaller apertures can be expected since the amount of background noise and background signal electrons are reduced, thus increasing the SBR and SNR and allowing for smaller apertures.

As an example to show the difference between day and night observations a simulation was run for Hayabusa, with a targeted SBR=0.1 and an arbitrary 2 second tracking time. The results for the optical instrument parameters aperture diameter, focal length, SNR, SBR and ground resolution are shown in Figure 5.5.

In the night observations, see Figure 5.5a, only the thermal irradiance of the Earth is taken into account and the reflected sunlight is omitted. The fact that the aperture diameters are still bigger than 10 meters in the Ultra violet band is due to the fact that Hayabusa does not emit enough radiation in that band to adhere to the desired SNR of 3. In Figure 5.5a can also be observed that the long-wave infrared solution is solely determined by the thermal infrared of the Earth (especially visible between 4500 nm and 5000 nm). The sunlight plays no significant role here (the solutions are in both cases almost the same for high mid-wave and long-wave infrared > 4000 nm).

Night time observations are, of course, not the worst case scenario. For day observations of Hayabusa, see Figure 5.5b, it can be observed that the solution is almost the same above >4000 nm. A small increase in aperture is needed to make up for the reflected mid-wave and long-wave infrared coming from the Sun. At and below shortwave infrared the day time observations are significantly different for most wavelengths. This is due to the reflected sunlight. It can be observed that in any case the night time calculated aperture diameters are smaller or equal to the day time calculated aperture diameters. This is also true for the focal-length and SNR; the focal-length is always directly proportional to the aperture diameter and the SNR is

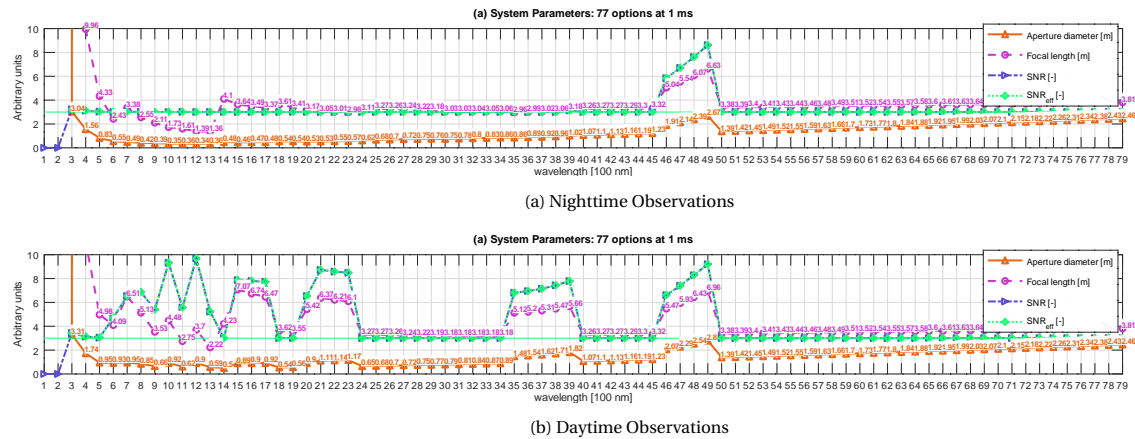


Figure 5.5: Two second tracking instrument parameter solutions for Hayabusa for day and night time observations, with desired  $SBR \geq 0.1$  and  $SNR \geq 3$ .

always bigger in the night for the same object due to less photo noise electrons being generated, due to the lack of background signal.

Therefore, when the daylight observations conditions are met it is automatically also true that the nighttime observation conditions can be met.

### 5.2.5. Telescope Limitations and Unaccounted for Detector Characteristics

The found optical instrument parameters within this research are not sufficient to design a full optical instrument. No detector sizes have been calculated, no distinction between effective and physical focal length has been made, no other readout times than 500 ms have been investigated, and full well capacity, dark current and dynamic range have not been addressed. These limitations will shortly be discussed below.

It might be the case that detector sizes needed to observe for example the whole Earth for a given aperture diameter and focal length, might be bigger than the aperture diameter itself. When the detector needed is bigger than the calculated aperture diameter, the optical aberrations might become large (Giancoli, 2009). Therefore, it is assumed that detector sizes are at maximum about 1/4th the size of the clear aperture diameter, which is derived from the maximum allowable secondary mirror diameter, if used<sup>1</sup>. For refracting telescopes the detector size might possibly be bigger, but for now 25% of the aperture diameter is assumed as a limit.

A secondary mirror would block some of the light into the primary mirror. With the assumption of the secondary mirror having a aperture diameter of 25% of the main aperture diameter, this blockage would be about 6.25%. Using this knowledge, our found aperture diameters should be increased by about 3.1% to make up for this blockage. For our found tracking aperture for Hayabusa of 10 cm, this would mean an increase of about 3 mm, almost negligible. For the biggest sub 1 meter aperture found of 87 cm, this would mean an increase of 2.7 cm. This last value is not negligible, but poses no large changes in the aperture diameter.

Ways to address the problem of a bigger detector needed than the aperture is using a smaller detector area which is feasible, and then either use moving/scanning mirrors or the whole instrument or use multiple small optical instruments if the size allows for it. Both options are used in the Meteosat 1st/3rd Generation (Aminou, 2002), for the Lightning Imager and the Flexible Combined Imager<sup>2</sup>. The Lightning Imager uses 4 copies of the same instrument to view the whole Earth, and the Flexible Combined Imager scans the whole Earth. The GOES-16 Lightning Mapper is however a full disk instrument (Goodman et al., 2013; Jenniskens et al., 2018).

To reduce the physical focal length to a size that fits better within a satellite, reflector telescopes can be used such as a three-mirror Anastigmat or a Cassegrain telescope (Everett, 1993). The first one is used on the James Webb telescope and reduces the focal length from 130 m to sub 10 m physically<sup>3</sup>. A Cassegrain usually

<sup>1</sup>"Astronomical Optics. Part 2: Telescope & Eyepiece Combined" handprint.com <http://www.handprint.com/ASTRO/ae2.html> (Accessed February 26, 2019).

<sup>2</sup>"MTG Design" eumetsat.int <https://www.eumetsat.int/website/home/Satellites/FutureSatellites/MeteosatThirdGeneration/MTGDesign/index.html> (Accessed February 20, 2019).

<sup>3</sup>"Webb Vital Facts" jwst.nasa.gov <https://jwst.nasa.gov/facts.html> (Accessed February 26, 2019).

reduces the focal length needed by 3-15 times<sup>4</sup>. For a satellite system an advanced reflector (mirror) optical system is almost always a must, such to reduce aberrations and physical sizes to make it able to be launched at lower cost or even to fit within the fairing of a launch vehicle. Using lenses is unfeasible for bigger apertures and is much more heavy (Giancoli, 2009).

As stated before, no other readout times were addressed other than 500 ms (Appeah, 2017). However, a readout time of 500 ms is quite determining on how much exposures can be made during the tracking of objects. For the performed analyses in Section 5.2.2, it only determines the pixel gaps in between two exposure observations and thus the amount of observations made in a tracking run. When the readout time gets lower, the pixel gaps get smaller. It is almost in any case advantageous to have a small readout time, since more observations can be made. Especially for use in a scanning device or the observation of fast meteors this is an advantage. A scanning device will have to make multiple pictures in succession of different areas. For meteor observations this might be very limiting in getting pictures of the same area within a small time scale w.r.t. the duration of the meteor. However, the read out time is usually restricted by the detector used.

The full well capacity has not been accounted for in this research. The full well capacity dictates how much electrons can be captured in a single pixel. Usual numbers for the full well capacity are in the order of tens of 1000ths of electrons. For short integration times and small apertures this does not necessarily play a limiting role. However, at very high integration times and very big apertures many electrons can accumulate in the pixels. In a case the full well capacity is exceeded, it means that the pixel is overexposed, and it reaches the maximum value and cannot accumulate more. The reaching of the full well capacity can lead to the SBR requirement of 0.1 being useless, in case when the background itself is already over exposed. Each neighboring pixel has than the maximum value and can not be distinguished with or without object.

Dark current is a noise that, just like the read-out noise, comes from the chosen detector, and has not been accounted for in this research. Usually some electron noise is introduced in the system by just being active, this means that as long as the detector is working an amount of electrons per pixel per second are leaked into each pixel. This again, has most influence on higher integration times (Appeah, 2017). Some of the instruments listed in Appendix A have them listed in their specs and values 300 to 0.0005 electrons/pixel/s are not unusual. Due to this non-included effect, errors are introduced, especially in the atmospheric closed bands which are of interest for the object detections. For 1000 ms exposure times this means that either way 300 or less than one electron should be included as dark current, which would decrease the SNR. Although, looking at Figure 4.8 the SNR was not the limiting factor at the 1000 ms integration times, but rather the SBR. However, from this figure can not be determined how much electrons were collected from the object. Therefore, it can not be ruled out that the SNR would have become limiting or insufficient.

### 5.3. Other Interesting Observable Phenomena

More interesting phenomena and objects can be observed from GEO that might interfere with our desired observations of meteors and capsules. An interesting problem is the classification problem that comes with this.

Since the temperature profile per time is not known of those objects, a tracking solution can not be found adequately. The detection optical instrument parameters could be calculated for a given temperature or luminosity if those are given.

Both the detecting instrument parameters of those objects and the classification methods will not be addressed in particular. The information shown in this section is more a starting point for such analyses in the future. The information should be taken into account when designing a satellite system for the detection and tracking of meteors and capsules treated in this research. A few of the possible other observable phenomena and objects are discussed briefly.

#### 5.3.1. Space Debris

Space debris has been tried to be simulated with the written simulator, without any meaningful and accurate results. This is partially the case since our re-entry simulation code is not advanced enough to take into account important situations and effects, like tumbling, multiple material ablation and different shapes than spheres. However, these objects are still of interest, and could definitely be detected by systems discussed in this research. For example the Hayabusa spacecraft had a magnitude of about  $-10$  to  $-12$  at some point (Ohkawa et al., 2012), this means it should be detectable by systems similar to systems that can detect

<sup>4</sup>"Cassegrain Formulas and Tips by Mike Lockwood" loptics.com [http://www.loptics.com/ATM/mirror\\_making/cass\\_info/cass\\_info.html](http://www.loptics.com/ATM/mirror_making/cass_info/cass_info.html) (Accessed February 26, 2019).

met4V&V. Since all the other meteors have a fainter absolute magnitude, the systems designed to detect those should also be able to detect and track the Hayabusa Spacecraft.

The Automatic Transfer Vehicle 3 (ATV-3) and H-II Transfer Vehicle 3 (HTV3) re-entries have been analyzed in the past. From both those re-entries only the HTV3 re-entry was controlled. Both vehicles re-entries were recorded using a Reentry Breakup Recorder (REBR), which is a small capsule of about 36 cm in diameter, quite similar in size to the Hayabusa capsule (Ailor et al., 2013).

The maximum stagnation heat flux was estimated to be about  $750 \text{ kW/m}^2$  during the ATV re-entry, but later in the trajectory the front of the vehicle experienced heat fluxes in between  $50 \text{ kW/m}^2$  and  $350 \text{ kW/m}^2$ . The maximum external (shockwave) and internal temperatures reached were about 15,000 K and 1300 K respectively. But temperatures of 3000 K, where perforation of the body starts, have been estimated as well (Boutamine et al., 2007). This puts the ATV's temperature in about a 150-350 K higher range than the two capsules investigated in this research, which have a surface temperature of about 2650-2850 K.

An interesting research has been done regarding re-entry and demise of propellant tanks, after an earlier research showed that propellant tanks totally ablate during re-entry, but afterwards still propellant tanks were found on land that had survived re-entry. Temperatures of about 850 K are reached by the re-entering propellant tanks from spacecraft (Lips et al., 2017). This means that they, if assumed that they have a radiating surface towards GEO of about 1 square meter, emit 25,900 W at maximum. This is, assuming a 1800 W reference luminosity, a  $-2.9$  absolute magnitude object. Which means that only a system able to detect a Met3Common meteor is able to detect such a small piece of space debris, which is about 0.43 m in the 300 nm wavelength band at 10 ms integration time.

Space debris is usually first orbiting Earth and therefore has relatively low entry velocities of 6.1 till 7.9 km/s, but might also come from interplanetary trajectories like the Hayabusa spacecraft at about 12.1 km/s. A luminosity of  $10^8$  has been observed with the Hayabusa spacecraft re-entry, but might be 4 magnitudes lower in case of, for example, empty propellant tanks. The duration of the burn up of Hayabusa was about 45 seconds, and propellant tanks have been simulated with temperatures above 800 K for 25 seconds (Lips et al., 2017; Ueda et al., 2011).

### 5.3.2. Space Planes

Space planes are in some way similar to ballistic vehicles, although they exhibit a directional control and have entries that take way longer to reach the destination due to their lifting capabilities. Local skin temperatures reach 1600 K (Zalameda et al., 2010), which under assumption of an observer facing area of  $1 \text{ m}^2$ , and using Planck's formula, would irradiate  $3.6 \times 10^5 \text{ W}$ . The orientation of space planes is usually belly down to Earth, with a possible large bank angle, and thus space planes do not irradiate much towards space in their almost zenith (Mooij, 2016). From Earth space planes, and in particular the space shuttles, have been successfully observed (Horvath et al., 2007, 2013; Tack et al., 2010; Zalameda et al., 2010).

### 5.3.3. Nuclear Detonations

SBIRS and DSP are capable of detecting nuclear detonations of at least 8 kt TNT, since meteors of such magnitude have been observed up till at least 40 kt TNT (Nemtchinov et al., 1995).

Since one kt TNT is equal to  $4.18 \times 10^{12} \text{ J}$ , this means that a meteor of at least  $3.3 \times 10^{13} \text{ W}$  would be visible. No meteor discussed in Section 4.1.1 has this magnitude, but Chelyabinsk at about 500 kt would be detectable (Popova et al., 2013a).

As for nuclear detonations, for example Little Boy, used during World War 2, had an explosion equivalent to 20 kt of TNT and would thus be visible. This means that, since 20 kt is more than 8 kt, that smaller nuclear detonations are definitely visible in similar systems to DSP, which has an aperture of 60 cm (Lapin, 1975). Only for meteor Met3Common an aperture diameter bigger than 60 cm has been identified, for tracking of 2 seconds of these kinds of meteors an aperture of 87 cm was needed, see Table 5.1. In such a system nuclear detonations will thus always be visible. Inversely, when nuclear detections would be needed to be detected, meteors could be observed. This problem has been proven as the start of this subsection, in which DPS has seen meteors (Tagliaferri et al., 1995).

### 5.3.4. Rocket Launches and Ballistic Missiles

Rocket and ballistic missile launches can be observed from space, this has already been proven by DSP and SBIRS for non-civil applications (Lapin, 1975). In such cases the plume of the rocket emits enough radiation that it can be observed from GEO. Typical values for rocket plumes seen under an angle of  $45^\circ$  are  $11 \times 10^6 \text{ W}$  at 15 km altitude,  $5.7 \times 10^6 \text{ W}$  at 60 km and  $9 \times 10^5 \text{ W}$  at 120 km (Kellogg and Passman, 1955). These values

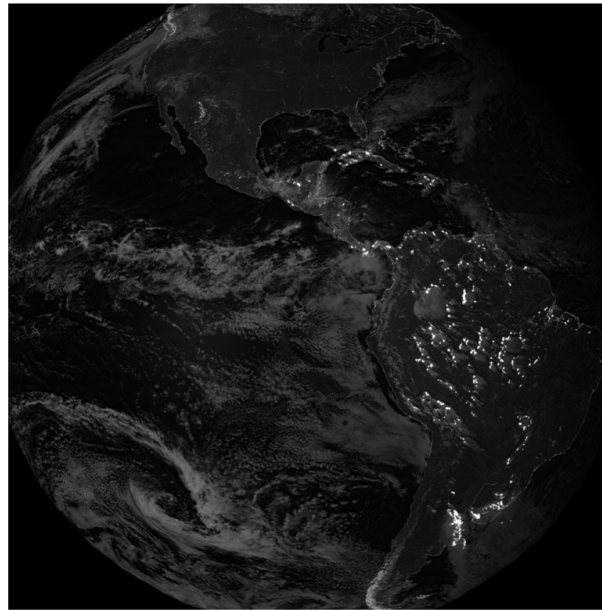


Figure 5.6: Example of a 20 minute capture (600,000 frames, on October 18, 2017, mostly daytime, 20:00-20:20 UTC) from the GLM on GOES-16 in the 777.4 nm near-infrared spectrum. Taken from [Goodman et al. \(2013\)](#).

are equivalent to meteors of absolute magnitude -9, -8.5 and -7 respectively, when comparing the values to meteor fingerprint values in Tables 4.1 and 4.2. This is then similar to meteors like Met2Rate, see Table 4.5, which means the rocket plumes should be observable from GEO with apertures of 13 cm in the 2500 – 2700 nm wavelengths at 1000 ms integration time. Of course systems that can detect fainter objects can detect this as well, like all but the met4VV systems.

The ascent of other ballistic objects and launchers could also be investigated, like DSP and SBIRS do ([Lapin, 1975](#); [Kellogg and Passman, 1955](#); [Everett, 1993](#)). A lot of heat is generated during the ascent phase, as well by both aerothermodynamics and the booster flame.

### 5.3.5. Lightning Strikes

Meteors of -14 absolute magnitude have been detected in the Geostationary Lightning Mapper (GLM) on board the GOES-16 weather satellite. It observes in a 777.4 nm wavelength (near infrared) at 500 Hz, 2 ms exposure time. It features a 1400x1300 pixel CCD, with a 8 – 12 km/pixel ground resolution, and about 20 – 30  $\mu\text{m}$  pixel size. The aperture diameter is 0.11 m with an f-number of  $f1.2$ , and the instrument has a view angle of about  $16^\circ$ , Earth full disk [Goodman et al. \(2013\)](#); [Jenniskens et al. \(2018\)](#). An example of an exposure is given in Figure 5.6.

The aperture diameter of the GLM is sufficient to track Met4VV, Hayabusa and Stardust, which needed a minimal aperture of at least 10 cm, see Table 5.1. The exposure time of 2 ms is too low for observing Hayabusa and Stardust, which both need at least a 100 ms integration time. However, Met4VV might be traceable since the 10 cm aperture diameter also is sufficient at an exposure time of 10 ms.

In order to avoid observations of these interfering with meteor observations from geostationary orbit, an option is to have such a long exposure time, that the lightning observations blend in with the background, i.e. their SBR drops.

This system is also capable of detecting meteors, which was proven by [Jenniskens et al. \(2018\)](#). In that research it was concluded that meteors with a brightness of at least -14 absolute magnitude could be detected with the GLM.

Based on our research, the GLM should be able to track Met4VV for 5 seconds with a peak absolute magnitude of -13.1 as well, given that the instrument can change the observation wavelength to 1800 nm. Interesting is that it should be able to track Hayabusa and Stardust in the 1800 nm wavelength for 20 seconds, although their peak absolute magnitude is about -5 and -6 respectively. The temperature profiles of the two capsules and meteor Met4VV, instrument facing area and tracking time have a lot to do with what "effective" absolute magnitude is observed by the instrument.

### 5.3.6. Classification Based on Fingerprints

Classification is of interest when observing multiple objects. Classification is possible in multiple different ways. Most common currently are the more complicated neural networks and machine learning methods. However, a simple decision tree may in some cases already be sufficient (Kotsiantis, 2007).

Based on the objects investigated in this research and the ones discussed in this section, a decision tree can be made. Different classification parameters could be velocity, luminosity, duration and size. A compilation of data found on these parameters of the different objects and phenomena are given in Table 5.2.

Table 5.2: Distinctive parameters of the objects that can, and should, be classified during their re-entry and/or observation phase where maximum luminosity is reached (Lips et al., 2010; Abe et al., 2011; Snively et al., 2014; Vojacek, 2011; Putnam and Braun, 2015; Jenniskens et al., 2018; Nemtchinov et al., 1995; Kellogg and Passman, 1955; Ailor et al., 2005).

Object	$V$ [km/s]	Luminosity [W]	Duration [s]	Traj. size [km]	Comments
Meteor	11 – 72	$100 - 10^{15}$	0.3 – 20	10 – 100	
Ballistic Capsule	7.2 – 12	$< 1.4 \times 10^6$	30 – 60	500	
Space Debris	6.1 – 7.9	$10^8$	30 – 45	1000	
Ballistic Missile	2.5 – 7.9	$100 - 400 \times 10^3$	40	20	
Space Plane	7.2 – 12	$3.6 \times 10^5$	120+	8000	Mind orientation
Lightning	0	$10^{12}$	0.03 – 0.2	8 – 190	
Rocket Launch	$< 7.8$	$< 11 \times 10^6$	150	100+	
Nuclear Expl.	0	$> 3.3 \times 10^{13}$	$< 10$	0.3	

The question is how these different parameters influence the optical parameters that have been calculated in this research. For example, the determination of an object's duration is limited somewhat by the integration time. Furthermore, the size of the trajectory has something to do with the ground resolution and total field of view. Determining the velocity has to do with integration time and ground resolution as discussed before.

Lets discuss how the two objects analyzed in this research can be distinguished, the meteor and re-entry capsule. From Table 5.2 can be clearly observed that the biggest difference is the duration and size of the phenomena. The velocity has a small 1 km/s overlapping range from 11 till 12 km/s. Above 12 km/s the object should always be a meteor according to the table.

Met4V&V and Hayabusa are taken as example of being observed at the same time. Since the solutions shown in Table 5.1 for both their tracking optical parameters were limited by the ground resolution equal to 2000 m, it actually means they should be able to be tracked longer than respectively 5 seconds and 20 seconds. Next to that, the absolute magnitude of met4V&V is  $-12$  and that of Hayabusa  $-5$  (Ueda et al., 2011). But, from Table 4.4 can be observed that a 200 kg meteor at 15 km/s would not last longer than about 9 to 14 seconds. This is anyway less than the duration of Hayabusa, and the tracking time of 20 seconds calculated for Hayabusa. Therefore, those objects can best be classified based on the amount of observations that are made.

## 5.4. Possible Satellite Systems Based on This Research

Based on all the results given in Chapter 4 and the just presented discussion and implications of all these results, a few systems can be identified that should be able to observe the selection of the addressed objects. The smallest apertures possible per object with their wavelength and integration time are given in Table 5.1.

From Table 5.1 three GEO satellite systems for tracking can be identified:

- **System 1:** An aperture of 13 cm with an integration time of 1000 ms at a wavelength of 2500 nm. This system would be able to track Met1Model and Met2Rate for 5 seconds at least.
- **System 2:** An aperture of 10 cm with an integration time of 100 ms at a wavelength of 1800 nm. This system would be able to track meteor Met4VV and both Hayabusa and Stardust capsules.
- **System 3:** An aperture of 87 cm with an integration time of 10 ms at a wavelength of 300 nm. This system would be able to track meteors Met3Common and Met5Pers.

Below each of the systems will be shortly addressed.

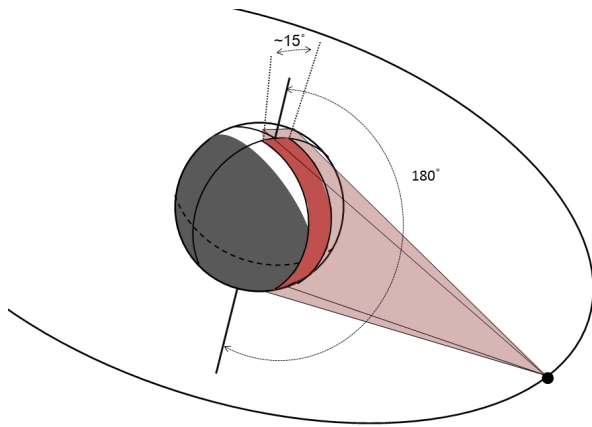


Figure 5.7: Possible design of a meteor diurnal, latitudinal and longitudinal influx model update satellite system.

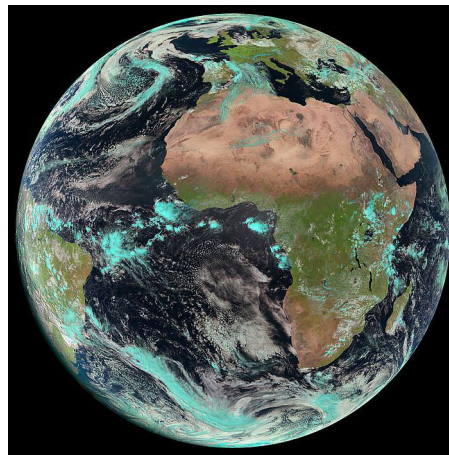


Figure 5.8: MSG view of Earth with Europa.

### System 1

System 1 could be used to update the diurnal and latitudinal model by Szasz et al. (2005) as proposed in Section 4.1.3. In order to update the model a telescope can be used with an aperture of 13 cm with an integration time of 1000 ms, operating at a wavelength of 2500 nm. A satellite could be designed to, for example, observe 15 degree wide longitude ( $360^\circ/24$  hrs) for over the total latitude range. With this then a meteor influx rate can be determined per hour of the day per latitude. See Figure 5.7.

First a field of view as seen in Figure 5.7 will be assumed for this system, meaning a observation angle of  $18^\circ$  by  $3^\circ$ . The 13 cm aperture and 64 cm focal length solution (f-number = 4.92) lead to an instantaneous pixel field of view of  $0.00269^\circ$  for this system. Thus an observation area of 6900 by 1150 pixels (24 Mpixel) would be needed to be observed, leading to a detector size of 20.7 cm by 3.5 cm, assuming a square pixel size of  $30 \mu\text{m}$  and no moving parts. This is on one side bigger than the aperture and this problem needs to be addressed somehow, since it is not feasible to have a side of the detector bigger than the aperture.

As explained in Section 5.2.5, it is assumed that the detector is at maximum about 25% the size of the aperture diameter, derived from the maximum allowable secondary mirror diameter<sup>5</sup>. Thus, for a 13 cm aperture diameter, the detector should not be bigger than 3.25 cm on any side. If multiple small telescopes with such a small detector are used, a matrix of 1 horizontal by 7 vertical, 7 telescopes of 13 cm aperture are needed. This would take up about at least 13 by 91 cm of space, not including any baffles of the telescopes. With a read out time of 500 ms, this system could make one picture of all latitudes in 1.5 second.

Another option is to use one of those telescopes and have a scanning mirror in front of the main mirror that sweeps across the latitudes of the Earth. With an integration time of 1000 ms, and a non baseline 30 ms readout time (<https://www.roperscientific.de/DualReadout.html>), and assuming a sufficiently fast scanning mirror, 7 pictures across all altitudes takes about 7200 ms. This would mean about 1 picture every 7 seconds of all latitudes of one given longitude camera. With a readout time of 500 ms, a full latitude scan takes about 10.5 seconds.

The last option with a scanning mirror needs way less space (1/7th) on the satellite itself, but involves the assumption of a faster read-out time and sufficiently fast moving scan mirrors, and produces not a lot of observations per meteor. Since the aperture diameters were determined based on a 5 second tracking time of the two meteors, see Table 5.1, the scanning mirror is not an option since it takes longer to make observations of the other areas than the tracking duration of the meteor. With the 7 multiple telescope setup about 3 observations can be made per meteor, wherever it enters within the field of view of the whole instrument.

With a satellite system such as the 7 telescopes with 13 cm aperture, a vast bigger and more accurate latitudinal variation model can be made, compared to the model of Szasz et al. (2005). First of all, no extrapolation is necessary over the whole Earth atmosphere based on selective sky observations. Secondly, also meteors not detectable with the radars used by Szasz et al. (2005), due to being non perpendicular to the instrument, can be observed.

<sup>5</sup>"Astronomical Optics. Part 2: Telescope & Eyepiece Combined" handprint.com <http://www.handprint.com/ASTRO/ae2.html> (Accessed February 26, 2019).

### System 2

Just to illustrate a problem regarding detector size, system 2 has a pixel pitch of  $30\ \mu\text{m}$ , pixel FOV of  $0.00269^\circ$  and ground resolution of 2000 m. If the whole Earth would be needed to be observed, which measures about  $18^\circ$ , a  $20.7 \times 20.7\ \text{cm}$  big detector would be needed. This is bigger than the aperture of 10 cm and is thus not feasible. As already discussed, options would be to use a scanning mirror in front of the telescope or use multiple telescopes with a smaller detector size.

The multiple telescopes would require a vast amount of  $7\ \text{by}\ 7 = 49$  telescopes, over an area of at least  $70\ \text{by}\ 70\ \text{cm}$ , not taking into account baffles of the telescopes. This is still a smaller area than a 1 m aperture diameter telescope.

However, it should be noted that capsules are not sporadic like Met4VV. Capsule re-entry locations are usually well known. So in case observations need to be made of a capsule re-entry from GEO, just 1 telescope with a scanning mirror that can scan the whole earth is sufficient. When a re-entry of a capsule is about to happen the telescope can be pointed at the location with a  $3^\circ\ \text{by}\ 3^\circ$ ,  $1150\ \text{by}\ 1150$  pixel, field of view.

A single scanning instrument with system 2 parameters would take, under assumption of 500 ms read out time and 100 ms integration time, about 30 seconds to scan the whole Earth. This is sufficient for one detection observation of Met4VV, Hayabusa or Stardust if the exposure is taken at the right time and the right place. The 30 second total Earth scan time of 30 seconds is namely bigger than the designed tracking time of 5 s and 20 s for Met4VV, and Hayabusa and Stardust respectively. The usefulness of such a system for meteor detection is thus questionable. If the read out time could be reduced to 30 ms, the whole earth can be scanned in 6.5 seconds, which would lead to at least 3 observations of the capsules, but again only one of Met4VV.

### System 3

System 3 has a pixel pitch of  $5\ \mu\text{m}$ , pixel FOV of  $0.000056^\circ$  and ground resolution of 42 m. A full field of view of the Earth would require a detector of  $1.6\ \text{by}\ 1.6\ \text{m}$ . This is 2 times bigger than the aperture diameter of the telescope. Adhering again to the 25% size limit about  $8\ \text{by}\ 8$  of these 87 cm aperture diameter telescopes are needed, which is unfeasible regarding the space they take up.

A single scanning system could be opted for. Taking about 64 images of 10 ms with a read out time of 30 ms would take about 2.6 seconds, which is definitely feasible. However, the 2.6 s is again more than the calculated tracking time of 2 seconds for Met3Common, and thus chances are that the meteor is not observed.

A middle ground could be that every 0.66 s a picture of the full earth should be made, such that for the 2 second tracking time 3 observations of the Met3Common are made. In 0.66 s 16 images can be made with system 3 optical instrument parameters. So 4 scanning telescopes of 87 cm are needed, which would take up about  $1.8\ \text{m}\ \text{by}\ 1.8\ \text{m}$  on the satellite. This is more than the desired maximum 1 m aperture diameter, however, it is an option in which faint meteors like Met2Rate can be observed 3 times in 2 seconds.

### Other Possible Satellite Systems

Other systems not discussed before are for example a ballistic vehicle re-entry detection system for a particular area, a system that detects meteors that usually lead into meteorite falls, a system that can supply data for trajectory determination of meteors, or a system that observes from GPS orbit at 20,000 km instead of GEO orbit.

A ballistic vehicle re-entry detection system like DSP (Lapin, 1975), could be used to detect if a certain area is prone to a re-entry of a destructive vehicle (Kellogg and Passman, 1955). When, for example, Europa needs to be observed for re-entering destructive ballistic vehicles an area of about 1/16th of the earth full disk needs to be observed, see Figure 5.8<sup>6</sup>. From Table 5.2 can be observed that a bright destructive ballistic vehicle has about the same luminosity as Hayabusa. Therefore, assuming a similar tracking requirement a 10 cm aperture diameter telescope could be used. Using the knowledge from System 2, this would then lead to about 4 of those telescopes needed to observe Europa in total. Assuming a 30ms readout time can be achieved, every 130 ms a full photo is taken of Europa in which the destructive ballistic vehicle would be visible.

It should be noted, that the re-entry takes at max about 40 seconds, and therefore the detection would probably be too late for cause of action. Therefore, usually destructive ballistic vehicle launches are tracked (Kellogg and Passman, 1955). Of course, also a bigger aperture could be used, allowing for a finer resolution.

A system made for the tracking of meteors which could lead to meteorite fall would need to be able to detect at least an absolute magnitude of about -6.5 (Halliday et al., 1996). A system like System 1 would

<sup>6</sup>"Meteosat Second Generation (MSG) Spacecraft Series" directory.eoportal.org. <https://directory.eoportal.org/web/eoportal/satellite-missions/m/meteosat-second-generation> (Accessed April 5, 2019).

be sufficient for that, but should be all Earth observing. Therefore, a big amount of 49 telescopes should be mounted on an area of about 1 m by 1 m to be able to satisfy these requirements. With such a system researches would track meteors with appreciable terminal masses of at least 100 grams ([Halliday et al., 1996](#)).

A total other satellite system would be able to determine the trajectory of meteors or capsules. For trajectory determination of meteors till now always at least 2 observation locations with sufficient spacing have been used ([Gural, 2012](#); [Koschny and Diaz del Rio, 2002](#); [Dmitriev et al., 2015](#)). Assuming this is also the case from space, at least 2 satellites are needed to determine trajectories of meteors, opposed to just the velocity based on streaks over multiple pixels or empty pixels between consecutive observations. This means a whole extra satellite needs to be launched.

The last possibility would be to do have a system observing from 20,000 km instead of 35,800 km. This would increase the amount of photons reaching the detector, however, it mainly has implications on the field of view, and the non-geostationary nature of the new orbit. Taking into account Equation (2.37), a decrease of the distance to the to be observed object of about 44%, would increase the input power by factor 3.2. This in turn would mean that 179% more photons reach the detector, from both the object and the background. Therefore, this lower orbit has no implications on the SBR, but increases the SNR. An increased SNR would allow for lower integration times.

One of the things to be analyzed is whether the trajectory can be determined in some fashion with only 1 satellite, opposed to the trajectory determination done for meteors based off of 2 separate observation stations ([Gural, 2012](#); [Koschny and Diaz del Rio, 2002](#); [Dmitriev et al., 2015](#))



## Conclusion and Recommendations

In this chapter the final conclusion and recommendations on the research are given in Sections 6.1 and 6.2 respectively.

### 6.1. Conclusion

A research on the detection and tracking of meteors and capsules observed from GEO has been presented in this report. At the beginning the topics of space debris and trajectory determination were still included, however, these were both dropped later in the research due to inability to validate the results and shortage of time respectively. Furthermore, in this chapter the answers to the research questions given in the introduction are answered. Answers are derived from the three chapters before, Chapters 3, 4 and 5.

- **What are the characteristics of meteors regarding their observability during re-entry and how well can this be simulated?**

First of all, meteor trajectories can be well simulated within a maximum error of 10% compared to other researches based on observations. The heat of ablation, heat transfer coefficient, temperature gradient and ablation fraction have a big impact on the outcome of the simulation. Next to that, fragmentation has been successfully implemented and is based on an independent wake model. For the bigger meteors, such as Forest Park and Chelyabinsk, the fragmentation model proved to be able to adequately reproduce the luminosity curve, but this required manual adjusting of the three fragmentation parameters initial strength, strength scaling parameter and amount of fragments per break-up.

The biggest problem with meteors is that based on observations not everything can be determined precisely. Therefore, determined masses based on observations do not readily reproduce the same light curve with this re-entry simulator as from the observations they were derived. For example, some trajectory data from other researches were derived by assuming straight meteor trajectories, which is in reality not the case, and is not assumed in our research either.

Another problem found was that our used heat flux model overestimated the amount of luminosity produced by meteors below 20 km/s, compared to the luminosity calculated with an empirical luminosity coefficient. This overestimation was about 900%. When another luminous coefficient was used, the overestimation was just 35%. Above 20 km/s the our model underestimated the luminosity by at maximum 900% compared to the empirical luminosity model. The cause for the overestimations is assumed to be the not used temperature gradient over the meteor surface. The cause for the underestimations is probably due to not taking into account the meteor trail, since when fragmentation is increased in our simulations the underestimation errors almost disappear. And heavy fragmentation would be similar to a dust trail. It need to be said that depending on which luminosity coefficient is used the overestimation could also be

Meteors exist over a wide variety of velocities and almost all thinkable masses; from micro grams to many tons. Their characteristic phenomena are that they fragmentate, happen randomly and have their maximum luminosity between  $5 \times 10^2$  W and  $2 \times 10^{11}$  W somewhere between 26 km and 70 km altitude. Meteors of less than 1000 kg have durations shorter than half a minute.

Based on our research every day between 3,000 and 250,000 meteors enter the Earth's atmosphere, between 0.1 gram and 1,000 kg. Our derived meteor influx rates are in between those of other researches.

In some cases our predicted influx rates are lower than other researches due to our higher predicted absolute magnitude for a given mass and velocity, due to fragmentation.

- **What are the optical instrument parameter values and detector settings needed for a GEO satellite system to detect and track meteors?**

The instrument parameters needed for observations of meteors are first of all determined by the requirement for day or night observations. Day time observations always need bigger instruments than night time observations, due to the reflected sunlight. The Earth's thermal radiance is always present in both cases. This also is true for the observation of re-entry capsules.

Aperture diameters needed for the detection of meteors during day time, at least the 5 sample meteors investigated in this research, ranging from -2.9 till -13.1 visual absolute magnitude, equivalent to about a luminosity of  $3 \times 10^4$  W to  $3 \times 10^8$  W, can be as small as 2 centimeters in the ultra violet up till about 43 centimeters in the shortwave infrared. The integration times needed, or detector settings needed, ranged for detection and tracking both between 10 ms and 1000 ms. Best wavelengths to observe meteors are the so called closed or most opaque bands in the atmosphere at 200-300 nm, 1800 nm and 2500-2700 nm. In these bands the background does not reflect back as much sunlight as in the open bands.

In order to make a distinction between different kind of objects, also called the classification of objects, requires enough information about each of those objects. With a simple one pixel observation, or as defined in this research as detection, not much can be said about the object. Therefore, the tracking mode was introduced, where the instrument parameters were calculated based upon a fraction lower than the maximum luminosity. This allows for longer or more observations of the object and thus enables to classify them.

As for classification a limiting factor is the very short duration of less than 1 second for some meteors. To be able to classify the short duration meteors, a short readout time and a short integration time are needed in the detector. This allows for at least 2 to 3 observations in the short duration of the meteor. With these multiple observations then the velocity and duration can be estimated. Furthermore, the ground resolution should ideally be small enough such that the length of the trail does overlap multiple pixels. Especially the duration and velocity play a big role in classification of objects.

Lightning strikes are a much occurring phenomenon with a high amount of power, however their duration is just less than a few milliseconds and they have no velocity. The lightning strike phenomenon is exactly why tracking is needed, to avoid meteor classified detection while actually those detections were lightnings strikes. The multiple observations in a straight line also lower the chances of the observations being a lightning strike.

The aperture diameters needed for 0.7 s till 5 s tracking of the 5 sample meteors, were in between 13 cm and 87 cm. Just as with the detection solutions, integration times were in between 10 ms and 1000 ms, and observation wavelengths at 200-300 nm, 1800 nm and 2500-2700 nm.

The errors induced by not including a temperature gradient and meteor dust trail in our heat flux model for meteors can increase the aperture diameter for meteors below 20 km/s by maximum 220%, and decrease the aperture diameters for meteors above 20 km/s by maximum 68%. When compared to another luminous coefficient the aperture should be increased by maximum 25%. All apertures calculated, except for the one of Met3Common, would still be below 1 m diameter in the case that our heat flux model is indeed not correct and the above corrections would be applied.

To update a meteor influx model of meteors like Met1Model and Met2Rate, a system of 7 telescopes with an aperture diameter of 13 cm each could be used, operating at a 2500 nm wavelength. This would allow for one observation per 1.5 seconds of an area equal to  $15^\circ$  longitudes by  $180^\circ$  latitudes. One single telescope of this size could also be used, with the use of a scanning mirror, but then only 1 observation per 7 seconds can be made. In the worst case that the overestimated luminosity for meteors is indeed increasing the aperture by 220%, this system could only be fitted in 2 cubic meter of space on a GEO satellite. 7 telescopes of 42 cm aperture would take up about that space. In case the increase of the aperture diameter is the only 25%, it could still be fitted in one cubic meter.

- **What are the characteristics of re-entry capsules regarding their observability during re-entry and how well can this be simulated?**

The peak radiation determined by this research happens in the near infrared wavelengths and their peak luminosity at about 50-60 km. Obviously is that the capsules do not fragmentate.

Sample re-entry capsule aerothermodynamics can be simulated with a maximum surface temperature error of 8% with the simulation program written for this research. Using information found on temperature gradients over the wet surface of the capsules and the amount of energy being taken away from the capsules by ablation, allowed for the correct determination of the amount of energy emitted by the capsule body. Furthermore, the trajectory of the Hayabusa capsule has been simulated with less than 0.3 km/s error at any point. With this, because of their similar size and shape, and the validated aerothermodynamics of Stardust, the trajectory of Stardust can be said to be simulated with high confidence in its correctness.

- **What are the optical instrument parameter values and detector settings needed for a GEO satellite system to detect and track capsules?**

Regarding the instrument parameters, apertures diameters of 10 cm are sufficient for both detecting and 20 second tracking of capsules. When the tracking is increased to 50 seconds, a 27 cm aperture diameter is needed for Hayabusa. The bigger size of the capsules compared to most of the meteors investigated means that they emit more radiation in general, and thus allows for smaller apertures than for most meteors. Furthermore, they have a more shallow luminosity profile. Re-entry of sample return capsules can be classified by their relatively long duration of about 30-50 seconds over a long range of about 500 km at a relatively low velocity of at maximum 12 km/s.

To observe and track re-entries such as the two investigated capsules over the whole Earth disk seen from GEO, a system of 49 telescopes with a aperture diameter of 10 cm each could be installed on a GEO satellite. The system would operate at a 1800 nm bandwidth. This system would allow for one observation of the whole Earth disk per 1.5 seconds in which a capsule like Hayabusa would be traceable. It is quite possibly so that these 49 small telescopes could be integrated in a space smaller than 1 cubic meter.

- **How does changing the detector settings or instrument parameters influence each other in general?**

Regarding the influence of the instrument parameters and detector settings onto each other, an increased integration time increases the total amount of electrons captured and does mainly increase the SNR. However, if the integration time is such high that the object is not the whole exposure time in one pixel anymore, the SBR will be reduced.

In case of reduced pixel size, the amount of background photons reaching the detector stays the same, however, due to the increased aperture that goes pared with the reduction of the pixel size, the amount of photons captured from the object increases, and thus the SBR and SNR increase. This positive effect is stopped when the pixel gets too small, the SNR will be reduced.

Reduction of the observation bandwidth will decrease the SNR, since less overall photons will be captured. The SBR would stay the same. However, this last statement depends on whether a change of bandwidth goes pared with a significant change in the observed wavelength atmospheric transparency. If the atmosphere gets more opaque in the total observed bandwidth this means that less background photons are captured and the SBR increases.

If a secondary mirror is used in the design of the telescope and a maximum size for it is assumed to be 25% of that of the main mirror, our found aperture diameters would need to be increased by 3.1%.

And with the above the main research question can be answered:

- **What are the typical optical instrument parameter values and detector settings needed to detect and track, meteors and capsules observed from GEO?**

Typical instrument parameters have been defined as aperture diameter, focal length, observation wavelength and bandwidth. The only adjustable detector setting is just one parameter, the integration time. Other detector parameters do not directly classify as settings, since they are detector bound, such as quantum efficiency and read out noise. In the determination of the optical instrument parameter settings the SNR and SBR are limiting values for the usefulness of such a system.

To detect and track meteors and capsules from GEO a satellite optical instrument smaller than 1 m is sufficient in most cases. The detection instrument parameter solutions lead to the smallest possible aperture for the observation of that object. But in case of tracking, is hugely dependent on the required tracking time. Low tracking times allow for smaller apertures, while higher tracking times leads to larger aperture diameters and generally shifts the observation wavelength to one of the opaque atmosphere bands of 300 - 400 nm, 1800 nm or 2500 - 2700 nm.

In general one should observe re-entering objects in Earth's atmosphere in the opaque atmospheric bands. The used observation bandwidth should match the bandwidth of the atmospheric opaque bands to capture as less as possible background photons. The object's photons are much less affected due to the object being above most of the atmosphere.

The integration time should be limited depending on the application of the optical instrument. Usually, the integration time should also be as long as possible, and theoretical equal to a value such that the object crosses exactly one pixel per exposure time. In that case, the object will give off as much as possible photons to one pixel, and only during that time the background is observed and not for longer, when the object has left the view of the pixel. In case of tracking, one might require the object to cross multiple pixels in one exposure to distinguish it from other phenomena and objects, then the atmospheric opaqueness is the most important to block as much as possible of the background radiation. On the other hand, for systems that must track fast and one wants as much as possible observations in the tracking time, the integration time, and read out time, should be as low as possible. This last option exhibits in most cases the observations from having streaks of the objects in the observations.

Typical aperture diameters for detecting meteors with absolute magnitudes between -2.9 and -13.1, at velocities between 10 and 59 km/s, are in the range of 2 cm to 43 cm. For 5 second tracking of 4 of the investigated meteors, the typical aperture diameters are in the range of 10 cm to 172 cm. The focal lengths for the last aperture diameter range given are in the range of 64 cm to 955 cm. A physical focal length of 10 meter is not feasible for on a satellite, and thus advanced telescope designs that could lower this length are needed. For both re-entry capsules the typical aperture diameters for 20 second tracking are 10 cm in size. Only at a tracking of 50 seconds, which is about as long as the re-entry of the capsules themselves, the aperture diameter needs to be larger at a size of 27 cm.

For 5 out of the 7 of objects investigated in this research it should be possible to track them with a GEO satellite system requiring less than 1 cubic meter of space on the GEO satellite.

## 6.2. Recommendations

In this chapter the recommendations based on this research are given. The recommendations are split up into how to update the current state of the research and into a section on what follow-up work can be done.

### 6.2.1. Possible Updates to This Work

The recommendations in this section are given in order to get more accurate and precise results compared to what was currently done. Due to time constraints, unavailability of data or lack of resources some of the things explained below could not be done.

The far most important recommendation is to address the errors in the heat flux model calculated luminosities for meteors. The overestimation of the luminosity for meteors below 20 km/s goes up till 35% to 900%. This overestimation means that the aperture diameters calculated in this research should be up 25% to 224% larger. To overcome this error a temperature gradient or more reduction by ablation should be investigated. The underestimation of the luminosity of 900% for meteors above 20 km/s is hypothesized to be due to not implementing a trail (McCrosky, 1958). Since, when increasing the fragmentation the luminosity switches to being overestimated instead of underestimated.

Secondly, it is recommended to use a better atmospheric transmission model. This research used a manually discretized atmospheric transmission model based on the NREL<sup>1</sup>. Maybe an interpolation between the data points provided by this model could be used, divided by the expected sunlight in that wavelength to get a better and non-discretized value for the transmittance at that wavelength. The importance of updating the atmospheric transmission is that it has direct influence on what the best closed wavelength band is to observe re-entering objects.

<sup>1</sup>"Reference Air Mass 1.5 Spectra" nrel.gov. <https://www.nrel.gov/grid/solar-resource/spectra-am1.5.html> (Accessed November 21, 2018).

Instead of an exponential atmosphere model as used in this research, the US standard atmosphere model could be used, which usually leads to lower (2-14 times) entry masses based on their observations, thus encountered less ablation. This suggests that with the use of such a different model the re-entry simulations done here will result in more terminal mass, deeper penetration in the atmosphere and less heat loads. Time and latitude dependent atmospheric model data can also be used, and will lead to more precise results. From other researches the best option is to use the time and latitude atmospheric models over the US standard atmosphere, and in turn use the US standard atmosphere over the exponential atmosphere (Lyytinen and Gritsevich, 2016). In this research the exponential atmosphere was used because of its easiness and still gives adequate results for the purpose of this research as has been shown in the verification and validation chapter. If the exponential atmosphere is used, the effect of different scale heights should be addressed. A higher scale height means a higher constant temperature. So when focusing more on the top of the atmosphere a lower scale height should be used corresponding with a lower temperature. However, the range of 7000 m to 8500 m for the scale height does leave some room for errors (Mooij, 2016; Putnam and Braun, 2015). Therefore, if continued to be used, the scale height should be investigated better.

Not yet implemented, are the influences of the reflectance and emissions of clouds and the off-nadir travel path of the photons through the atmosphere. Currently both effects are not incorporated. Clouds have a high albedo and might be present exactly under the to be observed object decreasing the SBR, also they have emissions themselves from re-radiated infrared. Furthermore, off-nadir observations observe objects that have more atmosphere in between it and the observer and thus more photons are absorbed, reducing the background and object signal.

Not only the albedo of the clouds should be investigated, but also the albedo of the surface of the Earth. A distinction between water and land should probably be investigated first, since water can reflect up till 100% of the sunlight if under small nadir angles. This would definitely mean that some re-entries can not be observed correctly due to the high background signal, if the Sun is almost directly behind the satellite observing above water. For that matter, the same holds for snow, since it has a very high albedo. But then again, on the equator where the GEO satellites will be, the chance for snow is low compared to higher latitudes.

A small effect that also has to do with albedo, is the reflected light of the Moon on the Earth's surface. Not expected to be much, since the Moon's albedo is not higher than average 13%, however it would be favorable to investigate the actual impact of it.

Regarding detectors updates are needed on the dark current, well capacity and quantum efficiency (Apeah, 2017). For larger integration times the dark current plays an important role in reducing the SNR. The well capacity plays an important role in long integration times and may in some cases exclude some higher integration times since the image will be over saturated. It is to be expected that both these effects are minimal on lower integration times. The quantum efficiency should be addressed as it not being a constant value but rather a changing value per wavelength. Most of these data can be found in figures, unfortunately not as usable data, so some discretization could be needed for that.

An assumption was made on how to calculate the average temperature of the wet surface of the re-entering objects. The change in area of the equally space rings here taken into account, and the true average temperature of the surface can indeed be found like how it is currently done. However, what needs to be investigated is how this effects the black body radiation calculated with just the average temperature. From the simulations and calculations it seems not to produce wrong values, but a proof for that has not been supplied in this research. So the question is whether the black body radiation should actually be calculated from each of those temperature rings, or that the average temperature gives also an adequate black body radiation profile. The difference could be that, since the stagnation point for example is way warmer than the average temperature, a lot more smaller wavelength irradiance is generated there. Maybe when the rings are small enough the sum of each of those rings does indeed form the same curve as just using the average temperature. The recommendation is thus to find proof or adjust the calculation such that the solutions from these calculations can be made with more confidence.

Regarding meteors the ion trains and dust trails should be investigated, next to just the head radiation (Cepelcha et al., 1998). This was already pointed out during the literature study performed preceding this research. It has been proven that the particle trail can be brighter than the meteor head itself (McCrosky, 1958), depending on the particle sizes. Ion trains might increase the visibility in very specific wavelengths, however these can be rather distinct for some meteors and are fairly faint (Beech, 1987; Jenniskens, 2014). The addition of these phenomena might be rather complicated, but might, especially for the trail, give a better estimation of the meteor's length and magnitude. A sputter model was also investigated and looked very promising, but has not been implemented (Stokan and Campbell-Brown, 2015).

The last proposed update is to do the meteor fingerprints with a computer with more memory. During the research the laptop used (with 8GB) of RAM, crashed multiple times, because it overflowed with data. The problem with the simulation was that, the termination conditions of minimal mass ( $10^{-9}$ ) or minimal altitude (10 km) were only reached after very long time, leading to more than 12,000 data points and crashing the computer. To avoid this each meteor discussed had its termination conditions tweaked. This however, leads to some wrong values in the duration of meteors, since sometimes it was still emitting enough light but the propagation was terminated, before that.

### 6.2.2. Follow-up Work

The recommendations provided now are for follow-up work and to extend this research into more areas or other uses.

First of all, the addition of space debris would bring this research back to its intended state. Unfortunately during the research, the simulation of space debris seemed rather complicated and could not be verified using ATV (Lips et al., 2010), HTV (Ailor et al., 2013) and propellant tank data found in other researches (Lips et al., 2017). The most probable cause for this is the different materials existing in space debris objects, where meteors can be assumed to exist out of one material and capsules only are in contact with the airflow with one kind of material. Space debris can mean a whole satellite existing out of multiple materials, or a propellant tank with a outer layer of carbon fiber and inner tank of aluminum. The current model assumes one spherical, solid and homogeneous object. For space debris these assumptions are usually not adequate. Furthermore, tumbling and odd shaped objects can not be simulated yet with the current re-entry simulator. These two aspects should be incorporated as well, although odd shapes are more needed than the tumbling, since some space debris can be de-orbited partially attitude controlled (Geul et al., 2018). A small adaptation to the current fragmentation model used for meteors could be investigated for space debris and is expected to give better results than non-fragmentating.

What was not possible, and not aimed for, in the current research is to implement a genetic algorithm, machine learning or other optimization process to find the absolute optimum. With the input parameters such as integration time, observation bandwidth and wavelength, an algorithm could find the most optimal system which is not possible in the current research due to the vast parameter space.

If trajectory determination would be needed to be implemented somehow, the re-entry simulation should be rewritten into a 3 dimensional simulation. An adequate trajectory would also be determined into 3-D. In order to verify and validate the working of a new designed tracking system, the 3-D trajectory could be used to check the determined 3-D trajectory from observations.

Spectroscopy has been named in the literature study, but not further investigated. Spectroscopy could be used to classify objects better, even at a very bad resolution it could already be helpful to identify if some materials are burning up which are only present in certain kinds of objects.

# **Appendices**





## Data on Different Detector Sensors

Not all detectors shown are space qualified, but most of them just serve for a way to estimate what should be possible. Usually space qualified hardware is not at the same efficiency levels as non-space qualified hardware.

Table A.1: Some detector parameters found, that give insight in what some typical values are for certain spectral bands. Detectors with a dot have their values used in this research.

Name	Manufacturer	Range [nm]	Pitch [ $\mu\text{m}$ ]	Resolution [px]	noise [ $e^-$ ]	$T_i$ [ $\mu\text{s}$ ]	QE [%]	Source
•CM-140GE-UV	JAI	200 - 1100	<b>4.65</b>	1392x1040	-	61 - 32000	70 (vis), <b>40</b> (uv)	<a href="http://graftek.biz">graftek.biz</a>
•C10600-10B	Hamamatsu	300 - 1050	<b>6.45</b>	1344x1024	<b>6 - 10</b>	10 - 70min	<b>55</b> (vis)	<a href="http://graftek.biz">graftek.biz</a>
•Mini SWIR JS	Senors Unlimited	900 - 1700	<b>12.5</b>	1280x1024	<b>75</b>	27 - 32000	<b>65</b> (nir)	<a href="http://sensorsinc.com">sensorsinc.com</a>
35MMFHDXM	Canon	370 - 730	19	2160x1200	10	-	55 (vis)	<a href="http://ioa.s.u-tokyo.ac.jp">ioa.s.u-tokyo.ac.jp</a>
•PIRT1280A1-12	Princeton IR Tech	400 - 1700	12	1280x1024	<b>45</b>	50 - 2min	20 (vis), 65 (nir)	<a href="http://princetonirtech.com">princetonirtech.com</a>
LSST sensor	-	X - 1000	10	4kx4k	10	16s	80 (vis)	<a href="http://lsst.org">lsst.org</a>
BIRS sensor	Senors Unlimited	1700 - 2000	25	640x480	-	-	-	( <a href="#">Filachev et al., 2003</a> )
Xeva 2.35-320	Xenics	1000 - 2300	30		150	? - 60ms	20-30	<a href="http://xenics.com">xenics.com</a>
•Photonetc.	ZEPHIR 2.9	850 - 2950	<b>30</b>		<b>150</b>	1 - 10ms	<b>70</b> (mwir)	<a href="http://photonetc.com">photonetc.com</a>



## Code Layout

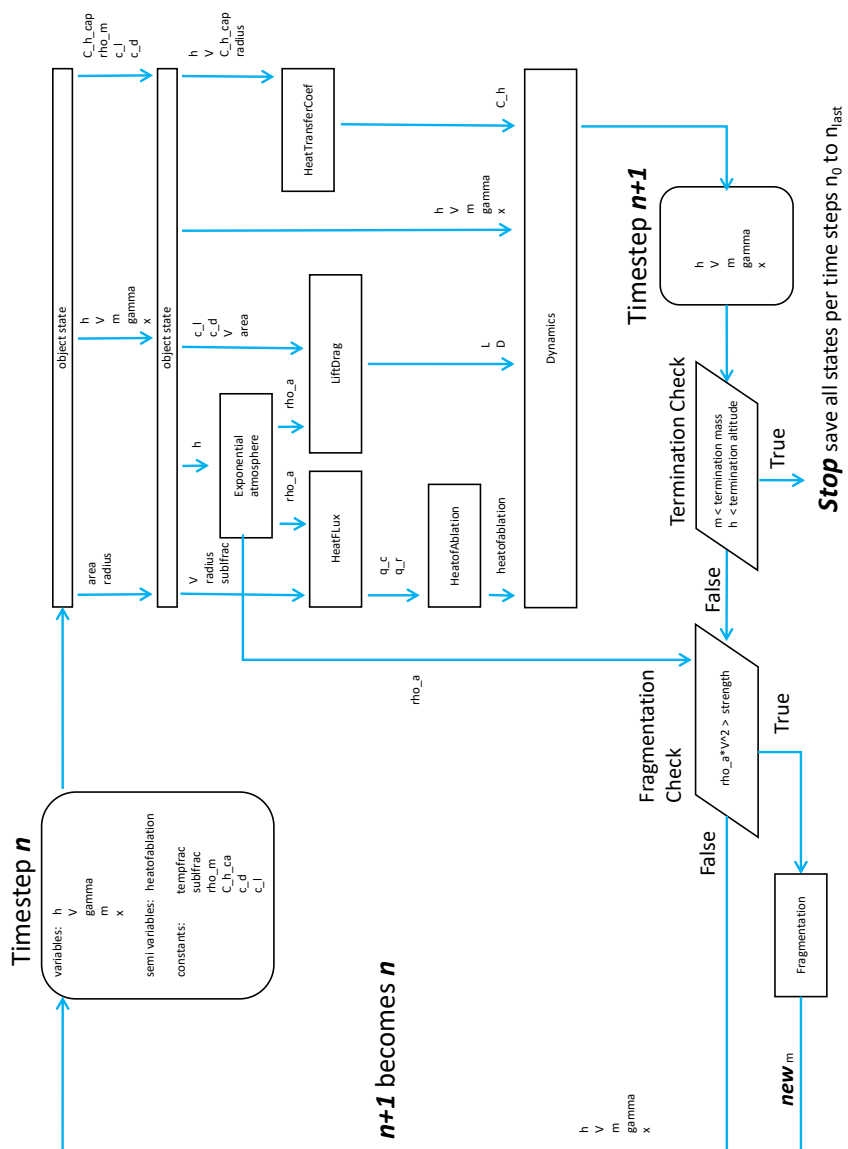


Figure B.1: Code Layout of the trajectory simulation part.

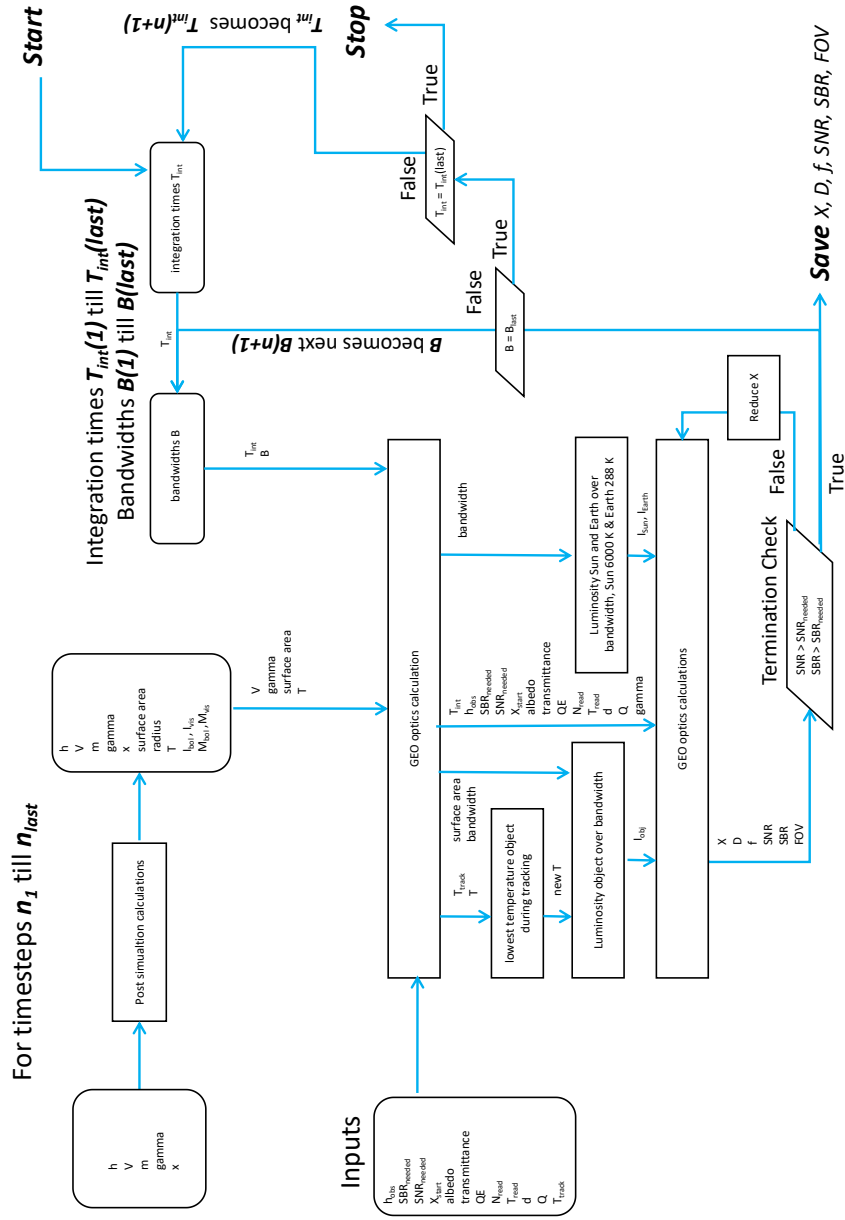


Figure B.2: Code Layout of the post trajectory simulation part and the GEO optic instrument parameter calculations part.



# Assumptions List for Both Written Codes

## C.1. Assumptions on the Re-entry State Simulation

For the re-entry simulations some assumptions were made, a recap of them is summarized below:

- **Uniform Gravity** - Gravity has been assumed to not change with altitude, which is not true in real life. But at about 150 km altitude, gravity is only about 5% lower as at Earth's surface ([Mooij, 2016](#)). This means that the re-entering objects experience less deceleration and a faster change in flight path angle. This leads to the objects penetrating deeper in the atmosphere and having a less straight trajectory.
- **All meteors are spherical** - For simplicity all meteors are assumed to be spheres. Other researchers have used brick shapes as well ([Halliday et al., 1996](#)).
- **Meteor non-lift generating rotation** - For meteors is assumed that there is a uniform ablation over the surface, this keeps the shape factor the same and thus also the shape of the meteor ([Gritsevich, 2007](#)). Next to that no force generation due to the Magnus effect is assumed, which in real life is present on rotating spherical objects like for example baseballs ([Sarafian, 2011](#)). This effect could have led to positive or negative lift making the trajectory less straight.
- **No sideways forces** - In the simulations no sideways forces were assumed, thus the trajectory can be described in a 2D plane.
- **Ideal gas** - The use of an exponential atmosphere is only allowed together with the assumption of ideal gases, since the exponential atmosphere is used it is assumed that the atmosphere consist of ideal gases ([Mooij, 2016](#)).
- **PICA as heat shield** - For simplicity all ballistic vehicles are assumed to have a PICA heat shield. This is definitely the case for Stardust ([Riccio et al., 2017](#)), but detailed information on other heat shield material could not be found, therefore the information found on PICA is used on all ballistic vehicles.
- **Black body Emissivity** - For all the calculations the emissivity  $\epsilon$  is assumed to be equal to 1, leading to a black body (opposed to  $\epsilon < 1$ , which then the body would be a gray body). In reality re-entry objects are usually more a gray body, which would mean they emit less radiation and thus their luminosity would be lower.
- **Black body radiation of separate slabs is the same as the black body radiation as the sum of the slabs** - For computational easiness is has been assumed that the black body radiation from the whole radiating surface with 1 average temperature is the same as the black body radiation of each different surface slab with each a different temperature, which makes up the average temperature. For infinitesimal small slabs the solution should reach that of the one using the average temperature.

## C.2. Assumptions on the GEO Instrument Parameter Determination

Some assumptions were made for the GEO instrument optical parameter determination code. A recap of the used assumptions is given below:

- **Equal travel length through atmosphere** - Although this is not true in reality, the travel distance through the atmosphere is assumed to be the same under any viewing angle. If this effect would be taken into account, the atmosphere would block and absorb more of the background and object irradiation. And reduce the power reaching the detector for both object and background. This has a bigger implication for the SNR than for the SBR, since now the readout noise has to be overcome.
- **Lambertian Reflection** - The property of this assumption is that the observed brightness is the same for an observer regardless of the observer's angle of view. This is important in case the Earth is observed off nadir. In that case the land surface is under an incidence angle, reducing the amount of observed irradiated power from that surface (assuming diffuse scattering/reflection). However, since one pixel has a fixed field of view, it will also observe a bigger area under that angle, which turns out, for Lambertian reflection to illuminate the first explained effect. This results in the fact that it doesn't matter under which angle a surface is observed it will always be observed as if from nadir.

$$I_0 = \frac{\text{Radiance under angle } \theta}{\text{Observed radiance under angle } \theta} = \frac{I \cos \theta d\Omega dA}{d\Omega_0 \cos \theta dA_0} = \frac{Id\Omega dA}{d\Omega_0 s A_0} \quad (\text{C.1})$$

This has as consequence that the diffuse background radiation is solely determined by where the Sun is w.r.t. the observing satellite. Also the program assumes maximum background reflection, which is only true in the sub satellite point. So if the Sun is not in the sub satellite point the SBR and SNR are higher than calculated with the code. A reasonable diffuse reflection background radiation is about 90-100  $W/m^2$ .

- **Uniform albedo** - For simplicity the albedo of the Earth is assumed to be a constant 30%, which is too low for snow, clouds, dry sand and ice, but in the right range for wet sand and soil, and an overestimation for forest, meadows and crops<sup>1</sup>.
- **No over sea observations** - In this research no over sea observations are assumed, this would increase the albedo of the background considerably (up till 100%) if the Sun is within a few degrees behind the observer. This is one of the only surface materials that is hugely influenced by the viewing angle and the Sun's location.

<sup>1</sup>wikipedia.com. <https://en.wikipedia.org/wiki/Albedo> (Accessed Jan 17, 2019).

# D

## Input Data for Re-entry Simulations

In this appendix all the input data for the simulations is shown including the sources where the values came from, or an explanation for it. Below are given Table D.1, with the constants used in the simulations, and Table D.2, with the simulation options used for each kind or specific object. In the meteor simulations it is important to note that the luminosity coefficient is calculated via the method used by [Stokan and Campbell-Brown \(2015\)](#), that the heat flux reduction by ablation (ablation shielding) comes from fractions given by [Bronshnten \(1983\)](#), the heat of ablation comes from [Johnston et al. \(2018\)](#) and that for sizes bigger or comparable to the capsules the temperature gradient can be taken the same as those, since it is based of CFD simulations of similar size and conditions ([Suzuki et al., 2014](#)).

Table D.1: Constants used in all simulations. All from ([Wertz and Larson, 2010](#); [Giancoli, 2009](#); [Mooij, 2016](#)).

Parameter	Symbol	Value	Units	Source
Stefan-Boltzmann Constant	$\sigma$	$5.67051 \times 10^{-8}$	[]	
Wiens Constant	$b$	$2.89777 \times 10^{-3}$	[]	
Speed of light	$c$	$2.99792458 \times 10^8$	[m/s]	
Electron Volt	$eV$	$1.6 \times 10^{-19}$	[J]	
Plancks Constant	$h$	$6.626075 \times 10^{-34}$	[]	
Boltzmann Constant	$k$	$1.380658 \times 10^{-23}$	[]	
Gravitational acceleration Earth	$g_0$	9.81	[m/s <sup>2</sup> ]	
Air Density at Sea Level	$\rho_0$	1.1225	[kg/m <sup>3</sup> ]	
Scale Height	$H$	7000-8500	[m]	( <a href="#">Mooij, 2016</a> ), NASA?
Radius Earth	$R_E$	6378	[km]	

Table D.2: Options used per object in the simulation code. ([Olynick et al., 1998](#); [Suzuki et al., 2014](#); [Johnston et al., 2018](#); [Riccio et al., 2017](#); [Bronshnten, 1983](#); [Stokan and Campbell-Brown, 2015](#))

Object	Temp gradient	$C_h$	Ablation shielding	$\tau$
Hayabusa Capsule	0.3	Variable (0.1 capped)	0.35	0.0003
Stardust Capsule	0.3	Variable (0.1 capped)	0.35	0.0003
Meteor	0.0-0.3	Variable (0.04 capped)	0.0-0.972	0.005-0.059
Hayabusa S/C	N/A	0.1	0.35	0.0017

## D.1. Meteors

To make sure the inputs for typical meteor simulations were taken correctly all the data that was found in this research has been summarized in Table D.3, based on info from Ortega (2016); Ceplecha et al. (1998); Nemtchinov et al. (1997); Gritsevich and Koschny (2011); Johnston et al. (2018); McKinley (1961); Brown et al. (2004); Tagliaferri et al. (1995); Popova et al. (2013a). Also info found on the Australian Space Academy<sup>1</sup> was included in the Table. Two meteor observation datasets have been obtained from both the Japanese MSSWG Orbit Database (1983-2009)<sup>2</sup> and Leiden University (1981-1993)<sup>3</sup>, with this an estimation of the frequency of the duration of meteors can be made, as well as with the data in the papers from Halliday et al. (1996); Ohsawa et al. (2018); Hawkins and Upton (1958). The Japanese dataset contained next to the usual big cluster below 0.5s (Japan: 57% and Leiden: 87%), also about 13% of the observations in the 3 – 4s range.

In Table D.4 simulation settings are given that were used in the meteor fingerprint results section.

Table D.3: Table with typical meteor info from various sources.

Time of the events	Average 0.3s ; Max 10s
Altitude	75-180km
Velocity	11-72.8 km/s
Density	500-3500-8000 kg/m <sup>3</sup>
Meteoroid size	micrometers - meters
Mass	10 <sup>-8</sup> - 10 <sup>7</sup> kg
Size of meteor wake	10 - 100 km
Max Temperature	4,400 K - 10,000 K
Magnitude	-27 to 6 and higher
Shape factor	0.8 - 1.2
Drag coef.	0.5 - 1.0
Heat of ablation	(0.1 – 10) × 10 <sup>6</sup> J/kg
Heat transfer coef.	0.005 - 0.6
Luminous efficiency	0.0002 – 0.08
Entry zenith angle	0° – 99°
Events	Sporadic (75%) Showers (25%)

Table D.4: Mass and altitude termination, tolerance settings used in the simulation code for meteor fingerprint results.

$V_{\infty}$ [km/s]	Simulation settings ODE45							
	$M_{\infty}$ [kg]							
	0.0001	0.001	0.01	0.1	1	10	100	1000
Tolerances [10 <sup>X</sup> ]	-14	-14	-14	-14	-14	-14	-14	-14
Minimal Mass [10 <sup>X</sup> kg]	-6	-6	-6	-5	-5	-5	-4	-4
Minimal Altitude [km]	45	45	45	30	30	30	25	7

Not all parameter ranges have been fully used, therefore, the used input parameters for some known meteors are given below in their respective subsections. Also the inputs for this research its generic meteor simulations is given.

### D.1.1. Small Generic Meteors

Below, in Table D.5, the values are given for the generic small meteor simulations. The data comes from different sources as discussed in the beginning of this section. It should be noted that a choice had to be made regarding some input parameters, since there were so many available parameter ranges. For example the density of the meteors is taken as 3500 kg/m<sup>3</sup>, but is by no means the only possible value (Babadzhanov and Kokhirova, 2009).

### D.1.2. Chelyabinsk

The Chelyabinsk was a big meteoroid colliding with Earth, its size of about 20 meters is the biggest in the beginning of the 20th century. The values used for the fragmentation version of the re-entry code are given in Table D.6. Note that there are small differences between the inputs for this research its fragmentation model, and the one it is based on regarding the 3 specific parameters (Wheeler et al., 2017; Mathias et al., 2017; Register et al., 2017). This is because no dust cloud was assumed in this research its fragmentation model.

<sup>1</sup>"METEOR FLIGHT THROUGH THE ATMOSPHERE." spaceacademy.net.au. <http://www.spaceacademy.net.au/watch/debris/metflite.htm> (Accessed June 6, 2018).

<sup>2</sup>imo.net. <https://www.imo.net/files/msswg/msswg.txt> (Accessed Juli 4, 2018).

<sup>3</sup>"FTP Listing of /pub/betlem/orbits/ at ftp.strw.leidenuniv.nl" ftp.strw.leidenuniv.nl. <ftp://ftp.strw.leidenuniv.nl/pub/betlem/orbits/> (Accessed Juli 4, 2018).

Table D.5: Parameters used in small meteor simulation.

Parameter	Symbol	Value	Units	Source
Drag Coefficient	$c_d$	1.0	[-]	(Halliday et al., 1996)
Lift Coefficient	$c_l$	0.0	[-]	Sphere doesn't generate lift
Meteor Density (Mean)	$\rho_m$	3500	[kg/m <sup>3</sup> ]	(Babadzhanov and Kokhirova, 2009) (Halliday, 1988)
Heat of Ablation	$\xi$	$8.3 \times 10^6$	[J/kg]	(Johnston et al., 2018)
Heat Transfer Coefficient Cap	$c_h$	0.04	[-]	(Johnston et al., 2018)
Luminosity Coefficient	$\tau$	0.005-0.059	[-]	(Stokan and Campbell-Brown, 2015)
Entry Mass	$m_e$	$1 \times 10^{-4} - 1 \times 10^6$	[kg]	Theoretically any value is possible
Entry Velocity	$V_e$	11 - 72	[km/s]	(Cepilecha et al., 1998)
Entry Altitude	$h_e$	100 - 180	[km]	Depending on atmospheric conditions
Entry Angle	$\gamma_e$	0 - 180	[deg]	

Table D.6: Parameters used in the Chelyabinsk simulation. Most information is from (Popova et al., 2013a).

Parameter	Symbol	Value	Units	Source
Drag Coefficient	$c_d$	1.0	[-]	
Lift Coefficient	$c_l$	0.0	[-]	
Meteor Density	$\rho_m$	3300	[kg/m <sup>3</sup> ]	(Popova et al., 2013a)
Heat of Ablation (LL5)	$\xi$	$6 \times 10^6$	[J/kg]	LL5
Heat Transfer Coefficient Cap	$c_h$	0.04	[-]	(Johnston et al., 2018)
Luminosity Coefficient	$\tau$	0.07	[-]	(Popova et al., 2013a)
Entry Mass	$m_e$	$13 \times 10^6$	[kg]	(Popova et al., 2013a)
Entry Velocity	$V_e$	19.16	[km/s]	(Popova et al., 2013a)
Entry Altitude	$h_e$	97	[km]	(Popova et al., 2013a)
Entry Angle	$\gamma_e$	18.3	[deg]	(Popova et al., 2013a)
Aerodynamic Strength	$\sigma_m$	0.3	[MPa]	(Popova et al., 2013a)
Fragments per break-up	$V_e$	2	[-]	Manual self best fit
Strength Scaling	$\alpha$	0.2	[km]	Manual self best fit

## D.2. RE-entry Capsules

Capsules are also simulated for their re-entry signatures. Note that Hayabusa is assumed to be a half sphere and stardust a whole sphere regarding their mass to radius relation.

### D.2.1. Stardust

Stardust was the first Sample Return Capsule (RSC) bringing extraterrestrial material back to Earth. The material was captured from the comet Wild 2's tail.

Table D.7: Parameters used in the Stardust SRC simulation.

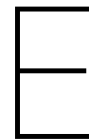
Parameter	Symbol	Value	Units	Source
Drag Coefficient	$c_d$	1.38	[-]	(Mitcheltree et al., 1999; Marraffa, 2008)
Lift Coefficient	$c_l$	0.06	[-]	(Mitcheltree et al., 1999)
Nose Radius	$R_n$	0.2202	[m]	SOURCE?(Davies, 2006) is different (2.3)
Capsule Density	$\rho$	1023	[kg/m <sup>3</sup> ]	Derived from mass, assumed spherical
Heat of Ablation	$\xi$	100-400×10 <sup>6</sup>	[J/kg]	(Ricchio et al., 2017)
Heat Transfer Coefficient Cap	$c_h$	0.1	[-]	(Nemtchinov et al., 1997), best fit
Luminosity Coefficient	$\tau$	0.0003	[-]	(Borovička et al., 2011)
Entry Mass	$m_e$	45.8	[kg]	(Davies, 2006)
Entry Velocity	$V_e$	12.6	[km/s]	(Davies, 2006)
Entry Altitude	$h_e$	120	[km]	
Entry Angle	$\gamma_e$	8.2	[deg]	(Davies, 2006)

### D.2.2. Hayabusa

Hayabusa was a spacecraft collecting surface samples from an asteroid and returning them with a capsule to Earth's surface.

Table D.8: Parameters used in the Hayabusa SRC simulation.

Parameter	Symbol	Value	Units	Source
Drag Coefficient	$c_d$	1.2	[-]	(Marraffa, 2008)
Lift Coefficient	$c_l$	0.0	[-]	
Nose Radius	$R_n$	0.202	[m]	(Davies, 2006)
Capsule Density	$\rho$	1000	[kg/m <sup>3</sup> ]	Derived from mass, assumed half sphere
Heat of Ablation	$\xi$	100-400×10 <sup>6</sup>	[J/kg]	(Ricchio et al., 2017)
Heat Transfer Coefficient Cap	$c_h$	0.1	[-]	(Nemtchinov et al., 1997), best fit
Luminosity Coefficient	$\tau$	0.0003	[-]	(Borovička et al., 2011)
Entry Mass	$m_e$	16.27	[kg]	(Davies, 2006)
Entry Velocity	$V_e$	11.3	[km/s]	(Davies, 2006)
Entry Altitude	$h_e$	120	[km]	
Entry Angle	$\gamma_e$	13.8	[deg]	(Davies, 2006)



## Circle Overlap Calculations in a Square

In order to get an estimation on how much of the point spread function (circle) will be on average in a square (pixel) a small program was written.

As input the user gives the square pixel size ( $d$ ), the circle radius ( $r_c$ ) and the middle-point of the circle ( $x_c$  and  $y_c$ ), the output will be a number between 0 and 1, equal to the fraction of the circle overlapping with the square. For this analysis a pixel size of 10, radius of 5 and random middle-point of the circle within the square were taken. The actual sizes don't matter since fractions are calculated, however, for this research the diameter of the circle should be the same as the length of one side of the square pixel (a diffraction limited optical system). The calculations needed are shown in Equations (E.1) till (E.11), see Figure E.1 for naming conventions and Figure E.2 for the 4 different cases that can arise (of course this can be mirrored to the left and down).

With this program then a Monte Carlo simulation can be ran, keeping the square pixel size and circle radius again at 10 and 5 respectively. Then from a random uniform distribution two random numbers between 0 and 10 are chosen, for respectively  $x_c$  and  $y_c$ . This means that the midpoint of the circle is always on the square, if it is not, it is the case on a neighboring pixel. This also means that the minimum amount of overlap is 25% and the maximum is 100%. The overlap code just described is ran and a fraction of overlap of the circle is given. This is done a 1,000,000 times, the mean of all the overlap fractions is calculated, giving a solution on the average fraction of the circle being in the square of 0.615 or thus 61.5%.

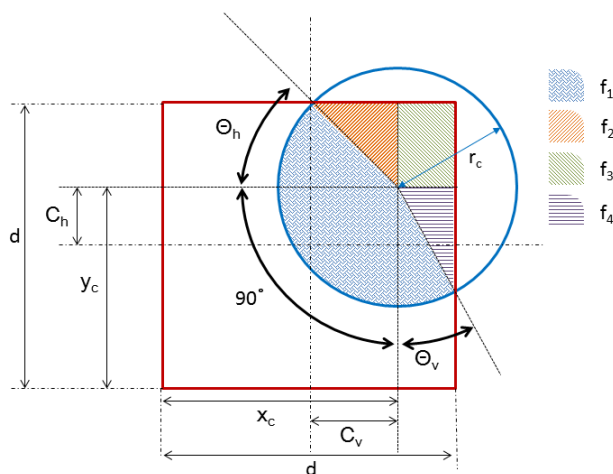


Figure E.1: Figure with naming conventions of the approach to the point spread function in square pixel problem. Not to scale.

$$C_h = |y_c - \frac{1}{2}d| \quad (\text{E.1})$$

$$C_v = |x_c - \frac{1}{2}d| \quad (\text{E.2})$$

$$\theta_h = \arcsin\left(\frac{\frac{1}{2}d - C_h}{\frac{1}{2}d}\right) \quad (\text{E.3})$$

$$\theta_v = \arcsin\left(\frac{\frac{1}{2}d - C_v}{\frac{1}{2}d}\right) \quad (\text{E.4})$$

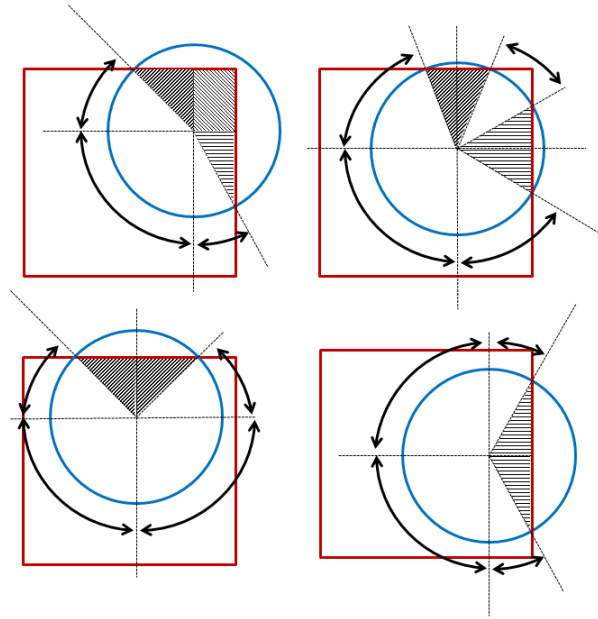


Figure E.2: Figure with the 4 cases that can arise in the determination of how much of the circle overlaps the square. Not to scale.

$$\theta_{tot} = \theta_h + \theta_v + 90 \quad (\text{E.5})$$

$$\theta_{test} = \theta_h + \theta_v \quad (\text{E.6})$$

$$f_1 = \theta_{tot} + \theta_{test} - 90 \quad (\text{E.7})$$

$$f_3 = \frac{\frac{1}{2}(\frac{1}{2}d - C_h)(\cos(\theta_h) * r_c)}{\pi r_c^2} \quad (\text{E.8})$$

$$f_4 = \frac{\frac{1}{2}(\frac{1}{2}d - C_v)(\cos(\theta_v) * r_c)}{\pi r_c^2} \quad (\text{E.9})$$

$$f_2 = \left| \frac{(\frac{1}{2}d - C_v)(\frac{1}{2}d - C_h)}{\pi r_c^2} \right| \quad (\text{E.10})$$

$$f_{tot} = f_1 + f_2 + f_3 + f_4 \quad (\text{E.11})$$

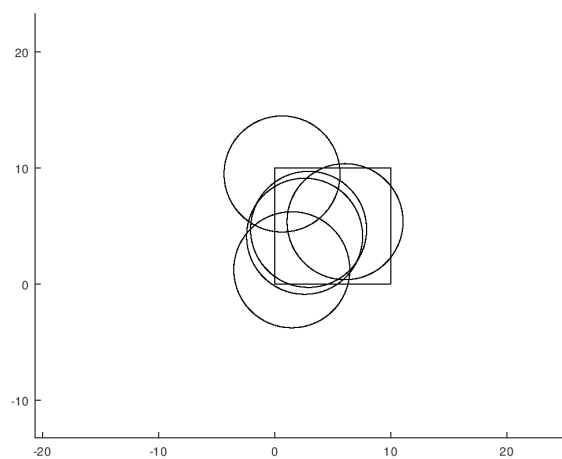
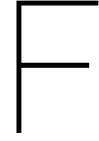


Figure E.3: Plot of 5 runs of the program stacked on top of each other.



## The Halliday Correction Factor

Halliday et al. (1996) assumes a brick shape of 2L by 3L by 5L, with the drag area  $A$  equal to the biggest surface. The density of the meteor is equal to  $3.5 \text{ g/cm}^3$ . From the observations made of meteors one can determine the fraction  $m_d/A$ . Halliday et al. (1996) derives the dynamic mass  $m_d$  as function of this fraction as follows:

$$\frac{m_d}{A} = \frac{30\rho L^3}{15L^2} = 2\rho L \rightarrow L = \frac{m_d}{A2\rho} \quad (\text{E1})$$

$$m_d = 30\rho L^3 \rightarrow m_d = 30\rho \left(\frac{m_d}{A2\rho}\right)^3 \rightarrow m_d = \frac{30\rho}{8\rho^3} \left(\frac{m_d}{A}\right)^3 \rightarrow m_d = 0.306 \left(\frac{m_d}{A}\right)^3 \quad (\text{E2})$$

Since in our research spheres are assumed, one can also do the same procedure for a spherical shape with the same density:

$$\frac{m_d}{A} = \frac{\rho \frac{4}{3}\pi r^3}{\pi r^2} = \frac{4}{3}\rho r \rightarrow r = \frac{3m_d}{4\rho A} \quad (\text{E3})$$

$$m_d = \rho \frac{4}{3}\pi r^3 \rightarrow m_d = \rho \frac{4}{3}\pi \left(\frac{3m_d}{4\rho A}\right)^3 \rightarrow m_d = \frac{108\pi}{192\rho^2} \left(\frac{m_d}{A}\right)^3 \rightarrow m_d = 0.1443 \left(\frac{m_d}{A}\right)^3 \quad (\text{E4})$$

So when Halliday et al. (1996) would have assumed spheres instead of bricks a 2.125 lower mass would have been obtained:

$$\frac{m_{dB}}{m_{dS}} = \frac{0.306}{0.1443} = 2.121 \quad (\text{E5})$$

When comparing the data from Halliday et al. (1996) and with spherical meteoroids, one might need to divide the mass given by Halliday et al. (1996) by this fraction of 2.121 to obtain the to spherical mass of the same meteoroid. This was not done for the validation process in this research. In those equations  $L$  is a length measurement,  $M_d$  the dynamic mass of the meteor,  $A$  the cross-sectional drag area of the meteor,  $\rho$  the density of the meteor equal to  $3500 \text{ kg/m}^3$  and  $r$  the radius of the meteor. Subscripts  $S$  and  $B$  mean sphere or brick respectively.



# G

## All Results for Instrument Parameter Calculations Per Object

In this appendix all the detecting and tracking results obtained for the 100 nm bandwidth over a spectral range of 100nm to 3000 nm, and at the 6 integration times are given for all 7 investigated objects:

- Met1Model
- Met2Rate
- Met3Common
- Met4VV
- Met5Pers
- Hayabusa
- Stardust

### G.1. Met1Model

Below all the results for Met1Model are shown.

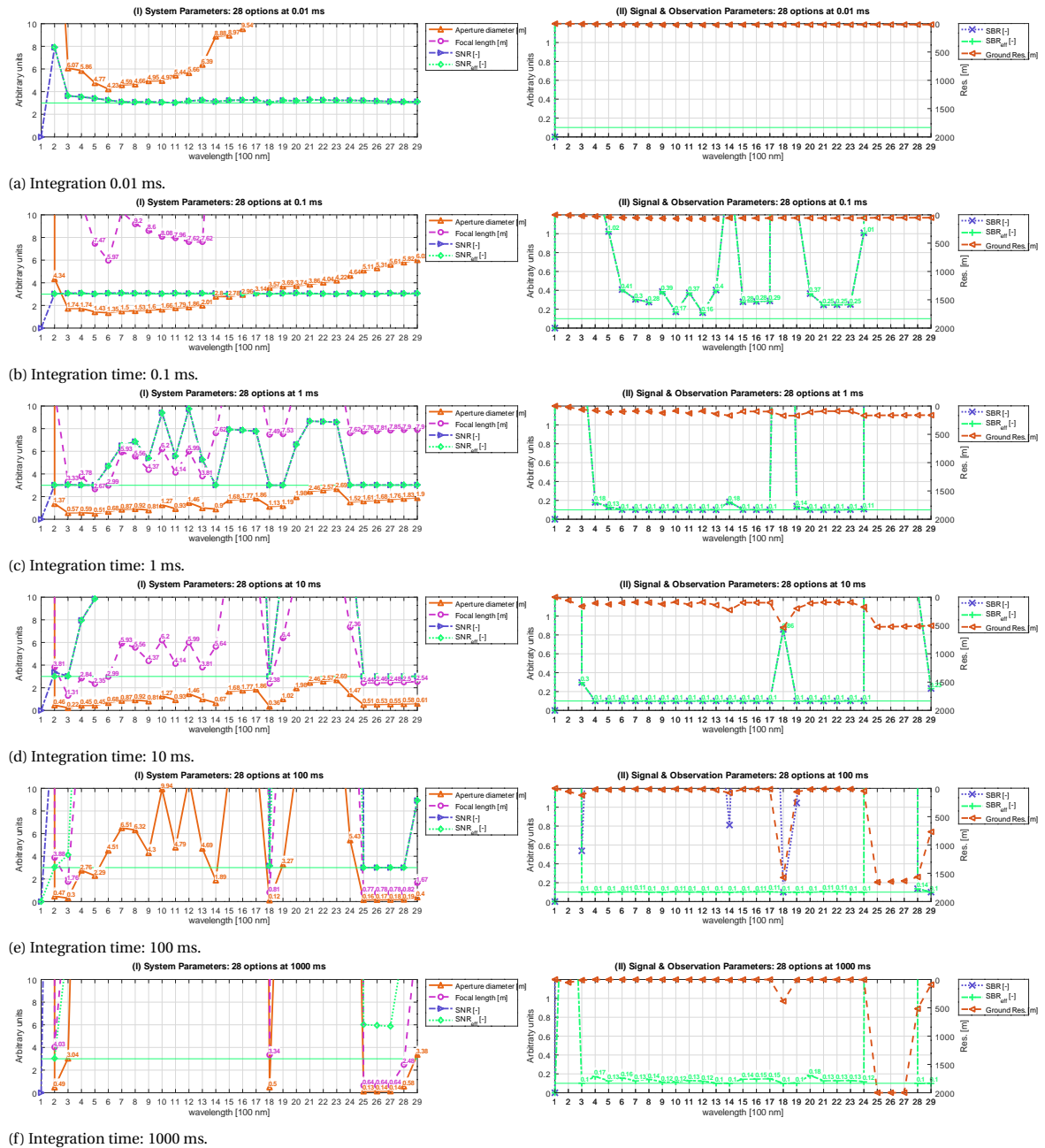


Figure G.1: Detection optical parameters for meteor Met1Model, values shown for  $SNR_{eff} > 3$  and  $SBR_{eff} > 0.1$ .

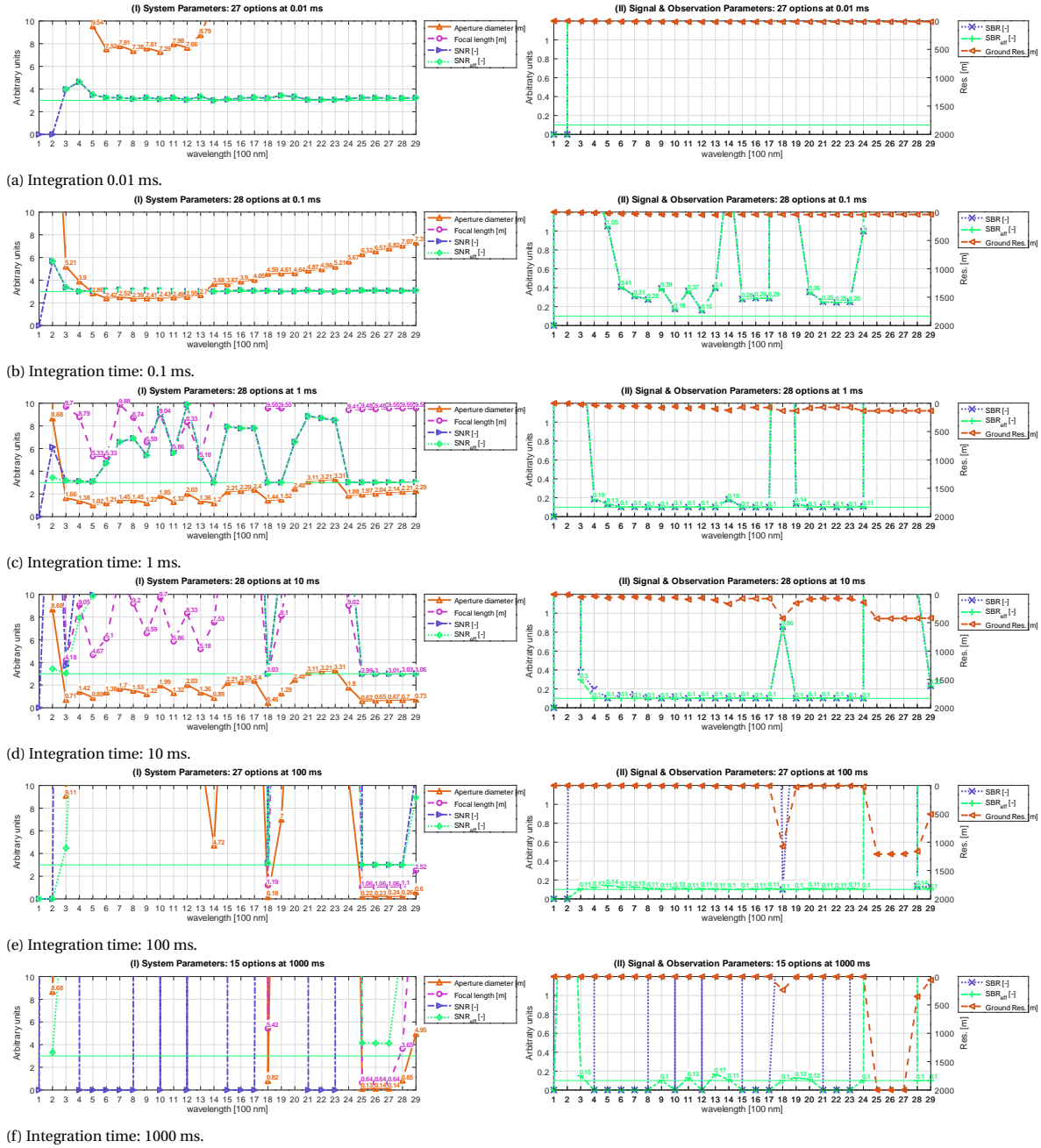


Figure G.2: Tracking optical parameters for the tracking of meteor Met1Model for 5 seconds, values shown for  $SNR_{eff} > 3$  and  $SBR_{eff} > 0.1$ .

## G.2. Met2Rate

Below all the results for Met2Rate are shown.

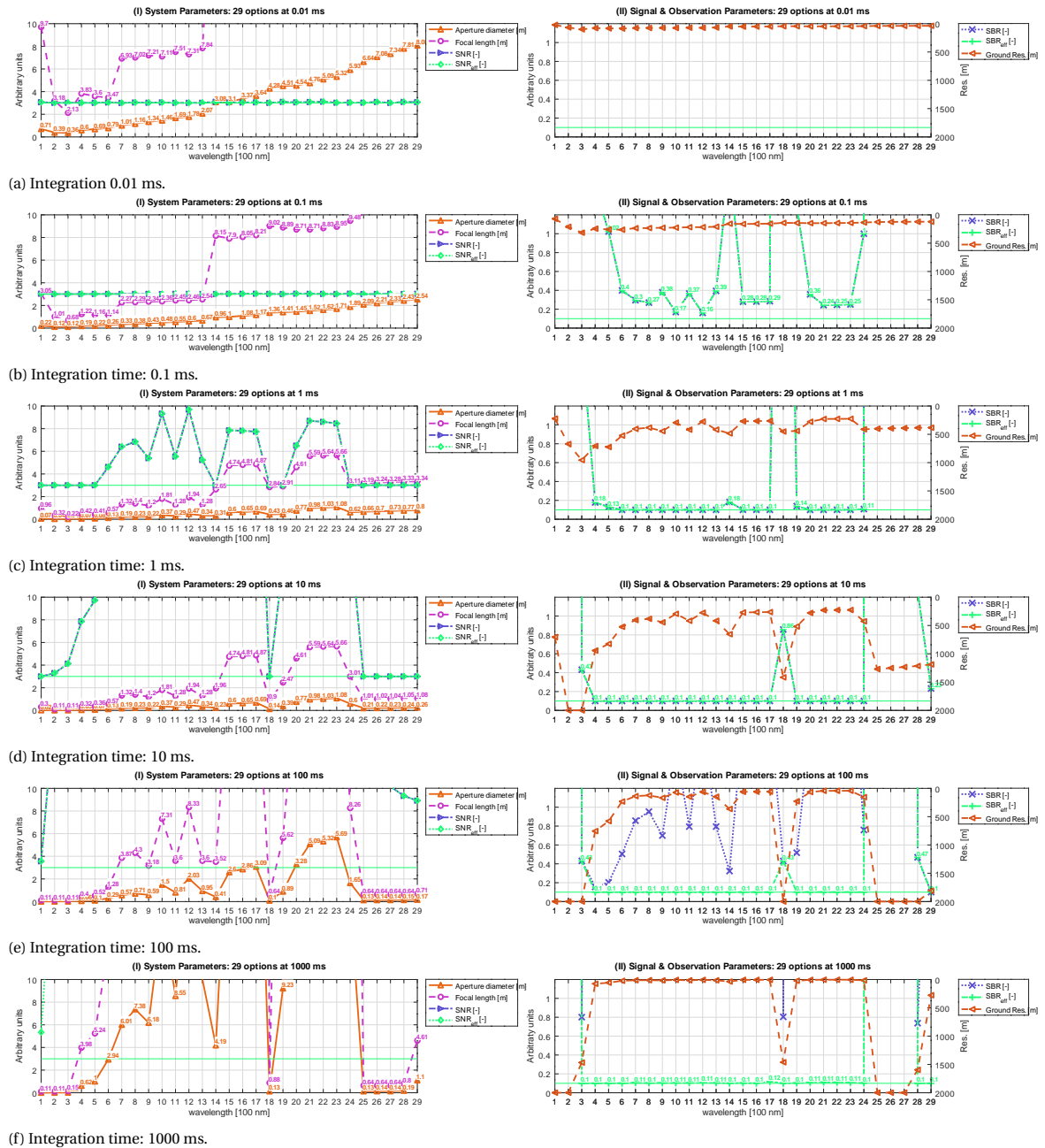


Figure G.3: Detection optical parameters for meteor Met2Rate, values shown for  $SNR_{eff} > 3$  and  $SBR_{eff} > 0.1$ .

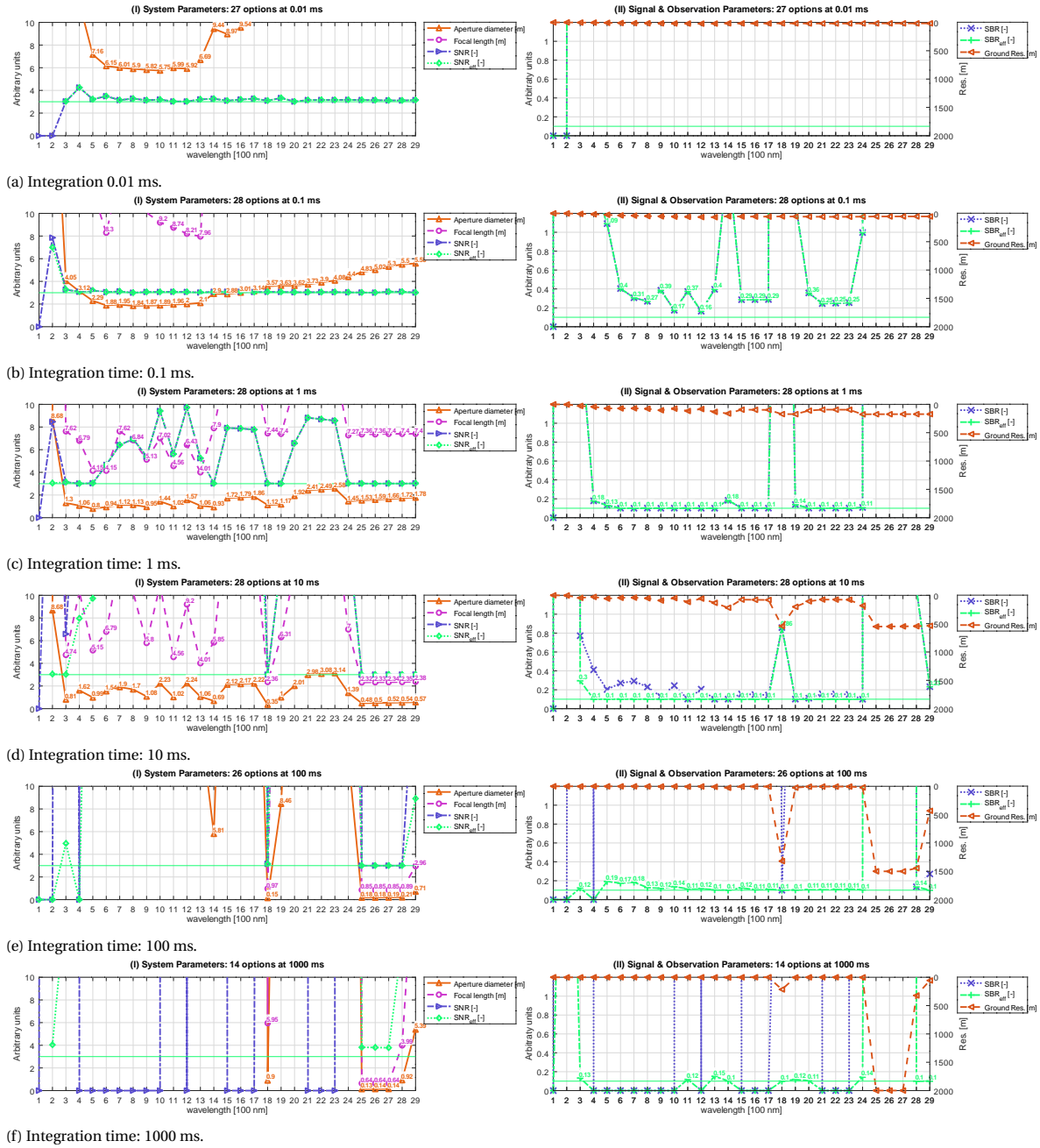


Figure G.4: Tracking optical parameters for the tracking of meteor Met2Rate for 5 seconds, values shown for  $SNR_{eff} > 3$  and  $SBR_{eff} > 0.1$ .

### G.3. Met3Common

Below all the results for Met3Common are shown.

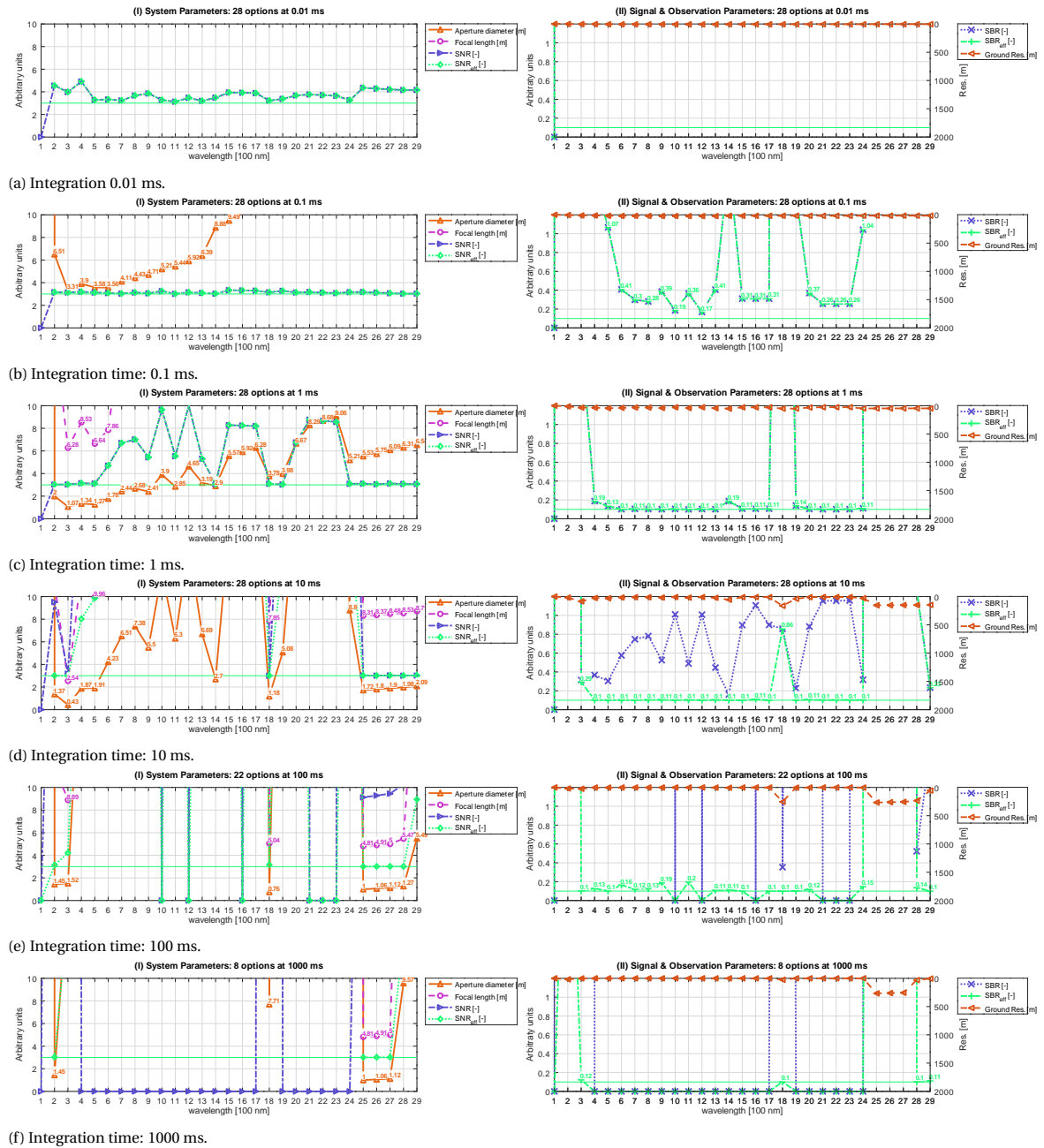


Figure G.5: Detection optical parameters for meteor Met3Common, values shown for  $SNR_{eff} > 3$  and  $SBR_{eff} > 0.1$ .

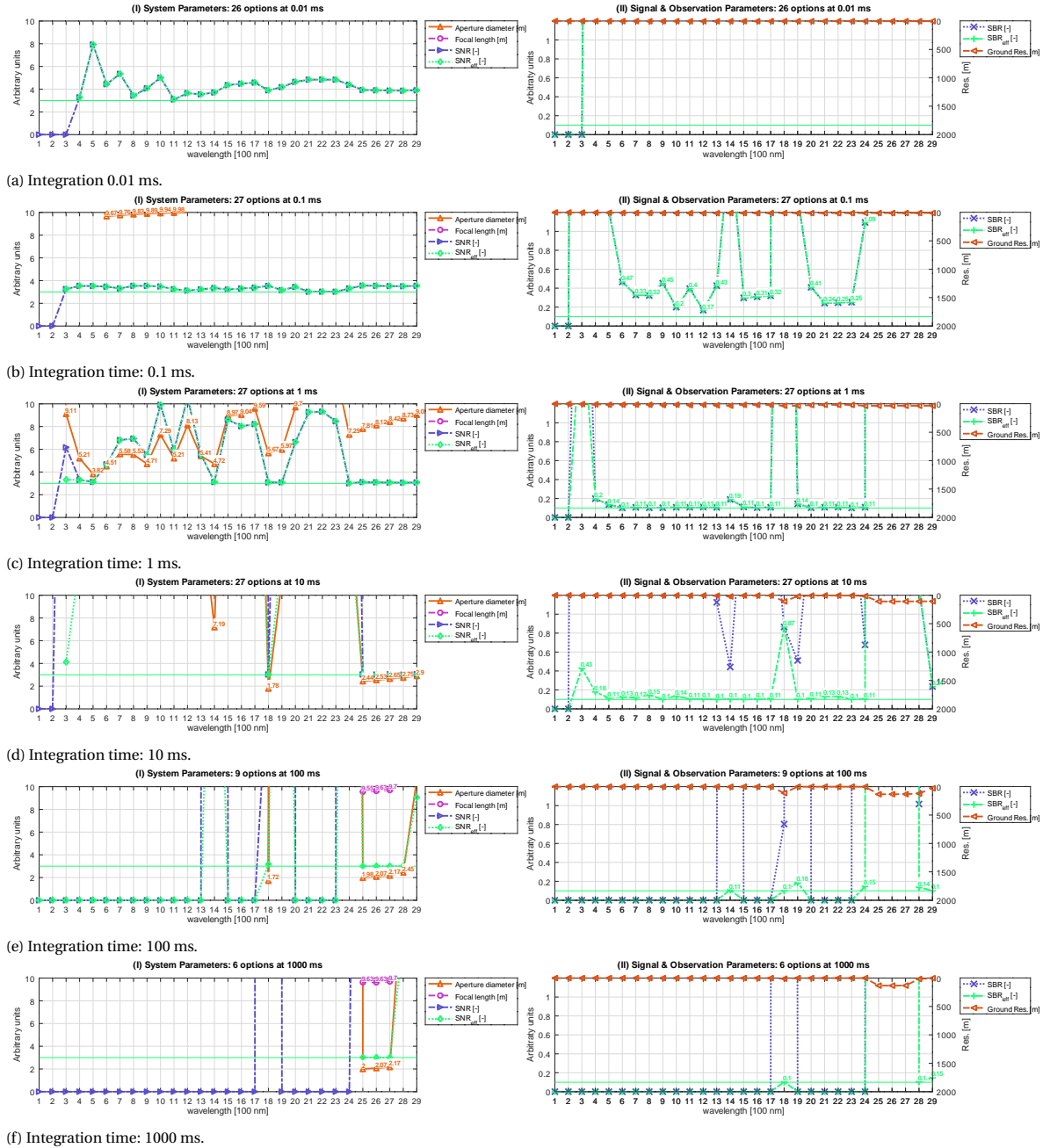


Figure G.6: Tracking optical parameters for the tracking of meteor Met3Common for 5 seconds, values shown for  $SNR_{eff} > 3$  and  $SBR_{eff} > 0.1$ .

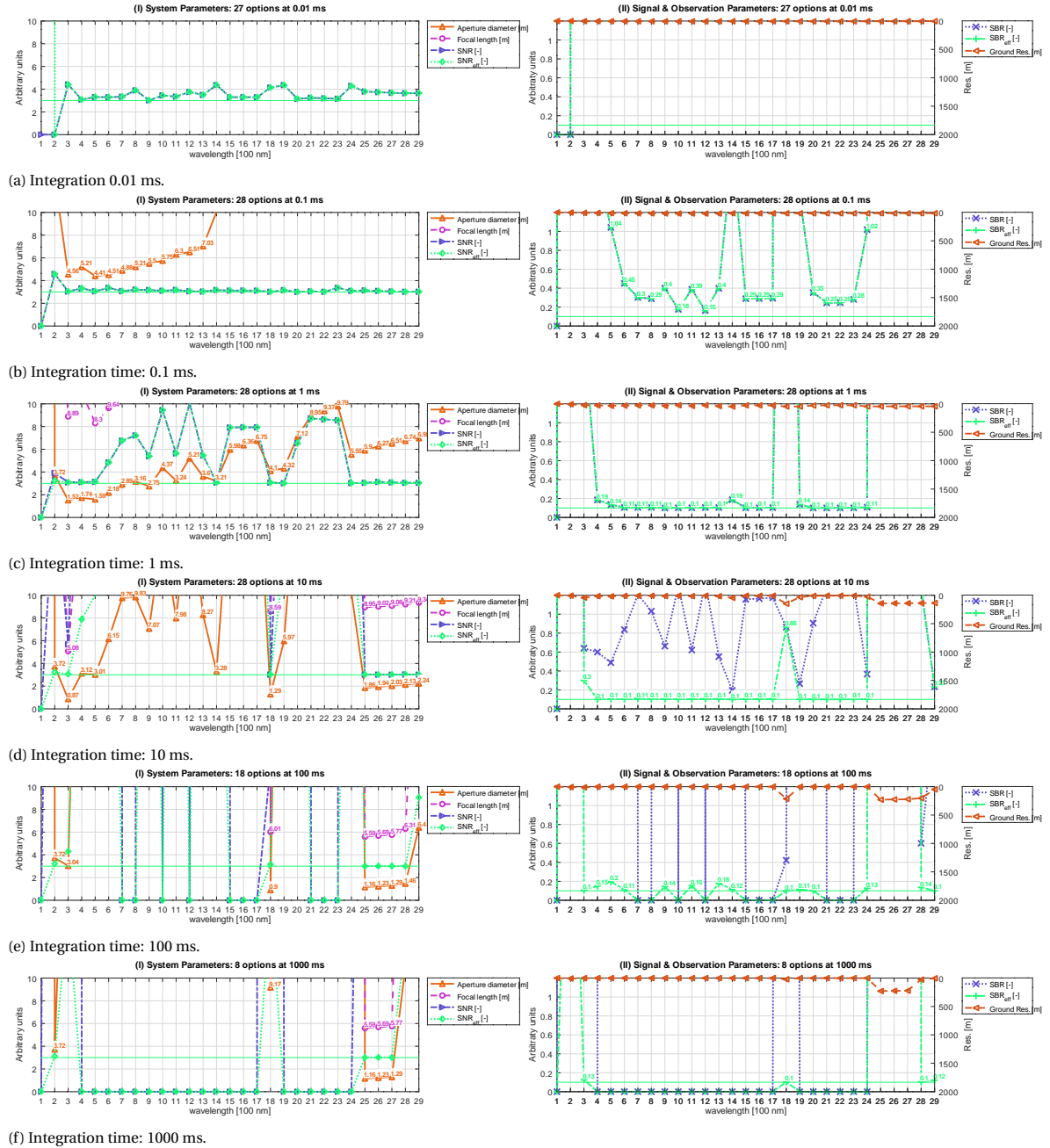


Figure G.7: Tracking optical parameters for the tracking of meteor Met3Common for 2 seconds, values shown for  $SNR_{eff} > 3$  and  $SBR_{eff} > 0.1$ .

### G.4. Met4VV

Below all the results for Met4VV are shown.

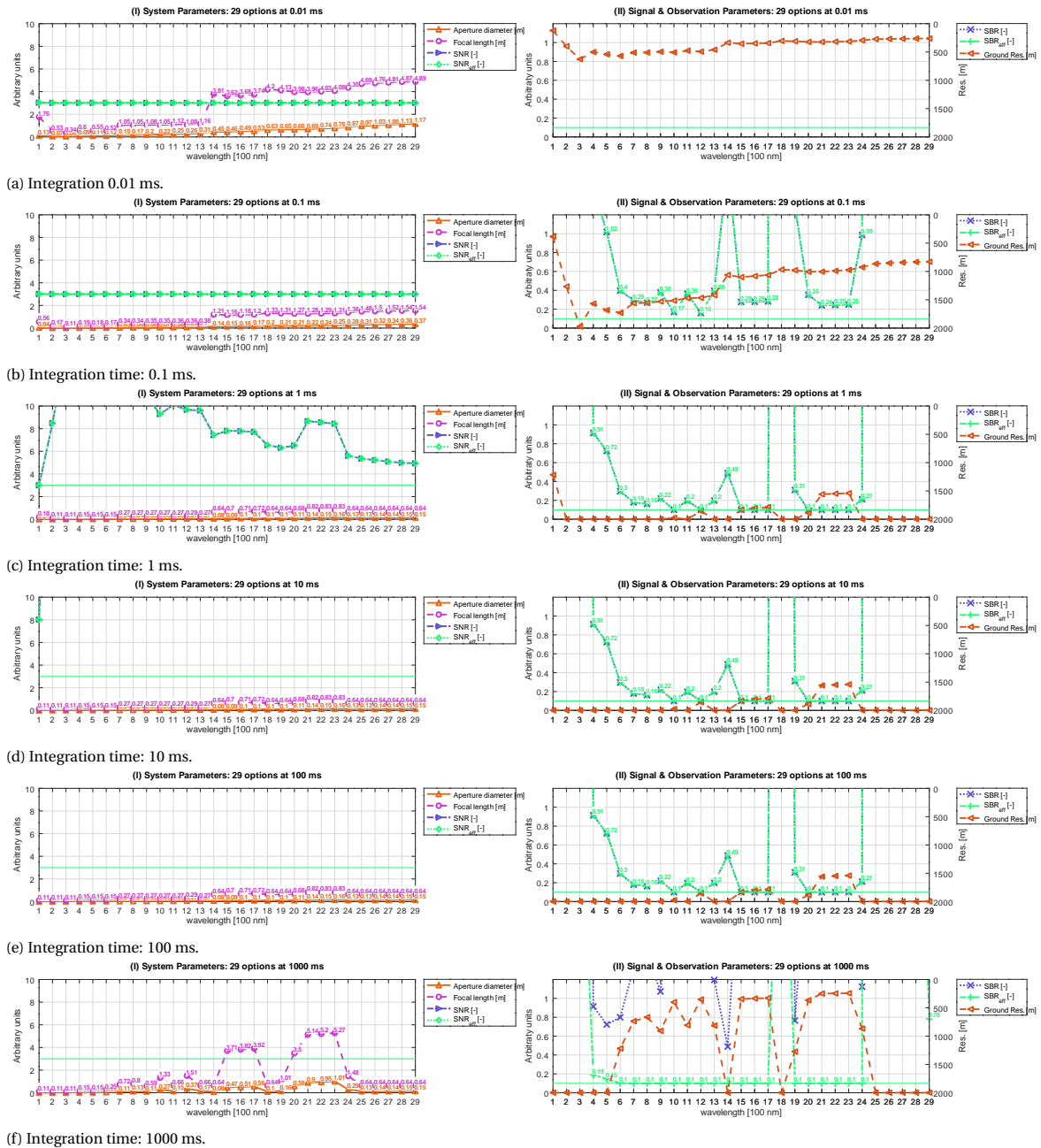


Figure G.8: Detection optical parameters for meteor Met4VV, values shown for  $SNR_{eff} > 3$  and  $SBR_{eff} > 0.1$ .

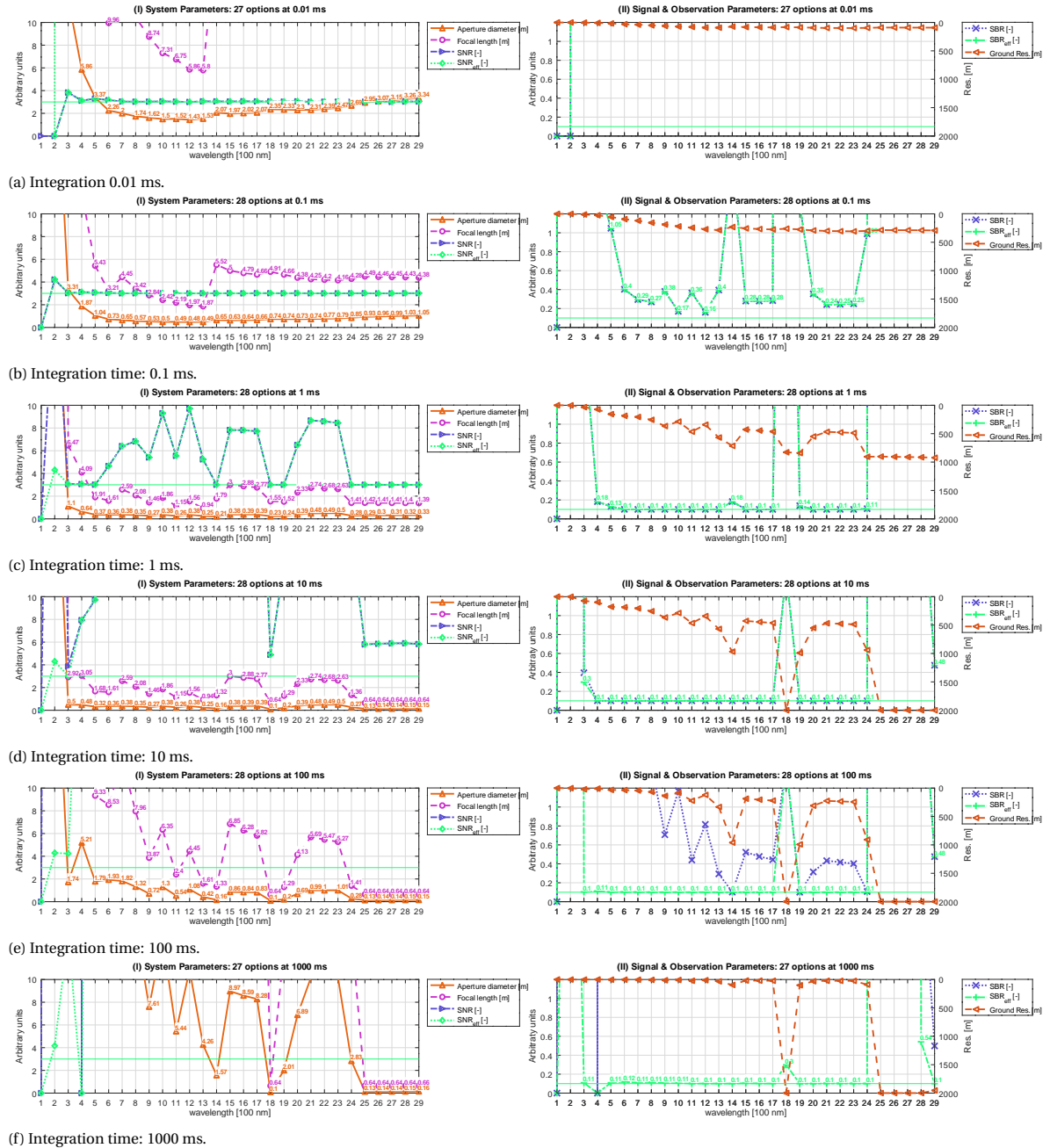


Figure G.9: Tracking optical parameters for the tracking of meteor Met4VV for 5 seconds, values shown for  $SNR_{eff} > 3$  and  $SBR_{eff} > 0.1$ .

### G.5. Met5Pers

Below all the results for Met5Pers are shown.

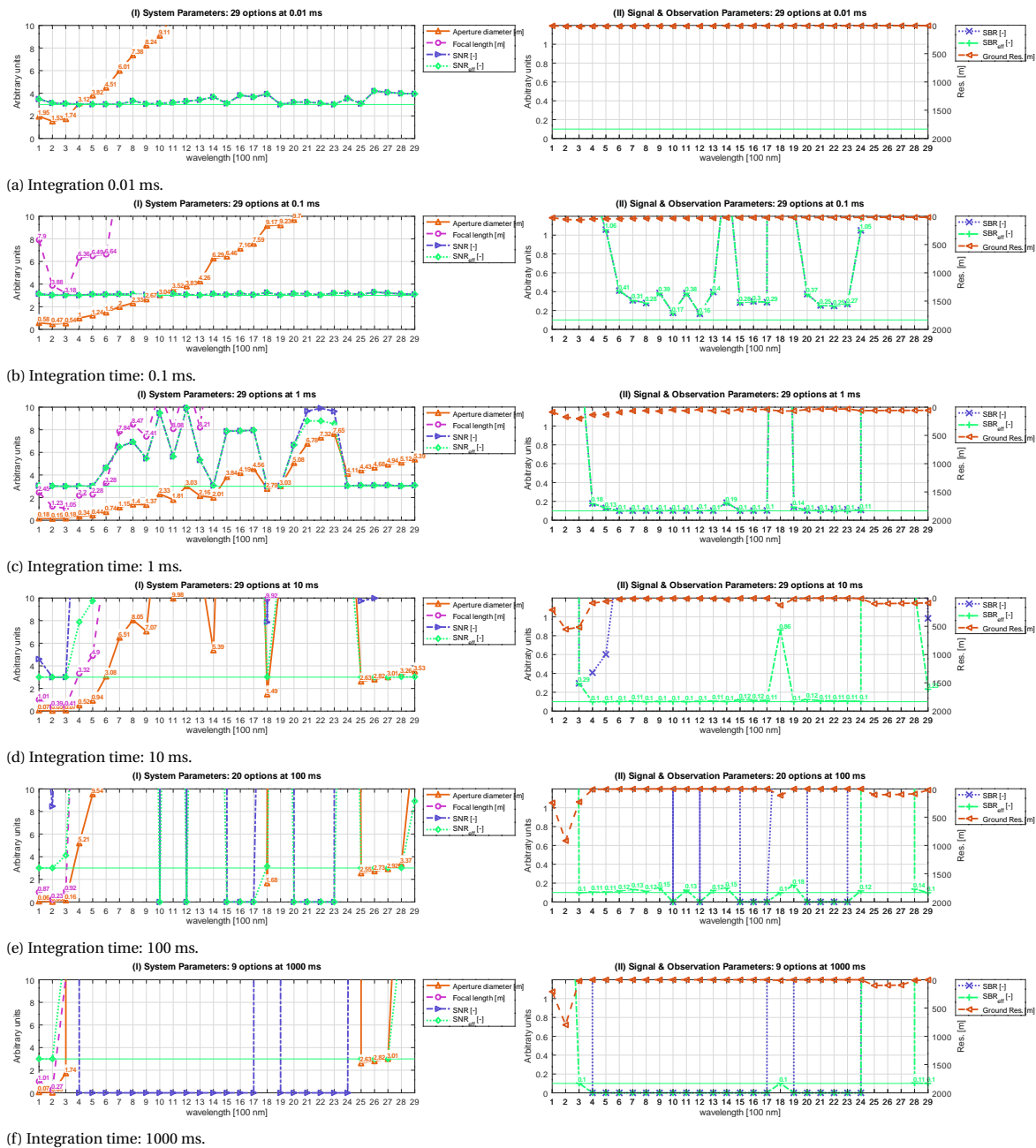


Figure G.10: Detection optical parameters for meteor Met5Pers, values shown for  $SNR_{eff} > 3$  and  $SBR_{eff} > 0.1$ .

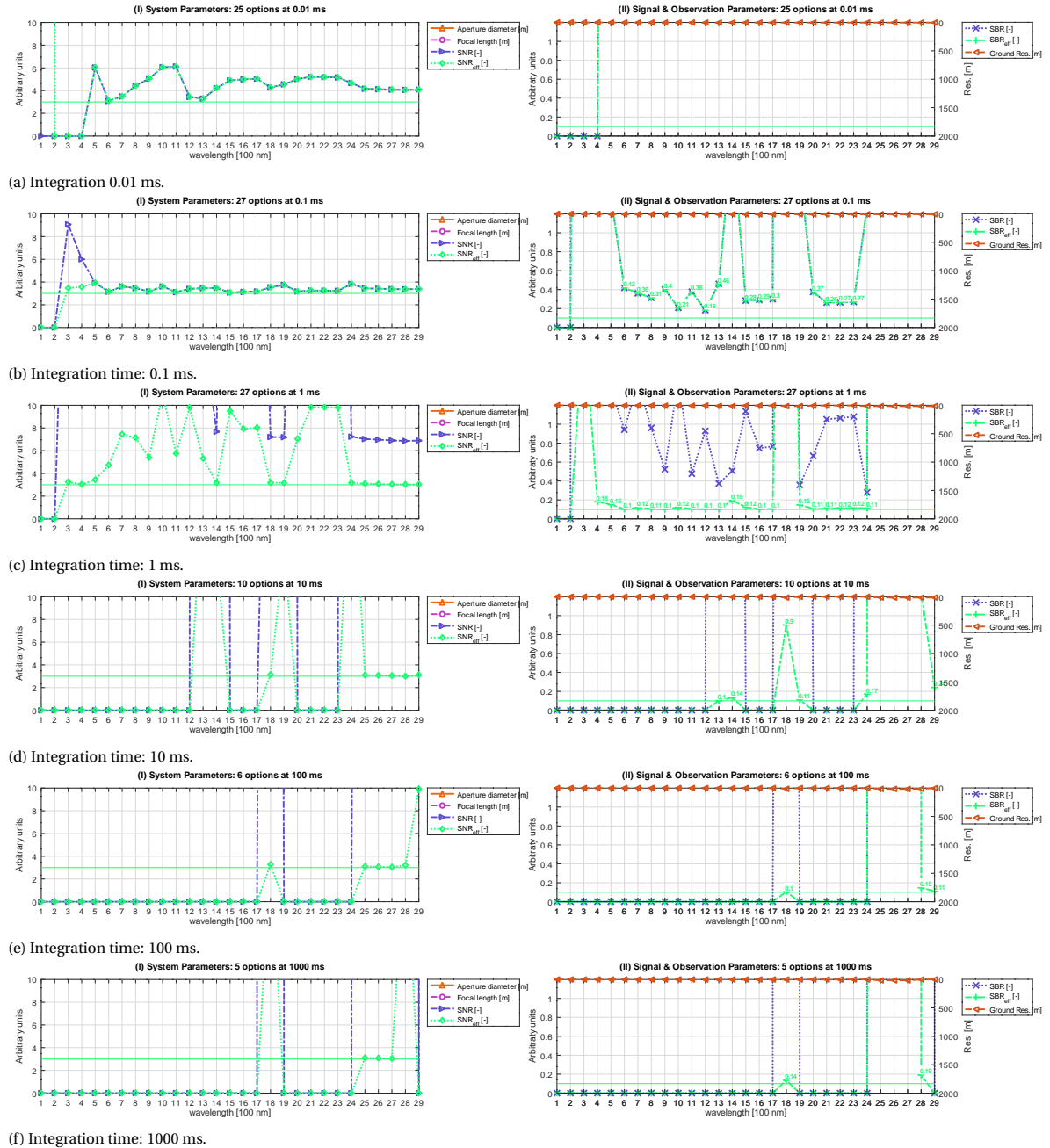


Figure G.11: Tracking optical parameters for the tracking of meteor Met5Pers for 2 seconds, values shown for  $SNR_{eff} > 3$  and  $SBR_{eff} > 0.1$ .

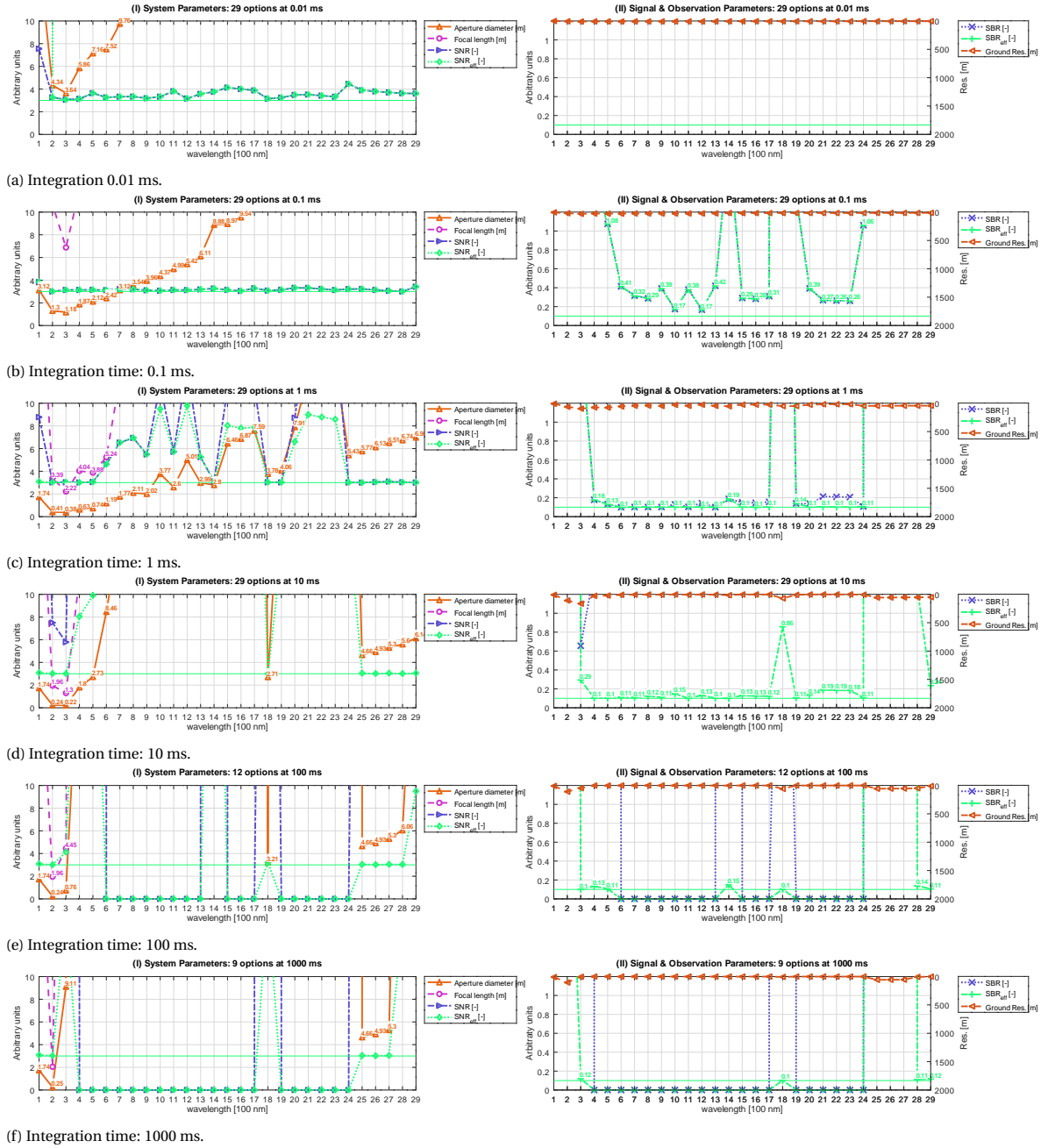


Figure G.12: Tracking optical parameters for the tracking of meteor Met5Pers for 0.7 seconds, values shown for  $SNR_{eff} > 3$  and  $SBR_{eff} > 0.1$ .

### G.6. Hayabusa

Below all the results for the detection of Hayabusa are shown.

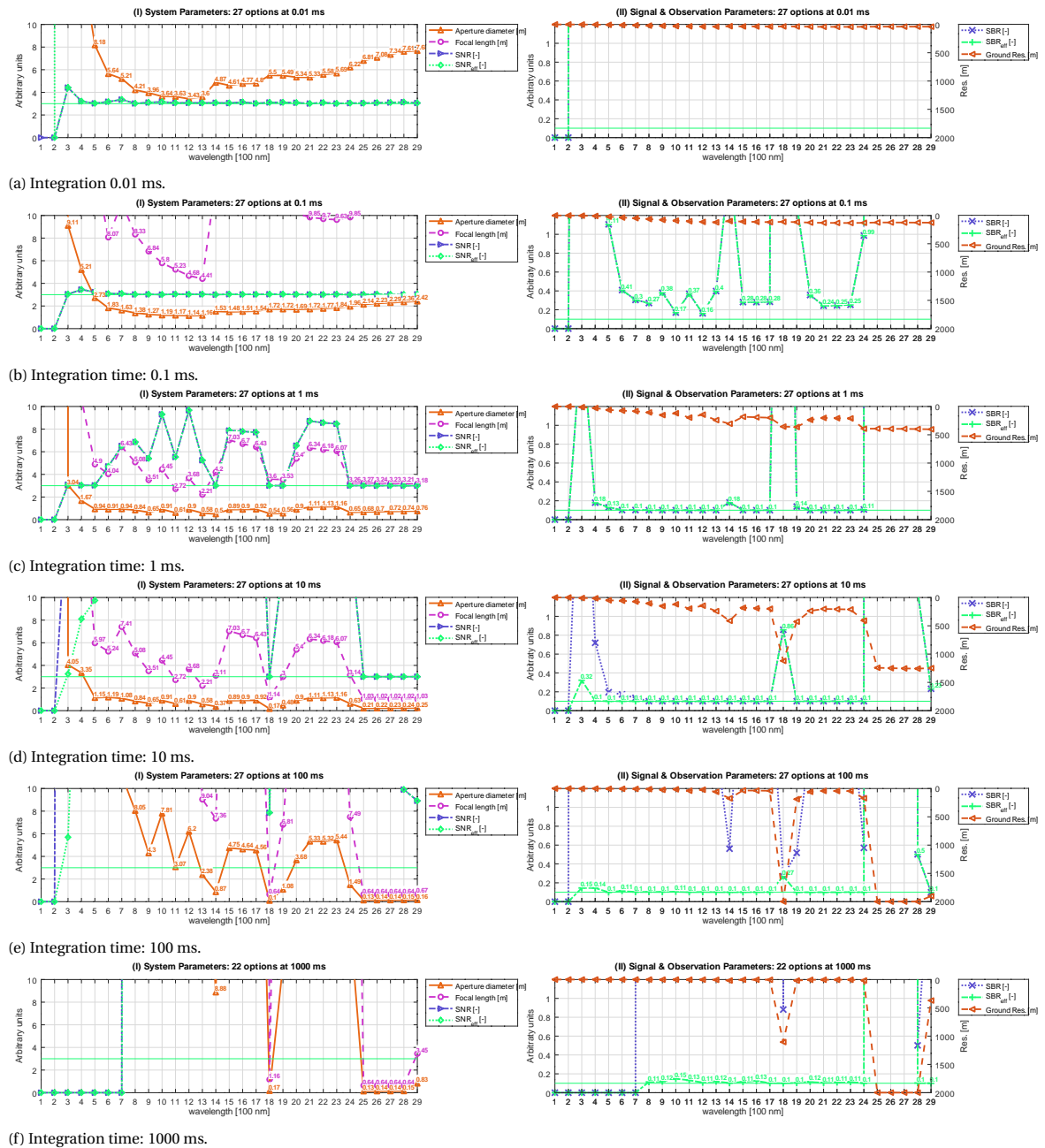


Figure G.13: Detection optical parameters for meteor Hayabusa, values shown for  $SNR_{eff} > 3$  and  $SBR_{eff} > 0.1$ .

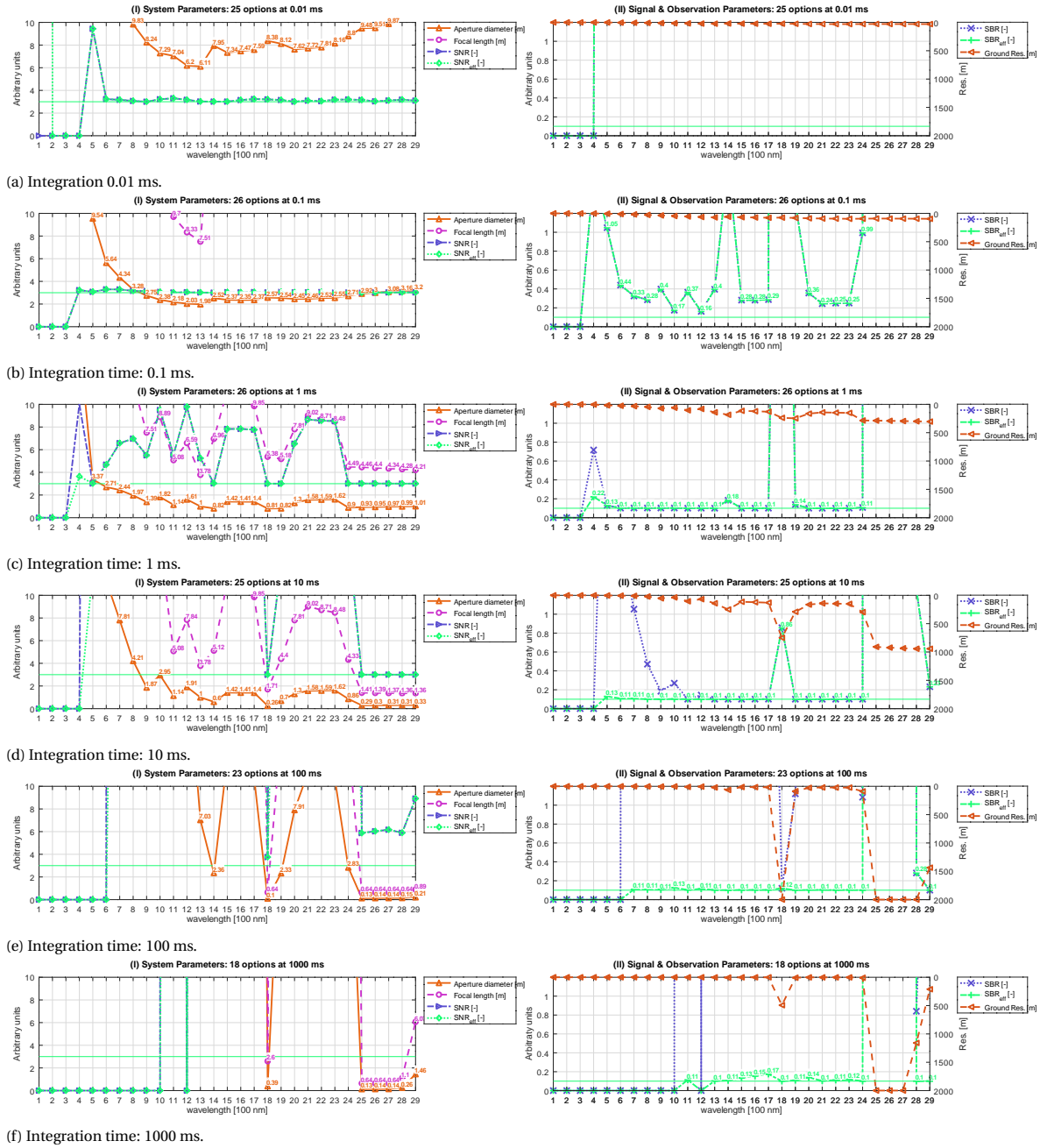


Figure G.14: Tracking optical parameters for the tracking of Hayabusa for 20 seconds, values shown for  $SNR_{eff} > 3$  and  $SBR_{eff} > 0.1$ .

### G.7. Stardust

Below all the results for Stardust are shown.

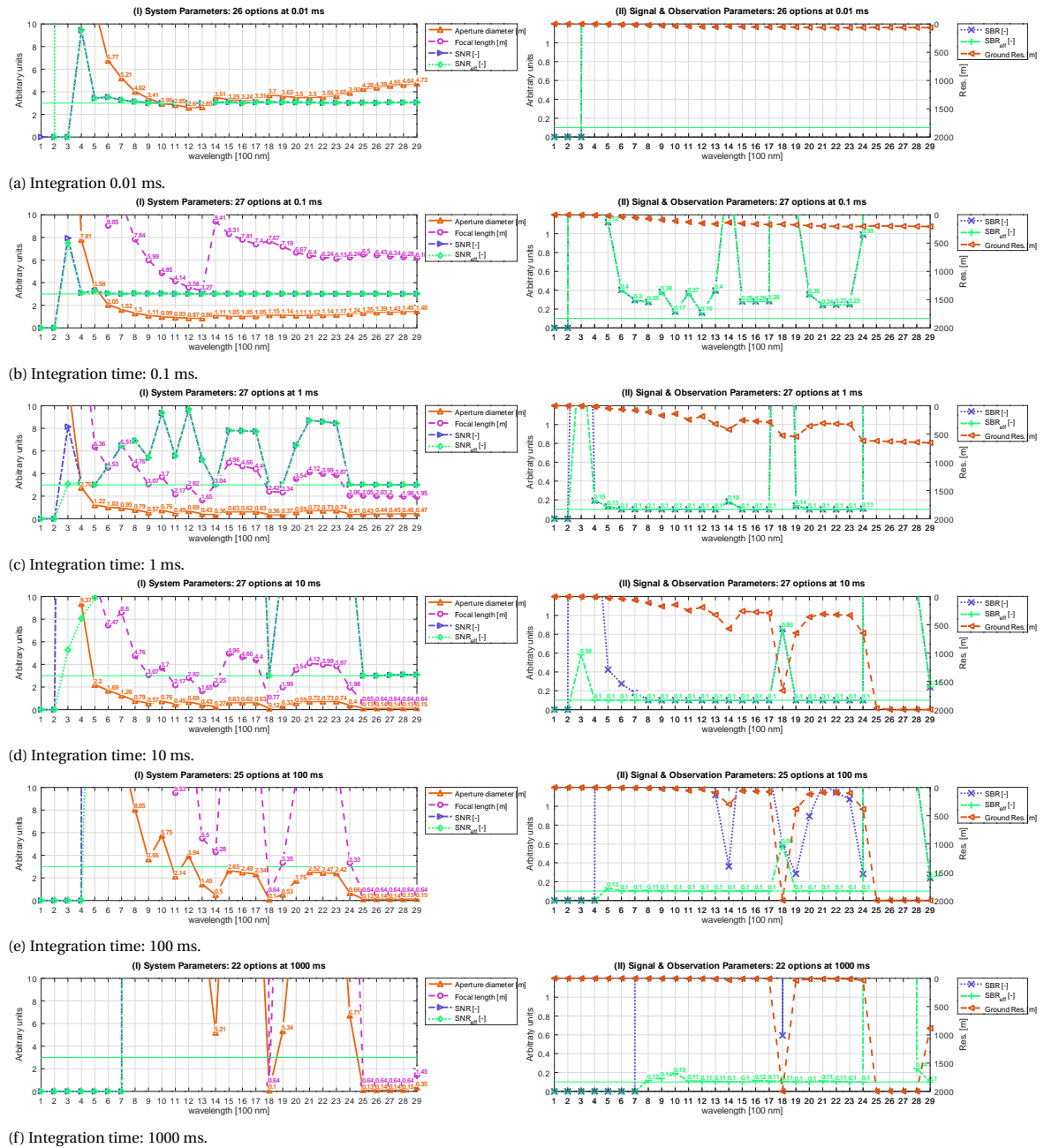


Figure G.15: Detection optical parameters for Stardust, values shown for  $SNR_{eff} > 3$  and  $SBR_{eff} > 0.1$ .

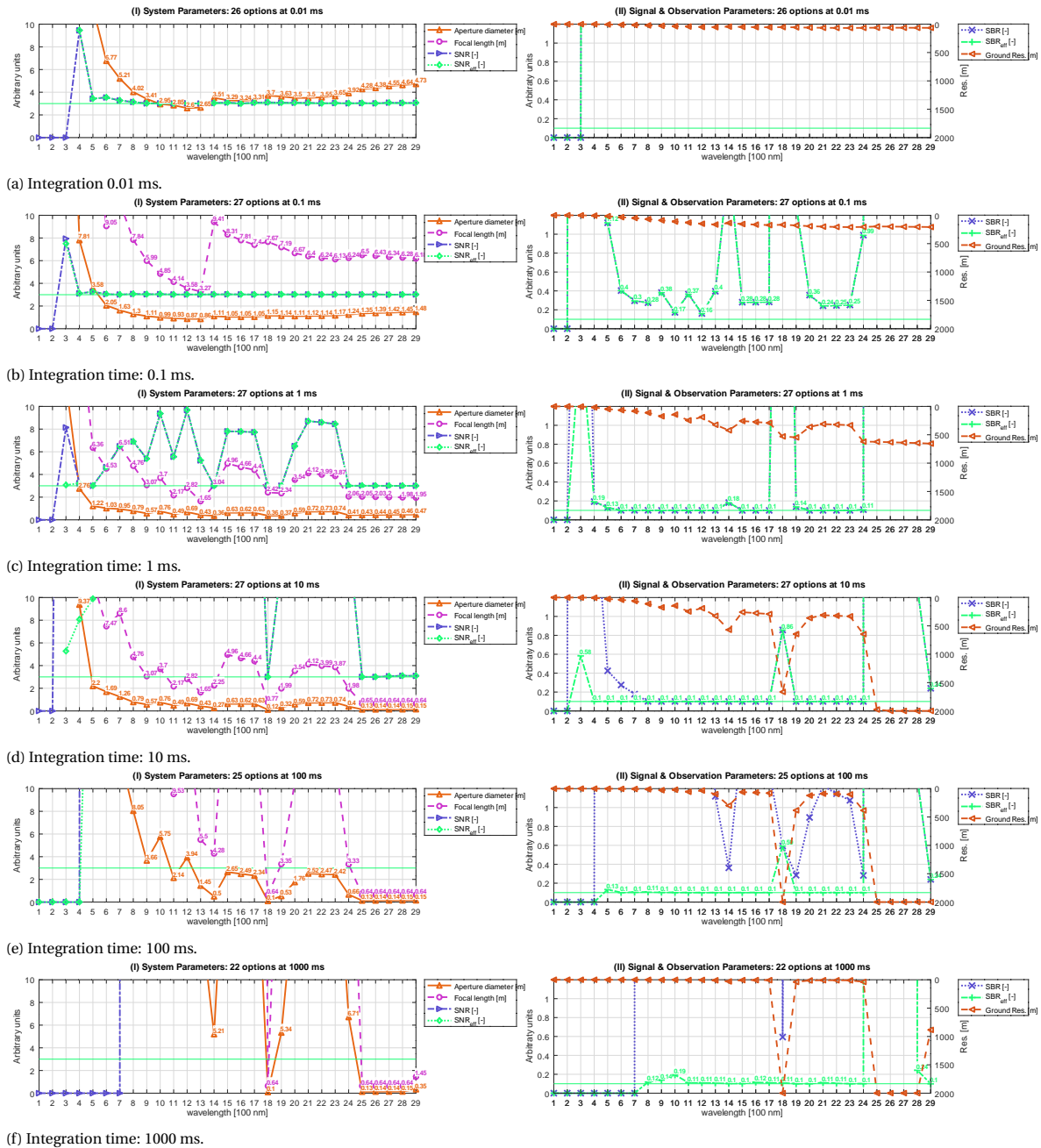


Figure G.16: Tracking optical parameters for the tracking of Stardust for 20 seconds, values shown for  $SNR_{eff} > 3$  and  $SBR_{eff} > 0.1$ .



# Bibliography

- Abe, S., K. Fujita, Y. Kakinami, O. Iiyama, H. Kurosaki, M. A. Shoemaker, Y. Shiba, M. Ueda, and M. Suzuki  
2011. Near-Ultraviolet and Visible Spectroscopy of Hayabusa Spacecraft Re-Entry. *Publications of the Astronomical Society of Japan*, 63(5):1011–1021.
- Ailor, W., W. Hallman, G. Steckel, and M. Weaver  
2005. Analysis of reentered debris and implications for survivability modeling. In *European Space Agency, (Special Publication) ESA SP*, number 587, Pp. 539–544.
- Ailor, W., M. Weaver, A. Feistel, and M. Sorge  
2013. Re-entry Breakup Recorder: Summary of Data for HTV-3 and ATV-3 Re-entries and Future Directions. In *6th European Conference on Space Debris*, volume 2013, Pp. 22–25.
- Allen, H. J. and A. Eggers  
1961. *A Study of the Motion and Aerodynamic Heating of Ballistic Missiles Entering the Earth's Atmosphere at High Supersonic Speeds*. Ames Aeronautical Laboratory.
- Aminou, D.  
2002. MSG 's SEVIRI Instrument. *Power*, Pp. 15–17.
- Anderson, J. D.  
2006. *Hypersonic and High-Temperature Gas Dynamics*, 2nd edition.
- Appeah, V.  
2017. Space-based Optical System Simulation.
- Ayers, W., R. McCrosky, and C. C.-Y. Shao  
1970. Photographic observations of 10 artificial meteors. *SAO Spec. Rep #317*, 317:40.
- Babadzhanov, P. B. and G. I. Kokhirova  
2009. Densities and porosities of meteoroids. *Astronomy and Astrophysics*, 495:353.
- Beech, M.  
1987. On the Trail of Meteor Trains. *Quarterly Journal of the Royal Astronomical Society*, 28:445–455.
- Borovička, J., S. Abe, L. Šrbený, P. Spurný, and P. A. Bland  
2011. Photographic and radiometric observations of the HAYABUSA re-entry.
- Bouquet, A., D. Baratoux, J. Vaubaillon, M. I. Gritsevich, D. Mimoun, O. Mousis, and S. Bouley  
2014. Simulation of the capabilities of an orbiter for monitoring the entry of interplanetary matter into the terrestrial atmosphere. *Planetary and Space Science*, 103:238–249.
- Boutamine, D. E., P. Reynier, R. Schmehl, L. Marraffa, and J. Steelant  
2007. Computational Analysis of Automated Transfer Vehicle Reentry Flow and Explosion Assessment. *Journal of Spacecraft and Rockets*, 44(4):860–870.
- Brandis, A. M. and C. O. Johnston  
2014. Characterization of Stagnation-Point Heat Flux for Earth Entry. In *45th AIAA Plasmadynamics and Lasers Conference*.
- Bronshten, V. A.  
1983. *Physics of Meteoric Phenomena*, 1 st edition. D. Reidel Publishing Company.
- Brown, P., D. Pack, W. N. Edwards, D. O. ReVelle, B. B. Yoo, R. E. Spalding, and E. Tagliaferri  
2004. The orbit, atmospheric dynamics, and initial mass of the Park Forest meteorite. *Meteoritics and Planetary Science*, 39(11):1781–1796.

- Brown, P. G., J. D. Assink, L. Astiz, R. Blaauw, M. B. Boslough, J. Borovička, N. Brachet, D. Brown, M. Campbell-Brown, L. Ceranna, W. Cooke, C. De Groot-Hedlin, D. P. Drob, W. Edwards, L. G. Evers, M. Garces, J. Gill, M. Hedlin, A. Kingery, G. Laske, A. Le Pichon, P. Mialle, D. E. Moser, A. Saffer, E. Silber, P. Smets, R. E. Spalding, P. Spurný, E. Tagliaferri, D. Uren, R. J. Weryk, R. Whitaker, and Z. Krzeminski  
2013. A 500-kiloton airburst over Chelyabinsk and an enhanced hazard from small impactors. *Nature*, 503(7475):238–241.
- Ceplecha, Z., W. G. Elford, D. O. ReVelle, R. L. Hawkes, M. Šimek, J. Borovička, and V. Porubčan  
1998. Meteor Phenomena and Bodies. *Space Science Reviews*, 84(3):327–471.
- Ceplecha, Z. and D. O. ReVelle  
2005. Fragmentation model of meteoroid motion, mass loss, and radiation in the atmosphere. *Meteoritics and Planetary Science*, 40(1):35–54.
- Davies, C.  
2006. Planetary Mission Entry Vehicles Quick Reference Guide. Version 3.0. *NASA STI/Recon Technical Report N*, 3:20.
- Dec, J. and R. Braun  
2006. An Approximate Ablative Thermal Protection System Sizing Tool for Entry System Design. In *44th AIAA Aerospace Sciences Meeting and Exhibit*.
- Dmitriev, V., V. Lupovka, and M. I. Gritsevich  
2015. Orbit determination based on meteor observations using numerical integration of equations of motion. *Planetary and Space Science*, 117:223–235.
- Everett, R. R.  
1993. *Space-Based IR Sensors*. Technical Support Group.
- Filachev, A. M., T. Ponomarenko, J. J. Taubkin, and M. B. Ushakova  
2003. Infra-red focal plane arrays: state of the art and development trends BT - Proceedings of SPIE. volume 5126, Pp. 52–85.
- Geul, J., E. Mooij, and R. Noomen  
2018. Analysis of Uncertainties and Modeling in Short-Term Reentry Predictions. *Journal of Guidance, Control, and Dynamics*, 41(6):1276–1289.
- Giancoli, D. C.  
2009. *Physics for Scientists & Engineers*, 4th edition. Pearson.
- Goodman, S. J., R. J. Blakeslee, W. J. Koshak, D. Mach, J. Bailey, D. Buechler, L. Carey, C. Schultz, M. Bateman, E. McCaul, and G. Stano  
2013. The GOES-R Geostationary Lightning Mapper (GLM). *Atmospheric Research*, 125-126:34–49.
- Grinstead, J. H., P. M. Jenniskens, A. M. Cassell, J. Albers, and M. Winterm  
2011. Airborne Observation of the Hayabusa Sample Return Capsule Re-Entry. *42nd AIAA Thermophysics Conference; 27-30 June 2011; Honolulu, HI*, 10.
- Gritsevich, M. I.  
2007. Approximation of the Observed Motion of Bolides by the Analytical Solution of the Equations of Meteor Physics. *Solar System Research*, 41(6):509–514.
- Gritsevich, M. I.  
2009. Determination of parameters of meteor bodies based on flight observational data. *Advances in Space Research*, 44(3):323–334.
- Gritsevich, M. I. and D. Koschny  
2011. Constraining the luminous efficiency of meteors. *Icarus*, 212(2):877–884.
- Gural, P. S.  
2012. A new method of meteor trajectory determination applied to multiple unsynchronized video cameras. *Meteoritics and Planetary Science*, 47(9):1405–1418.

- Hall, R.  
1960. The Lift and Drag on a rotating Cylinder in Supersonic Crossflow.
- Halliday, I.  
1988. Geminid fireballs and the peculiar asteroid 3200 Phaethon. *Icarus*, 76(2):279–294.
- Halliday, I., P. Feldman, and A. Blackwell  
1987. Evidence from meteor patrol photographs for a nonastronomical origin of the reported optical flashes in Perseus. *The Astrophysical Journal*, 320:L153.
- Halliday, I., A. A. Griffin, and A. T. Blackwell  
1981. The Innisfree meteorite fall: A photographic analysis of fragmentation, dynamics and luminosity. *Meteoritics*, 16(2):153–170.
- Halliday, I., A. A. Griffin, and A. T. Blackwell  
1996. Detailed data for 259 fireballs from the Canadian camera network and inferences concerning the influx of large meteoroids. *Meteoritics and Planetary Science*, 31(2):185–217.
- Hawkins, G. and E. Upton  
1958. The Influx Rate of Meteors in the Earth's Atmosphere. *The Astrophysical Journal*, 128(3):727–735.
- Hirschel, E. H.  
2015. *Basics of Aerothermodynamics*, 2nd, revis edition. Springer International Publishing Switzerland.
- Hirschel, E. H. and C. Weiland  
2009. *Selected aerothermodynamic design problems of hypersonic flight vehicles*.
- Horvath, T. J., S. Berry, S. Alter, R. Blanchard, R. Schwartz, M. Ross, and S. Tack  
2007. Shuttle Entry Imaging Using Infrared Thermography. *39th AIAA Thermophysics Conference*, (June):1–20.
- Horvath, T. J., M. F. Cagle, J. H. Grinstead, and D. M. Gibson  
2013. Remote observations of reentering spacecraft including the space shuttle orbiter. In *IEEE Aerospace Conference Proceedings*.
- Jacchia, L. G., F. Verniani, and R. E. Briggs  
1967. An Analysis of the Atmospheric Trajectories of 412 Precisely Reduced Photographic Meteors. *Smithsonian Contributions to Astrophysics*, 10(1):139.
- Jenniskens, P.  
2014. Meteors. 3:1279–1285.
- Jenniskens, P., J. Albers, C. E. Tillier, S. F. Edgington, R. S. Longenbaugh, S. J. Goodman, S. D. Rudlosky, A. R. Hildebrand, L. Hanton, F. Ciceri, R. Nowell, E. Lyytinen, D. Hladiuk, D. Free, N. Moskovitz, L. Bright, C. O. Johnston, and E. Stern  
2018. Detection of meteoroid impacts by the Geostationary Lightning Mapper on the GOES-16 satellite.
- Jenniskens, P., D. Kontinos, D. Jordan, M. Wright, J. Olejniczak, G. Raiche, P. Wercinski, P. N. Desai, M. J. Taylor, H. C. Stenbaek-Nielsen, and A. Hildebrand  
2005. Preparing for the Meteoric Return of Stardust. Technical Report 6.
- Jenniskens, P. M.  
2006. *Meteor showers and their parent comets*. Cambridge : Cambridge University Press, 2006.
- Johnston, C. O., E. C. Stern, and L. F. Wheeler  
2018. Radiative heating of large meteoroids during atmospheric entry. *Icarus*, 309:25–44.
- Jones, J. and T. Kaiser  
1966. The effects of thermal radiation, conduction and meteoroid heat capacity on meteoric ablation. *Monthly Notices of the Royal Astronomical Society*, 133:411–420.
- Kellogg, W. W. and S. Passman  
1955. Infrared Techniques Applied to the Detection and Interception of Intercontinental Ballistic Missiles.

- Klinkrad, H.  
2005. Scarab -a Multi-Disciplinary Code for Destruction Analysis of Space-Craft during Re- Entry.
- Koschny, D. and J. Diaz del Rio  
2002. Meteor orbit and trajectory software to determine meteor position. *Journal of International Meteor Organization*, 30(4):87–101.
- Kotsiantis, S.  
2007. Supervised machine learning: A review of classification techniques. *Informatica*, 31:249–268.
- Lapin, E. E.  
1975. Surveillance by Satellite.
- Lips, T., B. Fritsche, R. Kanzler, T. Schleutker, A. Gülhan, B. Bonvoisin, T. Soares, and G. Sinnema  
2017. About the demisability of propellant tanks during atmospheric re-entry from LEO. *Journal of Space Safety Engineering*, 4(2):99–104.
- Lips, T., S. Lohle, T. Marynowsky, D. Rees, H. C. Stenbeak-Nielsen, M. L. Beks, and J. Hatton  
2010. Assessment of the ATV-1 re-entry observation campaign for future Re-entry missions. In *European Space Agency, (Special Publication) ESA SP*, volume 680 SP.
- Loehle, S., F. Zander, T. Hermann, M. Eberhart, A. Meindl, R. Oefele, J. Vaubailon, F. Colas, P. Vernazza, A. Drouard, and J. Gattaccca  
2017. Experimental Simulation of Meteorite Ablation during Earth Entry Using a Plasma Wind Tunnel. *The Astrophysical Journal*, 837(2):112.
- Löhle, S., A. Mezger, and H. Fulge  
2013. Measured surface temperatures of the Hayabusa capsule during re-entry determined from ground observation. *Acta Astronautica*, 84:134–140.
- Lyytinen, E. and M. I. Gritsevich  
2016. Implications of the atmospheric density profile in the processing of fireball observations. *Planetary and Space Science*, 120:35–42.
- Marraffa, L.  
2008. Reentry technologies for Sample Return capsules. Technical report.
- Mathias, D. L., L. F. Wheeler, and J. L. Dotson  
2017. A probabilistic asteroid impact risk model: assessment of sub-300 m impacts. *Icarus*, 289:106–119.
- McCrosky, R.  
1958. The Meteor Wake. *The Astronomical Journal*, Pp. 97–105.
- McCrosky, R. and A. Posen  
1968. Special data-reduction procedures for Prairie Network meteor photographs. *Smithson. Astrophys. Obs. Special Report*, 273:1–88.
- McKinley, D. W. R.  
1961. *Meteor Science and Engineering*. McGraw-Hill Book Company.
- Mitcheltree, R. A., R. G. Wilmoth, F. M. Cheatwood, G. J. Brauckmann, and F. A. Greene  
1999. Aerodynamics of the Stardust Sample Return Capsule. *Journal of Spacecraft and Rockets*, 36(3):436–441.
- Mooij, E.  
2016. AE4870B - Re-entry Systems Lecture Notes.
- Murcray, D. G., F. H. Murcray, and W. J. Williams  
1965. Variation with altitude of the transmittance of the Earth's atmosphere with grating resolution. Technical report.
- NASA  
2012. Aerothermodynamics Course. In *Thermal & Fluids Analysis Workshop*, P. 142.

- Nemtchinov, I., R. Spalding, C. Jacobs, E. Tagliaferri, N. Artemieva, A. Golub, I. Kosarev, O. Popova, V. Svetsov, and V. V. Shuvalov  
1995. Assessment of the Large Meteoroid Characteristics from the Light Curves Obtained by Satellite and Groundbased Networks.
- Nemtchinov, I. V., V. V. Svetsov, I. B. Kosarev, A. P. Golub', O. P. Popova, V. V. Shuvalov, R. E. Spalding, C. Jacobs, and E. Tagliaferri  
1997. Assessment of kinetic energy of meteoroids detected by satellite-based light sensors. *Icarus*, 130(2):259–274.
- Ohkawa, T., Y. Iijima, M. Sato, K. Ohnishi, Y. Kagaya, T. Tanabe, and J. I. Watanabe  
2012. Brightness of HAYABUSA spacecraft reentry: Artificial fireball. *Publications of the Astronomical Society of Japan*, 64(1).
- Ohnishi, K., J. I. Watanabe, M. Sato, T. Ohkawa, and N. Ebizuka  
2011. Spectroscopic observation of the re-entry capsule of HAYABUSA spacecraft. *Publications of the Astronomical Society of Japan*.
- Ohsawa, R., S. Sako, Y. Sarugaku, F. Usui, T. Ootsubo, Y. Fujiwara, M. Sato, T. Kasuga, K. Arimatsu, J. ichi Watanabe, M. Doi, N. Kobayashi, H. Takahashi, K. Motohara, T. Morokuma, M. Konishi, T. Aoki, T. Soyano, K. Tarusawa, Y. Mori, Y. Nakada, M. Ichiki, N. Arima, Y. Kojima, M. Morita, T. Shigeyama, Y. Ita, M. Kokubo, K. Mitsuda, H. Maehara, N. Tominaga, T. Yamashita, S. Ikeda, M. Morii, S. Urakawa, S. ichiro Okumura, and M. Yoshikawa  
2018. Luminosity function of faint sporadic meteors measured with a wide-field CMOS mosaic camera Tomo-e PM.
- Ohsawa, R., S. Sako, H. Takahashi, Y. Kikuchi, M. Doi, N. Kobayashi, T. Aoki, K. Arimatsu, M. Ichiki, S. Ikeda, Y. Ita, T. Kasuga, H. Kawakita, M. Kokubo, H. Maehara, N. Matsunaga, H. Mito, K. Mitsuda, T. Miyata, K. Mori, Y. Mori, M. Morii, T. Morokuma, K. Motohara, Y. Nakada, S.-i. Okumura, H. Onozato, K. Osawa, Y. Sarugaku, M. Sato, T. Shigeyama, T. Soyano, M. Tanaka, Y. Taniguchi, A. Tanikawa, K. Tarusawa, N. Tominaga, T. Totani, S. Urakawa, F. Usui, J. Watanabe, J. Yamaguchi, and M. Yoshikawa  
2016. Development of a real-time data processing system for a prototype of the Tomo-e Gozen wide field CMOS camera. Pp. 1–8.
- Olynick, D., Y.-K. Chen, and M. E. Tauber  
1998. Aerothermodynamics of the Stardust Sample Return Capsule. *Journal of Spacecraft and Rockets*, 36(3):12–15.
- Ortega, M.  
2016. Design of a 3U Cubesat for Meteor Detection and Characterization. (February):26–30.
- Popova, O.  
2005. Meteoroid ablation models.
- Popova, O. P., P. Jenniskens, V. Emel', A. Kartashova, E. Biryukov, S. Khaibrakhmanov, V. Shuvalov, Y. Rybnov, A. Dudorov, V. I. Grokhovsky, D. D. Badyukov, Q.-Z. Yin, P. S. Gural, J. Albers, M. Granvik, L. G. Evers, J. Kuiper, V. Kharlamov, A. Solovyov, Y. S. Rusakov, S. Korotkiy, I. Serdyuk, A. V. Korochantsev, M. Y. Larionov, D. Glazachev, A. E. Mayer, G. Gisler, S. V. Gladkovsky, J. Wimpenny, M. E. Sanborn, A. Yamakawa, K. L. Verosub, D. J. Rowland, S. Roeske, N. W. Botto, J. M. Friedrich, M. E. Zolensky, L. Le, D. Ross, K. Ziegler, T. Nakamura, I. Ahn, J. I. Lee, Q. Zhou, X.-H. Li, Q.-L. Li, Y. Liu, G.-Q. Tang, T. Hiroi, D. Sears, I. A. Weinstein, A. S. Vokhmintsev, A. V. Ishchenko, P. Schmitt-Kopplin, N. Hertkorn, K. Nagao, M. K. Haba, M. Komatsu, and T. Mikouchi  
2013a. Chelyabinsk Airburst, Damage Assessment, Meteorite Recovery, and Characterization. *Science and Technology Center of the Social and Youth Initiatives Organization*, 36:29.
- Popova, O. P., P. Jenniskens, V. Emel'yanenko, A. Kartashova, E. Biryukov, S. Khaibrakhmanov, V. Shuvalov, Y. Rybnov, A. Dudorov, V. I. Grokhovsky, D. D. Badyukov, Q. Z. Yin, P. S. Gural, J. Albers, M. Granvik, L. G. Evers, J. Kuiper, V. Kharlamov, A. Solovyov, Y. S. Rusakov, S. Korotkiy, I. Serdyuk, A. V. Korochantsev, M. Y. Larionov, D. Glazachev, A. E. Mayer, G. Gisler, S. V. Gladkovsky, J. Wimpenny, M. E. Sanborn, A. Yamakawa, K. L. Verosub, D. J. Rowland, S. Roeske, N. W. Botto, J. M. Friedrich, M. E. Zolensky, L. Le, D. Ross, K. Ziegler,

- T. Nakamura, I. Ahn, J. I. Lee, Q. Zhou, X. H. Li, Q. L. Li, Y. Liu, G. Q. Tang, T. Hiroi, D. Sears, I. A. Weinstein, A. S. Vokhmintsev, A. V. Ishchenko, P. Schmitt-Kopplin, N. Hertkorn, K. Nagao, M. K. Haba, M. Komatsu, and T. Mikouchi  
2013b. Supplementary Materials for Chelyabinsk airburst, damage assessment, meteorite recovery, and characterization. Technical Report 6162.
- Proud, S. R.  
2013. Reconstructing the orbit of the Chelyabinsk meteor using satellite observations. *Geophysical Research Letters*, 40(13):3351–3355.
- Putnam, Z. R. and R. D. Braun  
2015. Extension and Enhancement of the Allen–Eggers Analytical Ballistic Entry Trajectory Solution. *Journal of Guidance, Control, and Dynamics*.
- Register, P. J., D. L. Mathias, and L. F. Wheeler  
2017. Asteroid fragmentation approaches for modeling atmospheric energy deposition. *Icarus*, 284:157–166.
- ReVelle, D. O. and W. N. Edwards  
2007. Stardust - An artificial, low-velocity "meteor" fall and recovery: 15 January 2006. *Meteoritics and Planetary Science*, 42(2):271–299.
- Riccio, A., F. Raimondo, A. Sellitto, V. Carandente, R. Scigliano, and D. Tescione  
2017. Optimum design of ablative thermal protection systems for atmospheric entry vehicles. *Applied Thermal Engineering*, 119:541–552.
- Salmond, D. and H. Birch  
2001. A particle filter for track-before-detect. In *Proceedings of the 2001 American Control Conference. (Cat. No.01CH37148)*, Pp. 3755–3760 vol.5.
- Sarafian, H.  
2011. Trajectory of a baseball and its characters under the influence of a drag force and the magnus effect. In *Proceedings - 2011 International Conference on Computational Science and Its Applications, ICCSA 2011*, Pp. 51–59.
- Silber, E. A., M. Boslough, W. K. Hocking, M. I. Gritsevich, and R. W. Whitaker  
2018. Physics of Meteor Generated Shock Waves in the Earth's Atmosphere - A Review. *Advances in Space Research*.
- Silber, E. A., W. K. Hocking, M. L. Niculescu, M. I. Gritsevich, and R. E. Silber  
2017. On shock waves and the role of hyperthermal chemistry in the early diffusion of overdense meteor trains. *Monthly Notices of the Royal Astronomical Society*, 469(2):1869–1882.
- Snively, J. B., M. J. Taylor, P. Jenniskens, M. W. Winter, M. J. Kozubal, R. F. Dantowitz, and J. Breitmeyer  
2014. Near-Infrared Spectroscopy of Hayabusa Sample Return Capsule Reentry. *Journal of Spacecraft and Rockets*, 51(2):424–429.
- Stokan, E. and M. D. Campbell-Brown  
2015. A particle-based model for ablation and wake formation in faint meteors. *Monthly Notices of the Royal Astronomical Society*, 447(2):1580–1597.
- Stulov, V. P.  
1993. Heat transfer, mass entrainment, and luminosity of bolides. *Journal of Engineering Physics and Thermophysics*, 64(6).
- Suzuki, T., K. Fujita, T. Yamada, Y. Inatani, and N. Ishii  
2014. Postflight Thermal Protection System Analysis of Hayabusa Reentry Capsule. *Journal of Spacecraft and Rockets*, 51(1):96–105.
- Szasz, C., J. Kero, A. Pellinen-Wannberg, J. D. Mathews, N. J. Mitchell, and W. Singer  
2005. Latitudinal variations of diurnal meteor rates. *Earth, Moon and Planets*, 95(1-4):101–107.

- Tack, S., D. M. Tomek, T. J. Horvath, H. A. Verstynen, and E. J. Shea  
2010. Cast Glance Near Infrared Imaging Observations of the Space Shuttle During Hypersonic Re-entry. *48th Aerospace Science Meeting Conference*, (January).
- Tagliaferri, E.  
2010. Observation of meteoroid impacts by space-based sensors.
- Tagliaferri, E., R. Spalding, C. Jacobs, and Z. Cepelcha  
1995. Analysis of the Marshall Islands Fireball of February 1, 1994. *Earth, Moon, and Planets*, 68(1-3):563–572.
- Tagliaferri, E., R. E. Spalding, C. Jacobs, S. p. Worden, and A. Erlich  
1994. Detection of Meteoroid Impacts by Optical Sensors in Earth Orbit. In *Hazards Due to Comets and Asteroids*, Pp. 199–220. The University of Arizona Press.
- Tartakovsky, A. G. and J. Brown  
2008. Adaptive spatial-temporal filtering methods for clutter removal and target tracking. *IEEE Transactions on Aerospace and Electronic Systems*, 44(4):1522–1537.
- Trumble, K. A., I. Cozmuta, S. Sepka, P. Jenniskens, and M. Winter  
2010. Postflight Aerothermal Analysis of the Stardust Sample Return Capsule. *Journal of Spacecraft and Rockets*, 47(5):765–774.
- Ueda, M., Y. Shiba, M. Y. Yamamoto, K. Fujita, J. I. Watanabe, M. Sato, S. Abe, Y. Kakinami, S. Uehara, S. Okamoto, Y. Fujiwara, and T. Tanabe  
2011. Trajectory of HAYABUSA reentry determined from multisite TV observations. *Publications of the Astronomical Society of Japan*, 63(5):947–953.
- Vinković, D.  
2007. Thermalization of sputtered particles as the source of diffuse radiation from high altitude meteors. *Advances in Space Research*, 39(4):574–582.
- Vojacek, V.  
2011. Analysis of Fragmentation and Radiation of Meteoroids in the Atmosphere. Pp. 7–12.
- Wertz, J. R. and W. J. Larson  
2010. *Space Mission Analysis and Design*, 3rd edition. Microcosm Press and Springer.
- Weryk, R. J. and P. G. Brown  
2013. Simultaneous radar and video meteors - II: Photometry and ionisation. *Planetary and Space Science*, 81:32–47.
- Wheeler, L. E., P. J. Register, and D. L. Mathias  
2017. A fragment-cloud model for asteroid breakup and atmospheric energy deposition. *Icarus*.
- Winter, M., R. McDaniel, Y.-K. Chen, Y. Liu, D. Saunders, and P. Jenniskens  
2012. Radiation Modeling for the Reentry of the Hayabusa Sample Return Capsule. In *50th AIAA Aerospace Sciences Meeting including the New Horizons Forum and Aerospace Exposition*.
- Yanagisawa, M.  
2015. Radiative characteristics of the Chelyabinsk superbolide. *Planetary and Space Science*, 118:79–89.
- Zalameda, J. N., A. B. Tietjen, D. M. Gibson, J. C. Taylor, S. Tack, B. C. Bush, C. D. Mercer, and E. J. Shea  
2010. Application of a near infrared imaging system for thermographic imaging of the space shuttle during hypersonic re-entry. *48th AIAA Aerospace Sciences Meeting Conference*, (January).
- Zhang, T., M. Li, Z. Zuo, W. Yang, and X. Sun  
2007. Moving dim point target detection with three-dimensional wide-to-exact search directional filtering. *Pattern Recognition Letters*, 28(2):246–253.